IS-T-690

RADIATION DAMAGE IN VANADIUM DOPED WITH OXYGEN

Ram Bajaj

Ph. D. Thesis Submitted to Iowa State University

Ames Laboratory, ERDA
Iowa State University
Ames, Iowa 50011

Date Transmitted: October 1975

PREPARED FOR THE U.S. ENERGY RESEARCH AND DEVELOPMENT ADMINISTRATION UNDER CONTRACT NO. W-7405-eng-82

DISCLAIMER

Available from: National Technical Information Service
U. S. Department of Commerce
P.O. Box 1553
Springfield, VA 22161

Price: Microfiche $2.25

Radiation damage in vanadium doped with oxygen

by

Ram Bajaj

A Dissertation Submitted to the
Graduate Faculty in Partial Fulfillment of
The Requirements for the Degree of
DOCTOR OF PHILOSOPHY

Department: Materials Science and Engineering
Major: Metallurgy

Approved:

Monroe S. Wechsler
In Charge of Major Work

For the Major Department

For the Graduate College

Iowa State University
Ames, Iowa
1975

TABLE OF CONTENTS

LIST OF TABLES

LIST OF FIGURES

Page

Page

Page

Page

Radiation damage in vanadium doped with oxygen

Ram Bajaj

Under the supervision of Monroe S. Wechsler
From the Department of Materials Science and Engineering
Iowa State University

Radiation damage caused by neutron irradiation was studied in vanadium containing various amounts of oxygen by transmission electron microscopy, tensile testing and hardness measurements. The major motive of the study was to delineate the role of an interstitial impurity (namely oxygen) on radiation damage in vanadium. Irradiation of polycrystalline samples containing 60-640 wt. ppm oxygen was carried out at 105°C to a dose of 1.2×10^{19} n/cm^2 (E>1 MeV) and tensile tests were carried out at room temperature following irradiation and post-irradiation annealing. Lower yield stress measurements indicate that neutron irradiation results in greater radiation hardening for specimens with larger oxygen concentration. Also, the further increase in strength upon post-irradiation annealing (radiation-anneal hardening) is enhanced by increasing oxygen content. It was concluded that the radiation-anneal hardening was caused by trapping of oxygen at the radiation-produced defect clusters. Similar behavior was exhibited by measurements of microhardness.

Radiation-produced defect clusters were studied by transmission electron microscopy in as-irradiated and post-irradiation-annealed single crystal vanadium irradiated to a dose of 1.4×10^{19} n/cm^2 (E>1 MeV) at 95°C. It was found that the number density of defect clusters increases with

increasing oxygen content and the average size decreases with increasing oxygen content. Upon post-irradiation annealing the defect clusters grow in size and decrease in density but the coarsening tendency is reduced for material containing higher oxygen concentrations. It is believed that oxygen acts as a nucleating agent for the defect clusters and stabilizes the clusters upon post-irradiation annealing by being trapped at the clusters.

Strain aging studies carried out on unirradiated and irradiated vanadium by tensile testing at room temperature indicate that the strain aging tendency increases with increasing oxygen concentration in both unirradiated and irradiated vanadium. However, comparison between irradiated and unirradiated materials indicates a reduced tendency for strain aging in the irradiated vanadium as measured by time of reappearance of yield drop. It is contended that the delay in reappearance of the yield drop is a manifestation of trapping of oxygen atoms at the radiation-produced defect clusters before they can reach dislocations and cause strain aging.

Dislocation channels were observed by transmission electron microscopy in as-irradiated and post-irradiation-annealed specimens deformed at room temperature, irrespective of oxygen content. The mechanism of channeling formation is still uncertain. However, the mechanism involving annealing of defect clusters by heat of plastic deformation appears plausible.

I. INTRODUCTION

A metal subjected to neutron bombardment undergoes changes in its physical and mechanical properties. In recent years there has been considerable interest in trying to interpret the changes upon neutron irradiation in terms of the defect structure produced. Until a few years ago most of the research on radiation damage in metals was centered on the face-centered cubic (f.c.c.) metals. In recent years, however, increasing attention has been devoted to radiation effects in body-centered cubic (b.c.c.) metals and alloys. In particular, refractory metals have been investigated because of high temperature applications. Among these, niobium and vanadium are of special interest because of their low neutron cross sections.

In the b.c.c. refractory metals the interstitial impurity content is of major importance since marked changes in physical and mechanical properties occur with interstitial impurities (e.g., O,C,N). Therefore, it is of interest to know how neutron bombardment will alter the properties of b.c.c. refractory metals with various impurity contents. The interstitial impurity chosen in this study is oxygen. The effects of neutron irradiation in vanadium doped with oxygen are important from both fundamental and applied points of view.

A. Fundamental Aspects

1. Origin of radiation-anneal hardening (RAH) and Stage III annealing

Radiation-anneal hardening (RAH) in b.c.c. metals is defined as the

increase in yield stress upon post-irradiation annealing. Stage III annealing in b.c.c. metals is the annealing stage observed in the vicinity of 0.2 T_m, where T_m is the melting temperature in degrees Kelvin. Since Stage III and RAH occur over the same temperature range, the two phenomena are assumed to stem from the same atomic rearrangements.

The earlier observations of RAH were interpreted in terms of intrinsic defects produced by radiation. Since then, other authors have observed similar effects in b.c.c. metals. There is still a controversy over the mechanism of RAH and Stage III in b.c.c. metals. Some investigators, however, believe that RAH and Stage III are caused by extrinsic defects (interstitial impurities) being trapped by radiation-produced defects and defect clusters and not due to migration of intrinsic defects such as vacancies or self-interstitials produced by irradiation.

There is some evidence in the work performed in this laboratory to suggest that the extrinsic mechanism is more probable, based on internal friction and electrical resistivity measurements on vanadium doped with oxygen. The present study is an attempt to give better insight into the mechanism of RAH and systematically delineate the role of interstitial impurities.

2. Radiation-produced defect clusters

a. Nucleation and density and size distribution The bombardment of metals with neutrons creates vacancies and interstitials which cluster together to form defect clusters and dislocation loops resolvable in an electron microscope. The nucleation of defect clusters is an important factor. It is of fundamental interest to know whether defect clusters

nucleate homogeneously or heterogeneously and the influence of interstitial impurities on the nucleation of defect clusters.

The density and size distribution of defect clusters govern the yield stress and the ductility of materials, a matter of importance from the basic as well as design points of view. Interstitial impurity atoms may have a considerable effect on the size and density of defect clusters. This study is intended to achieve a better understanding of the influence of interstitial impurities and post-irradiation annealing on the density and size distribution of defect clusters and to relate them to mechanical properties.

3. Strain aging phenomenon

Body-centered cubic metals containing interstitial impurities exhibit an increase in yield and flow stresses in a pre-deformed material upon aging at suitable temperatures. The influence of interstitial impurity content and neutron irradiation on the strain aging tendency is being studied for vanadium as a function of oxygen concentration.

B. Applied Aspects

Although vanadium as the base metal for cladding material for liquid-metal fast-breeder reactors (LMFBR's) looks unfavorable at the present time because of its affinity for oxygen dissolved in liquid sodium coolant, it is a prime candidate for the controlled thermonuclear (CTR) first wall material because of its favorable neutronics. The properties that make it attractive for this application are: (a) moderately high melting point, (b) low fast neutron reaction cross section, (c) short half life of isotopes produced upon irradiation, hence low induced radioactivity, (d) low shutdown decay

power, and (e) favorable radioactive waste management.

Other considerations for the choice of vanadium in this investigation are: (a) it is available in relatively high purity and (b) the major radioactive isotope of vanadium (V^{52}) has a relatively short halflife (3.76 minutes) and therefore does not pose any serious problems in handling of irradiated samples.

In its application for LMFBR's or CTR's, vanadium will be subjected to neutron irradiation and its mechanical integrity and dimensional stability are of importance from the point of view of design and safety. These considerations contribute to the motivation for this study.

In this dissertation six closely related aspects of neutron radiation damage of polycrystalline and single crystal vanadium and the subsequent behavior of irradiated samples upon deformation will be reported. They are

1. Radiation-anneal hardening in polycrystalline tensile samples doped with three levels of oxygen using tensile tests.
2. Radiation-anneal hardening in single crystal vanadium doped with oxygen using microhardness measurements.
3. Transmission electron microscopy (TEM) of as-irradiated and post-irradiated-annealed single crystal vanadium-oxygen.
4. Strain aging behavior of irradiated and unirradiated vanadium oxygen samples.
5. Dislocation channels produced upon deformation of as-irradiated and post-irradiation-annealed samples.
6. Microstructure of material deformed at room temperature and at liquid nitrogen temperature prior to irradiation, as revealed by transmission electron microscopy.

II. LITERATURE REVIEW

There has been an increasing interest in recent years in radiation damage in metals in general and b.c.c. metals in particular, and consequently there is a large accumulation of literature in this field. This survey is an attempt only to set background for the present study. The literature review will be divided into the following sections: (a) Mechanisms of radiation damage, (b) Radiation hardening mechanisms, (c) Experimental observations of radiation hardening, (d) Radiation-anneal hardening (RAH) and Stage III annealing, (e) Direct observation of defect clusters, (f) Dislocation channeling and (g) Strain aging.

A. Mechanisms of Radiation Damage

Numerous authors (1-12) have contributed to the present understanding of mechanisms of radiation damage. In this section only a brief qualitative treatment of some of the important aspects of radiation damage theory will be presented. An energetic particle, say a fast neutron with energy greater than 1 MeV (E>1 MeV) moving through matter, loses energy by (a) elastic collisions with lattice atoms and (b) excitation and ionization of atoms through charge interaction. The first is capable of displacing atoms from their normal positions resulting in vacancies, interstitials and replacements. The second is of little importance in metals, appearing only as heat. The atom struck by the neutron (primary knock-on) may receive sufficient energy not only to displace it from its lattice site but also to cause additional displacements when it strikes other atoms (secondary displacements). Usually, therefore, each primary collision initiates

a cascade of collisions resulting in vacancies in excess of thermodynamic equilibrium. The displaced atoms often stop at interstitial sites or nonequilibrium positions, provided they do not recombine with a neighboring vacancy. A vacancy and its previously associated atom, now located interstitially elsewhere in the lattice, is called a displacement pair. If the energy transferred in a collision is less than the displacement energy or when the energetic particle makes a glancing collision with the atoms, the stationary atom experiences an increased amplitude of vibration. These excited atoms transfer energy to neighboring atoms in the order of a vibrational period (10^{-13} to 10^{-14} sec), resulting in more or less violent agitation briefly affecting all atoms in the vicinity. This is known as a "thermal spike" (1). As decay through dissipation of energy (heat) returns the region to equilibrium, the thermal spike will cause no permanent damage in metals. However, the metal within the spike is held at a higher pressure (1,3) by the surrounding lattice, resulting in plastic deformation at the center of the spike sufficient to generate dislocation loops with radii of 40 Å to 50 Å. These loops within the spikes will be retained as the thermal spike cools only if the cooling pattern does not reverse the loop growth process or the loop becomes entangled during the formation of the spike.

Another spike effect proposed in the form of a displacement spike by Brinkman (6) is produced at the end of the trajectory of a fast moving atom when the mean free path between displacement collisions becomes approximately equal to an atomic spacing. When the energy of the primary knock-on becomes less than a transition value (50-23,000 eV depending on

atomic number) the particle is very rapidly brought to rest amid an intense shower of secondary displacements which are not independent of each other. The atoms are violently raised to the molten state with turbulent flow and complete rearrangement, rapid quenching and resolidification occur over a very short time. The resolidified region is substantially in registry with the surrounding lattice since the parent lattice acts as nucleus for crystallization. It has been suggested that vacancies and interstitials more or less completely anneal in this region (6) with damage showing as small dislocation loops.

Silsbee (13) first called attention to the importance of focusing effects in radiation damage because of the crystallinity of metals. Seeger (10) and Seeger and Essmann (11) pointed out that the focusing effect discussed by Silsbee might lead to generation and propagation of dynamic crowdions. Dynamic crowdions differ from focusons proposed by Silsbee (13) in that they transport not only energy (and momentum) but also matter. Seeger proposed that the primary and secondary knock-ons collide with almost any atom towards the end of their paths, transferring small multiples of displacement energies which are sufficient to produce a large fraction of the displacements in the form of dynamic crowdions (shown in Figure 1). This results in a local high density of vacant sites, surrounded by a few nearby interstitials and a substantial number of distant interstitials separated from vacancies by the crowdion mechanism. A similar mechanism proposed by Seeger and Essmann (11) is called the replacement chain, which involves a sequence of replacement collisions in which a moving atom strikes and displaces a lattice atom but is trapped itself in the lattice site, thus

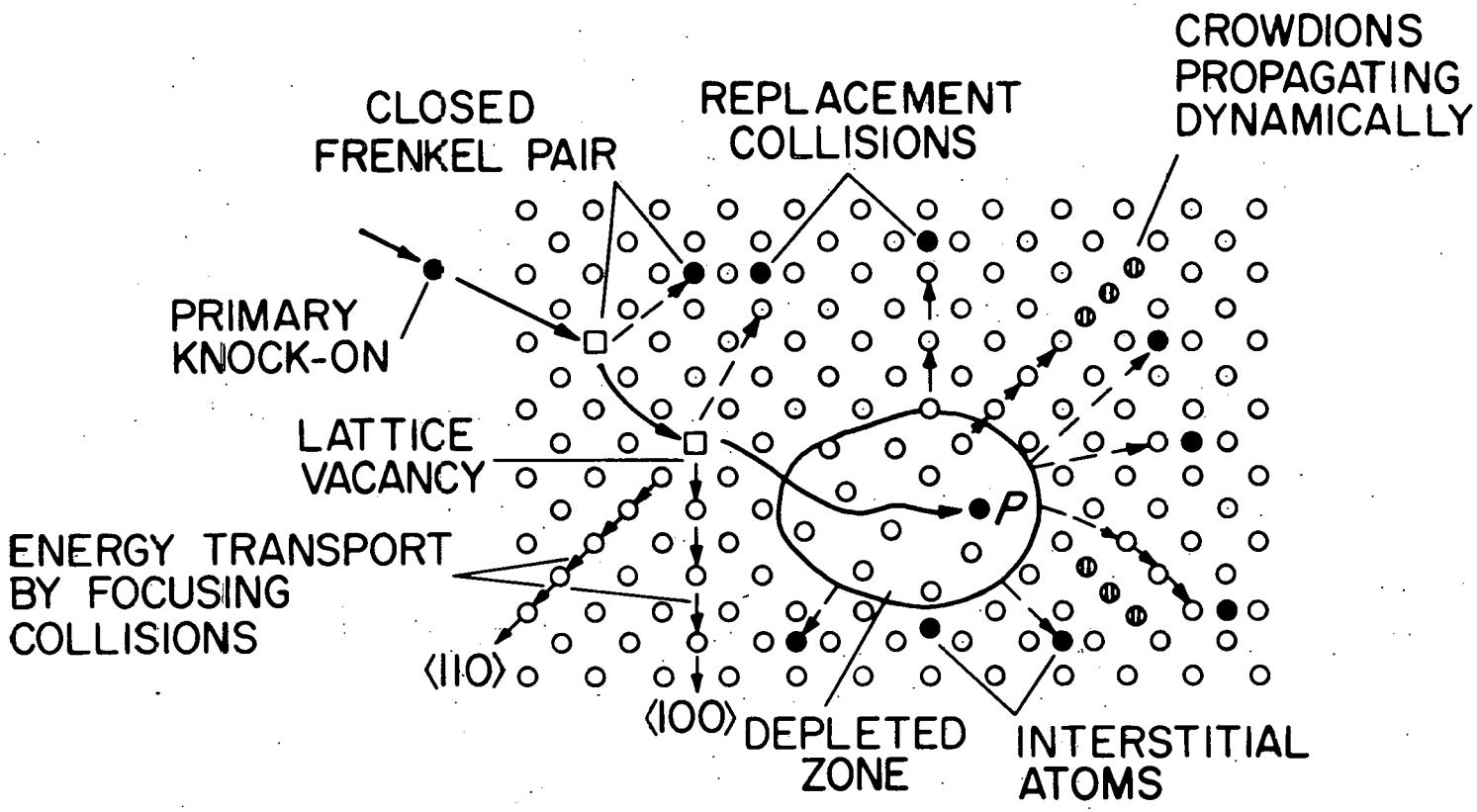

Figure 1. Schematic representation of formation of dynamic crowdions (after Seeger (10))

replacing the struck atom at the site. The struck atom undergoes the same process with a third atom and so on, resulting in a chain of replacements with an interstitial coming to rest at the end of the chain. Crowdions and replacement chains leave behind vacancy-rich regions in the displacement spikes while the interstitials come to rest at far distances from the vacancy-rich or depleted zones.

Another mechanism of importance in which energy may be lost in subthreshold interaction due to the regular arrangement of atoms in metals is called channeling. In channeling, the moving atom is deflected into open channels between the atom rows, where it undergoes glancing collisions with atoms along the walls of the channel (14). One evidence of channeling is the anomalously high penetration of ions bombarded on single crystals as compared to that for amorphous forms of the same material (15). Oen and Robinson (16) have treated the channeling phenomenon in detail. Noggle and Oen (17) bombarded single crystal gold films with 51 MeV iodine ions. They observed 14 times less damage when the ion beam was directed along channeling directions than when the beam was unaligned. However, the ion beam must be aligned to within one or two degrees and thus it seems unlikely that many recoiling atoms will emerge from a lattice site in a direction appropriate for channeling. Besides, the neighboring atoms would tend to block the struck atoms from the channels.

For a schematic diagram of radiation damage, see Figure 2.

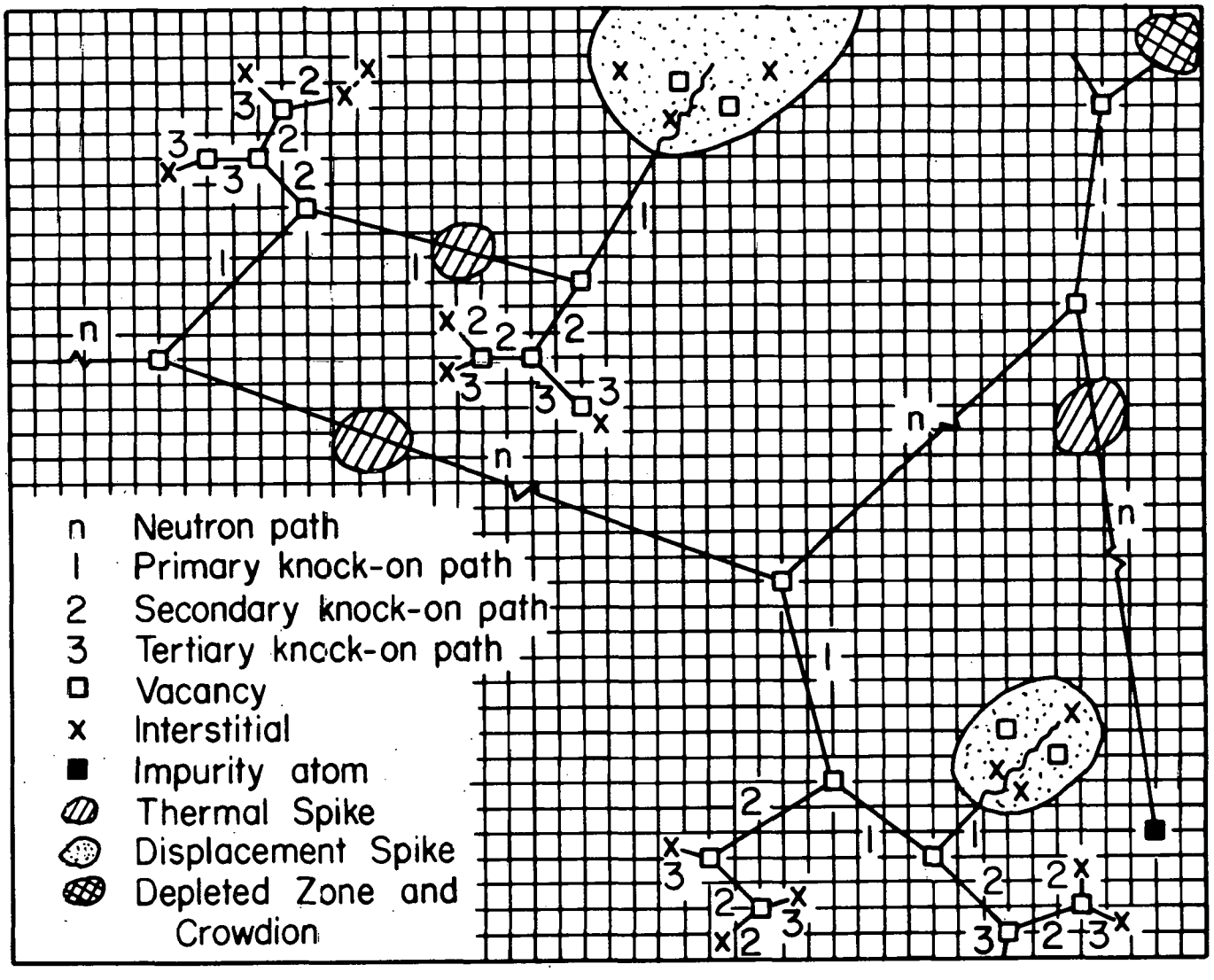

Figure 2. Schematic representation of radiation damage in metals (after Smith (12))

B. Radiation Hardening Mechanisms

It has been well established that neutron irradiation causes an increase in resistance to plastic deformation as is evidenced by the increase in yield stress and indentation hardness. The basis for models of radiation hardening is that irradiation introduces barriers in the form of defect clusters, which impede the motion of dislocations. The barriers may be displacement spikes, depleted zones, dislocation loops or aggregates of vacancies or interstitials.

In the dispersed barrier model, the barriers are assumed to be randomly distributed on the slip plane of the dislocations. During plastic deformation, these barriers act as obstacles to the movement of dislocations. Various versions of the dispersed barrier model have been developed. Orowan (18) evaluated the shear stress τ at which a dislocation will bow around strong barriers separated by a distance ℓ, as illustrated in Figure 3. It is given by

$$\tau = \frac{Gb}{\ell} \qquad (1)$$

where G is the shear modulus and b is the Burgers vector. Holmes (19) presented the expression for the critical shear stress (Figure 4)

$$\tau = \frac{1}{b\ell}(F_c - F_t) \qquad (2)$$

where F_c is the critical force for breaking through the barriers at absolute zero, F_t is an additional force facilitating surmounting the barriers due to thermal vibrations, and ℓ is the average barrier spacing on the slip

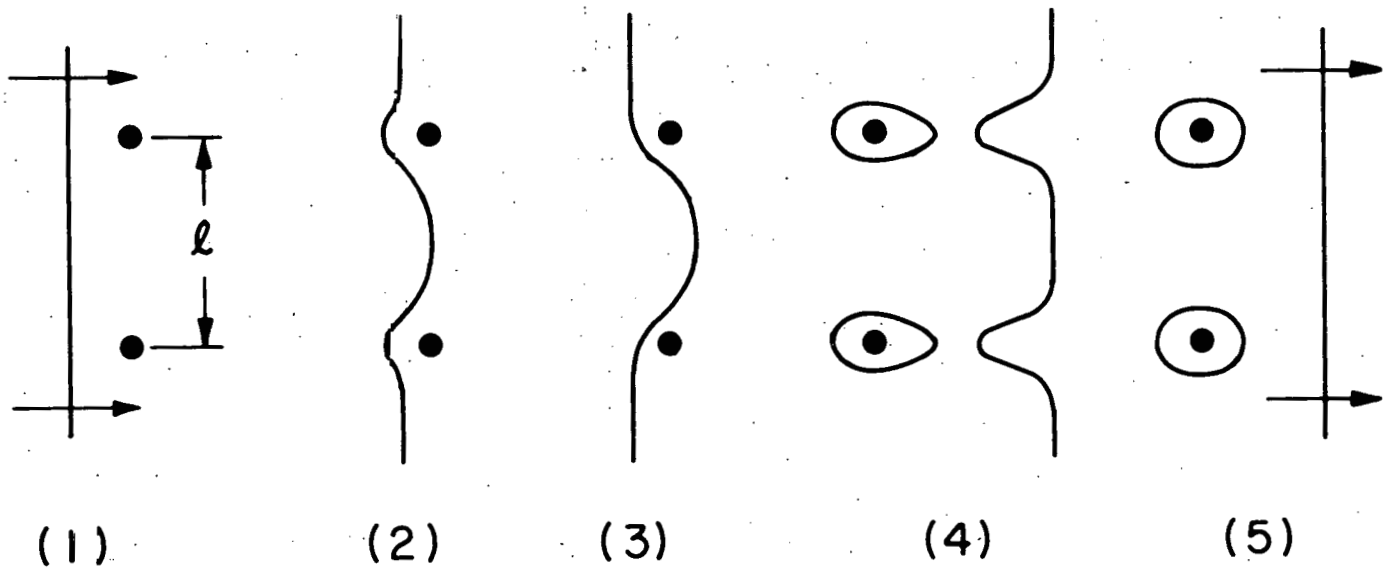

Figure 3. Schematic of stages in passage of a dislocation between widely-separated obstacles--Orowan's mechanism of hardening

plane. Fleischer (20) considered the barriers to be centers of tetragonal distortion due to vacancy or interstitial disks. He obtained

$$\tau = \frac{Gb}{3.7\ell} \tag{3}$$

where

$$\ell = \left(\sum_i n_i d_i\right)^{-\frac{1}{2}} \tag{4}$$

and n_i and d_i are the volume density and the diameter, respectively, of disks in the i-th size interval.

Foreman and Makin (21) performed a computer analysis of dislocation motion through a random planar array of point obstacles. For weak barriers, the critical shear stress was in agreement with the expression derived by Friedel (22)

$$\tau = \frac{Gb}{2n_A\ell^3} \tag{5}$$

where n_A is the number of barriers per unit area. For strong barriers, they found (21)

$$\tau = 0.81\,\frac{Gb}{\ell} \quad . \tag{6}$$

In another computer study, Foreman (23) determined the critical shear stress to be

$$\tau = A\,\frac{Gb}{2\pi\ell}\,\left(\ln\frac{\ell}{r_o} + B\right) \tag{7}$$

where A and B are constants and r_o is the dislocation core radius. Kocks

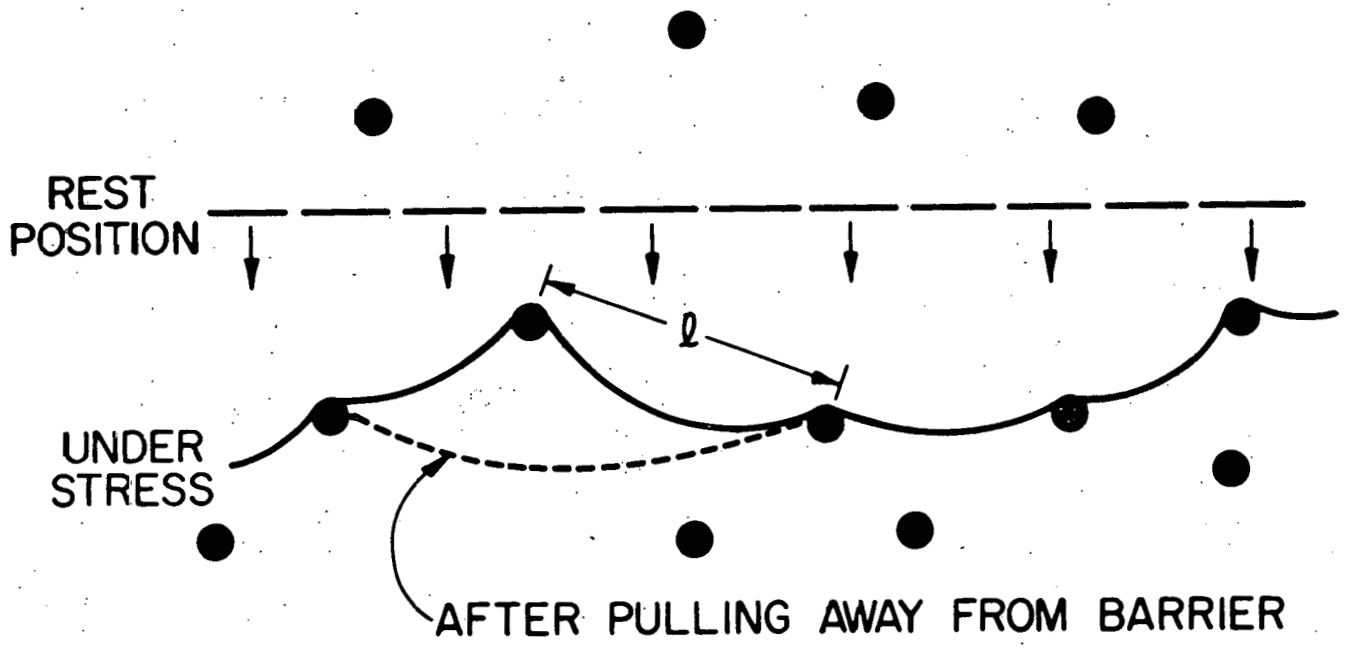

Figure 4. Dislocation line in a field of barriers dispersed in a slip plane (after Holmes (19))

(24) using a combination of statistical theory and graphical analysis for the case of infinitely strong barriers found the critical shear stress to be close to that given in Equation (6).

Westmacott (25) investigated the hardening in quenched aluminum due to dislocation loops and voids. For dislocation loops of diameter d and volume density n, the yield stress increase was given by

$$\Delta\sigma = \frac{Gbdn^{2/3}}{\beta} \tag{8}$$

which agrees with the expressions obtained by Friedel (22) and Kroupa and Hirsch (26) with β = 7.3 and 16, respectively. Westmacott et al. (27) pointed out that the nearest neighbor separation ℓ for a random distribution of n particles per unit volume of diameter d should be

$$\ell = 0.5\ (nd)^{\frac{1}{2}} \tag{9}$$

but the factor of 0.5 was not confirmed in the computer analysis by Foreman (28). Other expressions for ℓ based on various definitions are given by Kocks (29).

Seeger (5) developed a theory of radiation hardening that incorporated the thermal activation of slip. His treatment leads to the expression for the critical shear stress

$$\tau = \left(\frac{n_A}{Gb}\right)^{\frac{1}{2}} \left[\frac{U_o}{4\chi_o b}\right]^{3/2} \left\{ 1 - \left[\frac{kT}{\alpha U_o} \ln\left(\frac{Nb\nu_o}{n_A \dot{a}}\right)\right]^{2/3} \right\}^{3/2} \tag{10}$$

where U_o and χ_o are energy and distance parameters, respectively, in an

assumed energy profile, k is Boltzmann's constant, T is absolute temperature, ν_o is the frequency with which a dislocation attempts to overcome a barrier, $\dot{\varepsilon}$ is the strain rate, and α is a constant missing in the original paper, as pointed out by Schwink and Grieshammer (30). N is the number of dislocations per unit volume pressing against the n_A barriers per unit area. As above, G is the shear modulus and b is the Burgers vector. In deriving Equation (10) the interbarrier distance was taken as

$$\ell = \left(\frac{Gb}{\tau n_A}\right)^{1/3}$$

in accord with Equation (5), following Friedel (22,31). Equation (10) predicts a square-root dependence of τ on radiation dose Φ (assuming $n_A \propto \Phi$ and the predominant effect of n_A is in the first factor). It also predicts a temperature dependence of the form

$$\left(\frac{\tau}{\tau_o}\right)^{\eta} = 1 - \left(\frac{T}{T_o}\right)^{\eta} \qquad (11a)$$

where $\eta = 2/3$ and τ_o and T_o are functions of the parameters in Equation (10). By comparison, Fleischer's theory (32) predicts $\eta = 1/2$ in Equation (11a). The critical shear stress is sometimes considered to consist of two parts, viz.

$$\tau = \tau^*(T) + \tau_a \qquad (11b)$$

where τ_a is independent of temperature and represents a long-range interaction between slip dislocations and barriers and $\tau^*(T)$ is the temperature dependent component which represents a short-range interaction or the stress

required to overcome the Peierls stress (33). Such a simple resolution of τ into two components does not appear to be unambiguously predicted by Equation (10).

The grain size dependence of the yield stress if often represented by the Petch (34) relation

$$\sigma = \sigma_o + k_y d_G^{-\frac{1}{2}} \tag{12}$$

where $2d_G$ is the average grain diameter and σ_o and k_y are constants. This expression is used below to correct for variations in grain size in comparing results of various investigators.

An important question in radiation hardening is the way in which the barriers to dislocation motion in the unirradiated metal (U barriers) combine with those produced upon irradiation (I barriers). Tucker and Wechsler (35) have given a treatment of two possible cases:

1. U and I barriers acting independently

The net shear stress acting on a dislocation line at the I barrier upon yielding is $\tau - \tau_U$, where τ_U is the critical shear stress for the unirradiated material. An analysis similar to that giving Equation (2) yields

$$\sigma_I - \sigma_U = 2(\tau_I - \tau_U) = \frac{2F_I}{b\ell_I} \tag{13}$$

where σ_I and σ_U are yield stresses for the irradiated and unirradiated material, respectively, and τ_I and τ_U are corresponding shear stresses. The interbarrier distance between I barriers alone is ℓ_I, and the critical force required to surmount the I barriers is $F_I = (F_c - F_t)_I$ in a manner

analogous to Equation (2). If the diameter of the I barriers is d_I and they are distributed randomly with a volume density n_I, ℓ_I may be written

$$\ell_I = \frac{K_2}{\sqrt{n_I d_I}} \tag{14}$$

where I is a constant close to unity incorporating geometrical considerations as discussed by Kocks (29). If the barriers are present in a distribution of sizes, then

$$\ell_I = \frac{K_2}{\sqrt{\sum_i n_{I_i} d_{I_i}}} \tag{15}$$

where the subscript i denotes quantities pertaining to the i-th size interval. Then Equation (13) becomes

$$\sigma_I - \sigma_U = \frac{2F_I}{bK_2} \left(\sum_i n_{I_i} d_{I_i} \right)^{\frac{1}{2}} . \tag{16}$$

2. U and I barriers acting jointly

Now the interbarrier distance becomes

$$\ell = \frac{K_2}{\sqrt{n_U d_U + n_I d_I}} \tag{17}$$

where n_U and d_U are the density and size of the U barriers, and $\overline{F}$ is an effective critical force. Then

$$\sigma_I = \frac{2\overline{F}}{bK_2} \sqrt{n_U d_U + n_I d_I} . \tag{18}$$

Since $\sigma_I = \sigma_U$ when $n_I = 0$

$$\sigma_I^2 = \sigma_U^2 + \frac{4\bar{F}^2}{b^2K_2^2} (n_I d_I) . \quad (19)$$

For a distribution of sizes, the expression analogous to Equation (16) is

$$\sigma_I^2 = \sigma_U^2 + \frac{4\bar{F}^2}{b^2K_2^2} (\sum_i n_{I_i} d_{I_i}) . \quad (20)$$

It is instructive to note that Equations (16) and (20) are not of the same form except when $\sigma_u << \sigma_I$. For neutron-irradiated niobium, Tucker and Wechsler (35) found a somewhat better fit to Equation (20) based on TEM-observable defect clusters. For both cases, the barriers strengths were determined to be in the range $F = (0.5 - 0.8)Gb^2$. This corresponds to strong barrier hardening, i.e. to F values close to the bowing-around force indicated by Foreman and Makin (21) and Kocks (24) to be about $0.8Gb^2$ for a random distribution of barriers.

The expression most often used to describe radiation hardening is

$$\sigma_I - \sigma_U = \frac{2K_1}{K_2} Gb(n_I d_I)^{\frac{1}{2}} \quad (21)$$

which is obtained from Equations (13) and (14) by setting $F_I = K_1 Gb^2$, where α=1 for bowing around infinitely strong barriers. As before, if the barriers are present in a distribution of sizes, we have

$$\sigma_I - \sigma_U = \frac{2K_1}{K_2} Gb (\sum_i n_{I_i} d_{I_i})^{\frac{1}{2}} . \quad (22)$$

C. Experimental Observations of Radiation Hardening

In early experimental observations of radiation hardening, particular emphasis was placed on the dependence of yield stress on radiation dose. Blewitt et al. (36) observed that the yield stress of copper increased as the cube root of the dose over the range 10^{16} to 10^{20} n/cm^2. However, Diehl (37) and Rukwied and Diehl (38) found a square-root dependence at low doses, followed by a lower hardening rate (saturation) at higher doses. Similar observations were reported for iron by Seidel (39), Diehl et al. (40), McRickard (41), and Mogford and Hull (42).

In more recent work, investigators have attempted to correlate the yield stress with the density and size distribution of defect clusters, as well as with the radiation dose. For neutron-irradiated niobium, Tucker and Wechsler (35) and Loomis and Gerber (43) observed that the square-root dose dependence persists only up to about 7×10^{17} n/cm^2, followed by a sharply decreased rate of hardening. From the analysis of defect clusters, both investigations indicated that the interbarrier spacing (defined for example, by Equation (15)) decreased rapidly as a function of dose at first, but at higher doses the decrease was less rapid. However, Loomis and Gerber (43) reported that, particularly for higher-oxygen samples, the hardening rate increased again for still higher doses (above about 4×10^{18} n/cm^2), with an attendant further decrease in interbarrier spacing. They interpreted the radiation hardening of niobium to be due to defect clusters smaller than 70 Å.

In a review paper on radiation hardening in b.c.c. transition metals, Wronski et al. (44) concluded that source hardening (decreased operation of

dislocation sources) operates up to 10^{19} n/cm^2, but at higher doses, friction hardening (inhibition of dislocation motion) is superimposed on this. On the other hand, Evans et al. (45) concluded for niobium that friction hardening was the primary factor, which increased with increasing irradiation temperature.

In vanadium, Shiraishi et al. (46) and Boček et al. (47) observed the radiation hardening to follow a square-root dose dependence at lower doses, above which saturation was observed. However, radiation hardening did not show a tendency for saturation up to 4×10^{19} n/cm^2 (E > 1 MeV) in the work of Smolik and Chen (48). Smidt (49) applied Equation (21) to microhardness measurements on 0.002-inch-thick foils, where d_I was the average defect cluster diameter and n_I the total density of all sizes. Good agreement was obtained with K_1/K_2 equal to 0.55. On the other hand, Shiraishi et al. (46,50) found the observed radiation hardening to be at least several times greater than could be accounted for by Equation (22) with $K_1/K_2 \cong 1$.

The effect of irradiation on the temperature dependence of yielding has been studied in Cu (51-57), Fe (58-60), steel (61), Mo (62-64), Nb (58,65-68), and V (47,48,69-71). For vanadium, Arsenault (69) and Smolik and Chen (48) found roughly the same increase in yield stress upon irradiation for all test temperatures, as was also observed by Wechsler et al. for niobium (68). In terms of Equation (11b), this means that all of the radiation hardening resides in τ_a and none in τ^*. On the other hand, Arsenault and Pink (70) found an increase, decrease, and no change in the temperature dependence of yield stress depending on low (< 90 wt ppm),

medium (< 300 wt ppm), and high (880 wt ppm) oxygen concentrations, respectively. Wechsler et al. (71) also observed an increase in thermal stress (τ^*) upon neutron irradiation for low-oxygen (70 wt ppm) vanadium, particularly at low temperatures. However, the results for higher oxygen alloys are more complicated. It has been suggested (72) that the increased temperature dependence upon irradiation is more pronounced for higher purity materials, but additional work is needed to establish the point. A further complication, as shown in the work of Boček et al. (47), is that τ_a and τ^* may both be affected by irradiation in a way that depends on radiation dose. Boček and Elen (73) studied the dose dependence of activation volume of neutron-irradiated vanadium and concluded that the changes in activation volume upon irradiation are dependent on oxygen content and irradiation temperature. The effect of interstitial impurities to increase radiation hardening was pointed out in a short communication by Hasson and Arsenault (74).

The influence of irradiation temperature on the hardening behavior of refractory b.c.c. metals and alloys was discussed by Moteff et al. (75) and results are given for some elevated temperature irradiations of Mo, Mo - 0.5% Ti, Nb, and Nb - 1% Fr. Also, Rau and Moteff (76) performed tensile and TEM tests on tungsten irradiated at bout 70°C. Using Equation (21), they determined $2K_1/K_2$ to be 0.19.

D. Radiation-Anneal Hardening and Stage III Annealing

As has been pointed out in the last section, neutron irradiation causes an increase in yield stress of metals. Moreover in b.c.c. metals there is a striking further increase upon post-irradiation annealing which is

designated as radiation-anneal hardening (RAH). This hardening takes place upon post-irradiation annealing at lower temperatures before recovery towards the pre-irradiation value sets in upon higher temperature annealing. Makin and Minter (77) first observed this penomenon in niobium containing 1600 wt ppm oxygen and neutron irradiated to a dose of 1×10^{20} (E>1 MeV). They found that post-irradiation anneals between 100°C and 200°C caused the yield stress to increase and uniform elongation to decrease. The yield stress began to decrease at about 350°C and recovery to pre-irradiation strength was complete at about 600°C. Makin and Minter (77) attributed the radiation-anneal hardening at 100 - 200°C to the migration of vacancies produced during irradiation to dislocations on the basis of the activation energy (1.3 ± 0.1 eV) obtained from the radiation-anneal hardening rates at different temperatures.

Radiation-anneal hardening in niobium was also studied by Ohr et al. (78). They observed radiation-anneal hardening peaks at 150°C and 300°C, which they attributed to oxygen and carbon migration, respectively, to radiation-produced defect clusters, thereby strengthening them as barriers to slip dislocation motion. Ohr et al. (78) pointed out that the activation energy of 1.3 ± 0.1 eV reported by Makin and Minter (77) agrees with the energy for oxygen diffusion of 1.17 eV (79).

Radiation-anneal hardening has also been reported for Mo (64,80-82), W (76,82), Fe (66), and V (46,48-50,71,83-86). It is interesting, however, that experiments on other samples of these same metals, e.g., Fe (87), V (46,48), and V-Ti (86), have failed to reveal radiation-anneal hardening. If radiation-anneal hardening is attributable to the trapping of interstitial

impurities at radiation-produced defect clusters, as has been suggested (78,86,88), whether or not radiation-anneal hardening is observed will depend on the presence of sufficient interstitial impurities in solid solution in the as-irradiated materials. In a sense, then, radiation-anneal hardening is an analogue of stain-anneal hardening or stain aging (88). Other possibilities suggested in the literature are that radiation-anneal hardening may be due to agglomeration of defect clusters or interstitial impurities (46) or to condensation of vacancies onto dislocations (81).

Resistivity and internal friction measurements in irradiated and cold-worked metals have been used to provide an understanding of the origin of radiation-anneal hardening. The electrical resistivity in cold-worked and irradiated b.c.c. metals shows a pronounced annealing stage at about 0.2 T_m where T_m is the melting temperature in °K. This stage is designated as Stage III annealing by analogy with copper. The origin of Stage III in b.c.c. metals has been attributed to migration of intrinsic defects (self-interstitials, di-interstitials, vacancies, divancies, etc.) (80,89-98) or to interstitial impurity migration (48,49,71,72,88,99-111).

Peacock and Johnson (91) interpreted the Stage III recovery of electrical resistivity in neutron-irradiated molybdenum and niobium as due to vacancy migration to interstitial impurity atoms or to radiation-produced defect clusters. However, Nihoul (93) on the basis of his analysis of Peacock and Johnson's (91) data found that they obeyed second-order kinetics, suggesting that recovery was due to migration of self-interstitials to vacancies. Stals and Nihoul (94) and Schultz (95) then interpreted Stage III

annealing in niobium as being due to self-interstitial migration. Perepezko et al. (96) investigated Stage III resistivity recovery in cold-worked and neutron-irradiated vanadium and found an activation energy of 0.8 eV, which led them to conclude that recovery was caused by annihilation of some species of lattice defects (intrinsic defects) rather than to the redistribution of interstitial impurities.

Rosenfield (107) first pointed out that since the activation energies determined by various authors for Stage III in b.c.c. metals are quite similar to energies for interstitial impurity migration, the recovery was controlled by the impurities, and it was indeed shown by Kothe and Schlat (102), Dinter (103), and Cuddy (104) that in cold-worked materials containing very low impurity content, Stage III is absent. Further support for attributing the Stage III annealing and radiation-anneal hardening to extrinsic factors (interstitial impurities) is gained by various studies on electrical resistivity and internal friction of niobium by Williams et al. (99) who indicated that oxygen is the mobile agent responsible for the post-irradiation annealing stage on the basis of (a) annealing stage at 100-200°C in niobium does not occur unless oxygen is present, (b) decrease in resistivity is accompanied by a decrease in Snoek internal friction peak specifically due to oxygen, (c) resistivity decreases below pre-irradiation value, (d) the activation energy for the annealing stage is 1.2 eV (99) is in good agreement with that of oxygen jumping in niobium (79).

Stanley et al. (110) studied the effects of interstitial impurities (oxygen) on annealing of neutron-irradiated vanadium and found (a) magnitude

of resistivity annealing stage was larger for vanadium with higher oxygen and carbon content, (b) an activation energy of 1.2 $\pm$ 0.1 eV which corresponds to oxygen migration in vanadium (79), (c) Snoek peak due to oxygen and carbon decreased upon post-irradiation annealing at about 180°C. More or less similar conclusions were drawn by McIlwain et al. (83) on neutron-irradiated vanadium.

There is, however, a continuing debate in the technical literature (97,98,111) as to whether radiation-anneal hardening and Stage III annealing are due to intrinsic radiation-produced defects or to impurities. One of the goals of the present study is to help resolve the question by studying these phenomena in vanadium as a function of oxygen impurity concentrations. It is seen below that our results tend to support the view that impurities are an important factor in radiation-anneal hardening and Stage III annealing.

E. Defect Clusters - Direct Observation

When a metal is bombarded with neutrons, vacancies and interstitials are created in the displacement cascade regions. This defect structure is more complex than in quenched metals where only vacancies are retained. The agglomeration of defect clusters into sizes resolvable by transmission electron microscopy (TEM) is influenced by various factors. The homologous irradiation temperature clearly influences the mobility of the defects produced during irradiation and hence their agglomeration. The reactor ambient temperature may be widely different for different metals on a homologous temperature scale. The defect concentration produced upon

irradiation and the neutron energies also affect the agglomeration. The neutron spectra may vary from reactor to reactor, which may cause changes in agglomeration. In fact, the conflicting observations of the nature of defect clusters in copper may have been explained partly on this basis. The purity of the metal is also an important factor. Impurity atoms may act as heterogeneous nucleation sites, reduce the loss of energy in sub-threshold manner by causing dechanneling and defocusing and cause trapping of defects.

Apart from irradiation temperature, neutron energies and spectra, and impurity of the metal, post-irradiation annealing influences the defect cluster agglomeration by providing mobility to the defects and enhancing the agglomeration. In some cases, post-irradiation annealing is necessary in order that the clusters may grow and be resolvable by TEM. Even in cases where defect clusters are visible by TEM in the as-irradiated condition, it may be necessary to perform post-irradiation annealing in order for them to agglomerate to sizes which can be analyzed for their nature (interstitial or vacancy), although they may have been changed in the process of annealing.

Transmission electron microscopy (TEM) has been extensively used for the direct observation of defect clusters in irradiated metals. Since the first study in 1959 by Silcox and Hirsch (112), there has been considerable interest in the subject. Consequently there is an enormous amount of literature available on the subject. However, due to limited scope of this thesis, the review will be limited to direct clusters in b.c.c. metals with brief mention of some early studies on copper and aluminum. For defects

in quenched metals and general aspects of theory and review the reader is referred to references (113-134).

Silcox and Hirsch (112) first reported observation of black spots or dislocation loops in copper irradiated to doses in the range of 6.7×10^{17} to 1.4×10^{20} n/cm^2 (E>1 MeV) at temperatures of 35°C and 60-100°C, respectively. The loops were believed to be due to vacancies clustering in the displacement spikes and subsequent collapsing into discs. Radiation hardening was attributed to dislocations cutting the forest of loops. This was the first reported observation of radiation damage in metals by TEM. Subsequently black dots have been reported in various irradiated and quenched metals.

In a detailed study on neutron irradiated copper, Makin et al. (135, 136) found that irradiation leads to two kinds of defects: resolvable loops and small defect clusters (< 25Å) observed as black dots. The size distribution function (number of defects per unit volume in a size interval i.e., number cm^{-3} Å^{-1}) was found to decrease monotonically with increasing size of clusters. With increasing dose the concentration of loops of given size decreased and the size of largest loops increased, suggesting that loops grow in size by absorption of point defects and do not nucleate at their final size. The concentration of loops of a given size increased with increasing dose at a rate smaller than linear. In copper containing 0.1% silver the loop density was found to be roughly four times larger for the same dose than in pure copper (136) which suggests that the impurities act as nucleation sites for defect clusters. For other studies on copper, see references (137-143).

In aluminum, Silcox (144) and Thomas and Whitton (145) failed to observe loops even after irradiation to 10^{20} n/cm^2, whereas Bierlein and Mastel (146) were able to reveal loops in specimens irradiated up to a dose of only 3×10^{18} n/cm^2. The concentration of these loops was found to increase with increasing dose. Westmacott et al. (147) found loops in aluminum irradiated by fission fragments, suggesting that nucleation probability is strongly damage-rate dependent.

The literature with regard to TEM observations in b.c.c. metals has been amply reviewed by Tucker (67) and in the proceedings of recent conferences (148-151). It suffices, therefore, to simply cite the relevant references for iron and several of the b.c.c. refractory metals. For Nb and V, however, we shall describe the literature in more detail. Thus:

Iron: Hull and Mogford (152), Eyre (153), Eyre and Bartlett (154), Bryner (155,156), Ohr (157), Masters (158,159)

Tungsten: Lacefield et al. (160), Rau and Moteff (76), Rau et al. (161), Sikka and Moteff (162), Sikka and Moteff (163)

Molybdenum: Kerridge et al. (164), Mastel et al. (165), Downey and Eyre (80), Meakin and Greenfield (166), Brimhall et al. (167,168), Brimhall and Mastel (169), Rao and Thomas (170), Maher and Eyre (171), Eyre and Downey (172), Maher and Eyre (173), Eyre et al. (174), Moteff et al. (75), and Brimhall (175).

Defect clusters were first observed in niobium by Tucker and Ohr (176) following irradiation to 2×10^{18} n/cm^2 (E>1 MeV) at 50°C. In later work (35,58,67,78,177), the density and size distribution of defect clusters were observed following irradiation at 50°C to various doses from 2.2×10^{17} to 4.4×10^{18} n/cm^2 (E>1 MeV) and upon post-irradiation annealing up to 600°C. The results of Tucker and Wechsler (35) indicated that the total

defect cluster density increased from 1.3 x 10^{15} cm^{-3} for a dose of 2.2 x 10^{17} n/cm^2 (E>1 MeV) to 7.4 x 10^{15} cm^{-3} for 1.8 x 10^{18} n/cm^2 (E>1 MeV). The size distribution curves showed a peak in all cases. Loomis and Gerber (43) investigated the effect of oxygen on defect agglomeration in niobium irradiated to 4 x 10^{19} n/cm^2 at 30-50°C and found that oxygen has a pronounced effect on the diameter and density of defect clusters and loops and on radiation induced hardening. These authors found the size distribution function monotonically decreasing with increasing size.

Rau and Ladd (178) first investigated radiation damage by TEM in single crystal vanadium irradiated to a fluence of 5.4 x 10^{19} n/cm^2 at ~ 70°C. Following irradiation, anneals were carried out at temperatures ranging from 330 to 1175°C. In as-irradiated material the average estimated size of cluster was reported as 25-50 Å and estimated density as 10^{16} to 10^{17} per cm^3. Upon annealing at 330°C, 510°C, 650°C, 815°C and 1175°C the average size and clusters densities were 75 Å and 1.2 x $10^{16}/cm^3$, 125 Å and 4.6 x $10^{15}/cm^3$, 175 Å and 9.7 x $10^{14}/cm^3$, 400 Å and 2.1 x $10^{14}/cm^3$ and 500 Å and 1.1 x $10^{14}/cm^3$, respectively.

Smidt (49) observed a defect cluster density of 3.7 $\pm$ 0.7 x $10^{16}/cm^3$ after irradiation at 55°C to 1 x 10^{19} n/cm^3 (E>1 MeV). The size distribution function exhibited a peak when plotted against diameter of cluster. The average diameter was found to be 28.6 $\pm$ 2.0 Å. Upon annealing for 2 hrs. at 420°C, the density of 3.8 $\pm$ 0.8 x 10^{16} and a size of 34.6 $\pm$ 2.0 Å was reported and at 600°C anneal a density of 9.7 x $10^{14}/cm^3$ and a size of 180 $\pm$ 5.0 Å was observed. Upon higher temperature anneals (> 750°C) no defect clusters were observed.

Shiraishi et al. (50) irradiated 99.8% pure vanadium to a fluence of 8.2×10^{19} n/cm^2 at 200°C and observed a defect cluster density of 1.4×10^{16}/cm^3 and an average diameter of 70 Å in as-irradiated and 2.1×10^{14}/cm^3 and 300 Å, respectively, for 600°C post-irradiation annealed specimens.

Elen (179) investigated commercial purity vanadium (99.7%) irradiated to 7.2×10^{19} equivalent fission neutrons per cm^2 at 80°C and observed 2.3×10^{16} defect clusters/cm^3 of average size 70 Å in as-irradiated, 2.4×10^{16}/cm^3 and 86 Å in 200°C-annealed, 1.7×10^{16}/cm^3 and 92 Å in 400°C-annealed, 3.1×10^{15}/cm^3 and 157 Å in 500°C-annealed and 1.8×10^{15}/cm^3 and 229 Å in 570°C-annealed specimens, respectively. No clusters were observed upon annealing at 100°C. Boček and Elen (73) irradiated vanadium to 1×10^{19} n/cm^2 (E>1 MeV) at 150-250°C and at 250-350°C. For the lower irradiation temperature, they observed a defect cluster density of 2×10^{16} cm^{-3} and an average size of 30 Å, whereas for the higher irradiation temperature, the density was lower (5×10^{15} cm^{-3}) and the average size larger (80 Å). For the higher irradiation temperature, they also reported large platelets which they attributed to impurity precipitate particles.

Shiraishi et al. (46) reported an average defect cluster diameter of 30 Å and a density of 5×10^{16}/cm^3 in vanadium containing 190 ppm oxygen irradiated to 2.4×10^{19} n/cm^2 (E>1 MeV) at 70°C. The loop density decreased to $\sim 1 \times 10^{15}$/cm^3 upon post irradiation annealing at 600°C and the largest loop diameter was observed to be 150 Å following a post-irradiation anneal at $\sim$ 530°C.

The role of interstitial impurities in void formation in vanadium has

also been studied by various investigators (180-182). A typical study by Carlander et al. (180) indicated a marked decrease in the diameter and number density of voids with increasing oxygen content from 0.02 to 0.09 wt. percent. They also observed a bimodal void size distribution in the higher oxygen material.

In vanadium, Rau and Ladd (178) and Smidt (49) analyzed the loops remaining after a post-irradiation anneal at about 600°C to be of interstitial nature whereas Elen (179) and Shiraishi et al. (50) found large loops to be of vacancy type.

Shiraishi et al. (46) found defect clusters to be of interstitial nature with a/2 <111> Burger vector, in specimens irradiated to 7.5×10^{17} to 5.0×10^{19} n/cm^2 and post-irradiation annealed to 500 or 550°C. However, in the specimen irradiated to 1.0×10^{20} n/cm^2 and annealed to 550°C the large dislocation loops were analyzed to be vacancy loops having a Burgers vector of a/2 <111> on {111} plane.

It is evident from the above review of TEM observations for vanadium that wide variations in results have been obtained. One source of this variability is the impurity content of the various vanadium materials employed. There has been no systematic study of the effect of impurities on defect clusters in vanadium, and this has provided an additional motivation for the present work.

F. Dislocation Channeling

Dislocation channeling is a process by which slip dislocations eliminate defect clusters or dislocation loops produced upon irradiation or quenching. This results in a defect-free band or channel along the slip plane. Dislocation channeling was predicted by Cottrell (183) and first observed in neutron irradiated copper by Greenfield and Wilsdorf (184), Seeger (185), and Essmann and Seeger (186). The subject was recently reviewed by Wechsler (187).

Sharp (188) investigated dislocation channeling in neutron-irradiated copper as a function of deformation temperature, neutron dose, and strain. He observed a strong correspondence between the channels and surface steps at slip bands, and reported that 2 to 3 dislocations move down the channels per slip plane. In the case of Cu-8% Al alloy crystals, however, Brimhall and Mastel (189) observed that dislocation channels do not occur, which was attributed to the low stacking fault energy causing extended dislocations and inhibition of cross-slip. Nevertheless, dislocation channeling is quite widely observed in irradiated and in quenched metals, as indicated by the following:

Irradiated metals:	Cu (184-186,188,190), Mo (62,165, 169,175), Nb (35,58,68,78,177,191), V (46,50,192), Fe (153,154), and Re (193).
Quenched metals:	Al (194-199) and Au (200-201).

In almost all of the channeling observations the trace of the channel plane in the surface of view was consistent with the recognized slip plane for the metal under investigation. In Cu, for example, channels correspond

to {111} planes and in Mo and Nb to {110} or {112} planes.

It is sometimes possible to identify the crystallographic orientation of the channel plane and determine the Burgers vector of the slip dislocation by using diffraction contrast. By examining transmission electron micrographs, the amount of shear displacement and the number of dislocations per channel may be determined. In neutron-irradiated Nb Tucker et al. (191) found that the shear strain was about 1.2 - 3.7, and 1-3 channeling dislocations passed per atomic plane in agreement with Sharp's results (188).

The effect of annealing has also been studied on samples that were irradiated and deformed. Sharp (188) found that anneals for one hour at 200°C and 250°C did not cause any submicroscopic direct clusters within channels or widening of channels.

Huang and Arsenault (192) found mid-ribs in some of the channels of high purity samples which were explained as being due to two channels forming parallel to each other, the second channel forming as a result of a dislocation source being activated by stress field of dynamic pile-up occurring during the formation of the first channel.

The presence or absence of dislocations within the channel is a question of some interest. In general, only a few dislocations have been observed within channels. Dislocation tangles and debris were observed at channel intersections in niobium (191). Smidt and Mastel (202) observed tangled arrays of dislocations in neutron-irradiated and deformed iron. However, the neutron-produced clusters were invisible in their study. Channeling was deduced from the fact that tangled arrays of

dislocations of finite widths were observed along crystallographic directions. Huang and Arsenault (192) observed dislocation channels and dislocation arrays within channels which were independent of oxygen concentration.

The occurrence of channeling in radiation-anneal-hardened material is ambiguous. In Nb Tucker et al. (191) found that no channels were produced in a sample radiation-anneal hardened at 350°C for 1 hr, while Shiraishi et al. (50) observed channels in vanadium post-irradiation annealed at 400°C for 1 hr.

The removal of defect clusters or dislocation loops in the path of moving dislocations has been explained by various mechanisms. According to one mechanism the channels are produced by sweeping aside the defect clusters in the manner of a snow-plow. This mechanism can be discounted because it suggests higher defect cluster densities near the channel wall, which has not been observed in most cases. Another mechanism that relies on the annihilation of defect clusters by anti-defects does not seem plausible in view of Sharp's (188) observation that dislocation channeling takes place upon deformation at 4°K in irradiated copper which minimizes the importance of atomic diffusion.

Mechanisms of dislocation channeling have been discussed (203) in which dislocation loops are incorporated into the slip dislocation. However this requires that the loop and dislocation have the same or opposite Burgers vectors and that the loop interacts with the dislocation on the slip plane. However, as Sharp (188) has pointed out, many loops will have Burgers vectors included to the primary slip plane.

Another mechanism of dislocation interaction resulting in loop annihilation in f.c.c. metals was proposed by Foreman and Sharp (204) and is shown in Figure 5. This mechanism involves coalescence of a prismatic loop into the slip dislocation resulting in a slip dislocation with a semicircular hump. Such configurations have been seen in quenched single crystals of aluminum. A similar mechanism was proposed by Strudel and Washburn (205).

There is another mechanism proposed for channeling according to which the defects are removed by adiabatic heating due to the local rapid release of the energy of plastic deformation. This mechanism has been discussed briefly and applied to dislocation channeling in Nb by Tucker et al. (191).

G. Strain Aging

Body-centered cubic metals containing interstitial impurities exhibit a sharp yield drop and an increase in yield stress when pre-deformed material has been aged for a sufficient time at an appropriate temperature. Cottrell and Bilby (206) treated the phenomenon theoretically based on segregation of impurities to form atmospheres around the dislocations. Dislocations surrounded by the atmospheres can be torn away from them only by application of sufficiently high stress. When this critical stress is reached, the slip dislocations become highly mobile, producing sufficient plastic deformation to permit the usual hard tensile machine to unload somewhat. This is reflected in a decrease in flow stress from the upper yield stress to the lower yield stress, i.e., a yield drop is observed. A

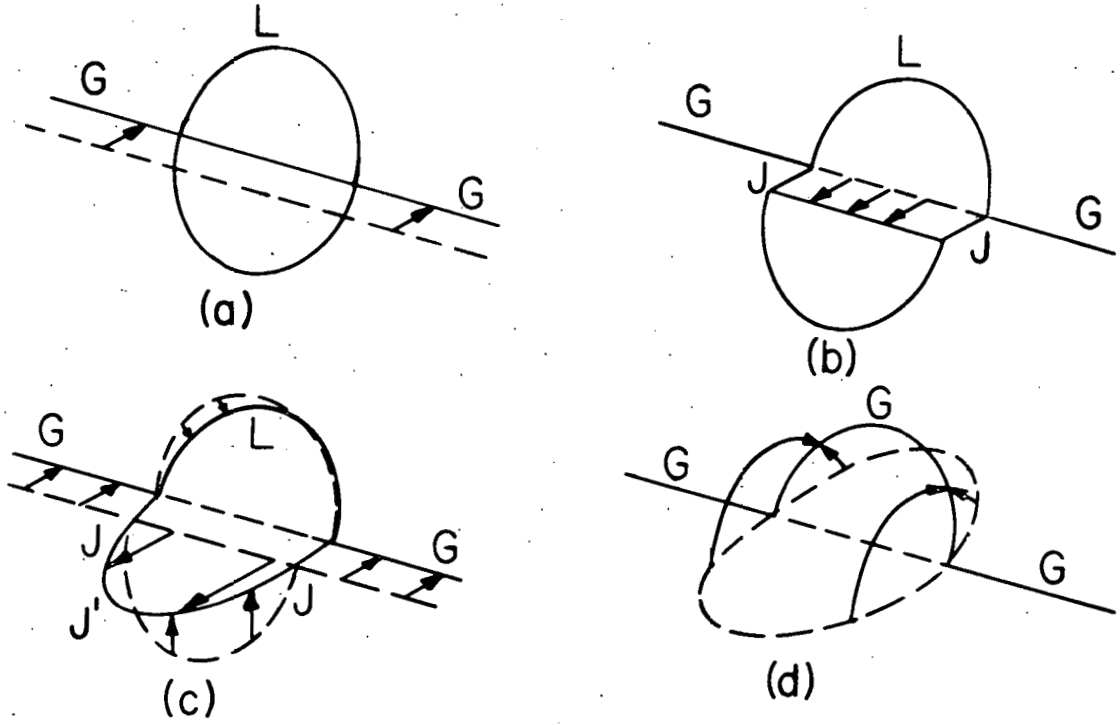

Figure 5. Schematic representation of dislocation channeling mechanism proposed by Foreman and Sharp (204)

specimen which is unloaded in this condition contains free dislocations and, on immediate reloading, shows no yield drop. But if the specimen is aged at a sufficient temperature for the interstitial impurities to migrate and form new solute atmospheres around dislocations, the yield drop returns. Cottrell and Bilby (206) found that in the initial stages the rate of accumulation of impurities in the dislocation core region is proportional to the two-thirds power of the time. They neglected, however, the impurity flow by diffusion due to concentration gradients and the depletion of impurities from the bulk material as the aging process proceeds. Bullough and Newman (207) made a more thorough theoretical analysis of the formation of equilibrium atmospheres around the dislocations.

Alternatively, Johnston and Gilman (208) have deduced from observations in LiF single crystals that grown-in dislocations remain locked and that plastic flow is initiated by heterogeneous nucleation and rapid multiplication of new dislocations. Hahn (209) extended this theory to account for yielding in b.c.c. metals. According to this theory three conditions must be satisfied for the occurrence of a yield drop: (1) initial dislocation density mu-t be small, (2) the dislocation velocity must not increase too rapidly with increasing stress, and (3) the dislocations must multiply rapidly. The first and most important condition can be achieved simply by "locking" the dislocation by impurity interaction in b.c.c. metals.

The initial observations of the strain aging phenomenon were limited to iron and steels, but later this phenomenon was observed in other b.c.c.

metals, e.g., W (210,211), Ta (212), and Nb (212-215). In vanadium, Bradford and Carlson (216) investigated the role of oxygen in strain aging and observed discontinuous yielding in temperature ranges of 150° to 175°C and also 350°C to 400°C. The magnitude and intensity of serrations in the stress-strain curve were found to vary considerably with oxygen content. From strain aging experiments employing a return of yield point criterion, the diffusing species responsible for this effect was shown to have an activation energy nearly equal to that of oxygen or carbon in vanadium. It was found that low-temperature serrations could be directly attributed to oxygen, but the tensile and yield strengths attained minimum rather than maximum values in this temperature range which is typical of strain aging behavior.

Keith and Iverson (217) found that oxygen and nitrogen cause strain aging in electro-refined vanadium at 300° to 400°C as evidenced by maxima in yield and tensile strengths and by Snoek internal friction peaks. Thompson and Carlson (218) studied strain aging in vanadium due to nitrogen. In the temperature range of 300° to 400°C, serrated stress-strain curves and maxima in tensile strength, yield strength and strain-hardening coefficients were found. An activation energy of 37.3 $\pm$ 3.7 Kcal/mole was obtained from strain rate dependence of the strain-aging peak and 36.2 $\pm$ 4.5 Kcal/mole from yield point return method. These values agree well with the activation energy of diffusion of nitrogen in vanadium, 34.1 Kcal/mole (79,102) indicating that nitrogen is associated with the strain-aging effects observed in vanadium.

Edington *et al.* (219) investigated strain aging of vanadium by

mechanical properties measurements and transmission electron microscopy and found four distinct stages of aging which were attributed to the diffusion of oxygen and/or carbon to the dislocations. The observations indicated that dislocations are fully locked by Cottrell atmospheres after an aging treatment of 60 min at 100°C. Also, they are unpinned on re-straining after aging for less than 60 minutes, but for longer aging times, new dislocations are created on re-straining. Segregation of impurities at dislocations was contended to be the mechanism for progressive increase in strength and a general rise in the stress-strain curve. Increase in work hardening rate observed on re-straining after long aging times has been attributed to an increase in the number of active dislocation sources compared with the number observed after shorter aging times. After a very long aging time, general softening was observed which was explained as being due to coarsening of precipitate particles on pre-strain dislocations.

The bombardment of metals with high-energy particles can be expected to produce point defects, mainly vacancies and interstitials, and local regions of severe damage. The excess vacancies produced by the irradiation can aid the diffusion process in metals. The accelerated diffusion and possible trapping of diffusing species can cause changes in the strain-aging behavior of irradiated metals. Fujita and Damask (106) compared the resistivity changes in irradiated and unirradiated quenched iron-carbon alloy and found five annealing stages in irradiated metal against two in the unirradiated metal. They concluded that carbon atoms are temporarily trapped by radiation-produced point defects and the trapping occurs only at

a temperature higher than that at which metastable carbide can form. No resistivity decay associated with formation of metastable carbide was observed in specimens irradiated to sufficient dosage to trap all carbon atoms.

In a previous study, Wagenblast and Damask (220) found that irradiation accelerated the disappearance of carbon from solution in iron by about three orders of magnitude over the thermal rate. Radiation-enhanced removal from solid solution of nitrogen in alpha iron was reported by Stanley (221).

Bement (222) investigated effects of neutron irradiation on iron-nitrogen and found that upon irradiation the strain aging tendency was reduced because of the reduction in the number of nitrogen atoms in solid solution contributing to strain aging. Ohr et al. (66) also reported a decrease in strain aging response in irradiated Fe-N, which is consistent with the removal of nitrogen from solid solution as it becomes trapped at radiation-produced defect clusters.

Investigating the effects of irradiation on the strain aging behavior of Zircaloy-2 by measuring the parameter $\Delta\sigma/\sigma$ (the ratio of increase in flow stress to flow stress at which the test was terminated), Veevers and Rotsey (223) and Veevers et al. (224) found that the strain aging decreased upon irradiation. It was suggested that the defects produced in Zircaloy-2 by fast neutron irradiation trapped oxygen atoms and prevented strain aging.

In the present work, strain aging due to oxygen in vanadium is decreased upon irradiation, which is again consistent with the trapping of

oxygen at radiation-produced defect clusters. A preliminary description of this observation was given by Wechsler and Bajaj (225).

III. MATERIALS AND EXPERIMENTAL PROCEDURES

A. Origin of Materials

Vanadium used for radiation-anneal hardening and strain-aging specimens was supplied by U.S. Bureau of Mines, Boulder City, Nevada through the courtesy of T. A. Sullivan. The material was in the form of electro-refined dendritic crystals. The composition of as-received material is given in Table 1. The chemical analysis was carried out at Ames Laboratory.

The material used for single crystal specimens for microhardness measurements, transmission electron microscopy and dislocation channeling studies was supplied by Argonne National Laboratory. The chemical analysis of this material is also given in Table 1.

B. Preparation of Tensile Samples

Since the investigation involves the effect of oxygen on radiation damage in vanadium, specimens with three different oxygen contents were prepared. The as-received material was designated as low-oxygen material and two other oxygen concentrations were obtained by co-arc melting vanadium metal and pre-weighed amounts of V_2O_5 in a gettered argon atmosphere. The material was cast into 100 gm fingers, which were then swaged into 0.100-inch-diameter rods. Two-inch long pieces were cut from the rods and machined into tensile specimens of one-inch gage length and 0.08-inch gage diameter using a tracer machining process to give specimens of precise dimensions and shape. The specimens were then electropolished in 20% H_2SO_4-80% methanol solution at 20 volts and 2.0 amps current at room

Table 1. Chemical analyses of as-received material in weight parts per million[a]

Element	Source	
	U.S. Bureau of Mines	Argonne National Laboratory
O	13	25
C	7	9
H	70	145
N	1	2
Fe	25	45
Ni	20	< 50
Al	< 20	27
Cr	50	< 80
Mg	< 20	< 20
Si	< 40	< 40
Cu	< 30	< 25
Ti	not detected	< 25

[a]Other impurities less than detectable spectrographic limits.

temperature. The specimen was rotated at a slow speed during polishing. The polished specimens were then successfully rinsed in water, acetone and alcohol and dried. The specimens were then carefully wrapped in tantalum foils in 3 separate batches and annealed at 900°C for 12 hours at a pressure of about 10^{-7} torr. Following the anneal, the analysis of oxygen, nitrogen, and hydrogen was carried out by gas fusion analysis and C, Ni, and Fe contents were determined by wet chemical methods. Other impurities were analyzed by spectrographic techniques. Grain size of the specimens was determined by analyzing micrographs obtained at 80X. The analyses and grain sizes are given in Table 2.

C. Preparation of Single Crystal Rods

Single crystal rods were grown from 3/16-inch swaged poly-crystalline rods, which had been pre-doped with oxygen by the method described above. The crystals were grown in a Materials Research Corporation electron-beam floating-zone refiner, Model EB2-93. The unit consists of a scanner assembly encased in a steel chamber which is evacuated using mechanical and diffusion pumps equipped with freon and liquid nitrogen cold-traps. The blank of pressure in the specimen chamber before zoning was 2-4 x 10^{-7} torr. The swaged rod was mounted on the scanner assembly in V-groove mounts and passed through an aperture in a cylindrically-shaped electron gun assembly. The electron gun, attached to a stage that moved vertically and parallel to the specimen axis was composed of a 2-mm-diameter annular filament of 0.5 mm diameter tungsten wire-enclosed in a molybdenum beam-focusing pillbox. Focusing of the electron beam was accomplished by two

Table 2. Chemical analyses of polycrystalline tensile samples in weight parts per million

Element	Low oxygen	Medium oxygen	High oxygen
	sample designation		
	V-60	V-205	V-640
Interstitial impurities			
O	60	205	640
C	30-40	50	60-80
N	1-6	2-6	2-4
H	2-8	10-12	15-18
Substitutional impurities[a]			
Fe	50-70	15-20	15-20
Ni	8-12	17-25	20-25
Al	< 20	< 20	< 20
Mg	< 20	< 20	< 20
Si	< 40	< 40	< 40
Average grain size in mm	0.024	0.142	0.146

[a]Total of other substitutional impurities, < 100 ppm.

grounded molybdenum annular plates 4 mm apart equally spaced to either side of the filament. The electron beam power supply was capable of a variable voltage to 10 kilovolts and a beam current of 500 milliamperes.

The swaged rods were prepared for single crystal growth by removing several mils from the surface using a chemical polishing solution of H_2SO_4:H_2O:HNO_3 in proportions of 1:1:1. The rods to be grown and the seed crystal with orientation close to [149] were mounted vertically with a separation of about 3 mm between them. The rod was mounted in the V-groove of the upper fixture and the seed crystal was mounted in the lower fixture with spring steel wires screwed to the fixtures. This method of mounting reduces the thermal stresses produced in the crystal due to heating and subsequent cooling.

The rod and seed crystal were concentrically aligned with the aperture in the electron gun assembly and were parallel to the direction of travel. After aligning, the chamber was closed and evacuation carried out to a pressure of 2-4 x 10^{-7} torr.

The power supply was operated so as to maintain a potential difference of about 2 kv between the tungsten filament and the rod, yielding a beam current of about 100 mA. The filament was maintained at temperatures lower than the molten zone of the rod in order to minimize contamination from tungsten. This was evidenced by the color of the filment and a thin deposit of vanadium seen on the filament. The deposit caused the filament to sag and reduced its life. Initially, the electron gun was positioned at the gap between rod and the seed so as to melt the lower end of the

rod onto the seed crystal. Then the gun position was adjusted from outside the vacuum chamber to melt the upper end of the seed crystal. The length of the molten zone, which is determined by the surface tension of the metal, beam current, beam voltage and beam focusing pillbox design, was adjusted to (1-1.5) times the diameter of the rod by adjusting the beam current. After these adjustments, the electron gun was set to travel automatically in an upward direction at a speed of approximately 12 inches per hour. During melting, the pressure in the specimen chamber rose to 4-6 x 10^{-5} torr. As the rod solidified, it had the orientation of the seed single crystal. After a single crystal of about 7-inch length was grown, the current was turned off and the crystal was then allowed to cool to the room temperature in vacuum. The surface of the single crystal was generally smooth.

The rods thus obtained were then analyzed for axial orientation using Laue back reflection x-ray techniques with a film-to-camera distance of 3 cm. The orientation of the 3 rods is given in Figure 6.

The single crystal rods thus obtained (one 7-inch rod of each of three oxygen concentrations) were cut in two and machined to $\sim$ 3.5 mm diameter. The rods were then cut into $\sim$ 9-mm-long pieces and $\sim$ 1-mm-thick slices using a high speed cutting wheel. From the 9-mm-long pieces, compression specimens 8-mm long x 3-mm diameter were prepared by mechanically polished on both sides to 0.5-mm-thick specimens for microhardness measurements and transmission electron microscopy.

The compression specimens and the slices were then cleaned and wrapped in tantalum foils in separate packages and annealed at 900°C for $\sim$ 20 hr.

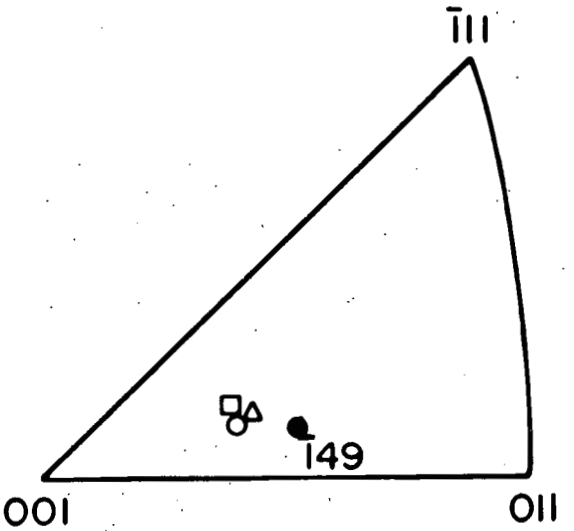

○ V-500ppm OXYGEN
□ V-300ppm OXYGEN
△ V-95ppm OXYGEN

Figure 6. Orientations of single crystal rods on a standard stereographic triangle

Following annealing, the specimens were analyzed. The analysis is given in Table 3.

D. Irradiation Procedures

1. Tensile samples

The polycrystalline tensile specimens used for radiation-anneal hardening and strain-aging studies were irradiated by packing them into three aluminum capsules with perforated ends stacked one over the other with a thermocouple in the middle capsule for temperature recording. The capsules were placed in an aluminum can with a 0.030-inch-thick Cd liner to shield off 97% of the thermal neutrons. The irradiation was carried out in the Ames Laboratory Research Reactor (ALRR) in the V-1 facility with reactor heavy water in contact with the specimens. A temperature of 106°C was recorded during the reactor operation (45° - 55°C during reactor shut down). Nickel foils were included in each package in close proximity to the specimens to monitor the flux.[1] The average fluence was determined to be 1.2×10^{19} n/cm^2 (E>1 MeV). Following de-encapsulation the specimens were observed to have a surface corrosion layer which was removed using a dilute nitric acid solution.

2. Compression, TEM, and microhardness samples

The irradiation of these single crystal specimens was carried out by enclosing them in vanadium capsules which were heliarc welded and sealed.

---

[1] The flux values are estimated to be accurate to an absolute error of 30% and relative error of less than 10%.

Table 3. Chemical analyses of single crystal TEM and compression samples in weight parts per million

Element	Low oxygen	Medium oxygen	High oxygen
	Sample Designation		
	V-95	V-300	V-500
Interstitial impurities			
O	95	290-315	480-520
C	37	29	30
N	3	5	6
H	3	2	3
Substitutional impurities[a]			
Fe	25	21	21
Ni	21	21	21
Al	< 20	< 20	< 20
Mg	< 20	< 20	< 20
Si	< 40	< 40	< 40

[a]Total of other substitutional impurities, < 100 ppm.

The capsules were then stacked in 3 tiers in a Cd-lined aluminum can using an aluminum stacking jig. Three nickel flux monitors placed in contact with the capsules were used for flux determination. A thermocouple was welded to a dummy sample used for temperature measurement. The irradiation was performed in the V-1 facility of the ALRR. An irridation temperature of 95°C was obtained, and the average fluence was determined to be 1.4×10^{19} n/cm^2 (E>1 MeV). The samples were removed from the reactor after required neutron exposure and after a waiting period of 2-3 weeks de-encapsulation was done to remove the specimens.

E. Tensile, Compression and Hardness Tests

Tensile tests for radiation-anneal-hardening and strain-aging experiments were performed on a 10,000 lb capacity Instron testing machine equipped with an automatic load-elongation chart recording system. The tests were performed at room temperature and a strain rate of 1.66×10^{-4} sec^{-1}.

The tensile samples for the radiation-anneal-hardening study were gripped in threaded collet grips made of heat-treated precipitation hardenable stainless steel. The samples were strained in a frame attached to the lower crosshead.

The strain-aging samples were gripped into 1/4-inch diameter, 1/2-inch long stainless steel grips. The grip section of the sample was first slipped into an 0.10-inch diameter threaded hole and the grip was then squeezed through $\sim$ 0.10 inch undersized die to achieve effective gripping. A pull rod attached to the load cell and a frame attached to the lower

crosshead were used to strain the sample.

Compression tests on single crystal samples for the dislocation channeling study and on unirradiated cold-worked samples were also performed with the 10,000 lb capacity Instron machine equipped with a compression load cell, surface ground stainless steel platens, and a jig to facilitate low temperature tests. MoS_2 was used as the lubricant. All tests were performed at a strain rate of 1.66×10^{-4} sec^{-1} at room temperature or at liquid nitrogen temperature.

Microhardness measurements were carried out on as-irradiated and post-irradiation-annealed specimens 0.5 mm thick and 3 mm diameter. The specimens were amounted in quick-mount resin and cast into molds. The molds were then removed and polished flat on the ends and rendered parallel to within $\pm$ 0.001 inch. The molds were then placed on the platform of the microhardness tester.

The hardness measurements were carried out using a Kentron microhardness tester equipped with a 136° diamond pyramid indenter. A load of 1 kg was applied for $\sim$ 10 sec to make an indentation on the specimen. At least three measurements were made on each specimen. Standardization was carried out using reference blocks.

After the indentation was made. the average length of the diagonals of the indentation was measured in filar units using a filar eyepiece and a 20X, 135 mm objective. The diagonal length in filar units was then converted into microns. The diamond pyramid hardness number was then determined using tables supplied with the equipment, taking the applied load into consideration.

F. Post-Irradiation Annealing Procedures

Tensile specimens for radiation-anneal hardening measurements were post-irradiation-annealed in a dual chamber high vacuum annealing furnace shown in Figure 7. Chamber 1 which lies inside the furnace is made of a stainless steel tube and is connected to a Ultek high vacuum system consisting of a mechanical pump-ion pump (capacity 200 l/sec) vacuum system. Chamber 2 lies outside the furnace, is connected to Chamber 1 by an o-ring seal, and consists of two quartz tubes, one inside the other. The inside tube can be pushed into Chamber 1 magnetically, using a nickel piece epoxied to its far end. The specimens were placed into the inside tube lengthwise and were pushed into the heating zone of a Lindberg split furnace (capable of providing temperatures up to 1200°C) after required temperature and vacuum (better than 10^{-7} torr) had been attained. The temperature was measured using a Pt-Pt 13% Rh thermocouple located in close proximity to the specimens. Isochronal anneals at various temperatures were performed for a duration of one hour measured after the equilibrium temperature was reached following the pushing of the specimens into the hot zone. In some annealing runs, unirradiated control specimens were annealed with the irradiated specimens.

The low temperature (up to 200°C) anneals for strain-aging specimens were performed in a stirred silicone oil bath equipped with an on-off temperature control system. The high temperature anneals were carried out in a tube furnace. The specimens (with grips) were sealed into quartz tubes under a vacuum of 10^{-7} torr or better. The temperature was measured using a chromel-alumel thermocouple and was controlled within $\pm$ 3°C.

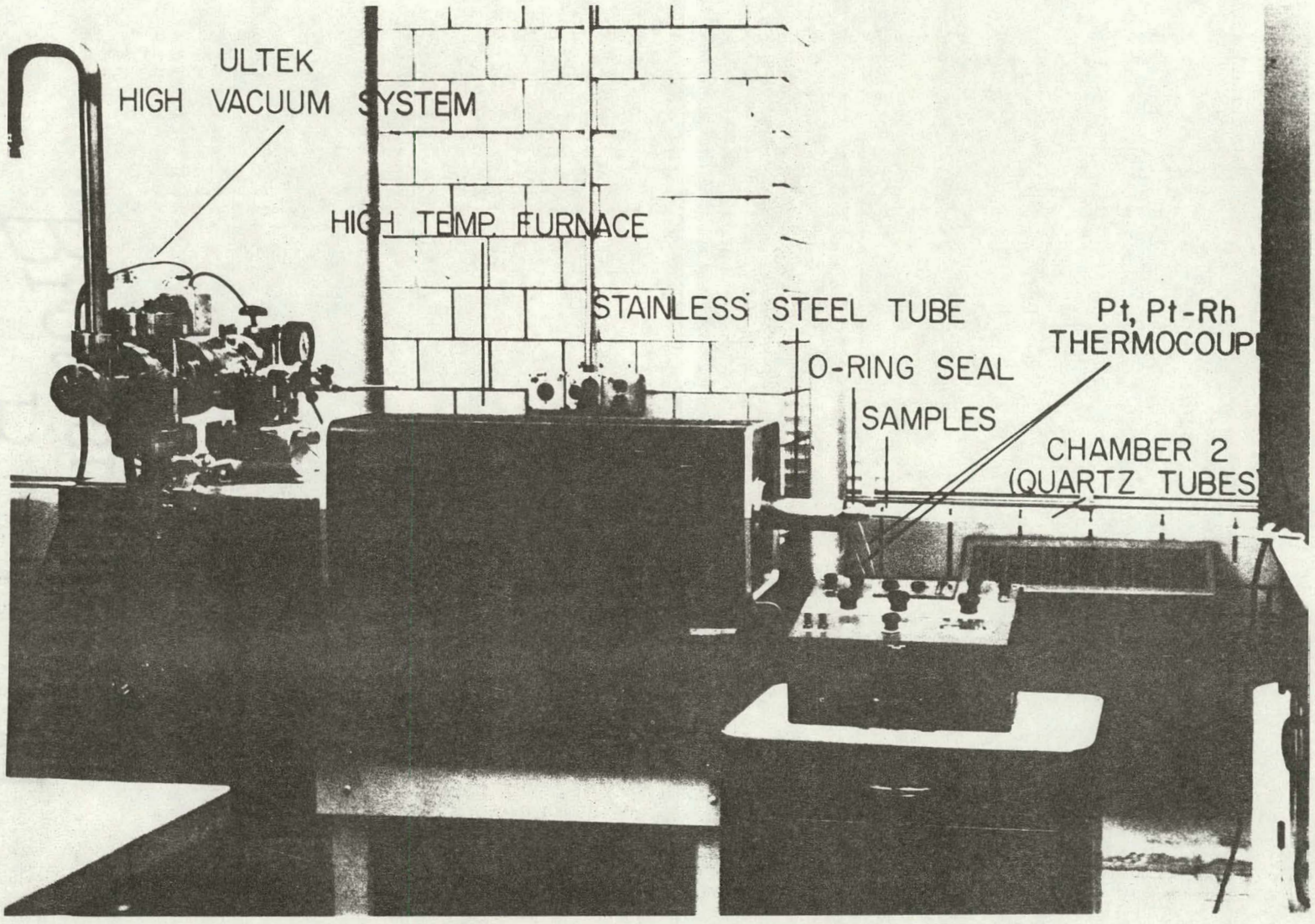

Figure 7. Dual chamber high vacuum annealing furnace used for post-irradiation anneals

The compression, TEM and microhardness specimens were annealed in a tube furnace, the specimens being sealed into quartz tubes under a vacuum of 10^{-7} torr or better. The annealing temperature was constant to within $\pm$ 3°C.

G. Preparation of Samples for Dislocation Channeling Studies

Single crystal compression samples of three oxygen contents were deformed 5% and 12% at room temperature, following irradiation as described previously. One sample of each oxygen content was deformed 5% under compression after a post-irradiation anneal at 400°C and one sample was deformed 12% after a post-irradiation anneal at 300°C. MoS_2 was sprayed on the compression platens to provide lubrication and a strain rate of 1.66×10^{-4} sec^{-1} at room temperature was used. Following the deformation the samples were cut into slices $\sim$ 0.8 mm thick using a high speed cutting saw using water with 5% green oil as coolant-lubricant. The slices were then mechanically polished on both sides into $\sim$ 0.5 mm thick samples for subsequent polishing for transmission electron microscopy. One low-oxygen sample was compressed to a strain of 5% at liquid nitrogen temperature and then sliced and polished into TEM samples.

One single crystal sample of each oxygen content was deformed before irradiation to 5% strain at room temperature and one specimen each to 5% strain at liquid nitrogen temperature. These samples were also prepared for TEM examination. The samples were then irradiated to 1.4×10^{19} n/cm^2 (E>1 MeV) with other single crystal samples as described elsewhere. For a complete scheme of TEM examination of samples, see Figure 8.

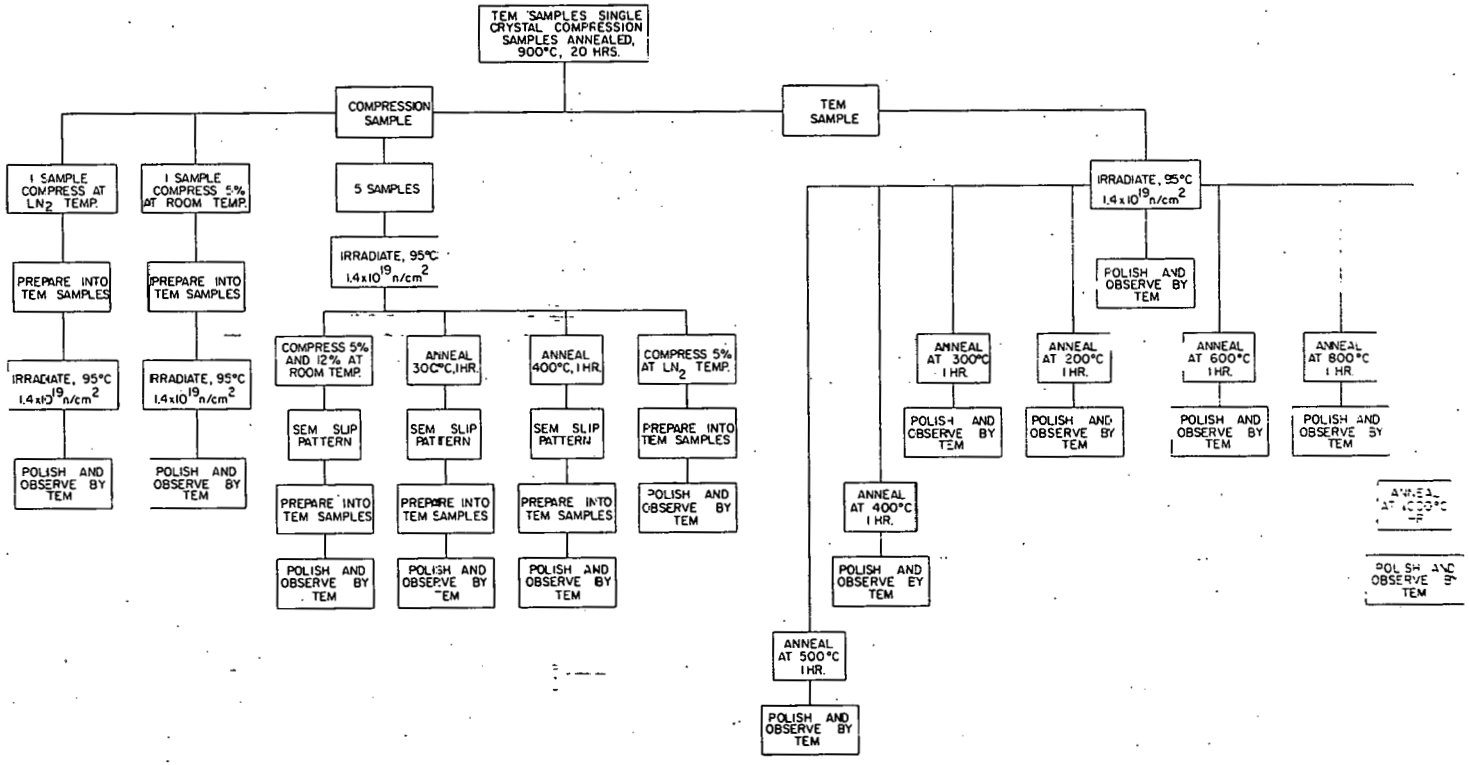

Figure 8. Scheme of transmission electron microscopy of single crystal material

H. Transmission Electron Microscopy

1. Sample preparation

For transmission electron microscope (TEM) examination the 0.5 mm x 3 mm diameter samples had to be electropolished to electron transparency. This was accomplished in two stages. In the first stage the sample was loaded into a teflon holder which exposed the central portion ($\sim$ 2 mm diameter) of the specimen to the polishing solution. The polishing was done by jetting (on both sides) 20% H_2SO_4, 10% HNO_3, 70% methanol solution through stainless steel jets (which act as cathode as well) using a persaltic pump. The electropolishing was carried out at room temperature at 20V and 100 mA current for $\sim$ 8 min. This process produced a dish in the central portion of the specimen about 50μ thick. In the second stage, the sample was held in plexiglass tweezers with an embedded platinum electrode which made contact with the specimen. A nickel cathode was used and polishing was carried out in unstirred 20% H_2SO_4, 80% methanol solution. The progress of polishing was observed continuously through a 3X microscope and light source at opposite ends of a glass container made of flat glass sheets for good viewing. The polishing was terminated by shutting off the supply of current as soon as a hole was observed in the specimen. Following the polishing, the sample was cleaned with distilled water, acetone, and ethanol, and then dried and stored in a desiccator.

2. Microscope operation

The microscope observations were made at Materials Science Division,

Argonne National Laboratory, in an electron microscope operating at 200 kilovolts and equipped with a goniometer stage capable of 30° tilt and 360° rotation. A liquid nitrogen trap was used at the sample chamber to reduce sample contamination. Before each period of examination the microscope was aligned.

The microscope was calibrated for the rotation of diffraction pattern with respect to the micrograph and for the magnification, which was related to intermediate and objective lens currents. The pictures were taken at magnifications between 40,000 and 68,000. The microscope plates were printed to give normal positive prints with the emulsion side of the plate facing the emulsion side of the print paper.

3. Spot counting procedure

The defect clusters and dislocation loops observed in electron micrographs were analyzed for size distribution and density determination. The size and distribution of clusters were determined for various specimens with the aid of Zeiss Particle Size Analyzer TGZ3. The electron microscope plates were enlarged to give magnifications of about 100,000 to 300,000. The particle size analyzer is a semiautomatic instrument in which an iris diaphragm is imaged by a lens and light source out of the plane of plexiglass plate. The micrograph is placed on the plate and by adjusting the iris diaphragm the diameter of the circular light spot penetrating through the micrographs can be changed and is adjusted to correspond with the individual clusters. Each aperture interval of the iris diaphragm is correlated with a counter which records where the foot-switch is depressed.

The cluster is counted in a given size interval and the puncher marks the cluster as counted.

From the counter readings the size of the clusters was reduced to actual size and then statistical analysis was carried out to determine average size and standard deviation, using conventional statistical formulae.

I. Determination of Density and Size Distribution of Defect Clusters

The volume density of the defect clusters was determined by counting the number of defect clusters on an enlarged micrograph. On the average about 1200 clusters were counted in each micrograph. In order to determine the volume of the foil under observation, it was necessary to estimate the thickness of the foil. The thickness was determined by counting the thickness contours (in bright and/or dark field) obtained under the same operating diffraction vector $\vec{g}$ = <200>. The extinction distance calculated in a manner described by Hirsch et al. (123) for an accelerating voltage of 200 kev was determined to be 510 Å.

All the micrographs used for the analysis of density and size distribution were taken under a two beam condition with $\vec{g}$ = <200> and deviation vector $\vec{S} \simeq 0$. The $\vec{g}$ was chosen as <200> so that all <111> type defect clusters would be visible, since then $\vec{g}.\vec{b}$ is always nonzero. The thickness of the foils ranged from 1500 to 3000 Å. The plane of the foil was determined from the electron diffraction pattern of the area and was assumed to be perpendicular to the electron beam. In all the foils examined for density and size distribution, the foils were rotated and tilted in

such a way that the foil normal was <100>. The conditions of microscope examination were made identical to facilitate the comparison of the results.

The size distribution function, n', expressed in number of defect clusters per cm^3 per Å, was determined by counting the number of clusters per unit volume in a size interval, divided by the interval size in Å. A histogram of the size distribution function versus the defect cluster size was then plotted and smooth curves were drawn joining the peaks of the histogram.

It should be pointed out that there are various errors involved in the density determination. The major source of error is the determination of foil thickness. Other sources of error include loss of defects to the surface, overlap of defects, operator judgment and difficulty in resolving smaller size defects from the background, especially in thicker foils.

IV. EXPERIMENTAL RESULTS

A. Radiation Hardening and Radiation-Anneal Hardening

1. Polycrystalline tensile samples

Polycrystalline samples of vanadium containing 60 ppm, 200 ppm, and 640 ppm oxygen,[1] irradiated to 1.2×10^{19} n/cm^2 (E>1 MeV) at 105°C, were cleaned first in dilute nitric acid to remove any surface corrosion layer. Isochronal anneals were then carried out on separate irradiated and unirradiated samples for one hour at temperatures from 120°C to 600°C at intervals of about 25°C. One-hour anneals were also carried out at 650°C, 700°C, and 800°C. For each anneal, two irradiated samples of each of the three oxygen contents were used. The tensile tests were performed on an Instron machine at room temperature at a strain rate of 1.67×10^{-4} per sec.

The results of tensile tests on polycrystalline vanadium with three levels of oxygen are shown in Figure 9, where lower yield stress is plotted against isochronal annealing temperature. Figure 9 also shows the yield stress of unirradiated materials, which were annealed under similar conditions. The lower yield stress was determined in conventional manner from stress-strain curves (0.2% offset, where yield drop was not observed).

It is clear from Figure 9 that unirradiated specimens are largely

---

[1] In what follows, the designation V-60 is used to refer to vanadium-60 wt ppm oxygen material, and similarly for material of other oxygen concentrations. See Tables 2 and 3.

Figure 9. Lower yield stress vs annealing temperature for unirradiated and irradiated polycrystalline samples. Irradiation dose and temperature: 1.2×10^{19} n/cm^2 (E>1 MeV) at 106°C. Test temperature 300°K, annealing time, 1 hr

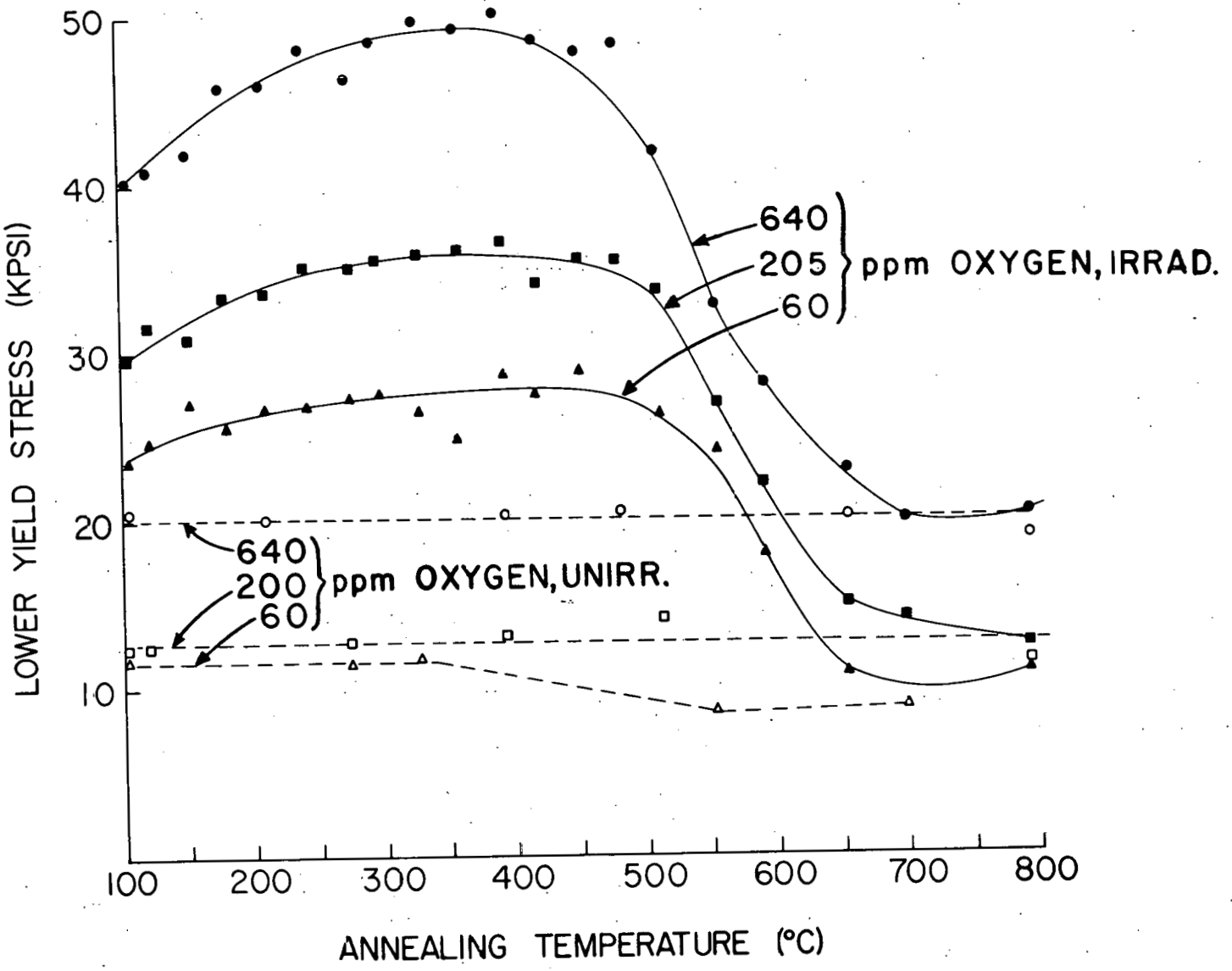
LOWER YIELD STRESS (KPSI)
50
40
30
20
10
640
205
60
ppm OXYGEN, IRRAD.
640
200
60
ppm OXYGEN, UNIRR.
100
200
300
400
500
600
700
800
ANNEALING TEMPERATURE (°C)

unaffected by the anneals and that the yield stress increases due to irradiation. It can be observed from Figure 9 that the yield stress of irradiated materials increases with increasing oxygen concentration. For V-60, the yield stress increases from 11.6 kpsi to 23.6 kpsi upon irradiation, whereas for V-640 the corresponding values are 19.8 kpsi and 40.3 kpsi, respectively.

Figure 9 also shows that the lower yield stress increases further upon annealing the irradiated materials (radiation-anneal hardening, RAH) for the three types of vanadium, and that RAH increases with increasing oxygen content of the specimens. This is more clearly revealed in Figure 10 where the difference between lower yield stresses for irradiated and unirradiated specimens are plotted against isochronal annealing temperature. One can see that for V-60 the increase in yield stress upon post-irradiation annealing amounts to 4.0 kpsi whereas for V-640 an increase of $\sim$ 9.5 kpsi is observed. From Figures 9 and 10 one sees that the RAH occurs up to about 400°C and beyond this temperature the yield stress recovers towards the original value for unirradiated material and this recovery is completed at about 700°C. The yield stresses in Figure 9 exhibit a fair amount of scatter, which is believed to be due largely to surface corrosion on vanadium as a consequence of specimen contact with reactor heavy water of the reactor during irradiation.

The increase in the yield stress upon irradiation is accompanied by a decrease in the uniform elongation and elongation to fracture for all three oxygen levels in vanadium. For V-640, for example, the uniform elongation decreases from 20% in the unirradiated condition to zero in as-irradiated

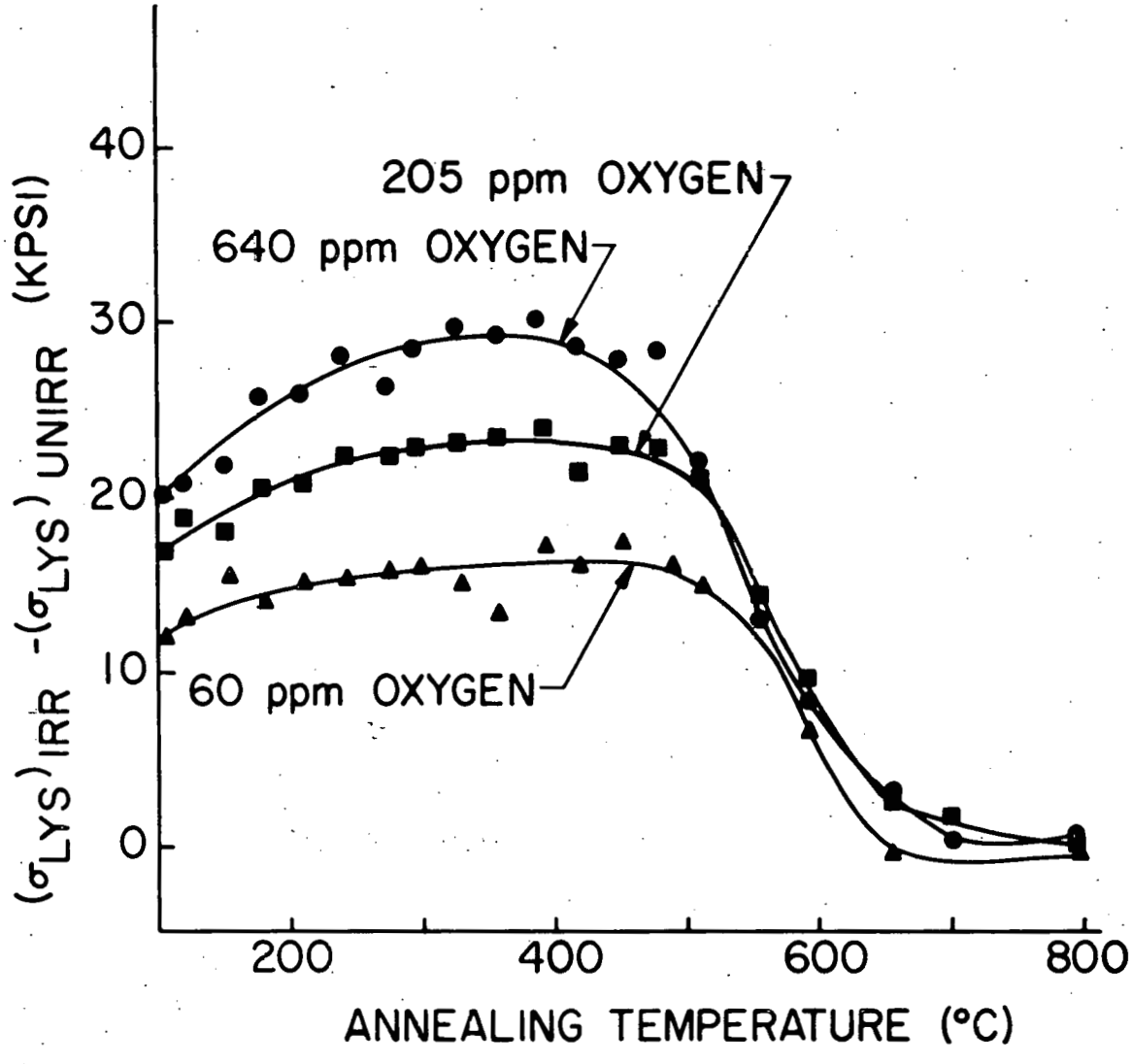

Figure 10. Difference between lower yield stresses for irradiated and unirradiated polycrystalline specimens vs annealing temperature

condition. The corresponding values for the elongation to fracture are 30% and 9% for unirradiated and irradiated samples, respectively. Similar observations on reduction in uniform and fracture elongations upon irradiation were made for vanadium with lower oxygen contents. However, the amount of reduction decreases with decreasing oxygen content. Upon annealing in the temperature range where radiation-anneal hardening occurs (up to 400°C), there is little change in uniform elongation, and the elongation to fracture shows considerable scatter.

An attempt was made to determine the effect of irradiation and annealing on reduction in area. For this purpose a number of fractured samples were examined by scanning electron microscopy (SEM). From the micrographs of the fracture surface, values of reduction in area were calculated. No meaningful conclusion could be drawn because of the scatter in the results; however, it was clear that the fracture was mostly ductile (characterized by large reduction in area at fracture) for irradiated as well as radiation-anneal-hardened material. Figure 11 shows typical SEM micrographs of fracture surface of V-640. Figure 11a shows the fracture surfaces of unirradiated material and Figures 11b and 11c show irradiated and radiation-anneal-hardened material, respectively. The corresponding reduction in area values are also indicated in Figure 11.

Upon irradiation, the rate of strain-hardening is reduced in vanadium. This reduction is more pronounced for V-640 than for material with lower oxygen content. Upon annealing the irradiated material to $\sim$ 400°C the strain hardening rate shows a slight decrease for V-60 and V-200 and remains virtually unchanged at a very low rate for V-640.

Figure 11. Scanning electron micrographs of fractured surfaces of vanadium--640 ppm oxygen samples: (a) un-irradiated, (b) as-irradiated, (c) post-irradiation annealed at 395°C

(a)

Annealed

R.A. = 100%

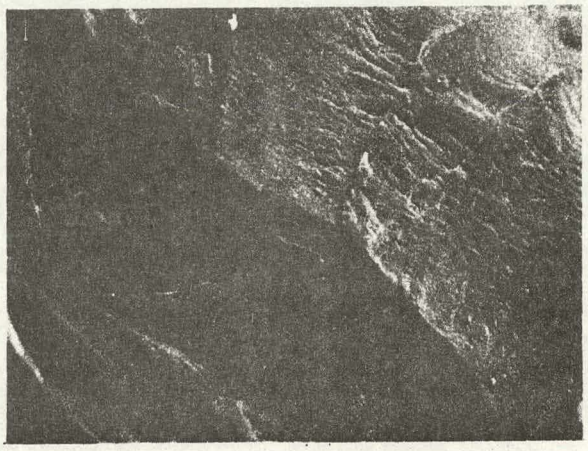

(b)

Irradiated and Annealed at 120°C

R.A. = 90.8%

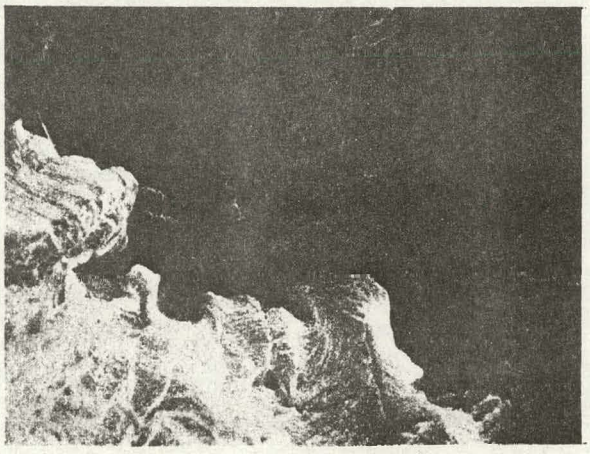

(c)

Irradiated and Annealed 395°C for 1 hr.

R.A. = 89%

2. Single crystal microhardness samples

Microhardness measurements were carried out on polished surfaces of 0.5 mm thick, 3 mm diameter slices. The single crystal samples containing 95, 300, and 500 wt ppm were tested in as-irradiated [irradiated to 1.4×10^{19} n/cm^2 (E>1 MeV) at 95°C] and post-irradiation annealed conditions. The post-irradiation isochronal anneals for one hour at temperatures up to 1000°C were carried out in a static vacuum of 1×10^{-7} torr or better. The hardness measurements were carried out using a 136° diamond indenter with a load of 1 kg applied for $\sim$ 10 sec. At least three measurements were carried out on each specimen.

Figure 12 summarizes the results of microhardness measurements. In this figure, diamond pyramid hardness number is plotted against isochronal annealing temperature for irradiated specimens. The dotted lines representing the microhardness measurements for unirradiated vanadium of similar chemical composition are taken from Bradford and Carlson's work (226).

From Figure 12 it can be observed that microhardness increases upon irradiation and that the increase in hardness increases with increasing oxygen content. V-500 undergoes an increase of 37 DPH while V-95 experiences an increase of only 18 DPH.

Figure 12 also shows that there is a further increase in hardness upon post-irradiation annealing (RAH) which reaches a peak at $\sim$ 300°C for V-500 and V-300. However, V-95 undergoes less RAH. Upon annealing above 400°C, the hardness tends to approach the unirradiated value and the recovery is complete at about 800°C.

Figure 12 thus indicates two effects of increasing oxygen content:

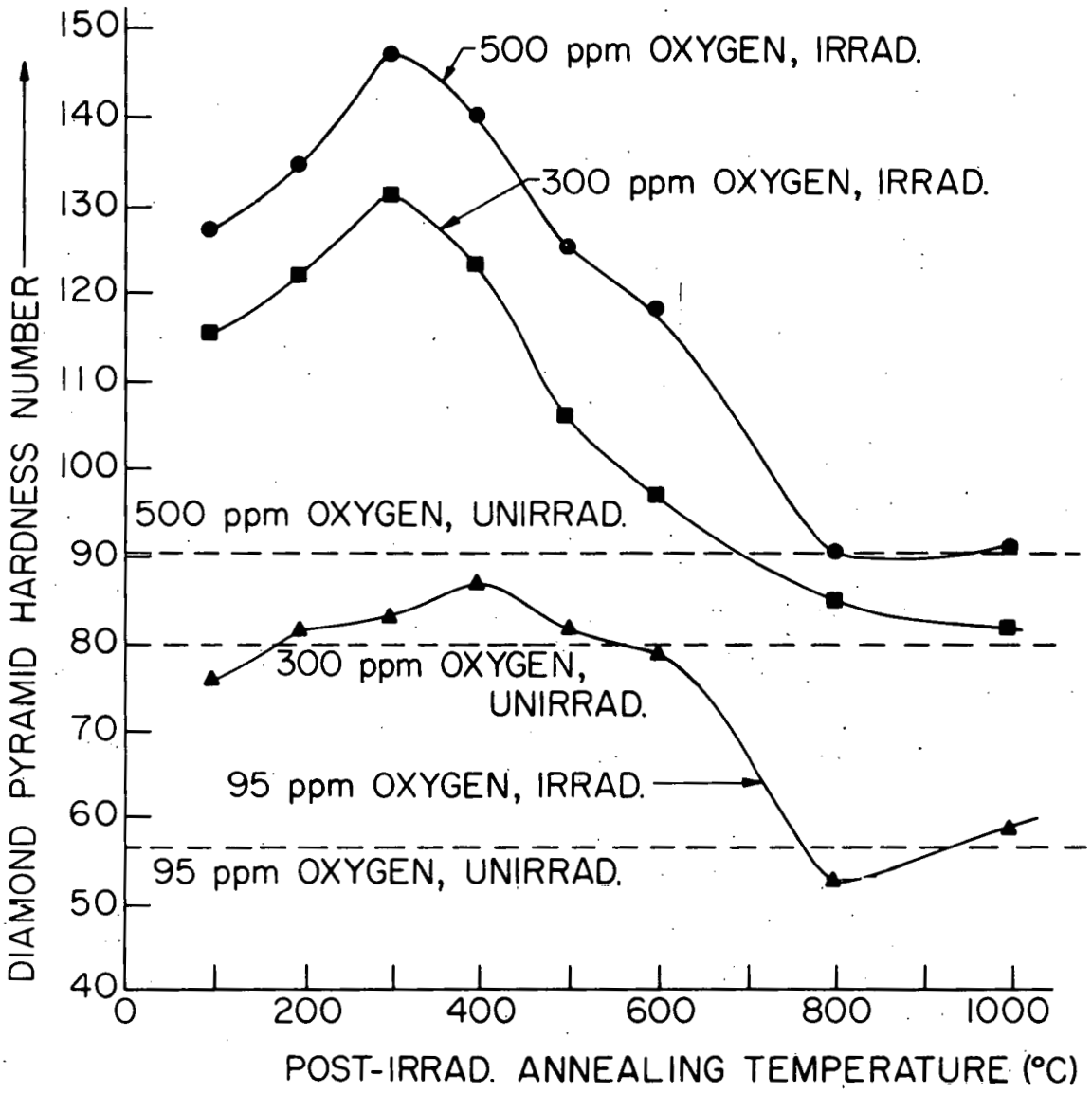

Figure 12. Diamond pyramid hardness vs annealing temperature for unirradiated and irradiated single crystal samples. Irridation dose 1.4 x 10^{19} n/cm^2 (E>1 MeV) at 95°C. Unirradiated hardness values from Bradford and Carlson (226)

(1) increasing radiation hardening in as-irradiated material, and (2) increasing RAH. These two observations are consistent with the results described above and shown in Figure 9 for tensile tests on polycrystalline samples.

In order to correlate the internal structure of the material with the mechanical properties, transmission electron microscopy (TEM) was carried out on single crystal samples treated under conditions similar to those for the samples described above in connection with microhardness measurements. The results are described in the next section.

B. Transmission Electron Microscopy

1. Density and size distribution of defect clusters

Figure 13 shows radiation-produced defect clusters as black spots for V-95 as-irradiated and post-irradiation annealed at 200 - 600°C. The specimens annealed at 800°C and 1000°C did not reveal any defect clusters; however, there was evidence of some precipitation, presumably of oxide of vanadium. At first glance, the Figures 13 (a)-(d) reveal no striking change in the size of the defect clusters as a result of annealing temperature up to 400°C. Beyond 400°C, however, the defect clusters grow in size considerably and the density is reduced. Determination of the defect cluster density size-distribution function, n', for as-irradiated and post-irradiation-annealed specimens indicates that indeed there is a change in the defect cluster distribution occurring upon post-irradiation annealing. Figure 14 represents a plot of n' versus defect cluster size for three samples as measured on a Zeiss Particle Size Analyzer. One can see from

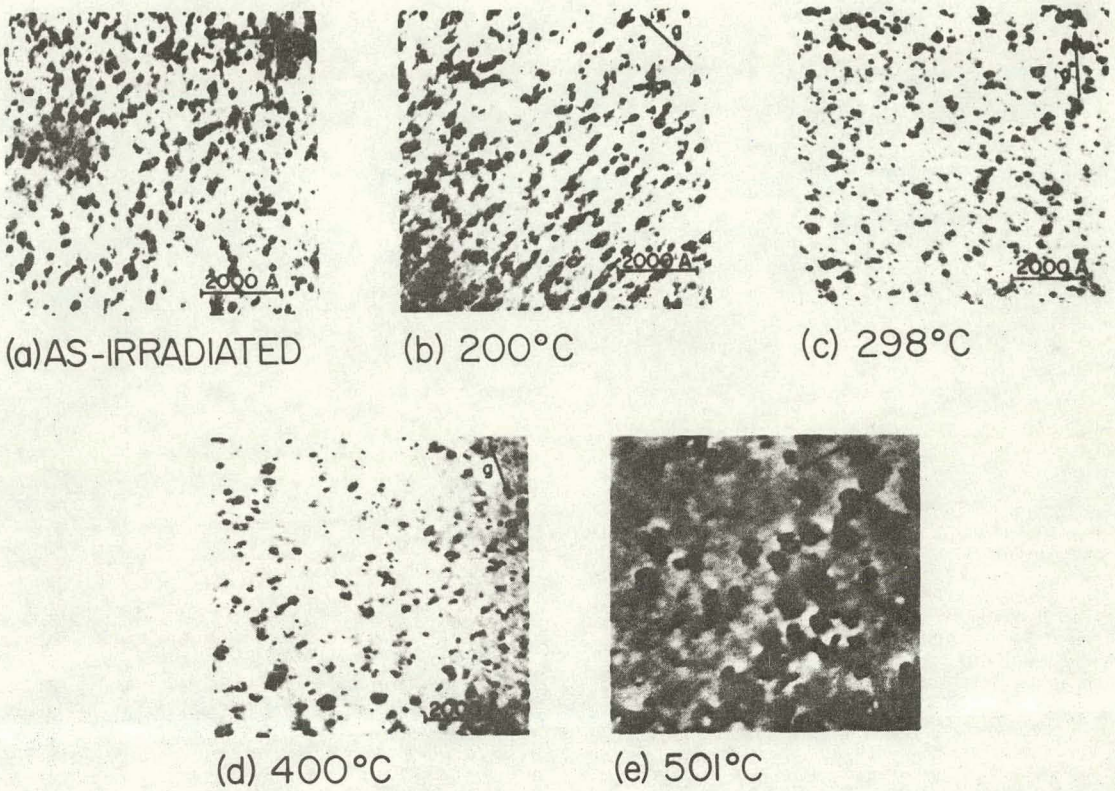

Figure 13. Defect clusters in as-irradiated and post-irradiation-annealed vanadium - 95 ppm oxygen. Irradiation dose, $\sim 1.4 \times 10^{19}$ n/cm^2 (E>1 MeV). Irradiation temperature, $\sim$ 95°C. Isochronal annealing time, 1 hr. $\vec{g}$ = <200>. Normal to foil, <100>

Figure 14. Defect cluster density size-distribution function, n', vs defect cluster size in as-irradiated and post-irradiation-annealed 1 hr at indicated temperatures vanadium - 95 wt ppm oxygen

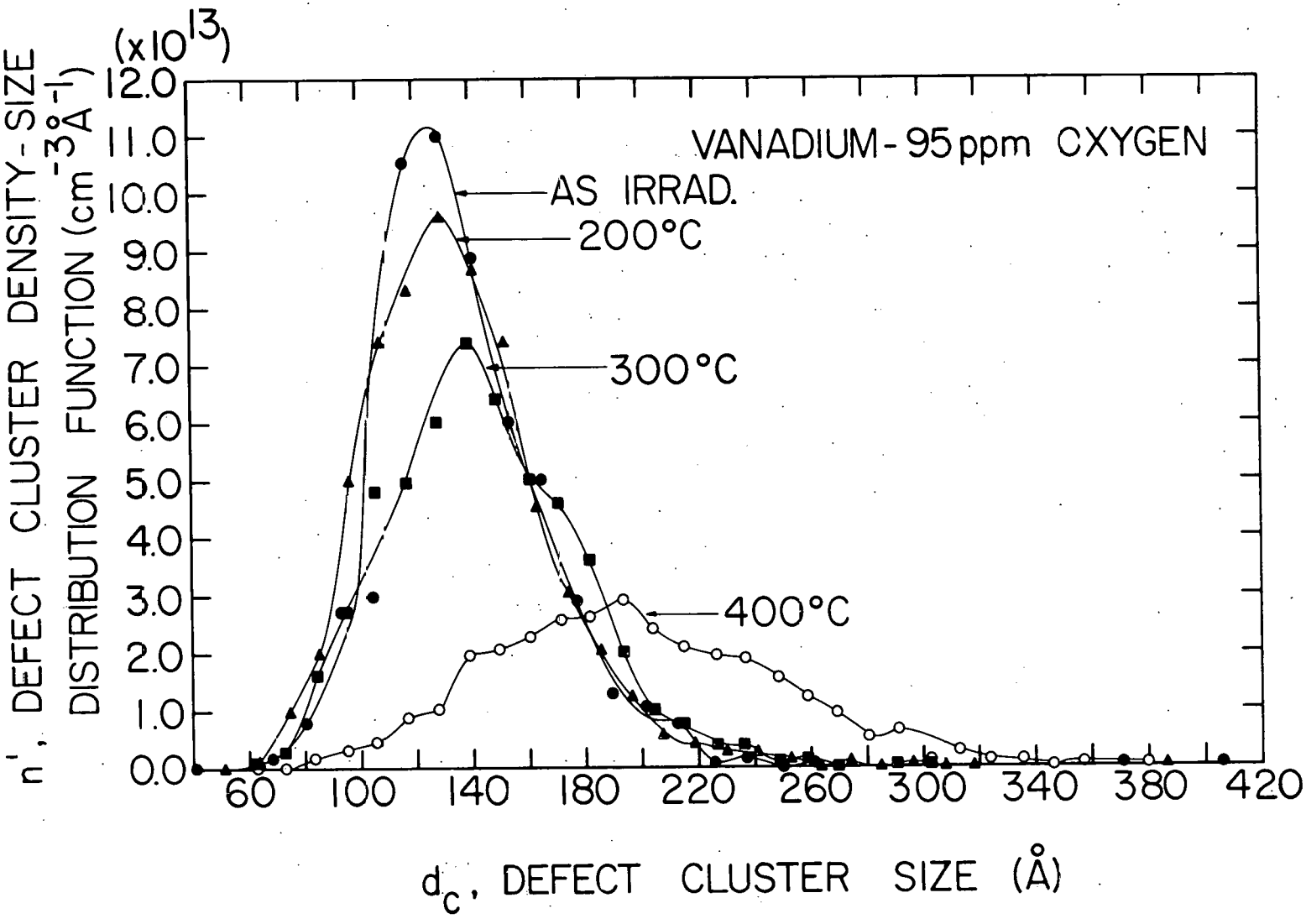
VANADIUM - 95 ppm OXYGEN
AS IRRAD.
200°C
300°C
400°C
n', DEFECT CLUSTER DENSITY-SIZE DISTRIBUTION FUNCTION (cm⁻³Å⁻¹)
(x10¹³)
12.0
11.0
10.0
9.0
8.0
7.0
6.0
5.0
4.0
3.0
2.0
1.0
0.0
60
100
140
180
220
260
300
340
380
420
d_c, DEFECT CLUSTER SIZE (Å)

Figure 14 that with increase in annealing temperatures the peak of the distribution curve shifts towards larger size and that density of the clusters (represented by the area under the distribution curve) is reduced. This is quite apparent for annealing temperature of 400°C.

Figure 15 displays radiation-produced defect clusters in as-irradiated and post-irradiation annealed V-300 samples. The size of the defect clusters appears to remain unchanged upon annealing up to 300°C. This is borne out by Figure 16 which shows size distribution curves for V-300 samples. Upon annealing at temperatures of 400°C and higher, the size of the clusters increases.

Figure 17 shows micrographs obtained from TEM examination of V-500 samples, irradiated and post-irradiation annealed. Figure 18 shows corresponding size distribution curves. It is apparent from Figures 17 and 18 that the size and density of the clusters do not change significantly up to an annealing temperature of 400°C.

As in the case of V-95, anneals at 800°C and 1000°C were carried out for V-300 and V-500 also, and some precipitation was observed.

Table 4 summarizes the results of analysis of defect clusters carried out on TEM micrographs. It provides the average size, $\bar{d}_c$, standard deviation, σ_c, total density, n, of defect clusters and interbarrier distance, ℓ. The average size, $\bar{d}_c$, is defined as

$$\bar{d}_c = \frac{\sum_{j=1}^{N} n_j d_j}{\sum_{j=1}^{N} n_j} \qquad (29)$$

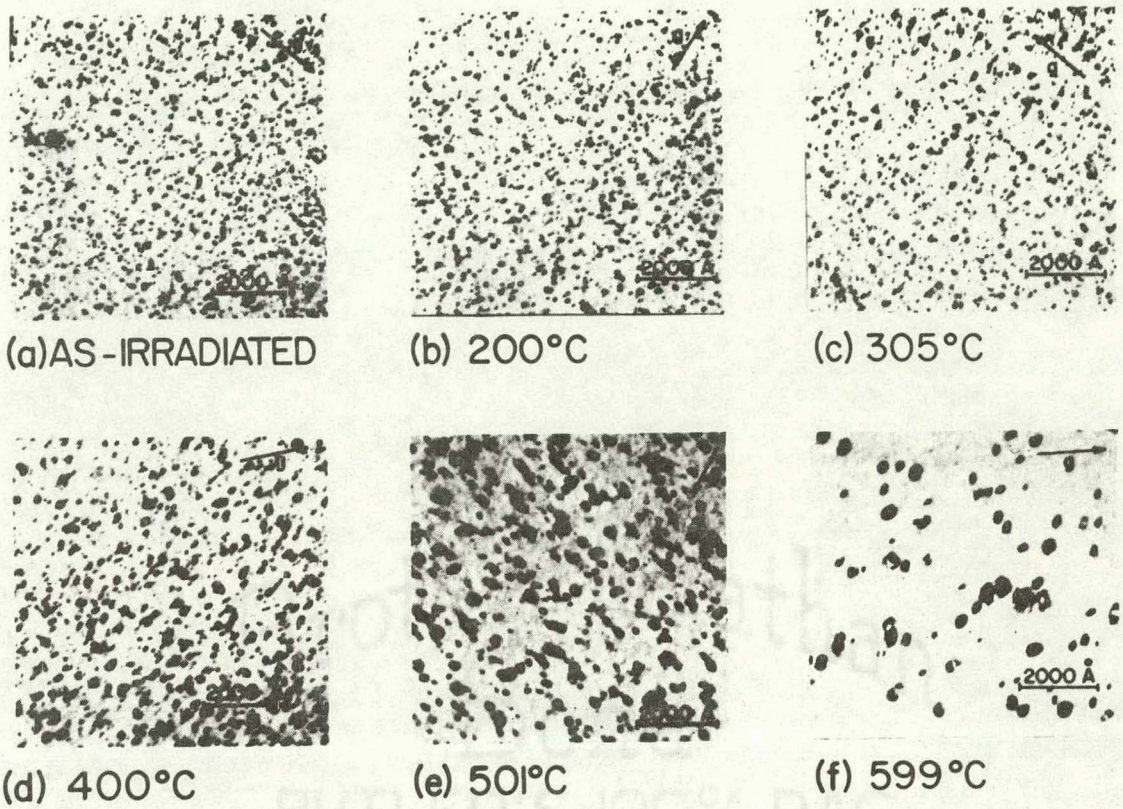

Figure 15. Defect clusters in as-irradiated and post-irradiation-annealed vanadium - 300 ppm oxygen. Irradiation dose, $\sim 1x4x10^{19}$ n/cm^2 (E>1 MeV). Irradiation temperature, $\sim$ 95°C. Isochronal annealing time, 1 hr. $\vec{g}$ = <200> . Normal to foil, <100>

Figure 16. Defect cluster density size-distribution function, n', vs defect cluster size in as-irradiated and post-irradiation-annealed 1 hr. at indicated temperatures vanadium - 300 wt ppm oxygen

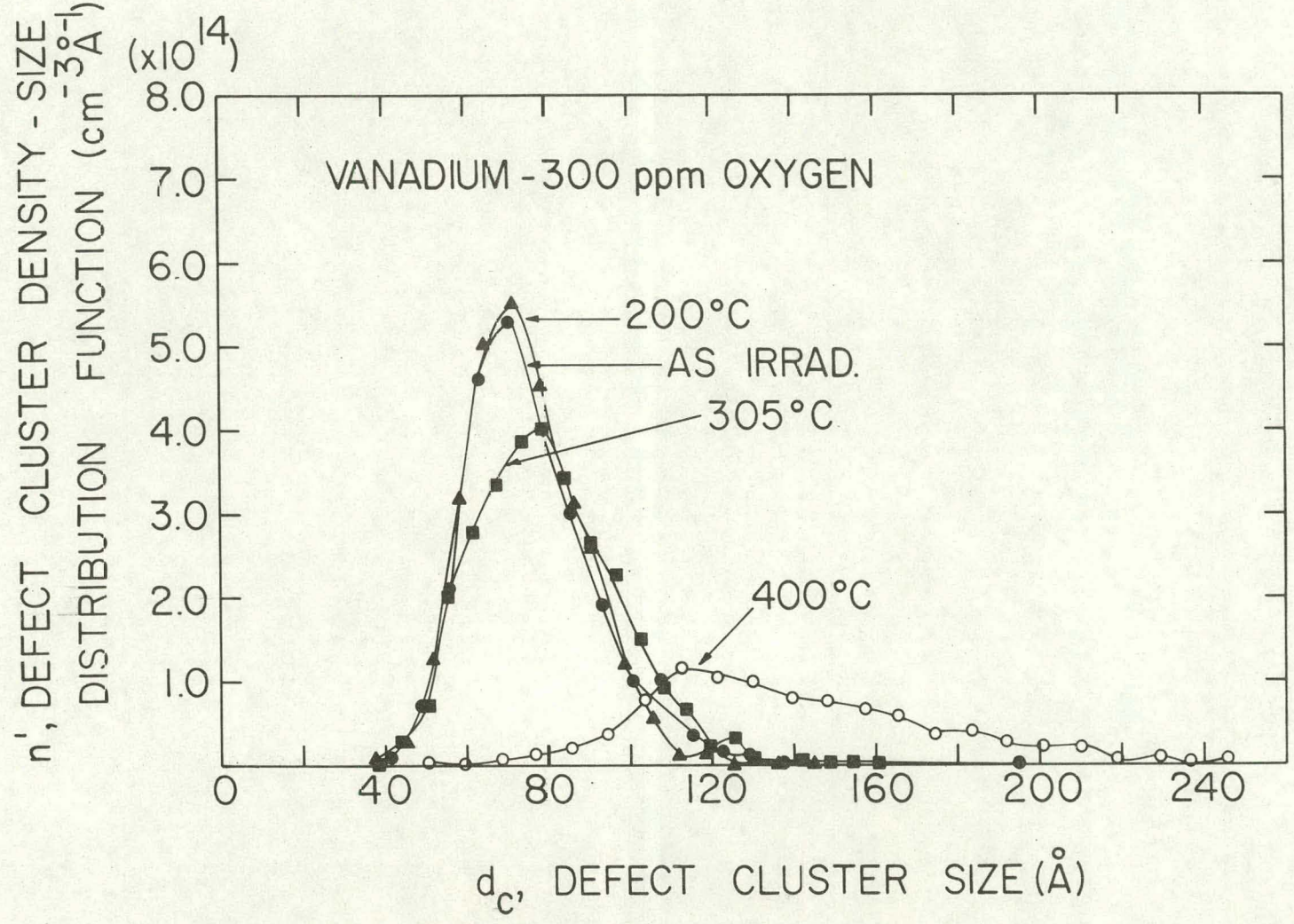
VANADIUM - 300 ppm OXYGEN
200°C
AS IRRAD.
305°C
400°C
n', DEFECT CLUSTER DENSITY - SIZE DISTRIBUTION FUNCTION (cm^{-3}Å^{-1})
(x10^{14})
8.0
7.0
6.0
5.0
4.0
3.0
2.0
1.0
0
40
80
120
160
200
240
d_c, DEFECT CLUSTER SIZE (Å)

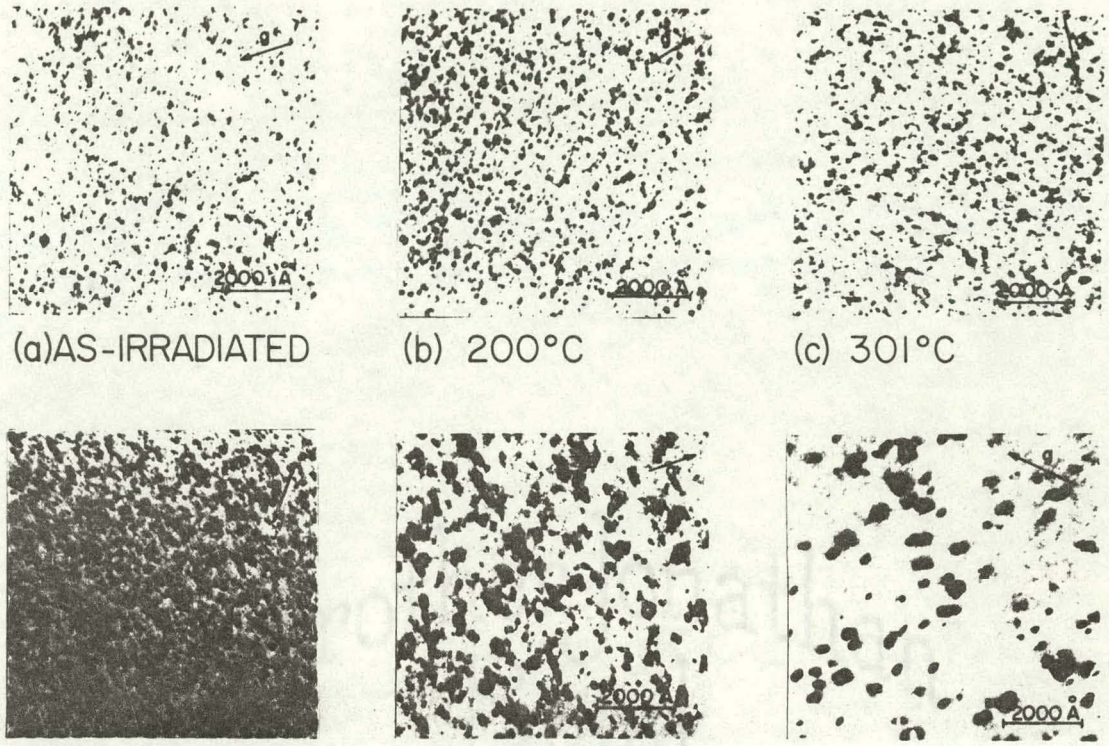

Figure 17. Defect clusters in as-irradiated and post-irradiation-annealed vanadium - 500 ppm oxygen. Irradiation dose, $\sim 1.4 \times 10^{19}$ n/cm^2 (E>1 MeV). Irradiation temperature, $\sim$ 95°C. Isochronal annealing time, 1 hr. $\vec{g}$ = <200> . Normal to foil, <100>

Figure 18. Defect cluster density size-distribution function, n', vs defect cluster size in as-irradiated and post-irradiation-annealed 1 hr at indicated temperatures vanadium - 500 wt ppm oxygen

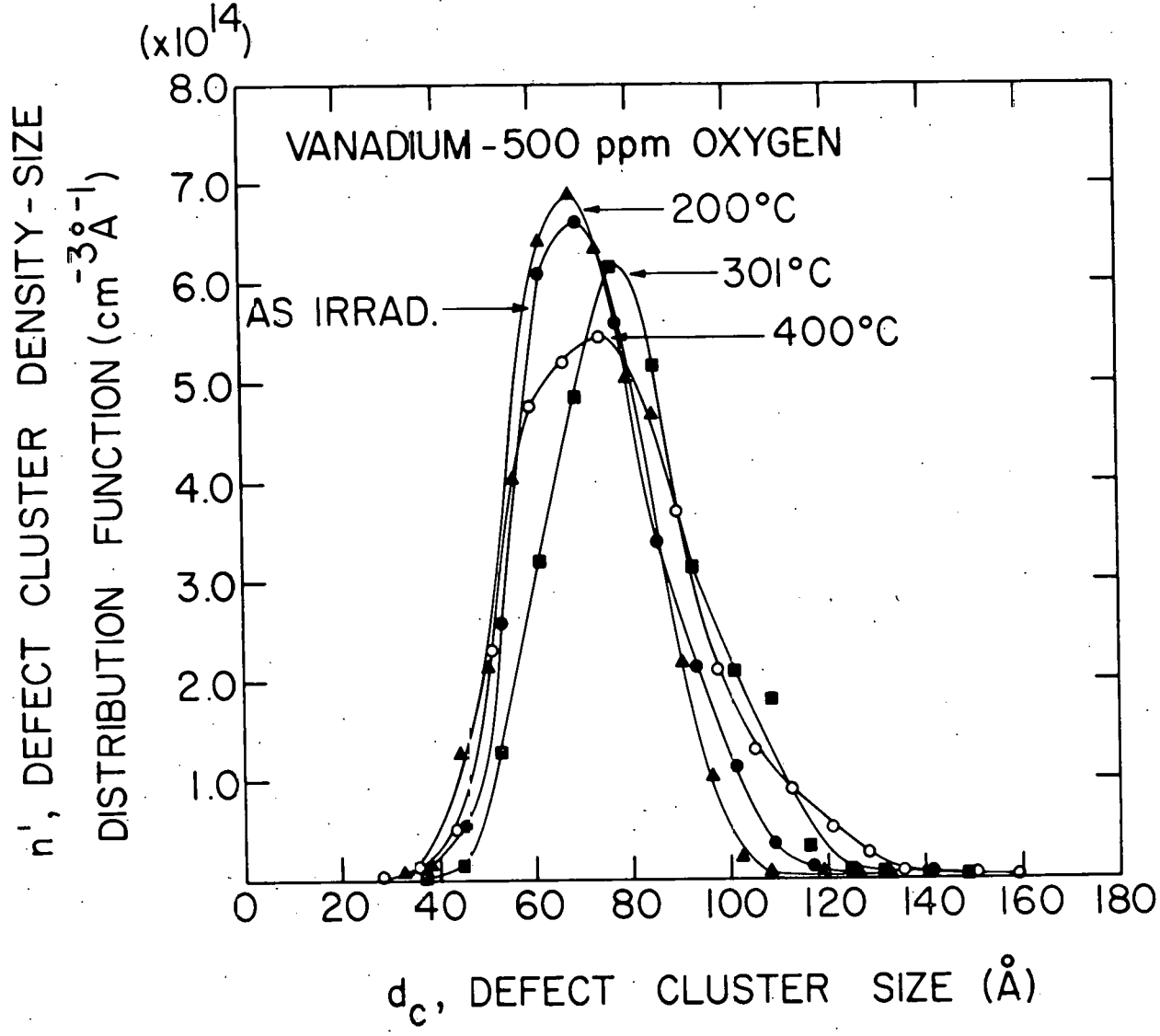
(x10^14)
8.0
7.0
6.0
5.0
4.0
3.0
2.0
1.0
VANADIUM - 500 ppm OXYGEN
200°C
301°C
400°C
AS IRRAD.
0
20
40
60
80
100
120
140
160
180
n', DEFECT CLUSTER DENSITY - SIZE DISTRIBUTION FUNCTION (cm^-3 Å^-1)
d_c, DEFECT CLUSTER SIZE (Å)

Table 4. Defect cluster parameters from TEM micrographs for as-irradiated and post-irradiation-annealed single crystal vanadium

Sample	Annealing temp.	Average diameter	Standard deviation	Total density	Total area per unit volume	Total loop length per unit vol.	Inter-barrier distance
	T_A	$\bar{d}_c$	σ	n	Ac	L_c	$\bar{\ell}$
	(°C)	(Å)	(Å)	(10^{15} cm^{-3})	($10^3 cm^{-1}$)	($10^{10} cm^{-2}$)	(10^{-6} cm)
V-95	As-irrad.	138	30	6.57	10.3	2.86	10.5
	200	136	33	7.22	11.1	3.08	10.1
	298	144	35	5.69	9.8	2.58	11.0
	400	197	51	3.08	10.0	1.90	12.8
	501	310	89	0.80	6.5	0.78	20.1
V-300	As-irrad.	77	16	17.75	8.6	4.28	8.6
	200	75	14	17.76	8.1	4.17	8.7
	305	80	18	16.51	8.7	4.15	8.7
	400	140	35	8.60	14.0	3.77	9.1
	501	191	61	2.41	7.6	1.44	14.7
	599	258	92	0.42	2.5	0.34	30.5
V-500	As-irrad.	73	15	23.64	10.4	5.45	7.6
	200	71	14	23.42	9.6	5.21	7.8
	301	79	15	22.70	11.7	5.67	7.4
	400	76	19	20.46	9.9	4.88	8.0
	501	157	60	3.46	7.7	1.71	13.6
	601	271	91	0.70	4.5	0.58	23.0

where n_j is the number of defects per cm^3 in the j^{th} size interval, d_j is the defect cluster diameter at the center of the j^{th} size interval and N is the number of intervals. The standard deviation, σ_c, which is a measure of deviation from the average cluster size, is defined as

$$\text{Standard Deviation, } \sigma = \sum_{j=1}^{N} f_j(d_j-\bar{d}_c)^2 \qquad (30)$$

where f_j is the fraction of defect clusters in the j^{th} size interval.

The effect of oxygen concentration and post-irradiation annealing on the average defect cluster size is illustrated in Figure 19. We see that the as-irradiated $\bar{d}_c$ decreases with increasing oxygen concentration. Furthermore, upon isochronal annealing, $\bar{d}_c$ stays fairly constant at first, but at higher temperatures, it increases rapidly. The temperature at which the defect clusters begin to coarsen increases with increasing oxygen concentration. Thus, $\bar{d}_c$ begins to increase at 300°C for the V-95 material, but the coarsening does not occur appreciably until 500°C is reached for the V-500 material. It is also apparent from a comparison of the defect cluster size distribution curves in Figures 14, 16 and 18, that the distribution curves become narrower with increasing oxygen concentration. A comparison of the standard deviations of the defect cluster sizes (σ_c, Table 4) also indicates this fact.

Another important factor is the density, n, or number of defect clusters of all sizes per cm^3. Figure 20 shows that n increases with increasing oxygen concentration in the as-irradiated material. Also, n decreases upon isochronal post-irradiation annealing. The onset of the decrease in n occurs

Figure 19. Average diameter, $\overline{d}_c$, of radiation-produced defect clusters vs annealing temperature

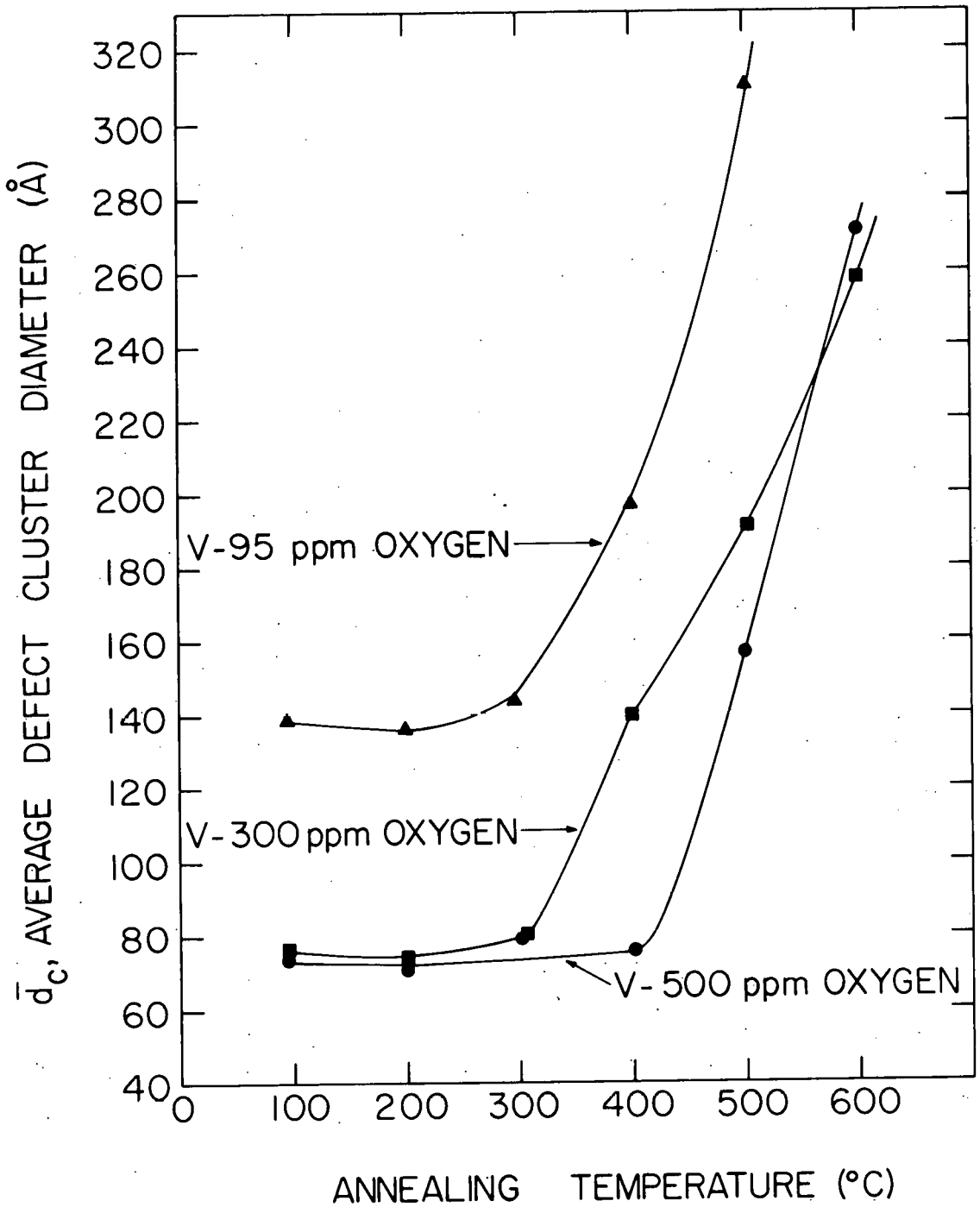
$\bar{d}_c$, AVERAGE DEFECT CLUSTER DIAMETER (Å)
320
300
280
260
240
220
200
180
160
140
120
100
80
60
40
0
100
200
300
400
500
600
ANNEALING TEMPERATURE (°C)
V-95 ppm OXYGEN
V-300 ppm OXYGEN
V-500 ppm OXYGEN

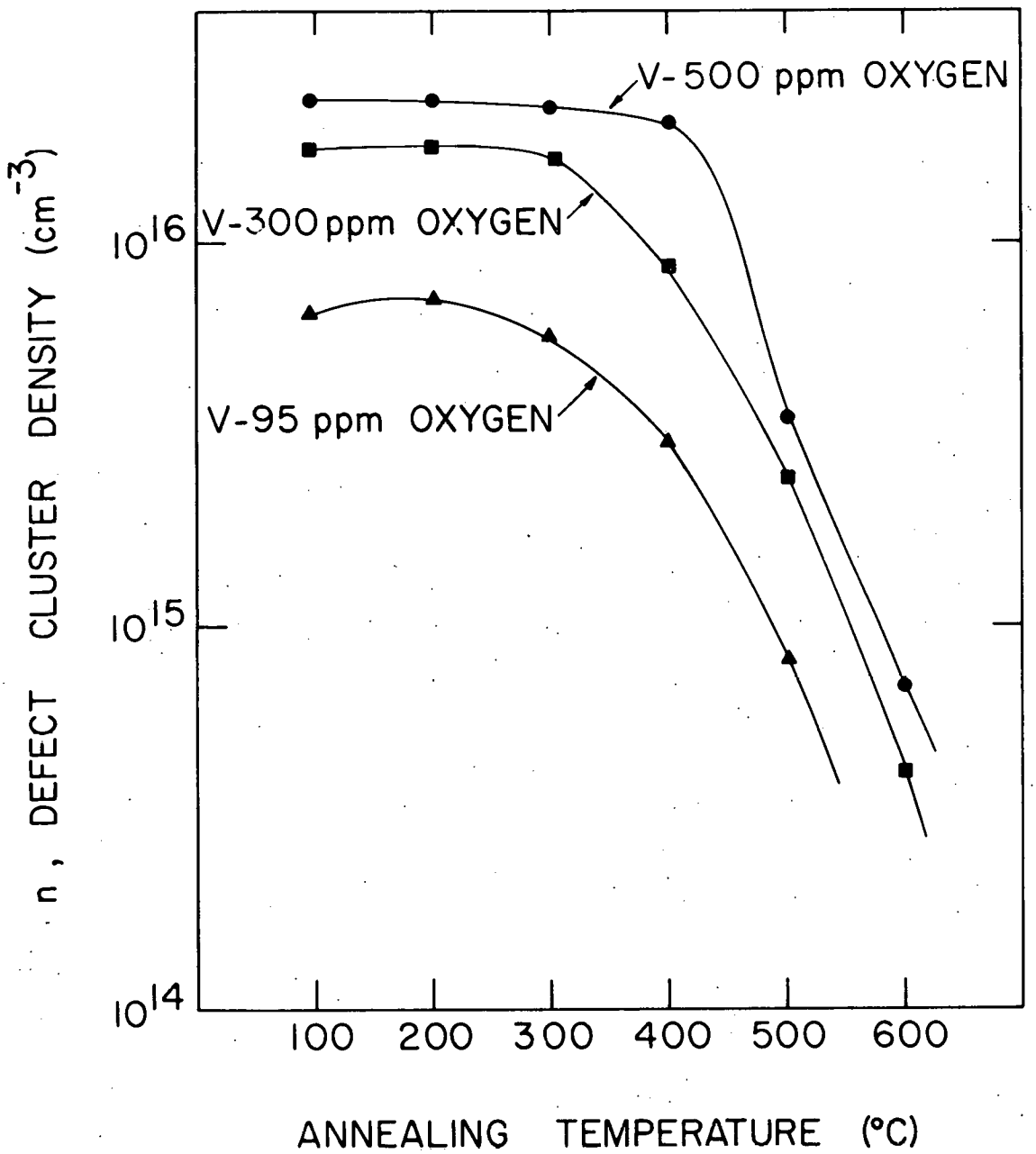

Figure 20. Density of defect clusters, n, vs annealing temperature for single crystal samples

at higher temperatures as the oxygen concentration is increased.

As was described above, a quantity of some significance in the analysis of radiation hardening is the average interbarrier distance on a plane, $\bar{\ell}$. This may be expressed as

$$\bar{\ell} = \frac{1}{\left[\sum_{j=1}^{N} n_j d_j\right]^{\frac{1}{2}}} = \frac{1}{(n\bar{d}_c)^{\frac{1}{2}}} \quad .$$

A plot of $\bar{\ell}$ versus annealing temperature is shown in Figure 21. We see that $\bar{\ell}$ decreases with increasing oxygen concentration and increases upon post-irradiation annealing. However, as for n and $\bar{d}_c$ separately, the increase in $\bar{\ell}$ occurs most readily for the lowest oxygen material.

2. Special features

It is worthwhile to mention several special features arising from apparent nonrandomness in the spatial arrangement and distribution of defect clusters. Figure 22 exhibits at A a region where defect clusters are bunched together along a line adjacent to a relatively defect-cluster free region in an as-irradiated V-300 sample. We may speculate that a dislocation segment was initially present at A at which the defect clusters were located preferentially and adjacent to which some denudation occurred. It is also possible that the dislocation segment was still present at A but was out of contrast for the diffraction vector employed. Figure 23 also displays a photomicrograph for the as-irradiated V-300 material. At A, again, there is a high concentration of defect clusters apparently along a dislocation line. Some depletion of defect clusters appears to have occurred at A,

Figure 21. Plot of interbarrier spacing, $\bar{\ell}$, vs annealing temperatures for single crystal samples containing three levels of oxygen

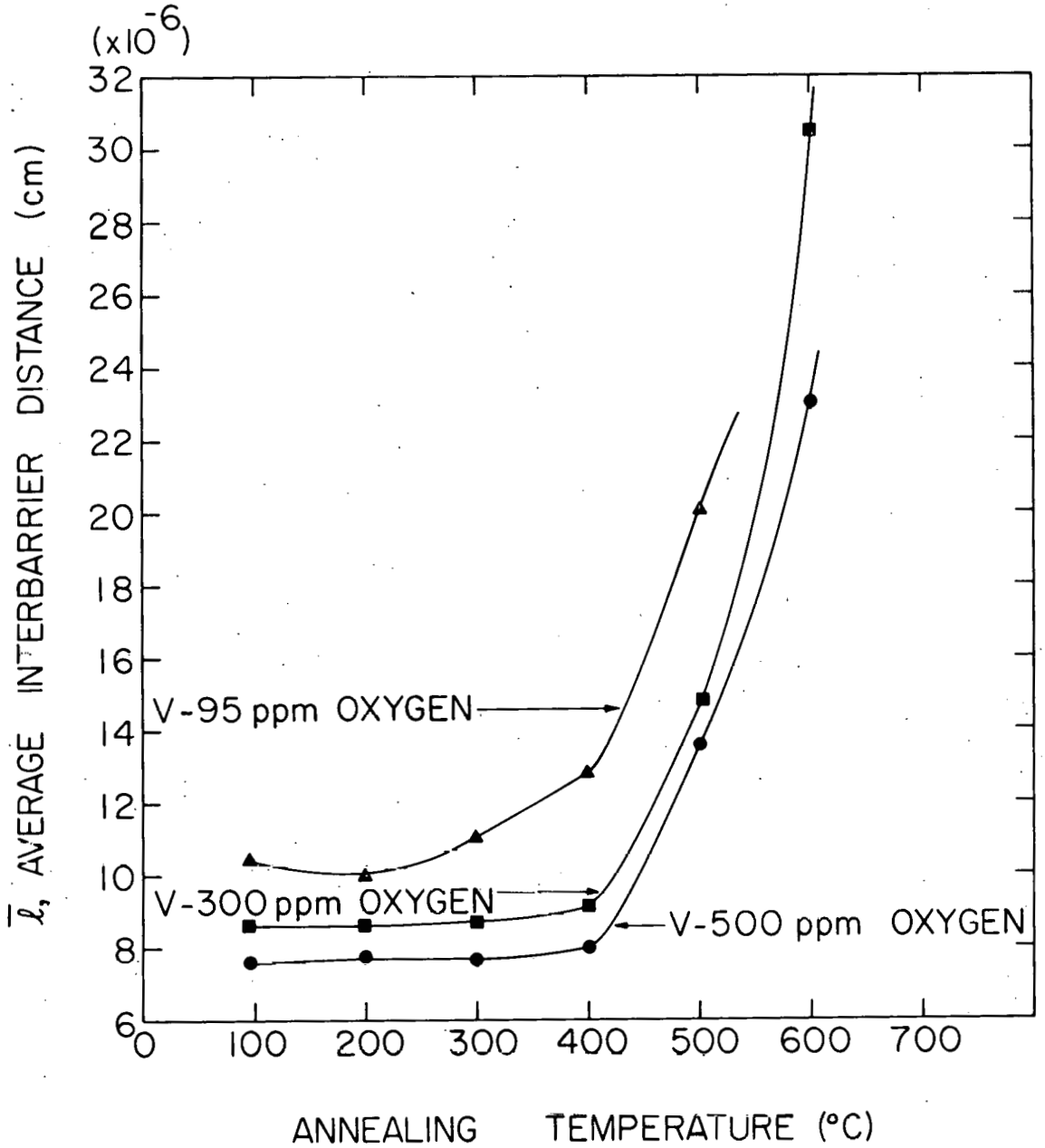
(x10^-6)
32
30
28
26
24
22
20
18
16
14
12
10
8
6
0
100
200
300
400
500
600
700
$\bar{\ell}$, AVERAGE INTERBARRIER DISTANCE (cm)
ANNEALING TEMPERATURE (°C)
V-95 ppm OXYGEN
V-300 ppm OXYGEN
V-500 ppm OXYGEN

Figure 22. Transmission electron micrograph of V-300 single crystal in as-irradiated condition. Region A indicates a linear arrangement of defect clusters adjacent to a denuded region

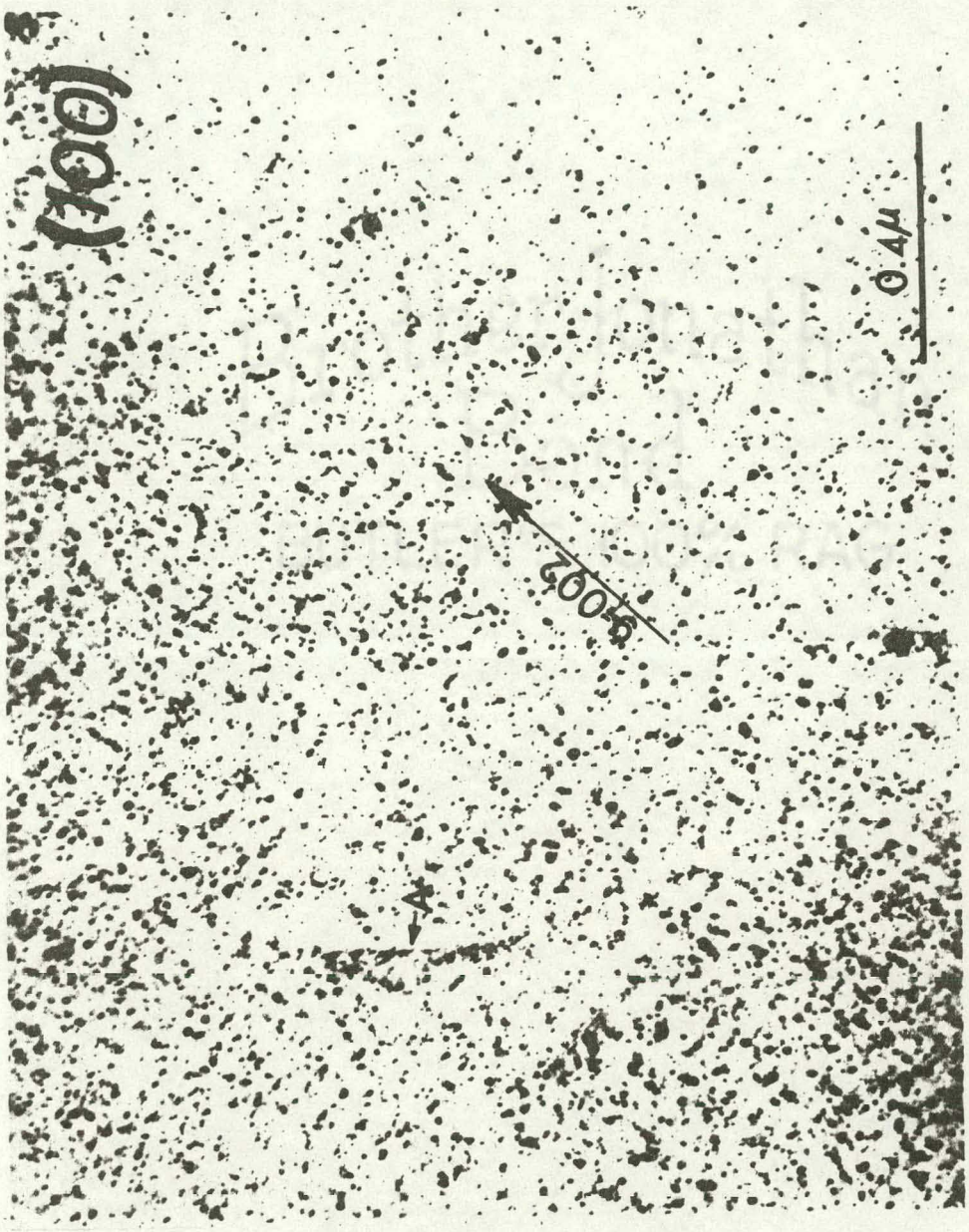
(101)
(002)
0.4μ

Figure 23. Transmission electron micrograph of V-300 sirgle crystal in as-irradiated condition, showing linear arrangements of defect clusters at A and C


(001)
A
B
[10-1]

seemingly from both sides of the line. At B and C denudation has also occurred, but primarily from only one side of the dislocation line.

Figure 24 illustrates another interesting feature. At first glance the defect clusters may appear to be randomly distributed. A careful examination, however, reveals that the clusters are frequently aligned along an arc or loop (for example, at A, B, and C) or in a chain-like manner at D and E. The micrograph in Figure 24 refers to an as-irradiated V-300 sample, but the feature under discussion here was observed in other samples including post-irradiation-annealed ones.

C. Strain Aging

The strain-aging study was carried out on polycrystalline tensile samples similar to those used for the radiation-anneal hardening study. The strain-aging experiments were carried out on both irradiated and unirradiated specimens. The purpose of this study was to determine the effect of neutron irradiation on the strain-aging behavior of vanadium and to compare the result with unirradiated material. It was also of interest to delineate the role of interstitial impurities, particularly oxygen, on the strain-aging behavior of irradiated vanadium.

The tests used for this study were load-unload-anneal-reload tests. The sample was deformed to a certain strain beyond elastic limit, it was unloaded, annealing was performed, and the sample was then reloaded. This was repeated for a number of annealing treatments on the same sample. Both isothermal and isochronal annealing treatments were performed. Isothermal anneals were carried out at 175°C to correspond to the center of the rising portion of the radiation-anneal hardening curves for vanadium (Figure 9).

Figure 24. Transmission electron micrograph of V-300 single crystal in as-irradiated condition. Letters A-E indicate regions where defect clusters appear to be arranged in chain-like fashion along an arc

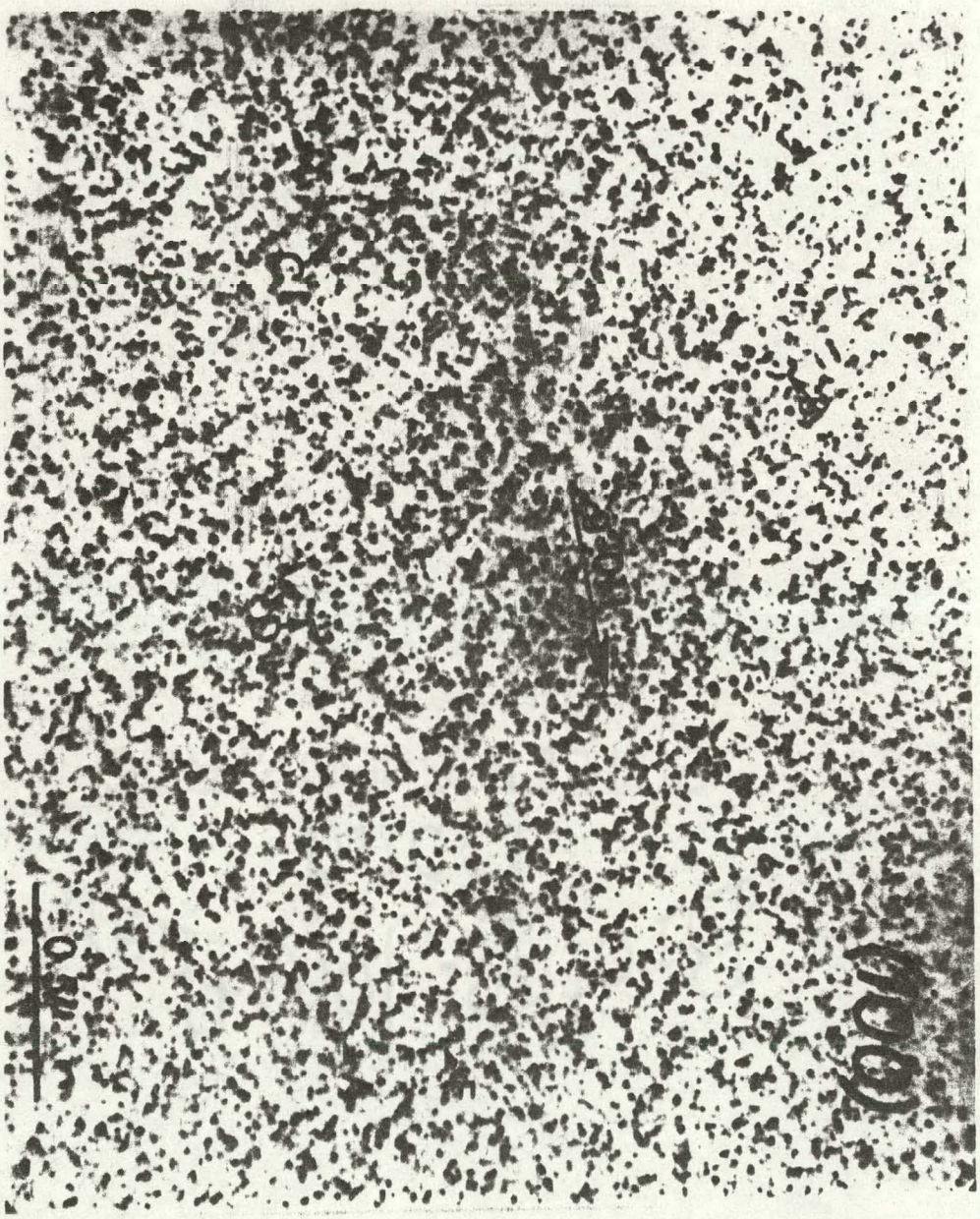
100 nm

The load-elongation plots were converted into true stress - true strain diagrams, using the conventional formulae for conversion of engineering stress and strain into true stress and strain.

Figure 25 shows results of strain-aging tests for V-60. The top portion of the figure represents a true stress - true strain diagram for unirradiated material and bottom portion that for irradiated material. The anneals were carried out at a temperature of 175°C. The times indicated on the curves are actual times of anneals at 175°C during unloading and not the cumulative times.

It can be observed from Figure 25 that the tendency for strain hardening is greatly reduced in irradiated material as evidenced by much smaller increase in stress level upon isothermal annealing and straining for irradiated material (20 kpsi to 30 kpsi) than unirradiated material (10 kpsi to 30 kpsi). Whereas for unirradiated material the yield drop returns after 30 minutes of annealing time (vertical arrow top figure), for irradiated material the yield drop returns after 12 hr (second 12 hr anneal, vertical arrow bottom figure). Thus the strain-aging tendency (reappearance of yield drop) is delayed in case of irradiated material.

Figure 26 shows results of strain aging tests on V-200. One can see that the appearance of yield drop is delayed in irradiated material to 7 hr as compared to 5 min for unirradiated material. Similar results were obtained for V-640 in which case the yield drop appears after 30 min of annealing in irradiated material, whereas it occurs after only 30 sec of anneal in case of unirradiated material (Figure 27).

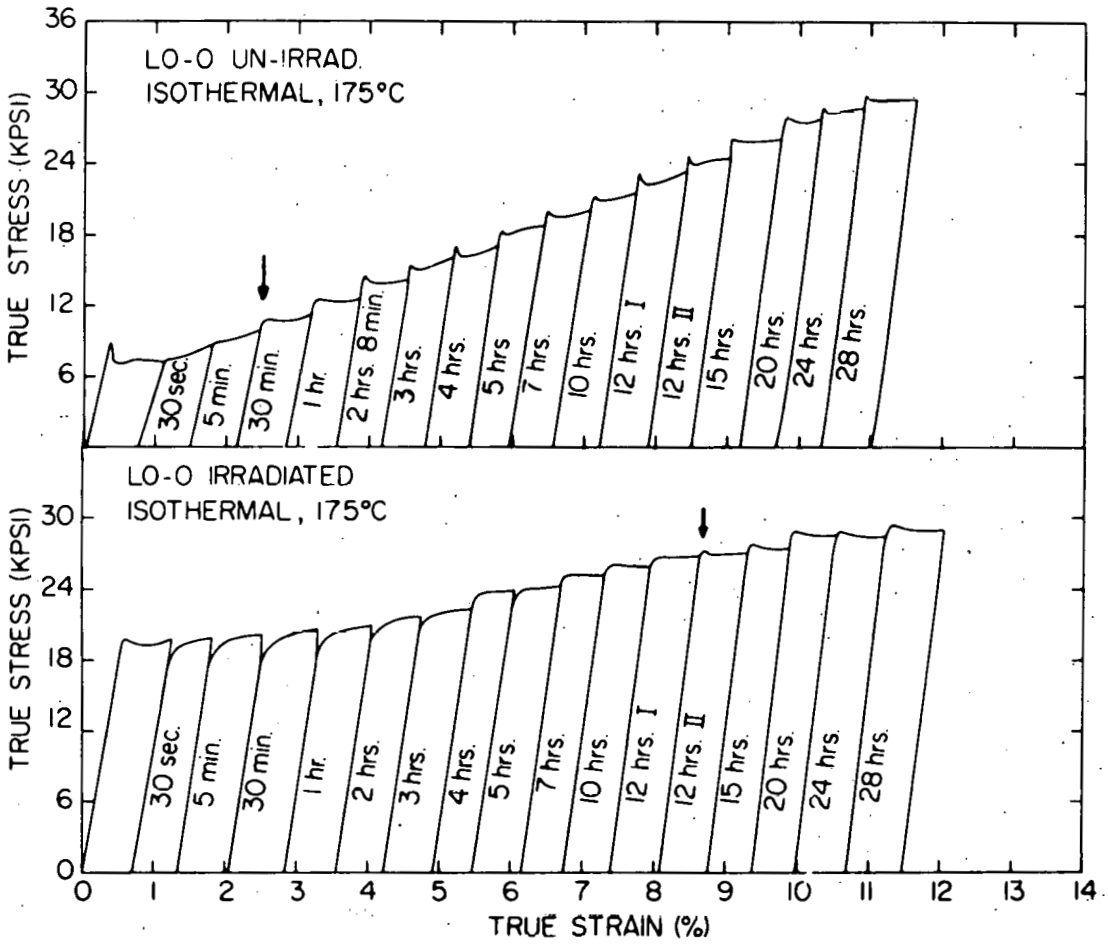

Figure 25. True stress vs true strain for unirradiated (above) and irradiated (below) specimens of vanadium - 60 wt ppm oxygen isothermally annealed at 175°C. Irradiation dose, 1.2×10^{19} n/cm^2 (E>1 MeV) at 105°C

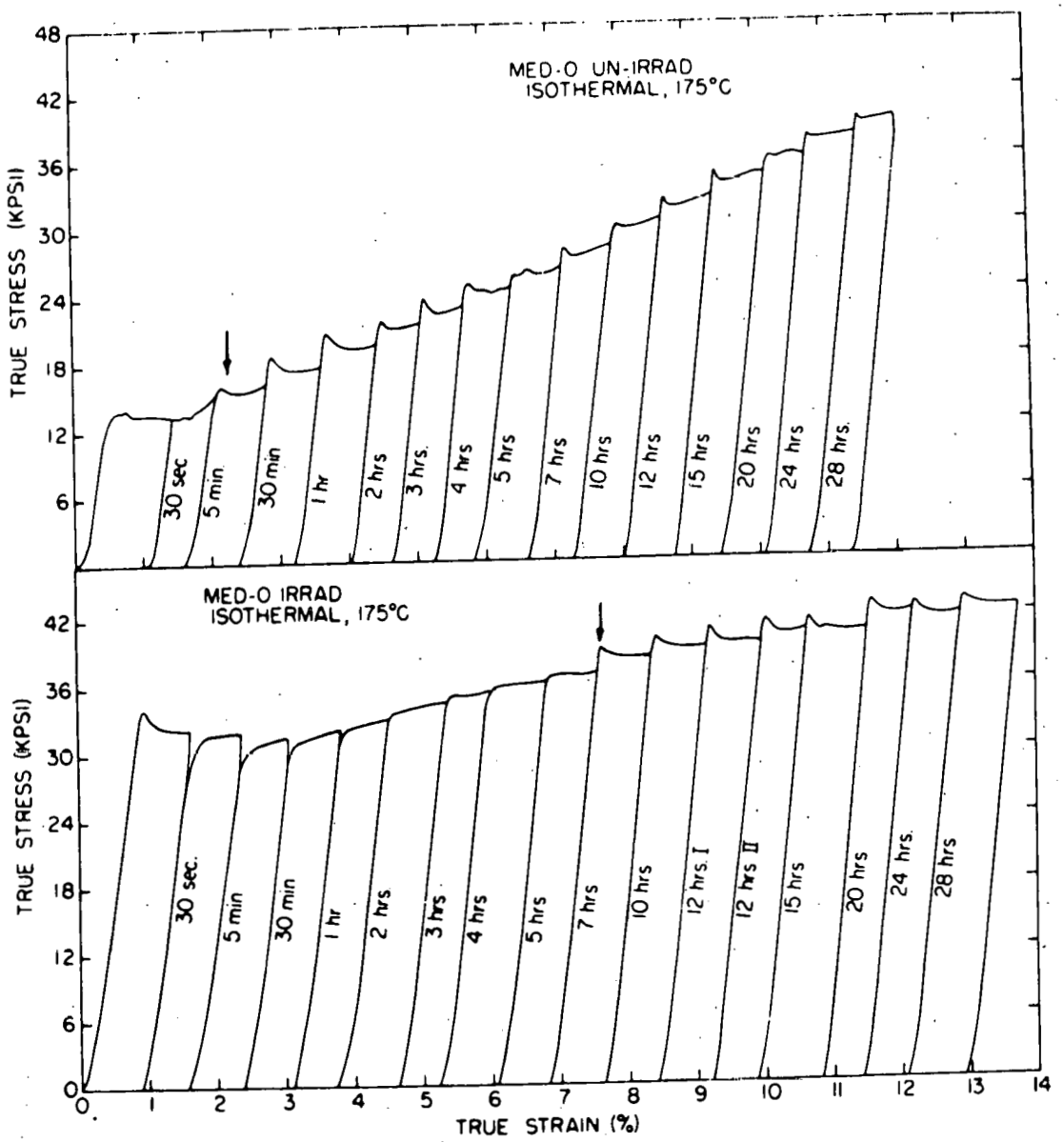

Figure 26. True stress vs true strain for unirradiated (above) and irradiated (below) specimens of vanadium - 200 wt ppm oxygen isothermally annealed at 175°C. Irradiation dose, 1.2×10^{19} n/cm^2 (E>1 MeV) at 105°C

Figure 27. True stress vs true strain for unirradiated (above) and irradiated (below) specimens of vanadium - 640 wt ppm oxygen isothermally annealed at 175°C. Irradiation dose, 1.2×10^{19} n/cm^2 (E>1 MeV) at 105°C

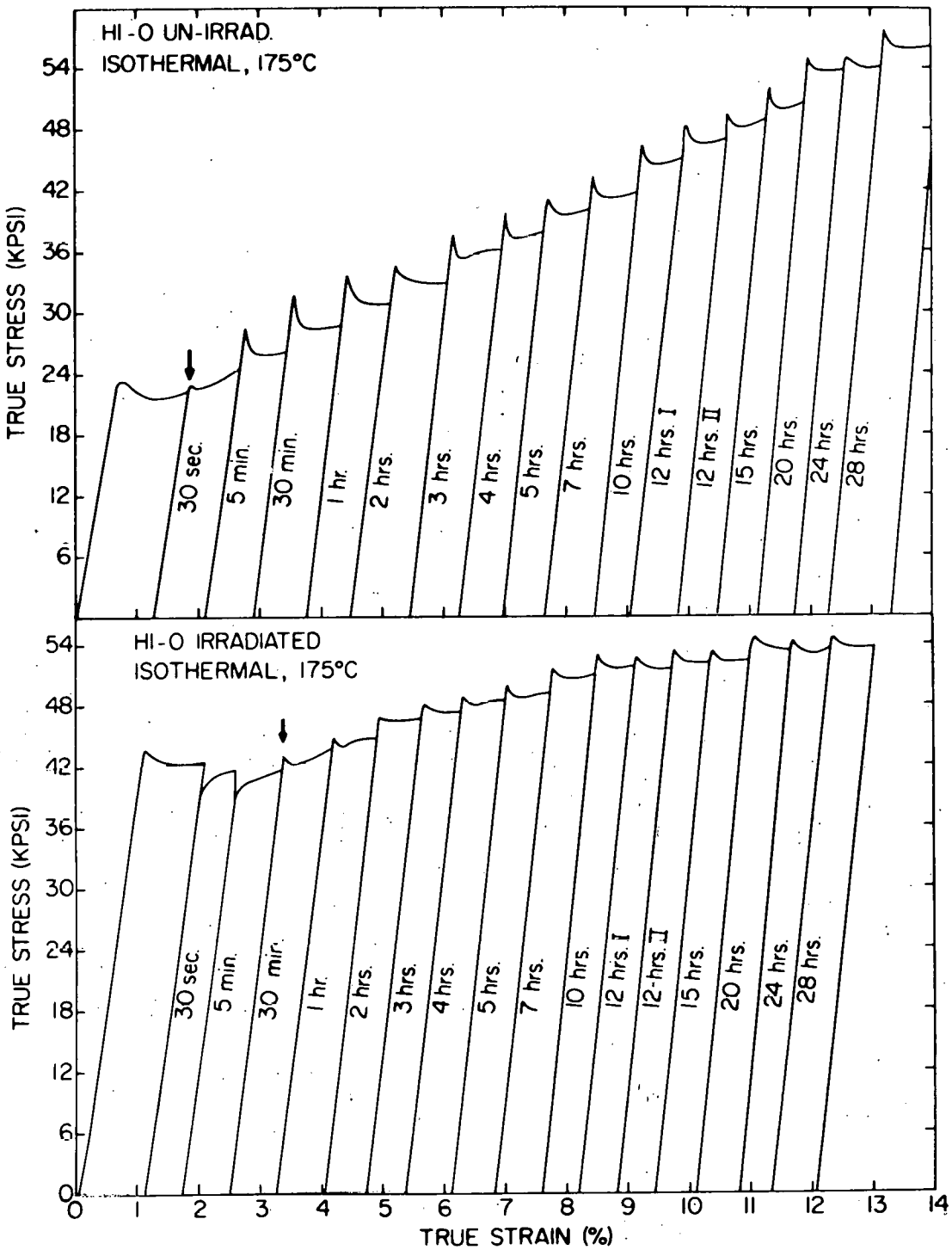
HI-O UN-IRRAD.
ISOTHERMAL, 175°C
TRUE STRESS (KPSI)
30 sec.
5 min.
30 min.
1 hr.
2 hrs.
3 hrs.
4 hrs.
5 hrs.
7 hrs.
10 hrs.
12 hrs. I
12 hrs. II
15 hrs.
20 hrs.
24 hrs.
28 hrs.
HI-O IRRADIATED
ISOTHERMAL, 175°C
TRUE STRESS (KPSI)
30 sec.
5 min.
30 mir.
1 hr.
2 hrs.
3 hrs.
4 hrs.
5 hrs.
7 hrs.
10 hrs.
12 hrs. I
12-hrs. II
15 hrs.
20 hrs.
24 hrs.
28 hrs.
TRUE STRAIN (%)

Table 5 below summarizes the aging times for reappearance of yield drop for unirradiated and irradiated materials.

Table 5. Aging time (sec) for reappearance of yield drop

Material	Unirradiated	Irradiated
V-60	1800	4.32×10^4
V-200	300	2.5×10^4
V-640	30	1.8×10^3

The following conclusions can be drawn from Figures 25-27:

1. Neutron irradiation reduces the tendency of strain hardening.

2. Neutron irradiation delays the appearance of the yield drop, thus reducing the strain-aging tendency.

3. With increasing oxygen content the strain-aging tendency increases in both unirradiated and irradiated material.

As mentioned above, isochronal tests were also performed during the strain-aging study. The isochronal annealing treatments were carried out for a duration of 1 hr.

Figures 28-30 show that in unirradiated material there is decrease in the flow stress upon annealing at about 500°C. The decrease in the flow stress from the stress in preceding deformation increases with increasing oxygen. The same behavior is apparent in the case of irradiated material.

Figure 28. True stress vs true strain for unirradiated (above) and irradiated (below) specimens of vanadium - 60 ppm oxygen isochronally annealed for 1 hr. Irradiation dose, 1.2×10^{19} n/cm^2 (E>1 MeV) at 105°C. Arrow points to an instant reloading

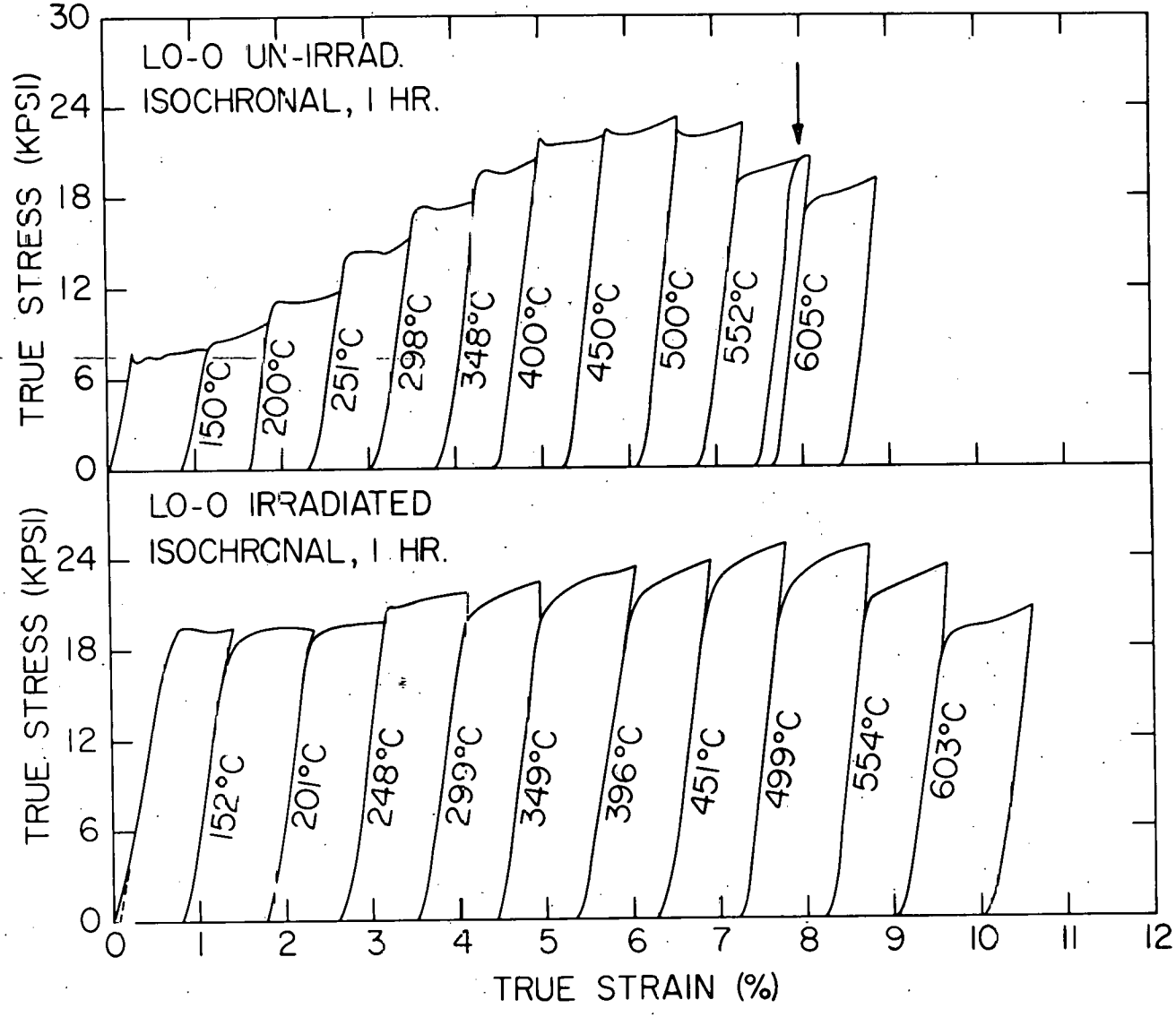
LO-O UN-IRRAD.
ISOCHRONAL, 1 HR.
TRUE STRESS (KPSI)
30
24
18
12
6
0
150°C
200°C
251°C
298°C
348°C
400°C
450°C
500°C
552°C
605°C
LO-O IRRADIATED
ISOCHRONAL, 1 HR.
TRUE STRESS (KPSI)
24
18
12
6
0
152°C
201°C
248°C
299°C
349°C
396°C
451°C
499°C
554°C
603°C
0
1
2
3
4
5
6
7
8
9
10
11
12
TRUE STRAIN (%)

Figure 29. True stress vs true strain for unirradiated (above) and irradiated (below) specimens of vanadium - 200 ppm oxygen isochronally annealed for 1 hr. Irradiation dose, 1.2×10^{19} n/cm^2 (E>1 MeV) at 105°C

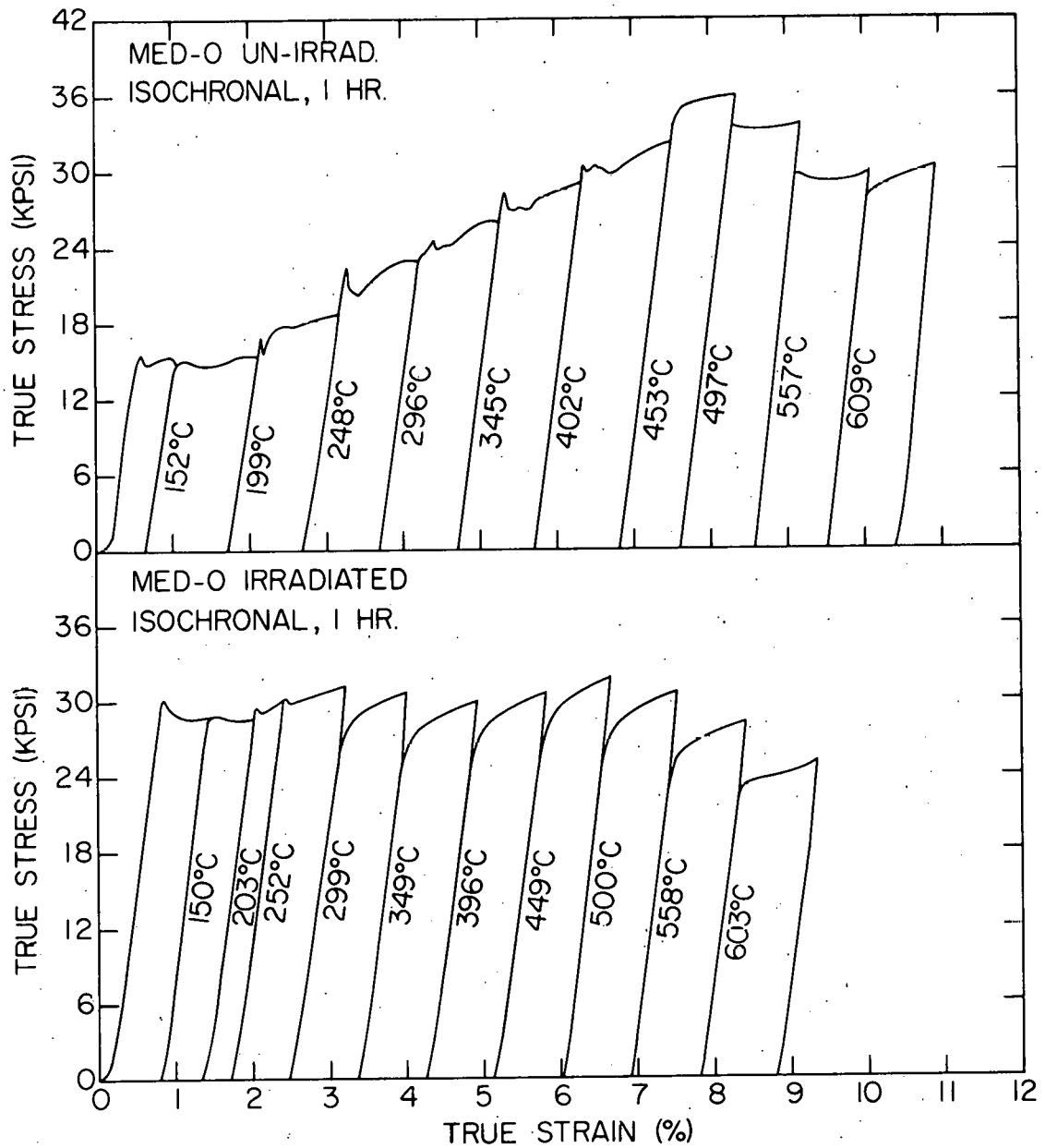
MED-O UN-IRRAD.
ISOCHRONAL, 1 HR.
TRUE STRESS (KPSI)
42
36
30
24
18
12
6
0
152°C
199°C
248°C
296°C
345°C
402°C
453°C
497°C
557°C
609°C
MED-O IRRADIATED
ISOCHRONAL, 1 HR.
TRUE STRESS (KPSI)
36
30
24
18
12
6
0
150°C
203°C
252°C
299°C
349°C
396°C
449°C
500°C
558°C
603°C
0
1
2
3
4
5
6
7
8
9
10
11
12
TRUE STRAIN (%)

Figure 30. True stress vs true strain for unirradiated (above) and irradiated (below) specimens of vanadium - 640 ppm oxygen isochronally annealed for 1 hr. Irradiation dose, 1.2×10^{19} n/cm^2 (E>1 MeV) at 105°C

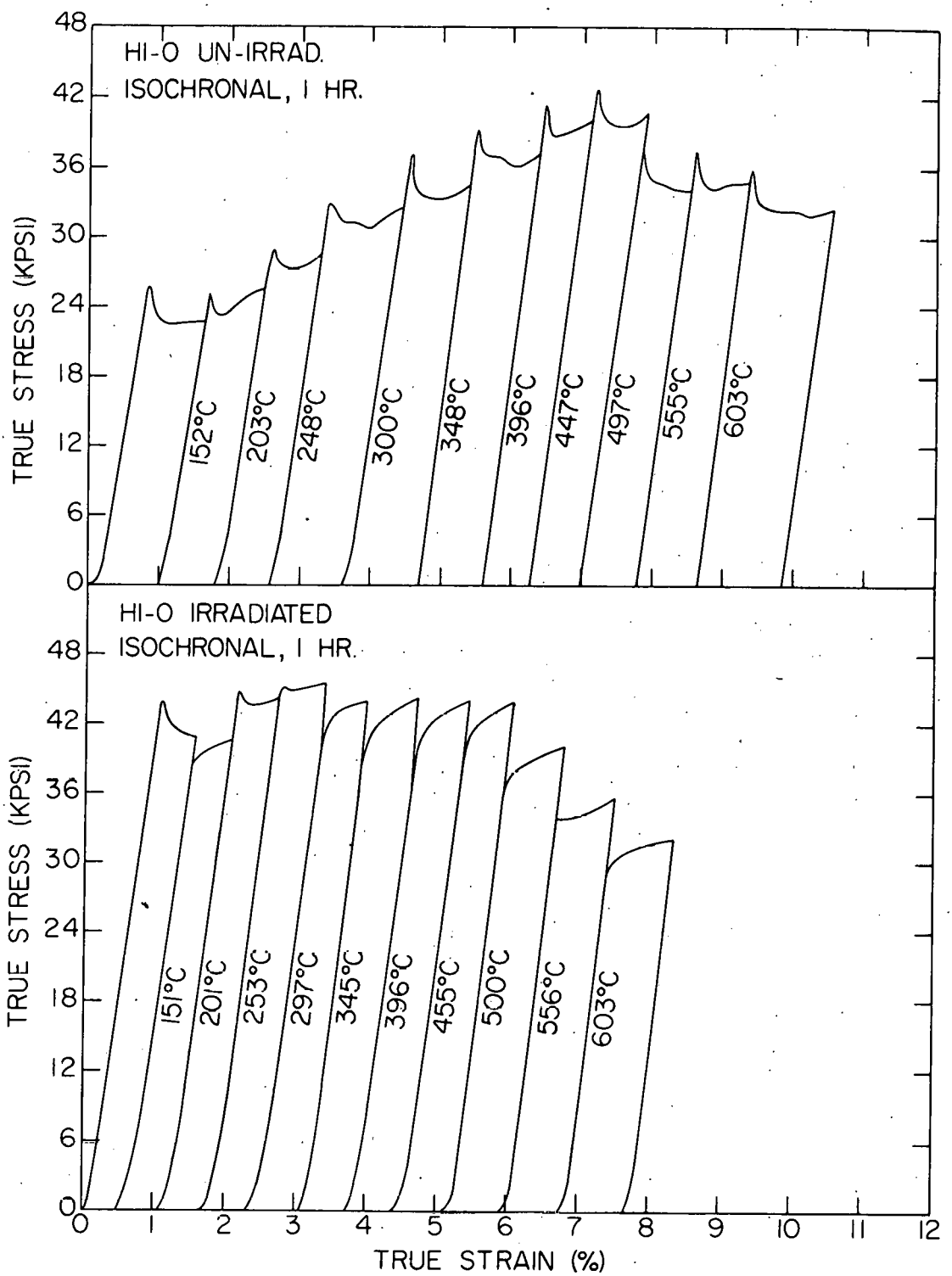
HI-O UN-IRRAD.
ISOCHRONAL, 1 HR.
TRUE STRESS (KPSI)
152°C
203°C
248°C
300°C
348°C
396°C
447°C
497°C
555°C
603°C
HI-O IRRADIATED
ISOCHRONAL, 1 HR.
TRUE STRESS (KPSI)
151°C
201°C
253°C
297°C
345°C
396°C
455°C
500°C
556°C
603°C
TRUE STRAIN (%)

However, in case of irradiated material there were no yield drops observed for V-60. In V-200 (Figure 29) yield drops were observed but were not well defined. In case of V-640 (Figure 30), however, yield drops were observed in curves for 201 and 253°C anneals. The temperature region between 150 and 300°C appears to be of significance here. Beyond 300°C no yield drop was observed in any of the three kinds of materials.

To determine the role of strain level in appearance of yield drop or in increase in stress upon isothermal annealing, the following experiments were performed. Separate samples of all three kinds of materials were strained about 3%, 6%, and 8% prior to a 2-hr anneal at 175°C. The results of these tests are represented in Figures 31-33 and can be summarized as follows:

1. Samples of V-60 and V-200 strained about 3%, annealed at 175°C for 2 hr and restrained showed no yield drop or increase in stress. V-640, however, showed a marked yield drop and increase in stress.

2. V-60 strained about 6% annealed at 175°C for 2 hr and restrained showed no yield drop or increase in stress. However, V-200 and V-640 showed yield drops and increase in stress. The magnitude of the yield drop for V-640 was larger than for V-200.

3. All three kinds of materials showed increase in stress upon restraining but only V-640 and V-300 show yield drop, and the magnitude of increase was larger for vanadium with higher oxygen concentration.

4. Upon annealing for longer times yield drop and/or increase in stress were observed in all three kinds of material even after only 3% prior strain.

Figure 31. True stress vs true strain for irradiated vanadium strained ∿ 3% prior to annealing at 175°C for specified times

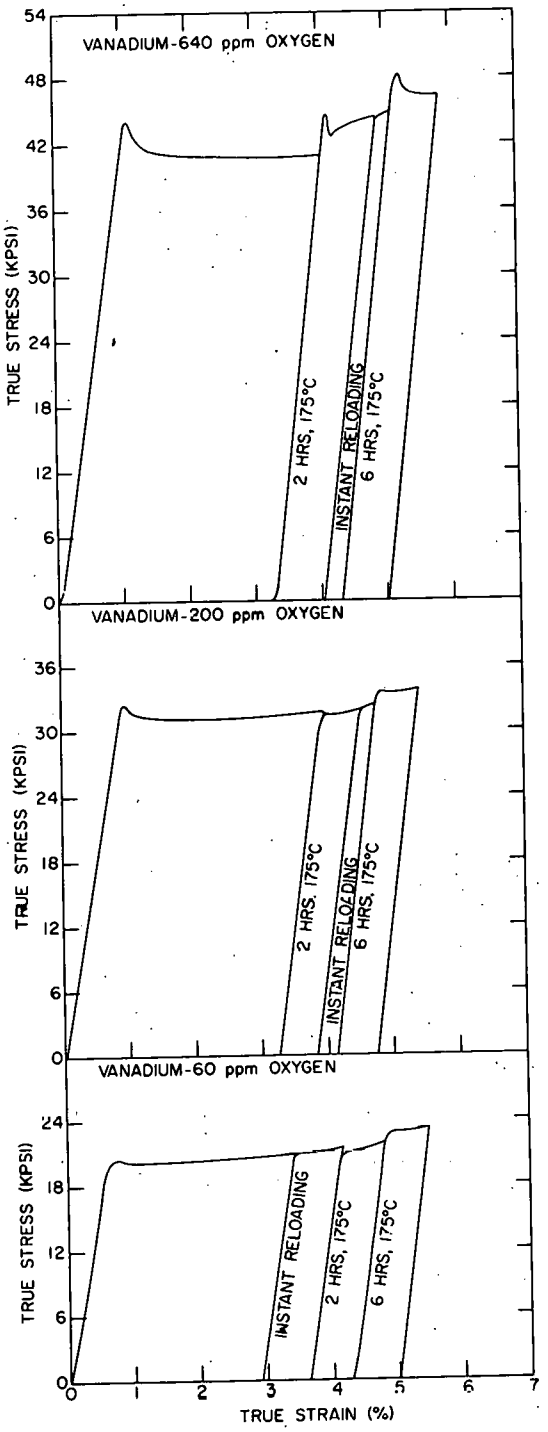
VANADIUM-640 ppm OXYGEN
TRUE STRESS (KPSI)
54
48
42
36
30
24
18
12
6
0
2 HRS, 175°C
INSTANT RELOADING
6 HRS, 175°C
VANADIUM-200 ppm OXYGEN
TRUE STRESS (KPSI)
36
30
24
18
12
6
0
2 HRS, 175°C
INSTANT RELOADING
6 HRS, 175°C
VANADIUM-60 ppm OXYGEN
TRUE STRESS (KPSI)
24
18
12
6
0
INSTANT RELOADING
2 HRS, 175°C
6 HRS, 175°C
0
1
2
3
4
5
6
7
TRUE STRAIN (%)

Figure 32. True stress vs true strain for irradiated vanadium strained ∿ 6% prior to annealing at 175°C for specified times

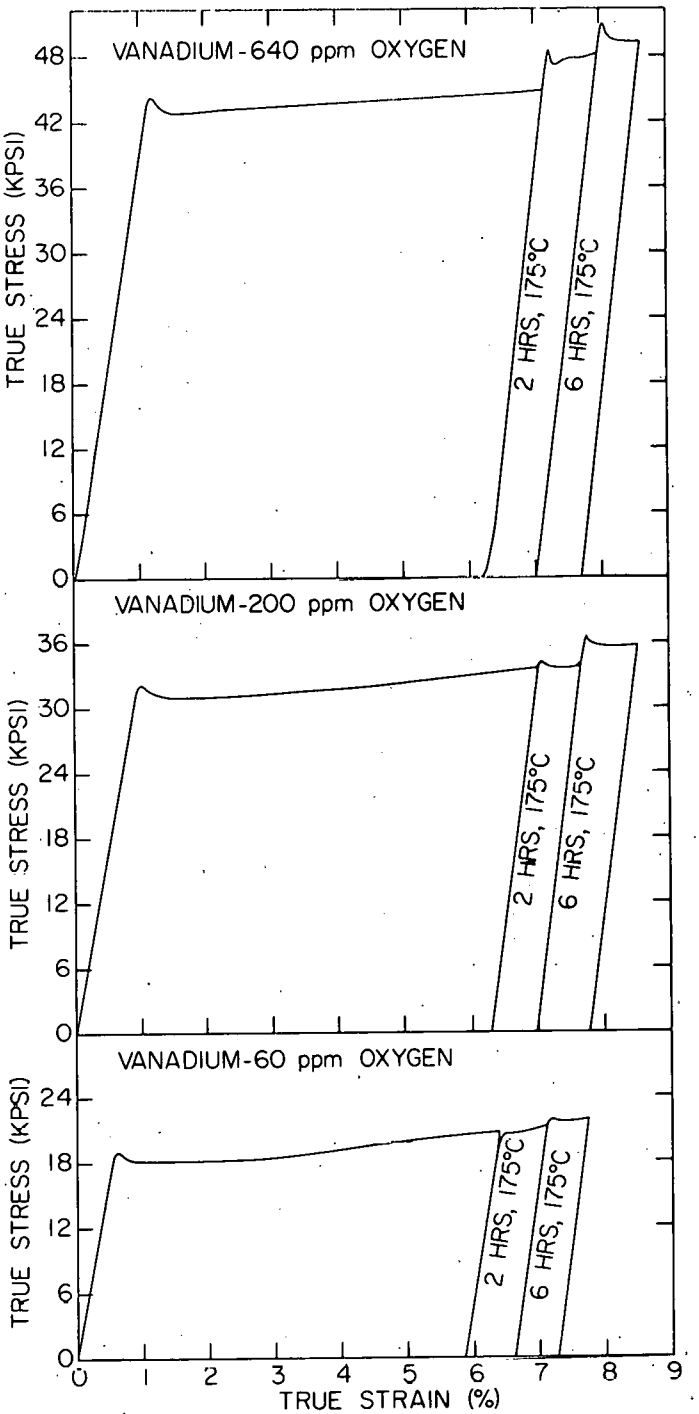
VANADIUM-640 ppm OXYGEN
TRUE STRESS (KPSI)
48
42
36
30
24
18
12
6
0
2 HRS, 175°C
6 HRS, 175°C
VANADIUM-200 ppm OXYGEN
TRUE STRESS (KPSI)
36
30
24
18
12
6
0
2 HRS, 175°C
6 HRS, 175°C
VANADIUM-60 ppm OXYGEN
TRUE STRESS (KPSI)
24
18
12
6
0
2 HRS, 175°C
6 HRS, 175°C
0
1
2
3
4
5
6
7
8
9
TRUE STRAIN (%)

Figure 33. True stress vs true strain for irradiated vanadium strained ∿ 8% prior to annealing at 175°C for specified times

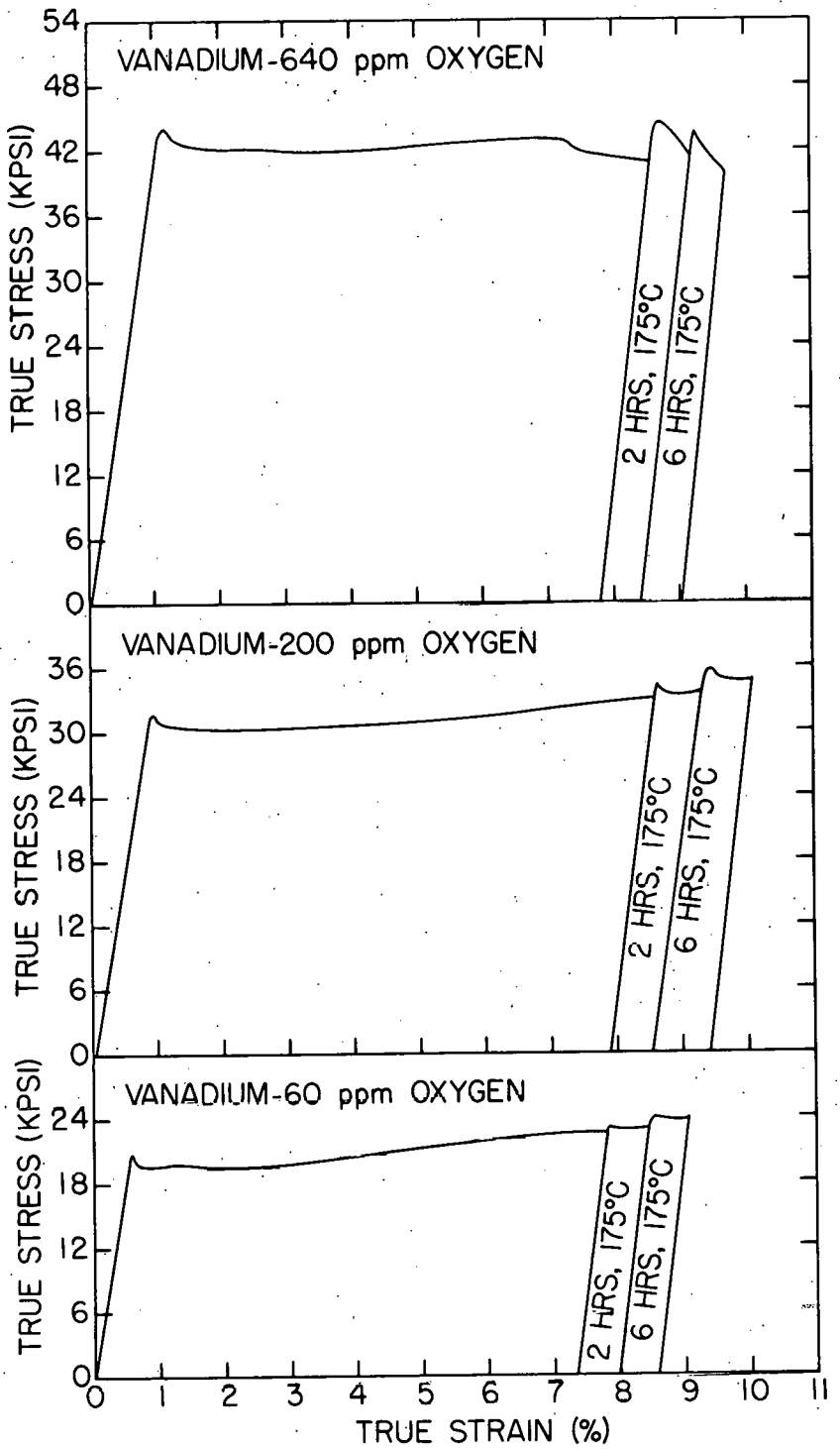
VANADIUM-640 ppm OXYGEN
2 HRS, 175°C
6 HRS, 175°C
TRUE STRESS (KPSI)
54
48
42
36
30
24
18
12
6
0
VANADIUM-200 ppm OXYGEN
2 HRS, 175°C
6 HRS, 175°C
TRUE STRESS (KPSI)
36
30
24
18
12
6
0
VANADIUM-60 ppm OXYGEN
2 HRS, 175°C
6 HRS, 175°C
TRUE STRESS (KPSI)
24
18
12
6
0
0 1 2 3 4 5 6 7 8 9 10 11
TRUE STRAIN (%)

D. Surface Slip Markings

Single crystal samples of vanadium - oxygen were deformed at room temperature and were observed in the scanning electron microscope (SEM). Figure 34a shows the scanning electron micrograph of a portion of unirradiated V-95 sample deformed about 12%. Figure 34b displays some material deformed after irradiation to the same strain. It can be observed that in case of irradiated material the slip markings are sharp, deep and rather inhomogeneously distributed along the length of the sample, whereas the slip lines in unirradiated material are not so clearly visible at the same magnification of 1000X as for the irradiated V-500 sample. In Figure 35a inhomogeneously distributed parallel slip lines can be observed whereas Figure 35b shows a group of parallel slip lines intersected by a coarser slip band, which splits into two, moving from left to right. Figure 35c displays two intersecting slip systems. In this case offsets in slip line A due to slip line B can be seen at X. It can be seen that the slip lines are not equally spaced in Figure 35.

The inhomogenity of deformation in irradiated material is probably responsible for the decrease in work hardening rate and uniform and fracture elongations in irradiated materials.

It has been demonstrated by various authors (186,188,192) that the surface slip markings on irradiated samples correspond to dislocation channels as observed by transmission electron microscopy.

E. Dislocation Channeling

When a neutron-irradiated material is plastically deformed and observed by transmission electron microscopy, it reveals channels that are

Figure 34. Scanning electron micrographs of vanadium - 95 wt ppm oxygen single crystals deformed 12% in compression at room temperature: (a) unirradiated specimen, (b) irradiated to 1.4×10^{19} n/cm^2 (E>1 MeV) at 95°C prior to straining

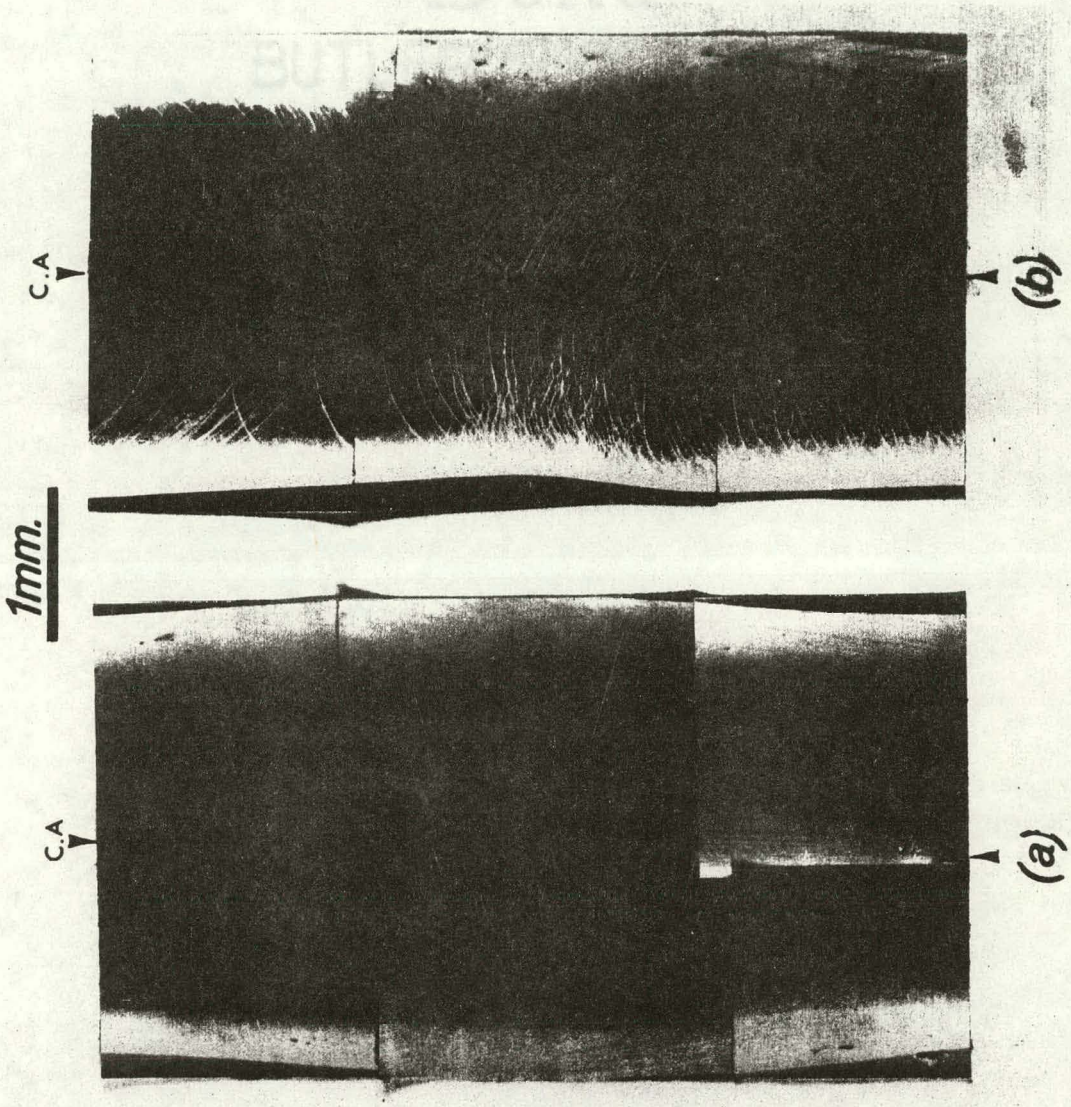
C.A
(b)
1mm.
C.A
(a)

Figure 35. High magnification scanning electron micrographs of slip lines in irradiated and deformed vanadium - 500 ppm oxygen single crystal

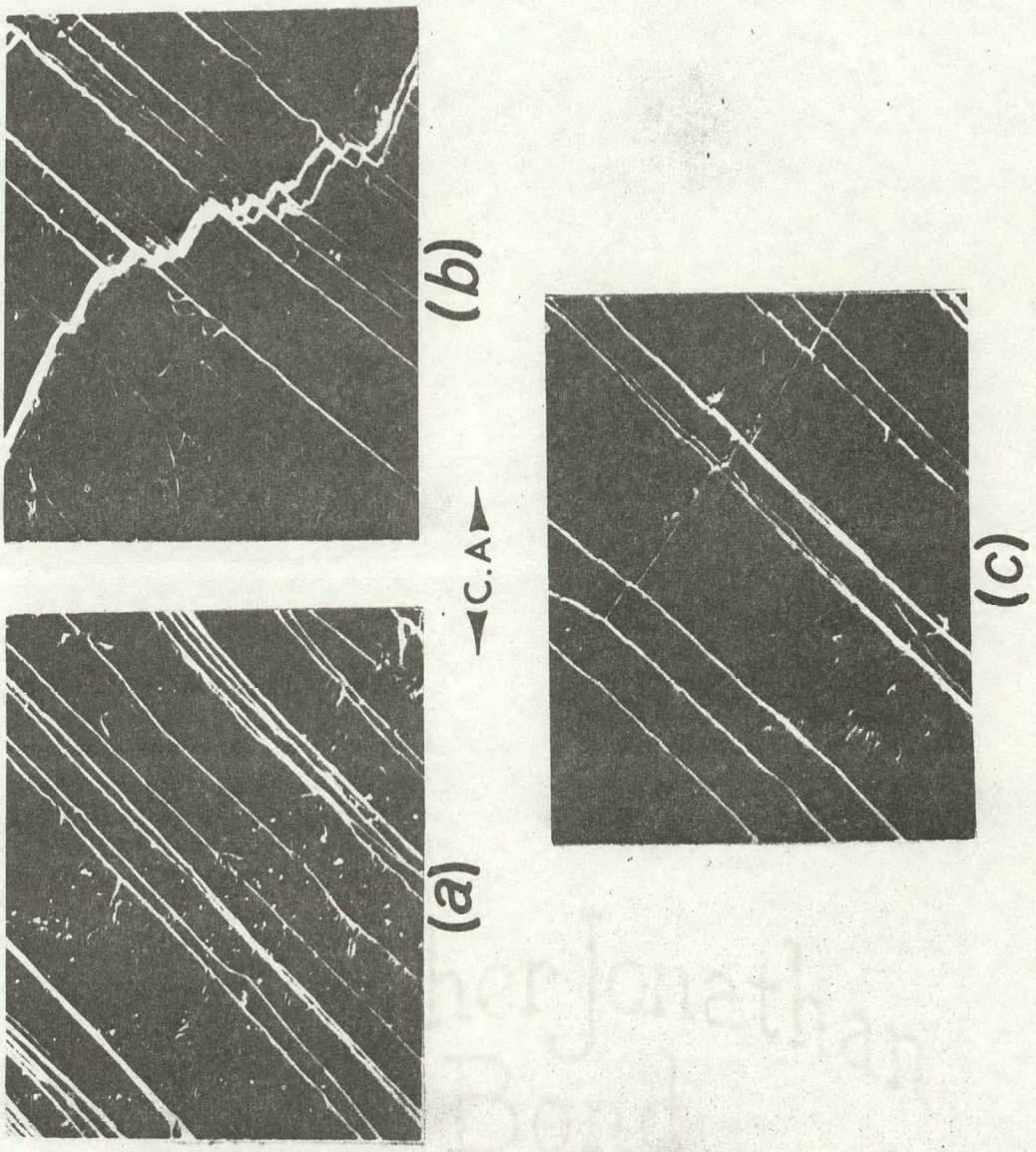
(b)
C.A
(a)
(c)

cleared of defect clusters in a matrix which retains its as-irradiated appearance. These cleared channels generally coincide with the traces of expected slip planes and hence it is reasonable to consider the channels as being the result of the motion of glide dislocation. These channels are called "dislocation channels." Subsequent deformation in the cleared channels is enhanced relative to the radiation hardened matrix resulting in stress concentrations. The channels observed by TEM are bound by the surface of the foil and the channel wall. The channel plane is the plane parallel to the channel wall and the channel trace direction is the direction along the line of intersection of the channel plane and the surface plane of the foil.

As described in Chapter III, plastic deformation of irradiated single crystal vanadium with three oxygen contents was carried out at strains of 5% and 12% at room temperature. Single crystal material post-irradiation annealed at 300°C and 400°C was also plastically deformed to 5% and 12% strains, respectively. Irradiated vanadium - 95 ppm oxygen was deformed to 5% strain at liquid nitrogen temperature for further examination. All the material described above was then prepared into TEM foils for observation.

1. General appearance and orientation

Figure 36 shows channels in a V-95 single crystal specimen deformed 12%. Two intersecting channels denoted by A and B can be observed. The operating reflection for the micrograph is $[\bar{2}11]$ and the plane of the foil is (111). The trace direction for channel A is approximately $[10\bar{1}]$ and

Figure 36. Dislocation channels in vanadium - 95 wt ppm oxygen single crystal, post-irradiation deformed 12% in compression at room temperature. Intersecting channels can be observed at A and B

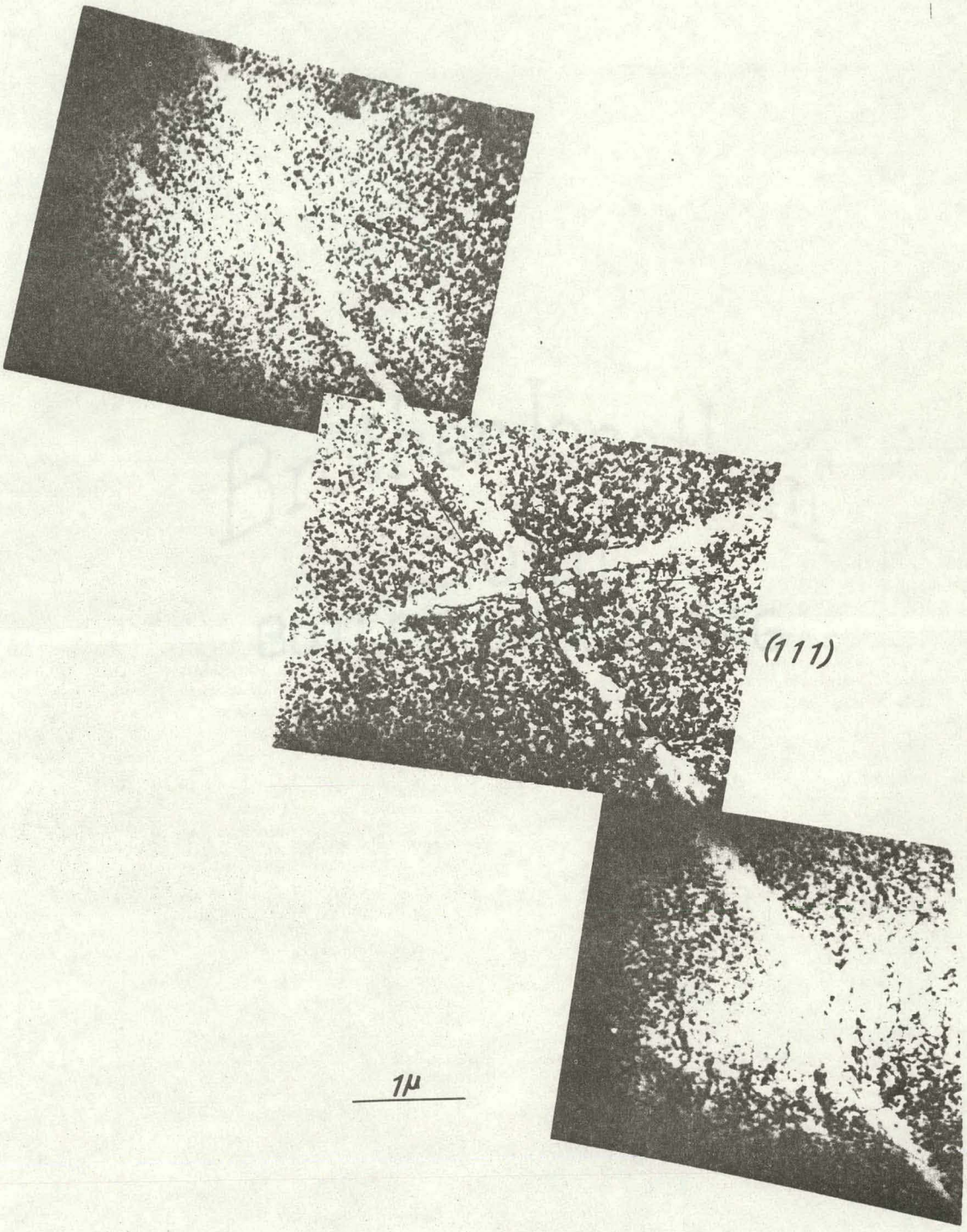
(111)
1μ

for B [1$\bar{1}$0]. Since channels in Figure 33 appear to be devoid of defect clusters, the channel walls may be assumed to be perpendicular to the plane of view. Hence it is deduced that the planes of the channels A and B are (1$\bar{2}$1) and (11$\bar{2}$), respectively. The channels are of nearly uniform width of about 1800 Å.

One can observe in Figure 36 that the defect density near the channel wall is the same as it is in the matrix. An increased density along the channel walls would indicate the snow-plow mechanism where the channeling dislocations sweep the defect clusters aside and deposit them at the channel wall.

Furthermore, if many dislocations penetrate the wall, they would annihilate the defect clusters. This can be observed at few places in Figure 36. At X and Y, for example, one can see dislocations penetrating the channels and the defect cluster density in the region around the dislocation is reduced, but this is only a localized effect.

One notes in Figure 36 that there is a dislocation tangle at the intersection of channels A and B. It can be seen that the tangle is a result of intersection of dislocations moving along two distinct slip planes. One can also observe dislocations associated with channel walls. On the top left hand position of the figure one sees dislocation segments associated with both walls of the channel A. In channel B, however, dislocations are mainly along one wall of the channel. At the bottom right position of the figure, which shows relatively thick section of the specimen, one can see dislocation tangles and a knot-like appearance in channel A which seems to have been offset by a channel (not well-developed)

running parallel to channel B. Another offset of about half the width of channel A due to channel B can be clearly seen at the intersection of the two channels.

Figure 37 shows TEM micrograph of V-300 deformed 5% at room temperature. The figure shows three parallel dislocation channels A_1, A_2, A_3 and a fourth channel B intersecting them. The channels in Figure 37 do not lie exactly perpendicular to the plane of the foil, but are inclined to it. Therefore it appears as if the channels are not completely cleared of defect clusters. The micrograph shows a relatively thick section of the foil. The plane in which the channels lie is probably (110) which is about 13° from (133). The widths of the channels in Figure 37 vary from about 700 Å to about 1150 Å. At X and Y, dislocation debris can be observed. A few dislocation segments can also be observed in Figure 37. The channel trace directions have been determined to be $[30\bar{1}]$ and $[\bar{3}21]$ from the diffraction pattern.

Figure 38 shows dislocation channels in V-500 material following post-irradiation deformation to about 5% in compression. A high concentration of slip dislocations can be seen in the channels.

2. Effect of strain on dislocation channels

As described earlier, samples were deformed at room temperature to 5% and 12% strain following irradiation. In this range of strain, the width of the dislocation channels generally increases with strain as measured on the TEM micrographs; however this conclusion is only tentative, since the channel width is not constant even in the same sample.

Figure 37. Dislocation channels in vanadium - 300 wt ppm oxygen single crystal, post-irradiation deformed 5% in compression at room temperature. Dislocation debris can be seen at X and Y

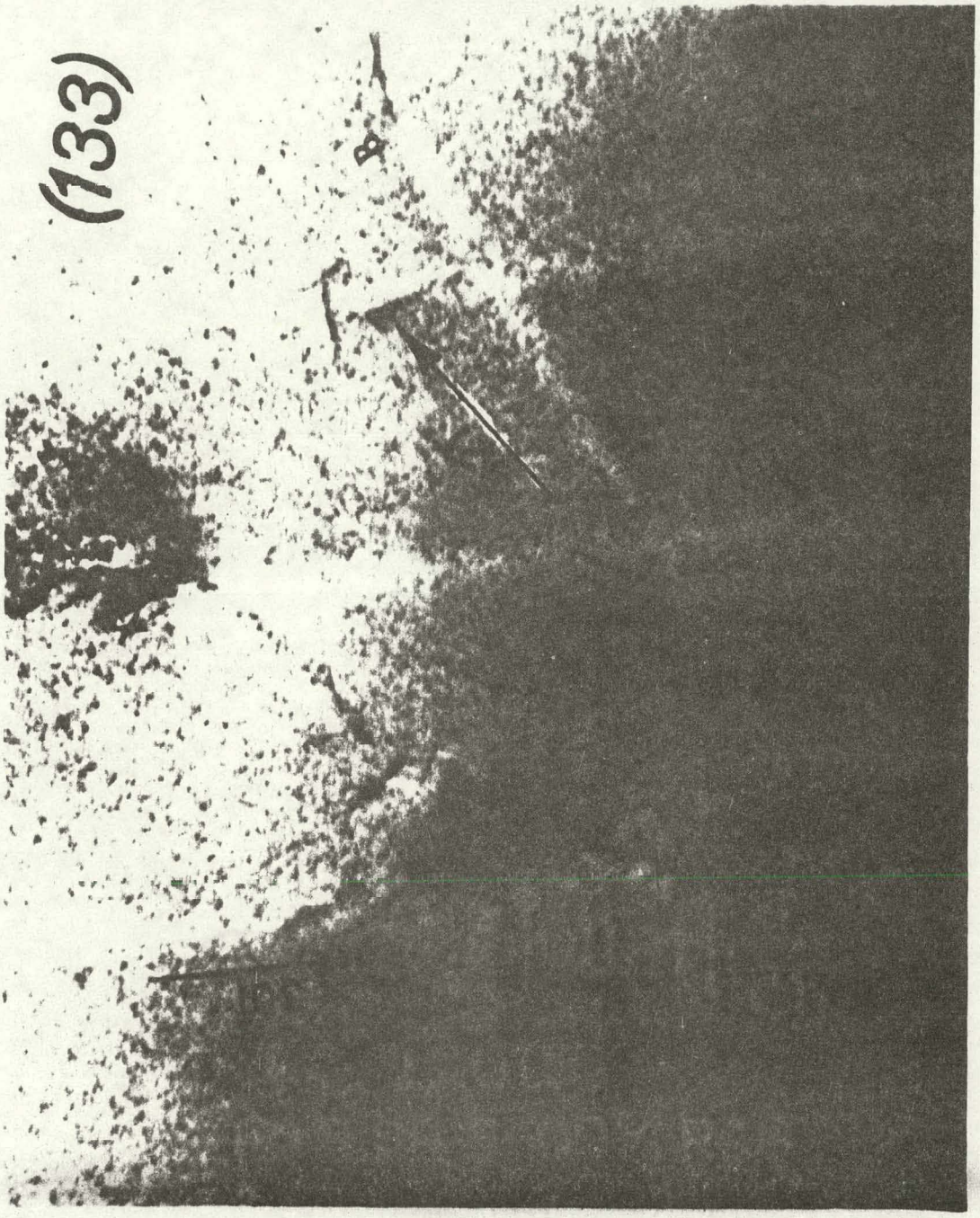
(133)

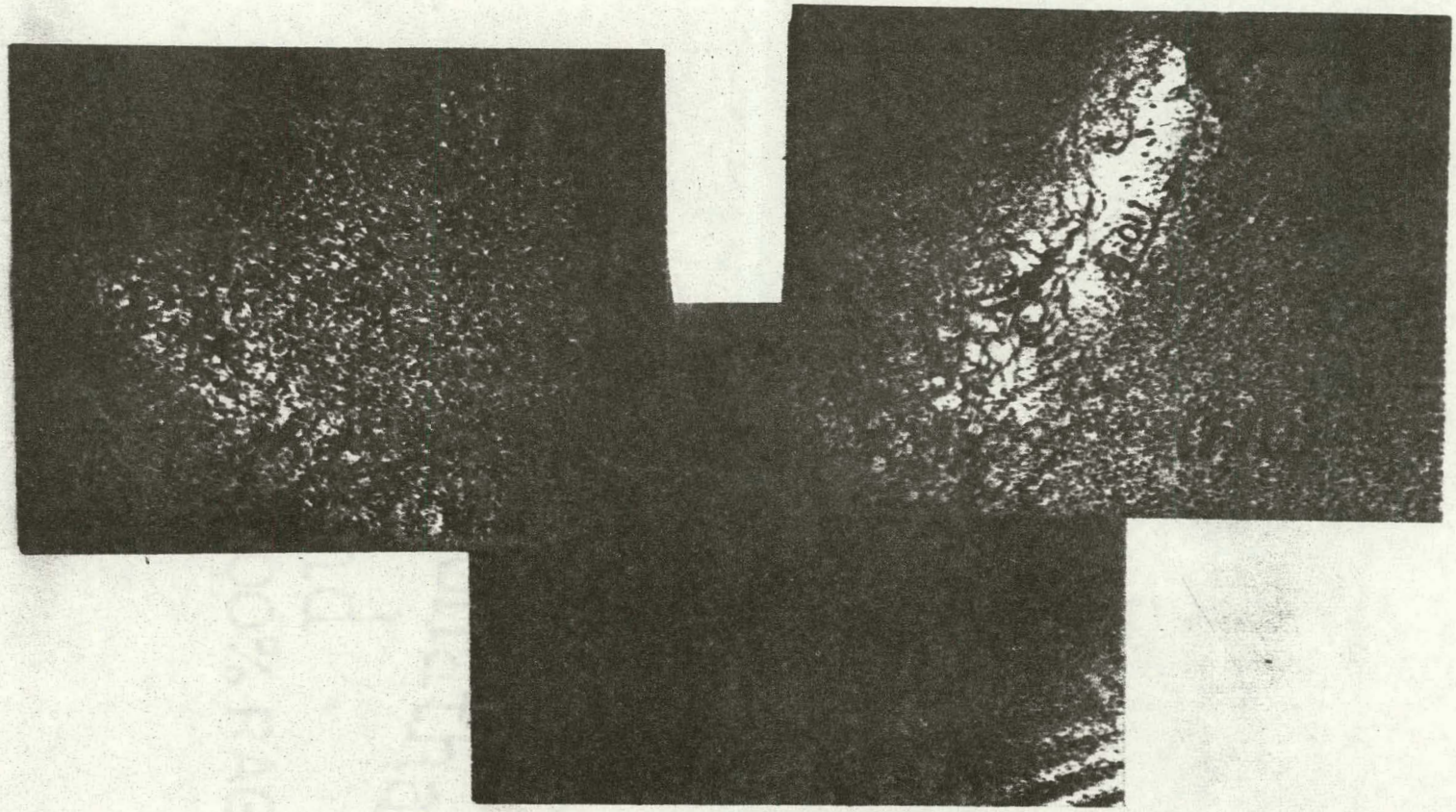

Figure 38. Dislocation channels in vanadium - 500 wt ppm oxygen single crystal, post-irradiation deformed 5% in compression at room temperature. A high density of slip dislocations can be seen within the channels

The number of channels observed increases with increasing strain in the range of 5% to 12%. The number of dislocations and dislocation tangles inside the channels also increases with increasing strain.

3. Effect of oxygen on dislocation channels

No definite conclusion can be drawn regarding the effect of oxygen on the width of the channels and on the number of channels produced with the same strain because of very limited amount of material which can be examined by TEM. However the amount of oxygen has an effect on the dislocations and dislocation tangles inside the channels. The dislocation tangles were observed in all three kinds of samples but the occurrence of tangles was more common in V-500 than in V-95 material.

An example of dislocation tangles in the V-95 material deformed 12% is shown in Figure 39. On the left hand top of the picture, which shows a relatively thinner section of the foil, the channel is rather clear whereas in the bottom right hand corner massive dislocation tangles can be observed inside the channel. The channel trace directions in Figure 39 are $[10\bar{1}]$ and $[\bar{1}10]$.

4. Dislocation channeling in material post-irradiation deformed at 77°K

Single crystal V-95 material was post-irradiation deformed 10% in compression at liquid nitrogen temperature (77°K) and examined by TEM. The low temperature deformation produced twins in the material as evidenced by clicks heard during the test and joggy load-elongation curves. Nevertheless, in the six foils prepared and examined by TEM, no region with twins could be observed. However, dislocation channels were observed in

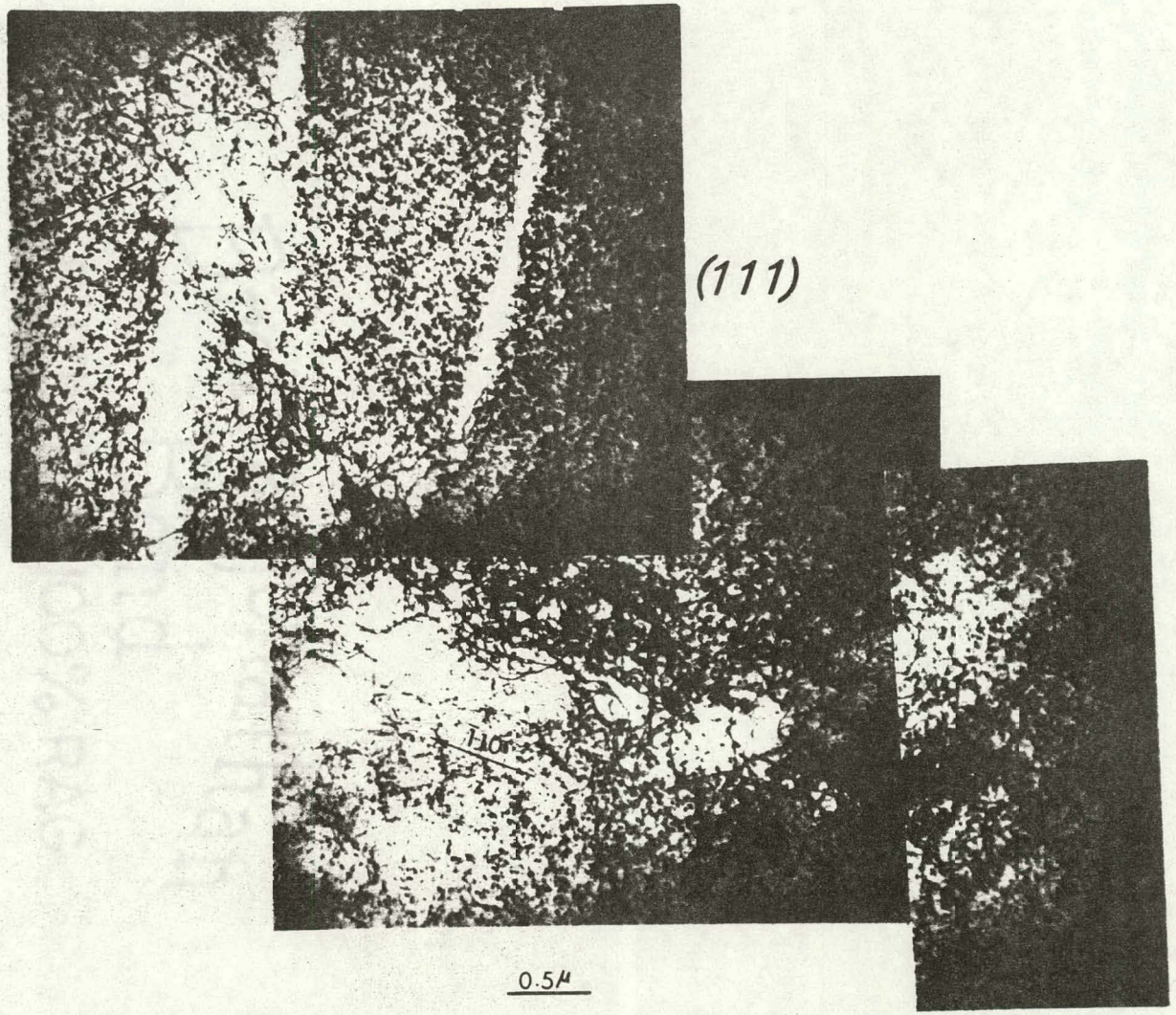

Figure 39. Dislocation channels in vanadium - 95 wt ppm oxygen single crystal, post-irradiation deformed 12% in compression at room temperature

some regions. One such channel is shown in Figure 40. It can be observed that the width of the channel does not remain constant along its length, varying instead from 1250 Å to about 3350 Å. In the right hand bottom section of Figure 40, there are a few defect clusters left behind inside the channel. The plane of the foil in Figure 40 is (100) and channel trace direction is [013]. At A defect clusters lined along a dislocation can be observed. At B one sees a bowed-out dislocation possibly pinned at defect clusters.

Figure 41 shows another region of a V-95 sample deformed at 77°K. The channel trace direction is $[\bar{1}1\bar{2}]$ in the (110) surface observed under $[00\bar{2}]$ operating vector. In this figure, bowed out dislocations extending across the channels can be observed at various places. Parallel dislocations outside the channel are also evident in Figure 41. It can be seen that only one wall of the channel is well defined and not all the defect clusters are completely removed from the channeled region.

5. Dislocation channeling in post-irradiation-annealed samples

Single crystal samples of vanadium of three oxygen contents were post-irradiation annealed at 300°C and 400°C for 1 hr and were deformed about 12% and 5% at room temperature. TEM examination of the foils revealed the presence of dislocation channels in all three kinds of material. As an example, Figure 42 shows channels in V-500, post-irradiation annealed at 300°C for 1 hr and deformed about 12% in compression at room temperature. Dislocation channels lying along $[1\bar{2}1]$, $[10\bar{1}]$ and $[01\bar{1}]$ can be observed on a (111) foil plane observed under $[1\bar{1}0]$ diffraction vector. The walls of

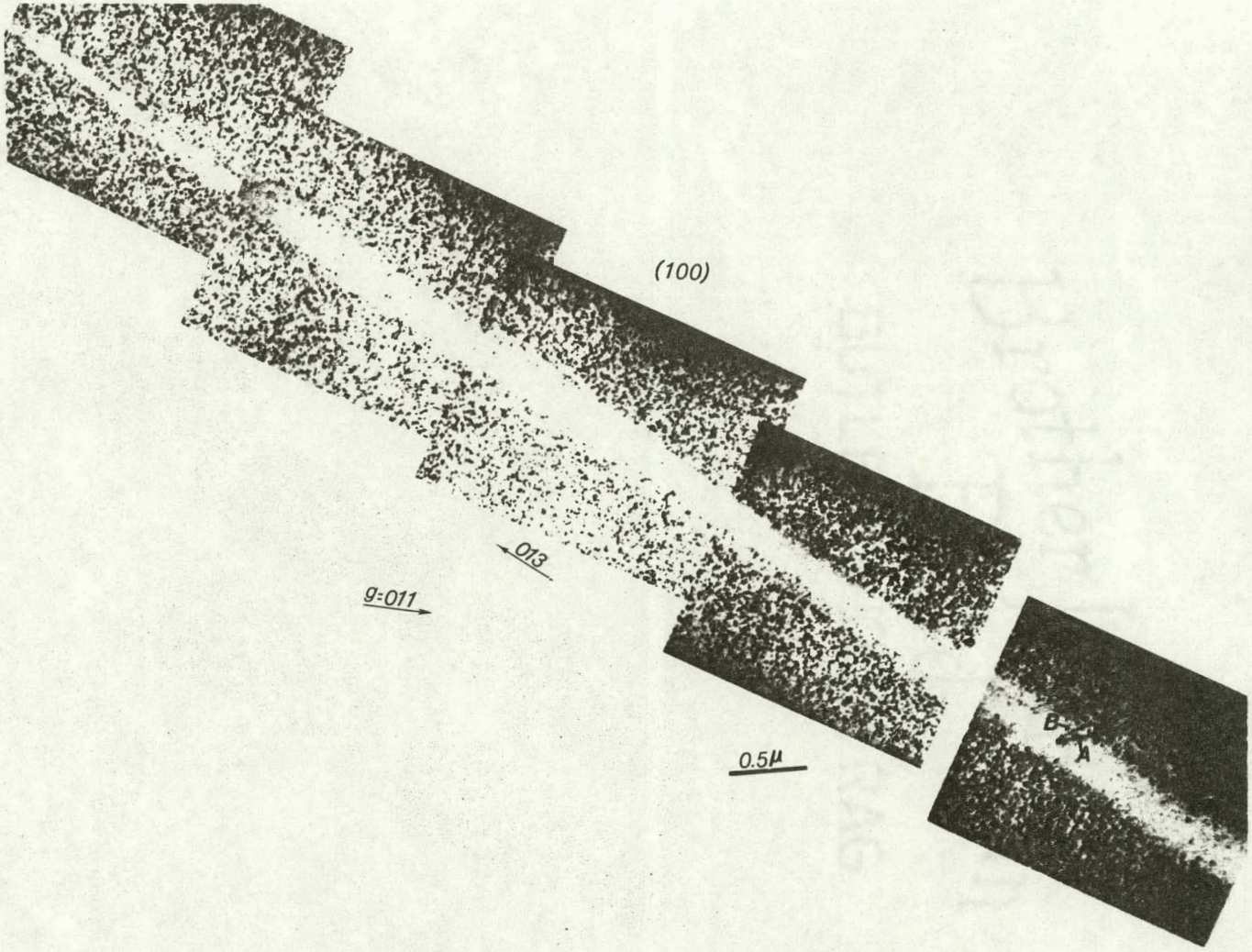

Figure 40. Dislocation channel in vanadium - 95 wt ppm oxygen single crystal, post-irradiation deformed 10% in compression at liquid nitrogen temperature

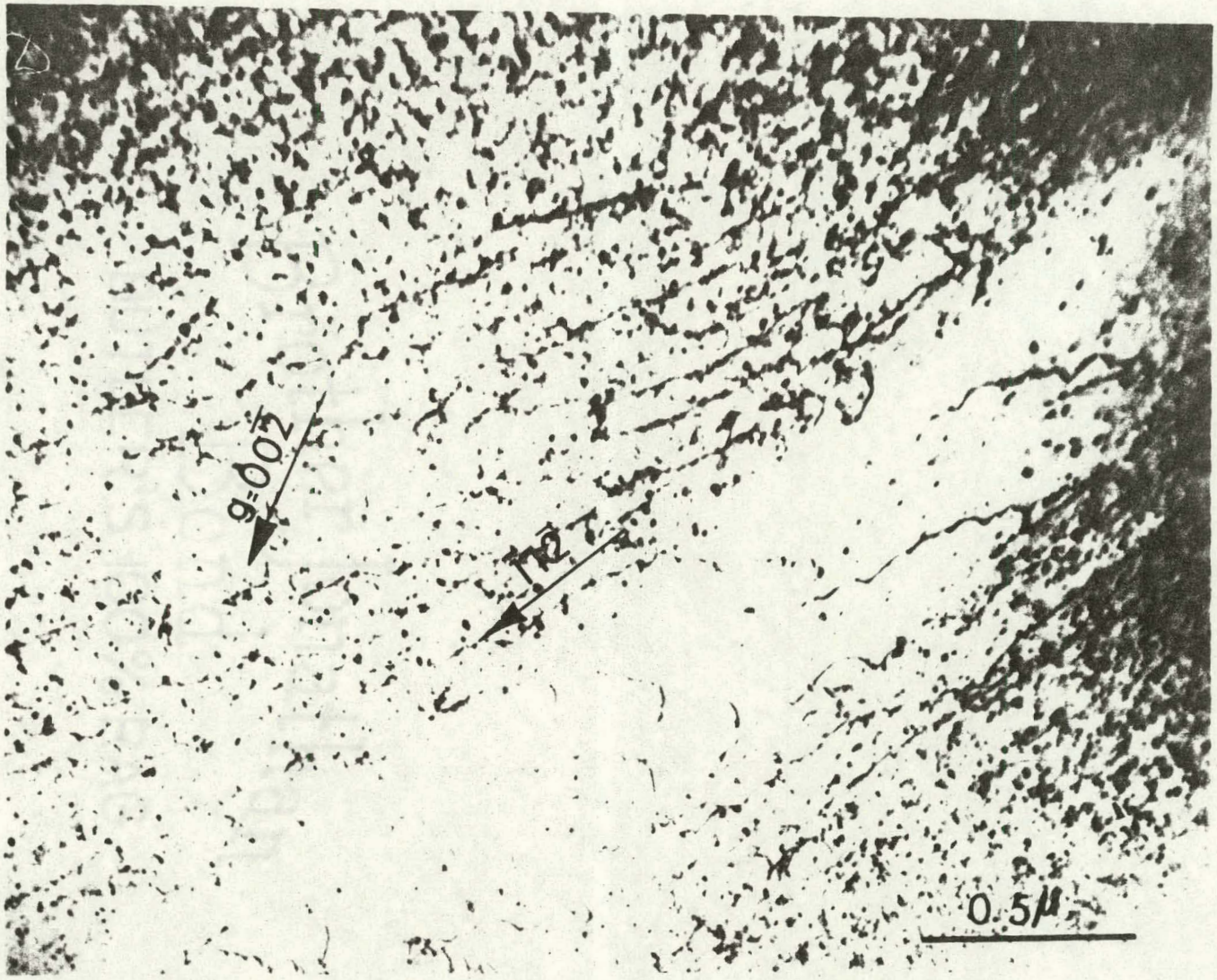

Figure 41. Dislocation channel in vanadium - 95 wt ppm oxygen single crystal, post-irradiation deformed 10% in compression at liquid nitrogen temperature

Figure 42. Dislocation channels in vanadium - 500 wt ppm oxygen single crystal, post-irradiation annealed at 300°C for one hour and deformed 12% in compression at room temperature

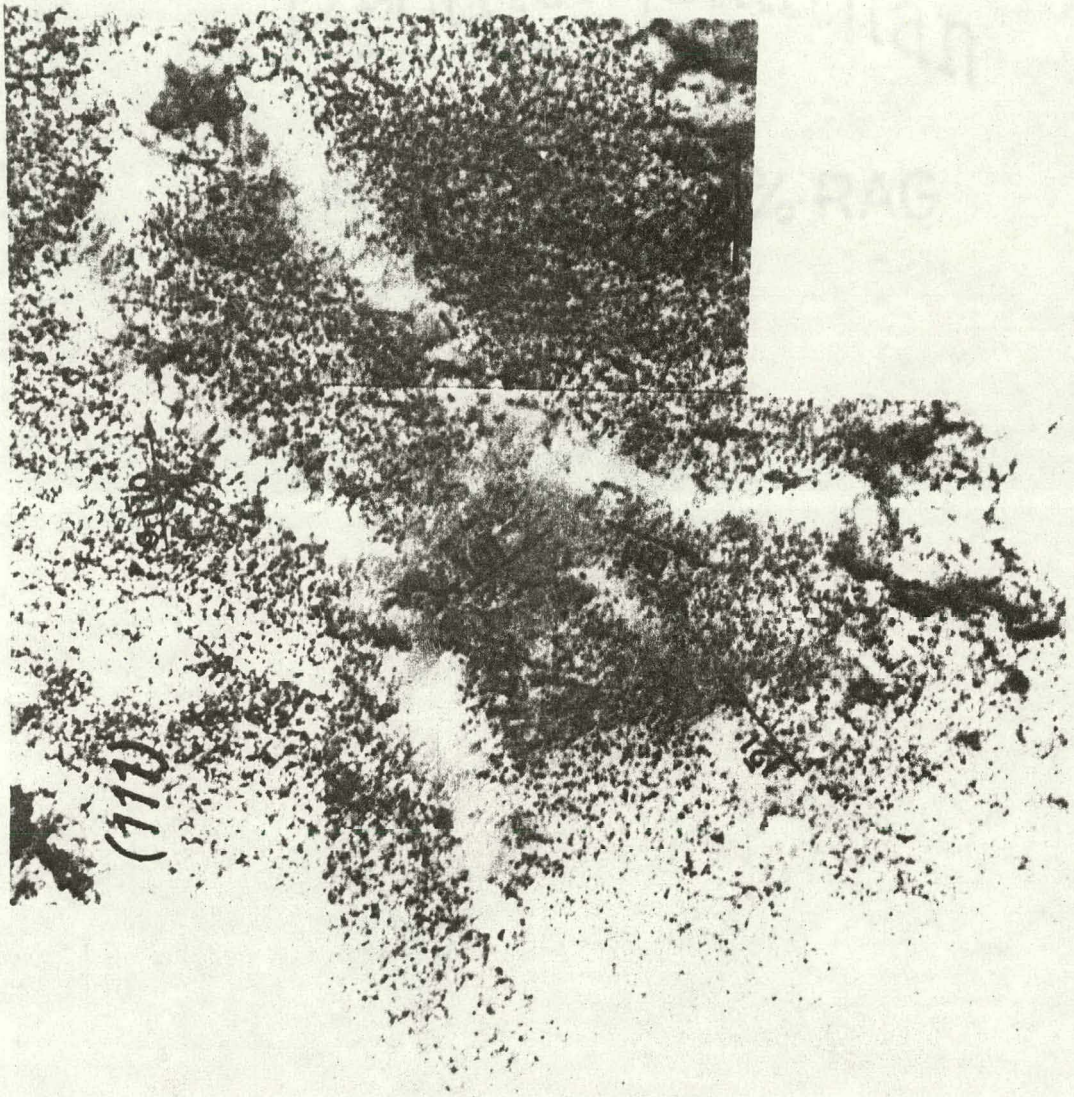
(110)
(111)

the channels in Figure 42 are not very well-defined. Dislocation segments along the walls and inside the channels can be observed at various places.

Figure 43 shows a dislocation channel in V-95 material, post-irradiation annealed at 300°C for 1 hr and deformed 12%. Massive dislocation tangles can be observed at top right hand corner of the figure in the thicker section of the foil, whereas the channel in the thinner section (bottom left) is relatively clear.

Figure 44 shows a region of V-500 post-irradiation annealed at 400°C for one hour and deformed 5%. One can observe dislocations and tangles in the micrograph. The tangles, however, are arranged along two parallel paths which are relatively denuded of defect clusters and give the appearance of dislocation channels.

The essential features of dislocation channeling in material post-irradiation annealed and deformed can be summarized as follows:

(1) The channel walls are not well defined.

(2) There are many dislocations and tangles inside channels.

(3) In many cases defect clusters are observed inside the channel. An example is shown in Figure 45.

F. TEM of Material Deformed Prior to Irradiation

Figure 45 shows a micrograph of V-95 sample deformed 5% at room temperature, irradiated to 1.4×10^{19} n/cm^2 (E>1 MeV) at 95°C and examined. One can observe dislocations lined preferentially in the [020] direction, with the dislocations occurring in bunches. Massive dislocation

Figure 43. Dislocation channel in vanadium - 95 wt ppm oxygen single crystal, post-irradiation annealed at 300°C for one hour and deformed 12% in compression at room temperature


111
0.5μ

Figure 44. Dislocation tangles in vanadium - 500 ppm oxygen single crystal, post-irradiation annealed at 400°C for one hour and deformed 5% in compression at room temperature

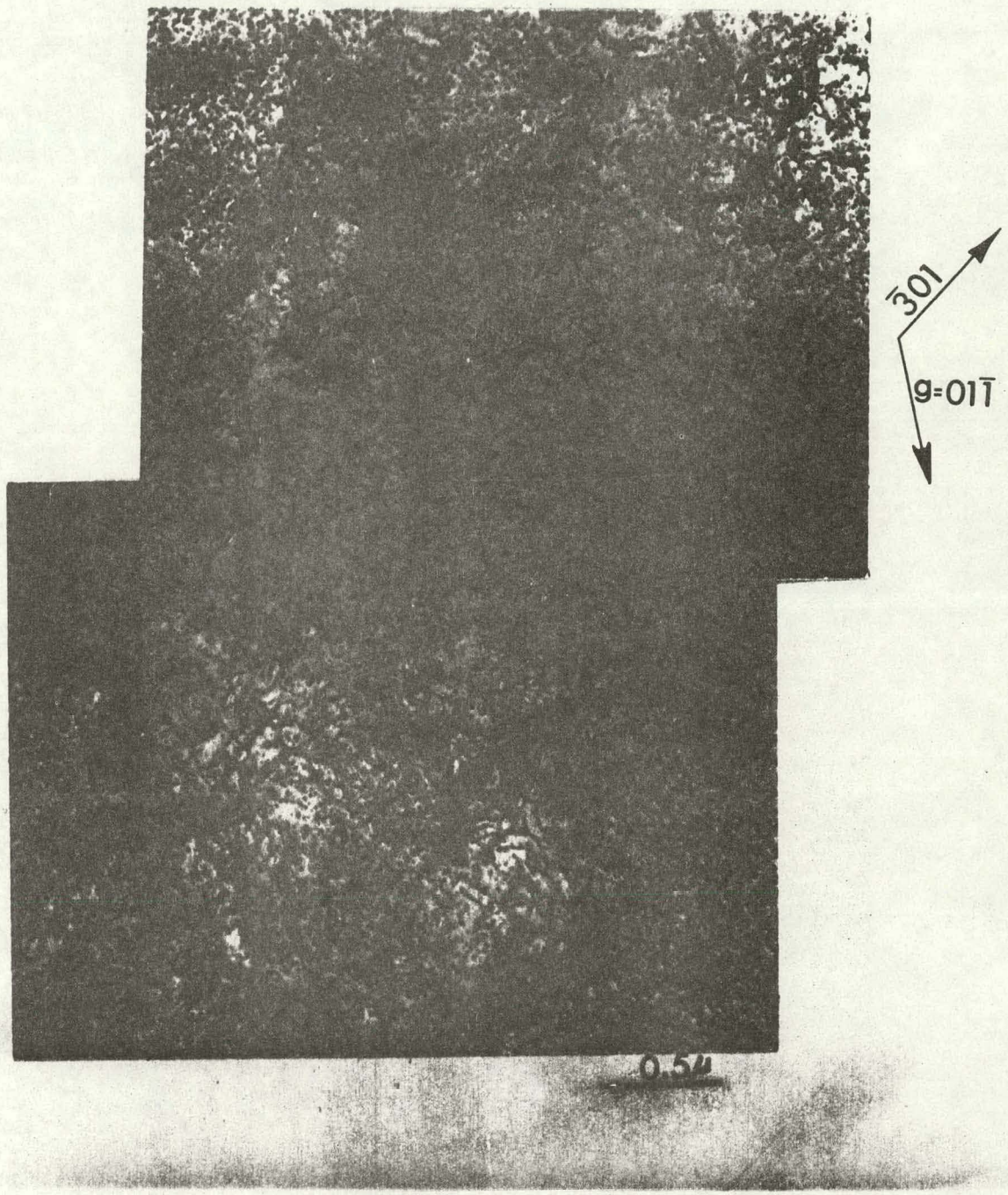
$\bar{3}01$
g=01$\bar{1}$
0.5μ

Figure 45. Dislocation channels in vanadium - 500 wt ppm oxygen single crystal, post-irradiation annealed at 300°C for one hour and deformed 12% in compression at room temperature. Defect clusters are observed inside the channels

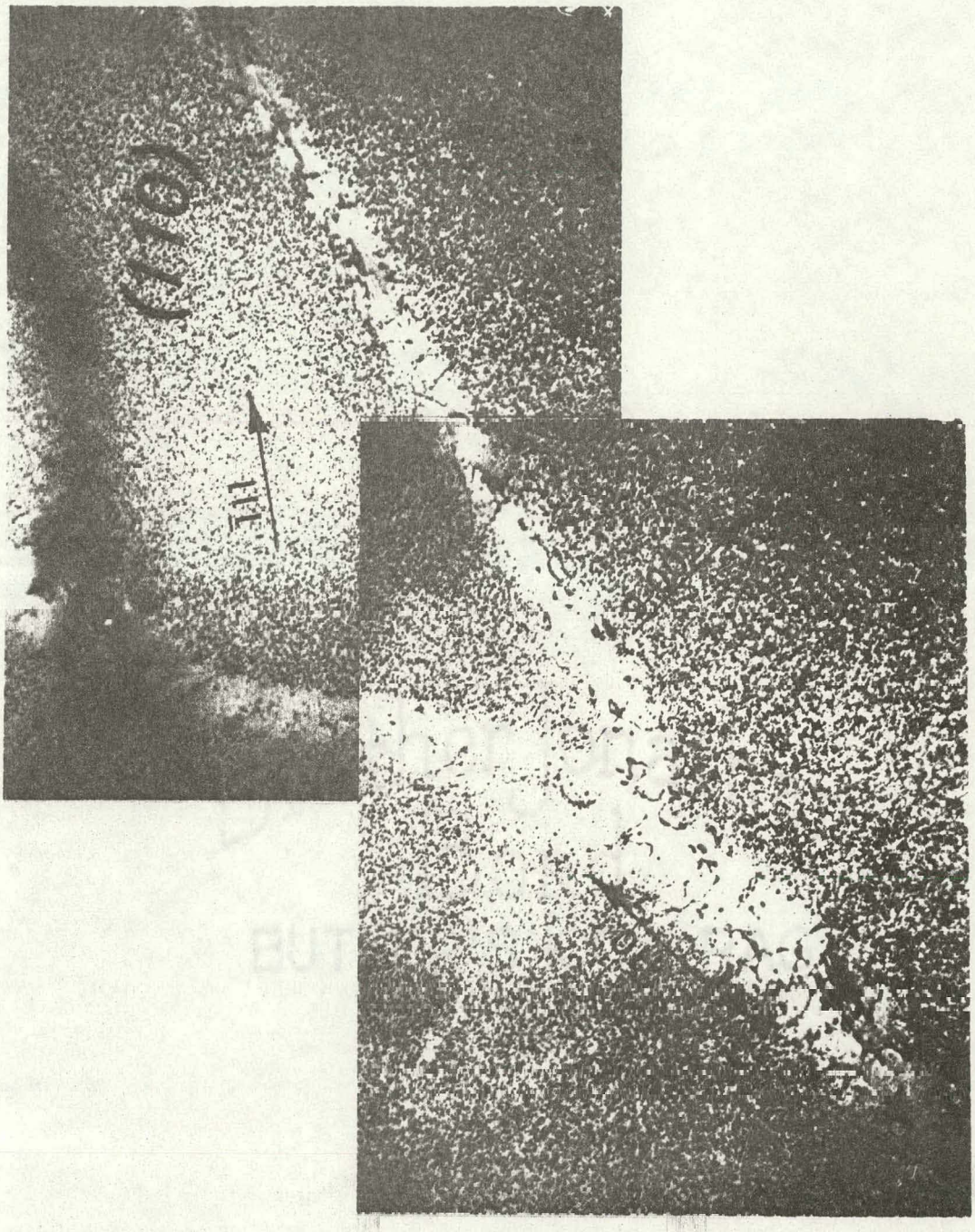
(110)
111

debris can be observed at X. A careful examination of the micrograph reveals denudation around the dislocations. This is seen more clearly in Figure 47 for V-300 sample, where the dislocations are lined along $[01\bar{1}]$ or $[11\bar{2}]$ directions on a (111) plane. Here again the dislocations occur in groups and are nonuniformly distributed. Figure 48 shows a micrograph of V-500 sample deformed prior to irradiation as described above. Only a few dislocations can be observed (e.g., at A, B and C) but the denudation around the dislocations is much more apparent.

Figure 49 shows a micrograph of V-95 sample deformed 5% at 77°K (liquid nitrogen temperature) irradiated to 1.4×10^{19} n/cm^2 (E>1 MeV) at 95°C and examined. A comparison of Figure 49 with Figures 13a and 43, reveals many differences. Figure 13a shows material irradiated in the annealed condition and Figure 43 shows material deformed 5% at room temperature prior to irradiation.

As against Figure 43, Figure 46 shows segments of dislocations distributed rather uniformly over the field of view. The average size of the defect clusters (which appear as fully developed loops) is larger in Figure 46 than in Figures 13a and 43. The temperature of deformation appears to have a major effect on the dislocation structure as the comparison of Figure 43 with 46 shows. The dislocations occur in groups lined along a few preferential directions in material deformed at room temperature (Figure 43) as against small segments distributed all over.

Figure 49 shows a micrograph of a V-95 single crystal sample deformed 5% in compression at 77°K (liquid nitrogen temperature), irradiated to 1.4×10^{19} n/cm^2 (E>1 MeV) at 95°C, and thinned and examined. It is

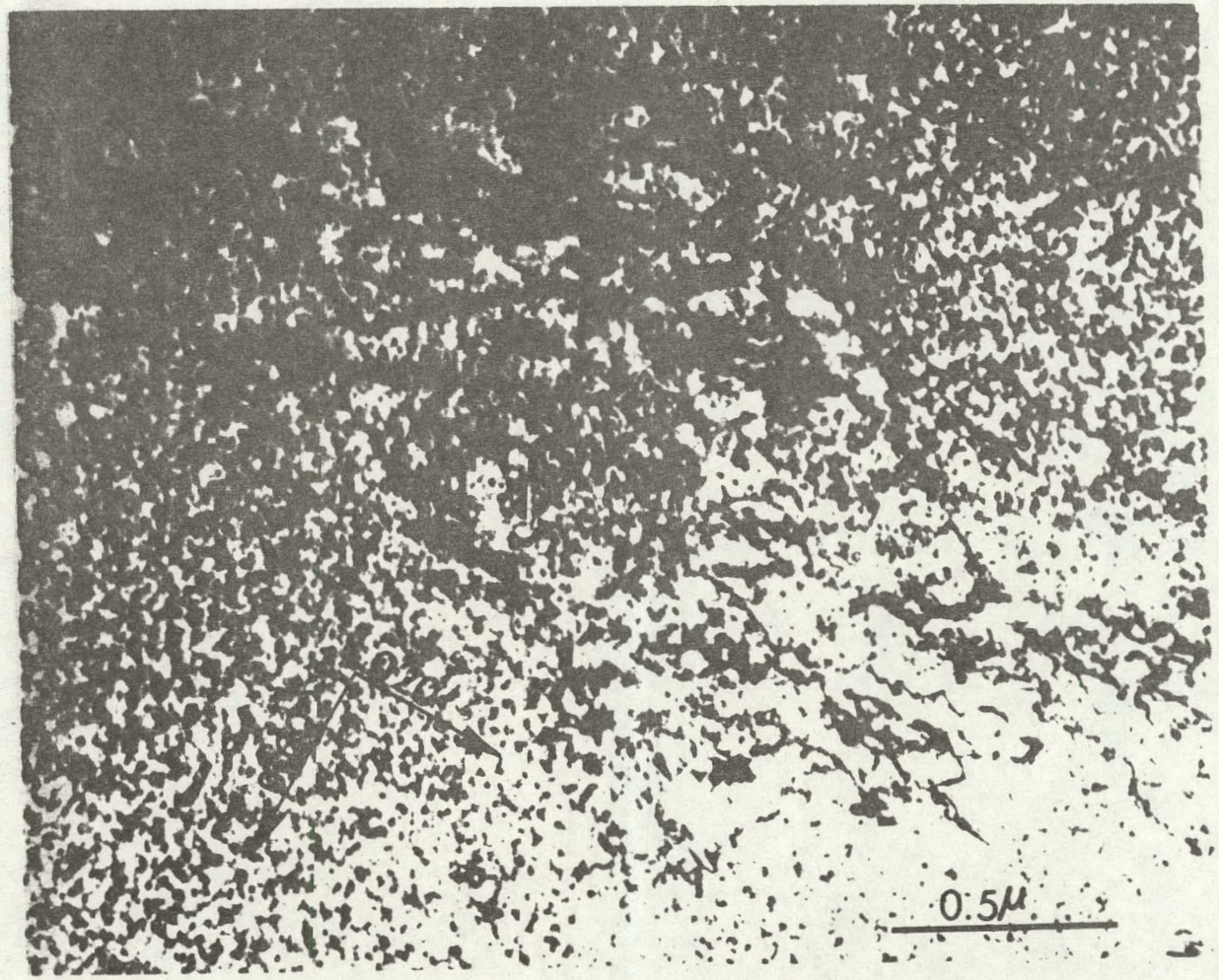

Figure 46. Transmission electron micrograph of V-95 single crystal deformed 5% at room temperature and irradiated to 1.4×10^{19} n/cm^2 (E>1 MeV) at 95°C

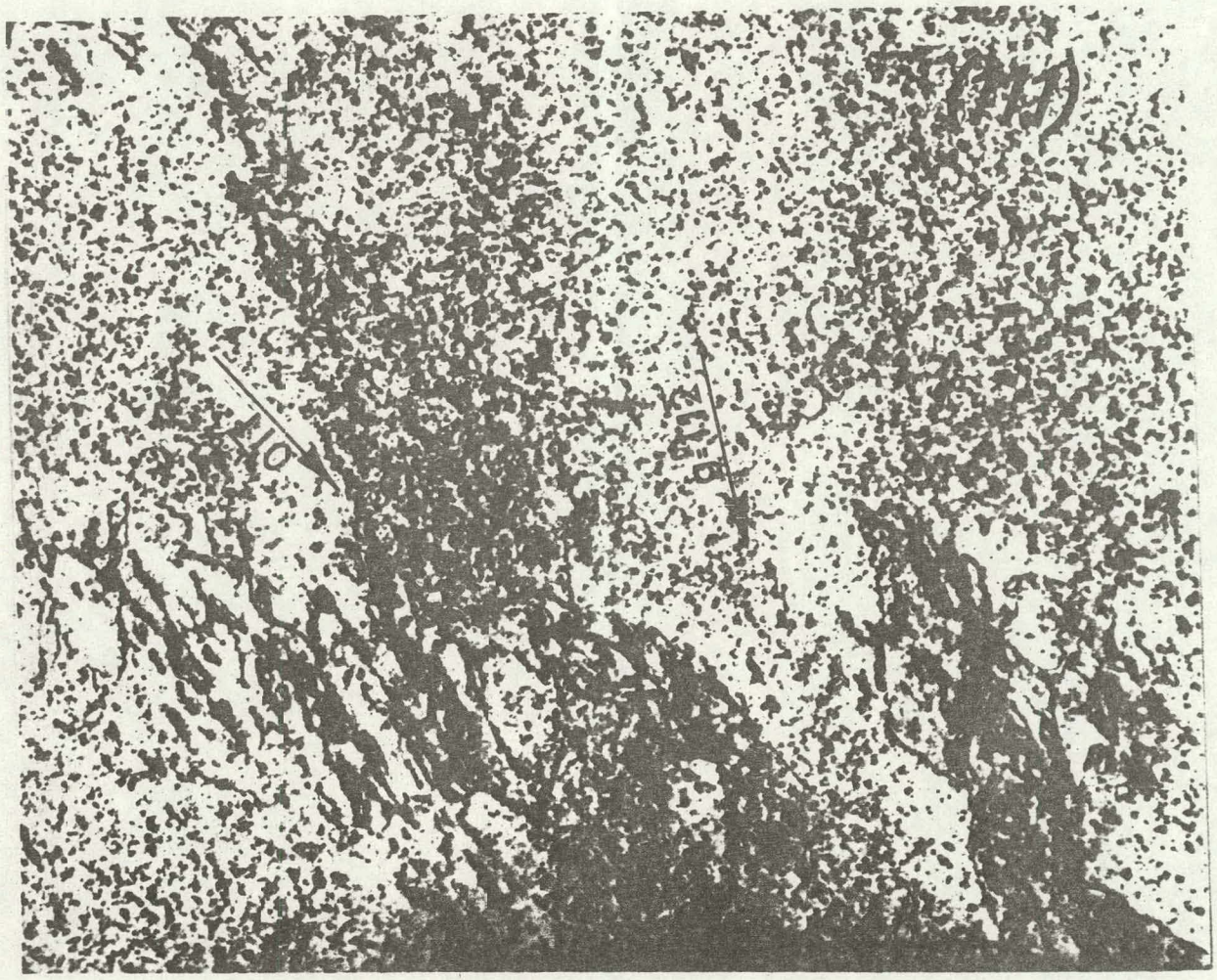

Figure 47. Transmission electron micrograph of V-300 single crystal deformed 5% in compression at room temperature and irradiated to 1.4×10^{19} n/cm^2 (E>1 MeV) at 95°C

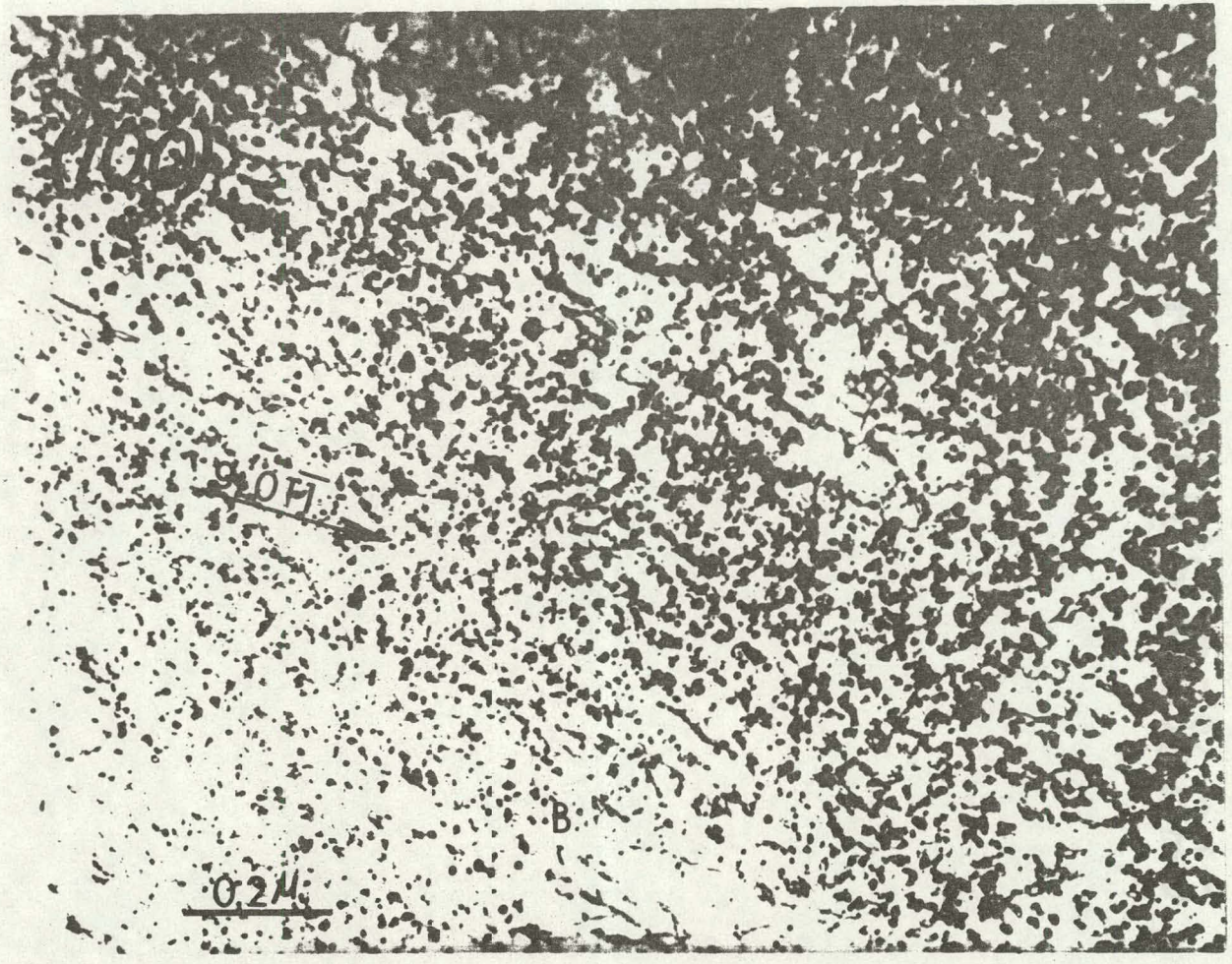

Figure 48. Transmission electron micrograph of V-500 single crystal deformed 5% in compression at room temperature and irradiated to 1.4×10^{19} n/cm^2 (E>1 MeV) at 95°C

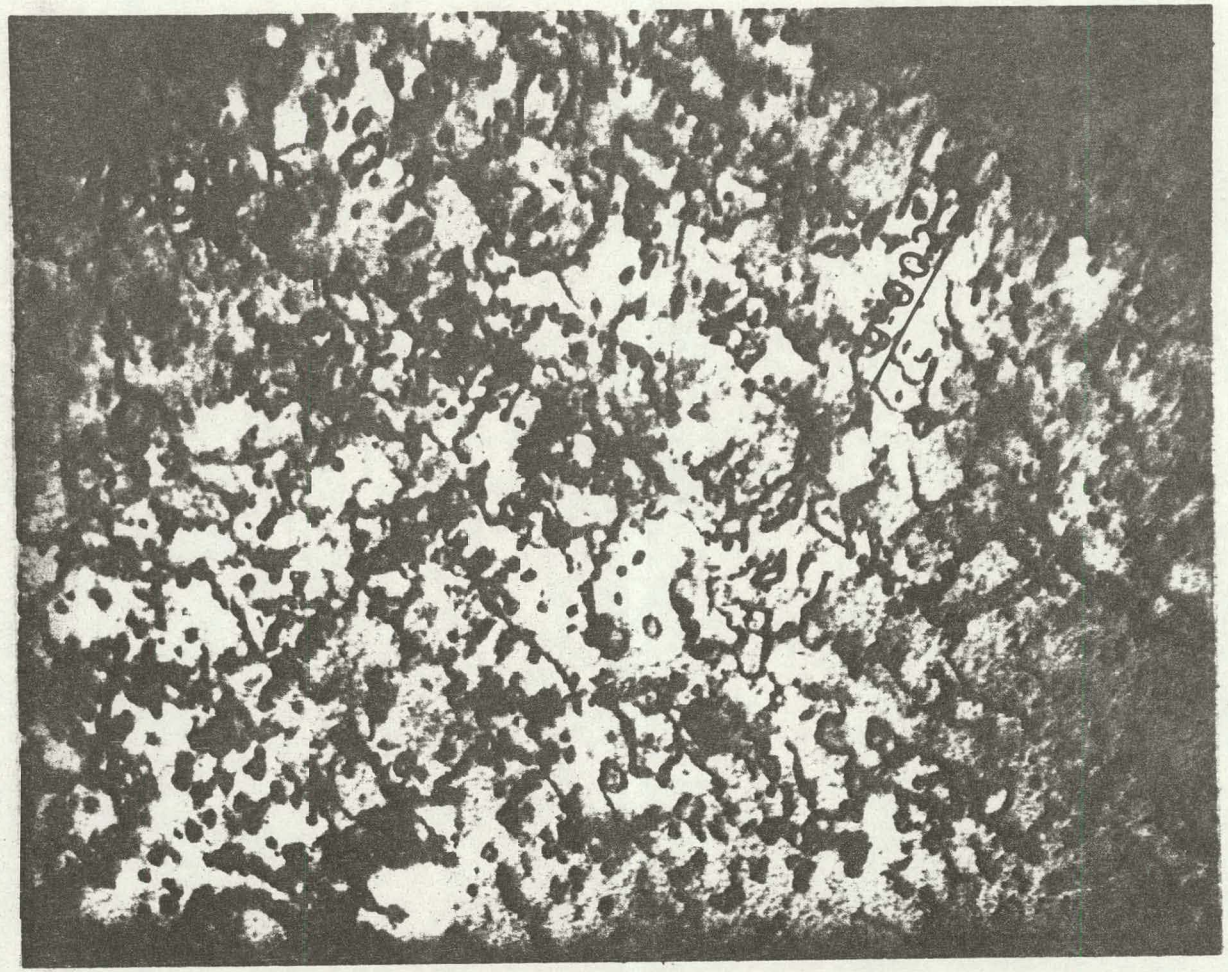

Figure 49. Transmission electron micrograph of vanadium - 95 ppm oxygen single crystal deformed 5% in compression at 77°K and irradiated to 1.4×10^{19} n/cm^2 (E>1 MeV) at 95°C

interesting to compare Figure 49 (V-95 deformed at 77°K and irradiated) with Figures 46 (V-95 deformed at room temperature and irradiated) and 13a (V-95 annealed and irradiated). These three photomicrographs appear together in Figure 50 for ease of comparison. We see that the defect clusters appear as fully developed loops in the material deformed at 77°K prior to irradiation (Figure 50a), whereas the defect clusters appear mostly as black spots in the room-temperature deformed and irradiated material (Figure 50b) and annealed and irradiated material (Figure 50c). It is also apparent from Figure 50 that the average size of the defect clusters is larger for the 77°K deformed material (Figure 50a) than for either the room-temperature deformed material (Figure 50b) or the annealed material (Figure 50c). Furthermore, there is a distinct difference between the dislocation structures in the 77°K deformed and room-temperature deformed materials. Figure 50a indicates that the slip dislocations are fairly uniformly distributed and are mostly wavy and convoluted in the material deformed at 77°K. By contrast, the slip dislocations in Figure 50b are bunched together in tangles and appear to have straighter segments in the room temperature deformed material.

Figure 51 displays micrograph of V-500 deformed 5% at 77°K, irradiated and examined. The plane of the foil is (311) and the diffraction vector is $[11\bar{2}]$. Here again, dislocation segments distributed over the field of view can be observed. The clusters appear to segregate along the dislocation segments. The defect clusters are smaller in size than those in Figure 49, but a comparison with material irradiated in annealed condition (Figure 17a) shows an increase in size (average size 73 Å in Figure 17a and

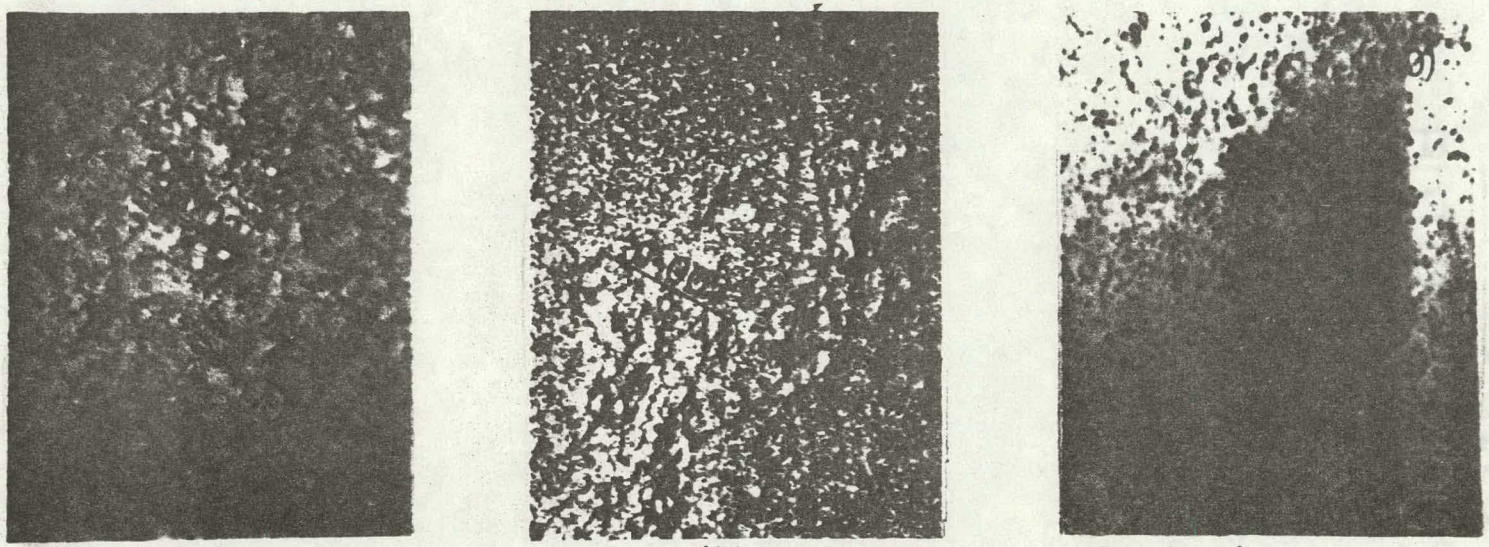

Figure 50. Transmission electron micrograph of vanadium - 95 ppm oxygen single crystals in the following conditions (a) deformed 5% in compression at 77°K and irradiated, (b) deformed 5% in compression at room temperature and irradiated, and (c) annealed and irradiated

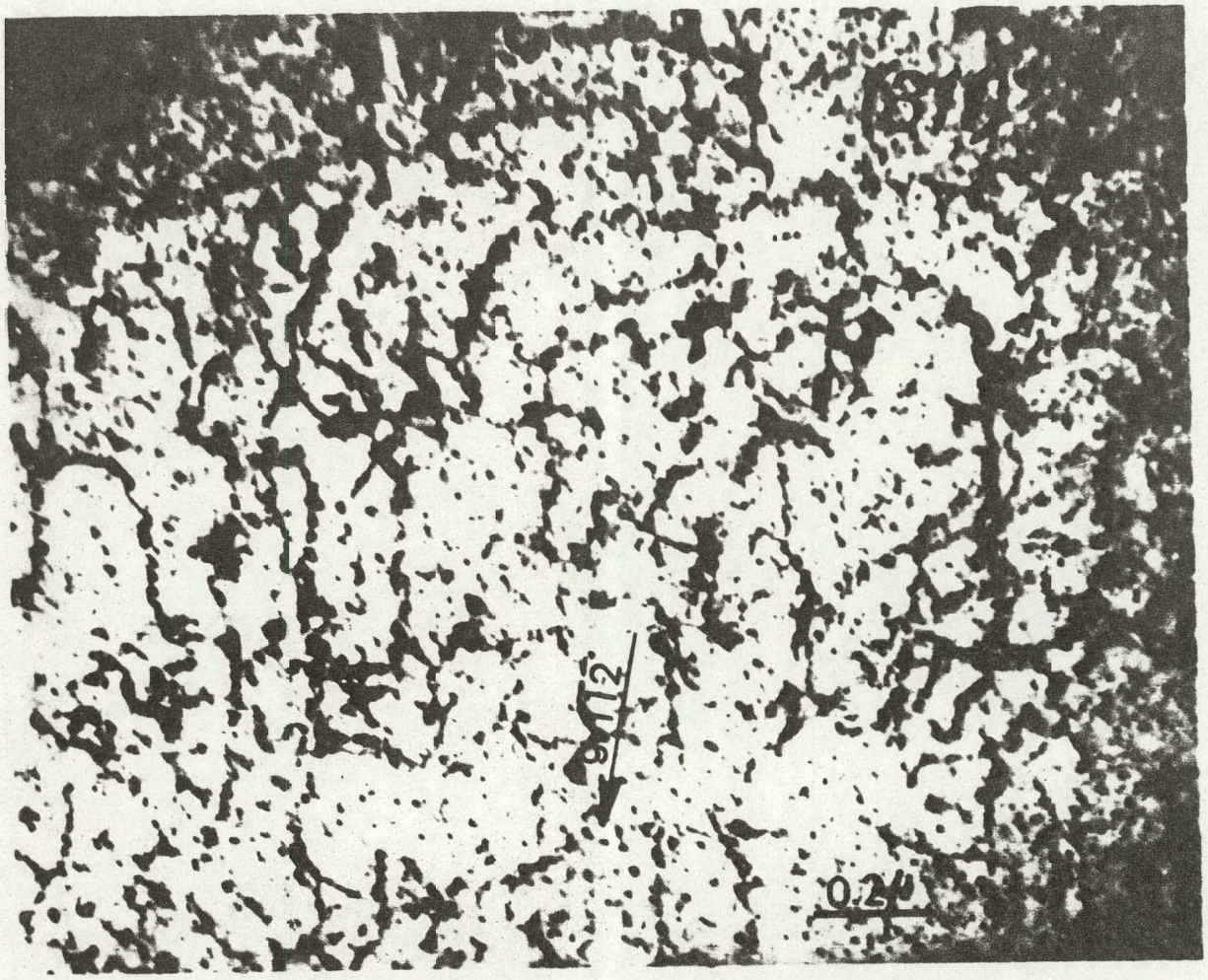

Figure 51. Transmission electron micrograph of vanadium - 500 ppm oxygen single crystal deformed 5% in compression at 77°K and irradiated to 1.4×10^{19} n/cm^2 (E>1 MeV) at 95°C

144 Å in Figure 51).

The photomicrographs for V-500 material in the three conditions (deformed at 77°K and irradiated, deformed at room temperature and irradiated, and annealed and irradiated) are shown in juxtaposition in Figure 52.

Figure 53 shows a size distribution curve plotted as percentage of defects in a size interval against the size in Å for V-95 and V-500 deformed 5% at 77°K prior to irradiation. An increase in the peak size of the clusters in comparison to that for material irradiated in the annealed condition is apparent. The average size of the cluster is also indicated in Figure 53.

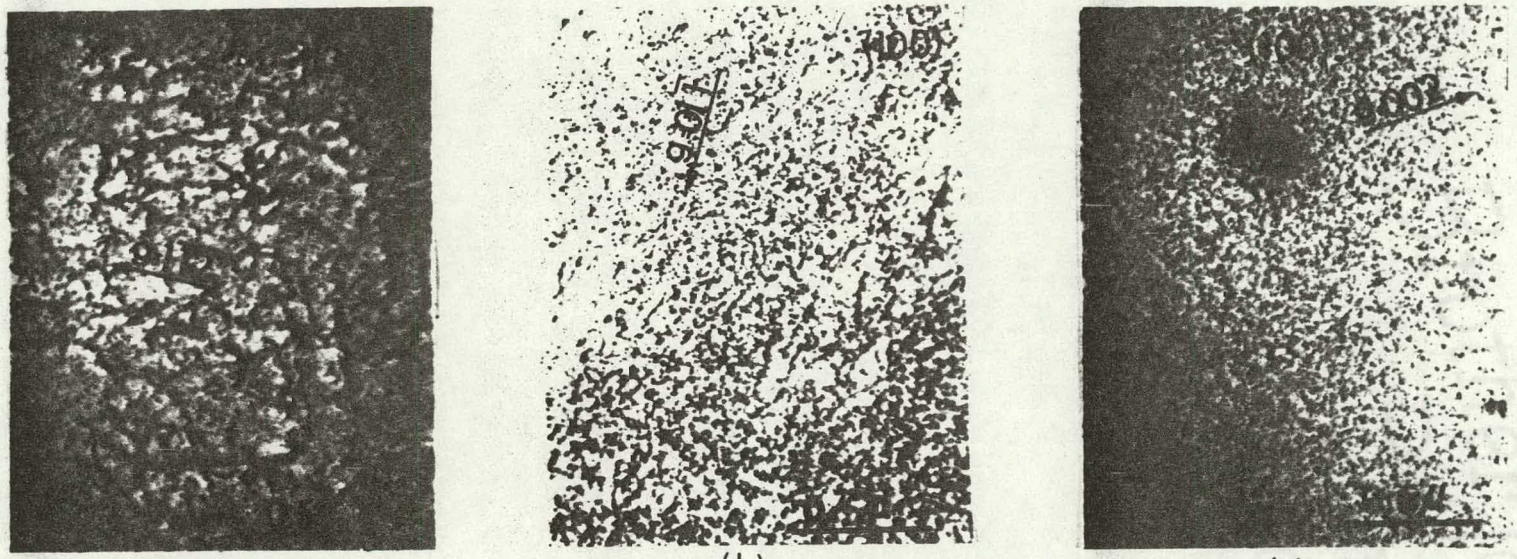

Figure 52. Transmission electron micrograph of vanadium - 500 ppm oxygen single crystals in the following conditions: (a) deformed 5% in compression at 77°K and irradiated, (b) deformed 5% in compression at room temperature and irradiated, and (c) annealed and irradiated

Figure 53. Size distribution curves for vanadium - 95 ppm oxygen and vanadium - 500 ppm oxygen single crystals in the following conditions: (a) annealed and irradiated and (b) deformed 5% in compression at 77°K and irradiated

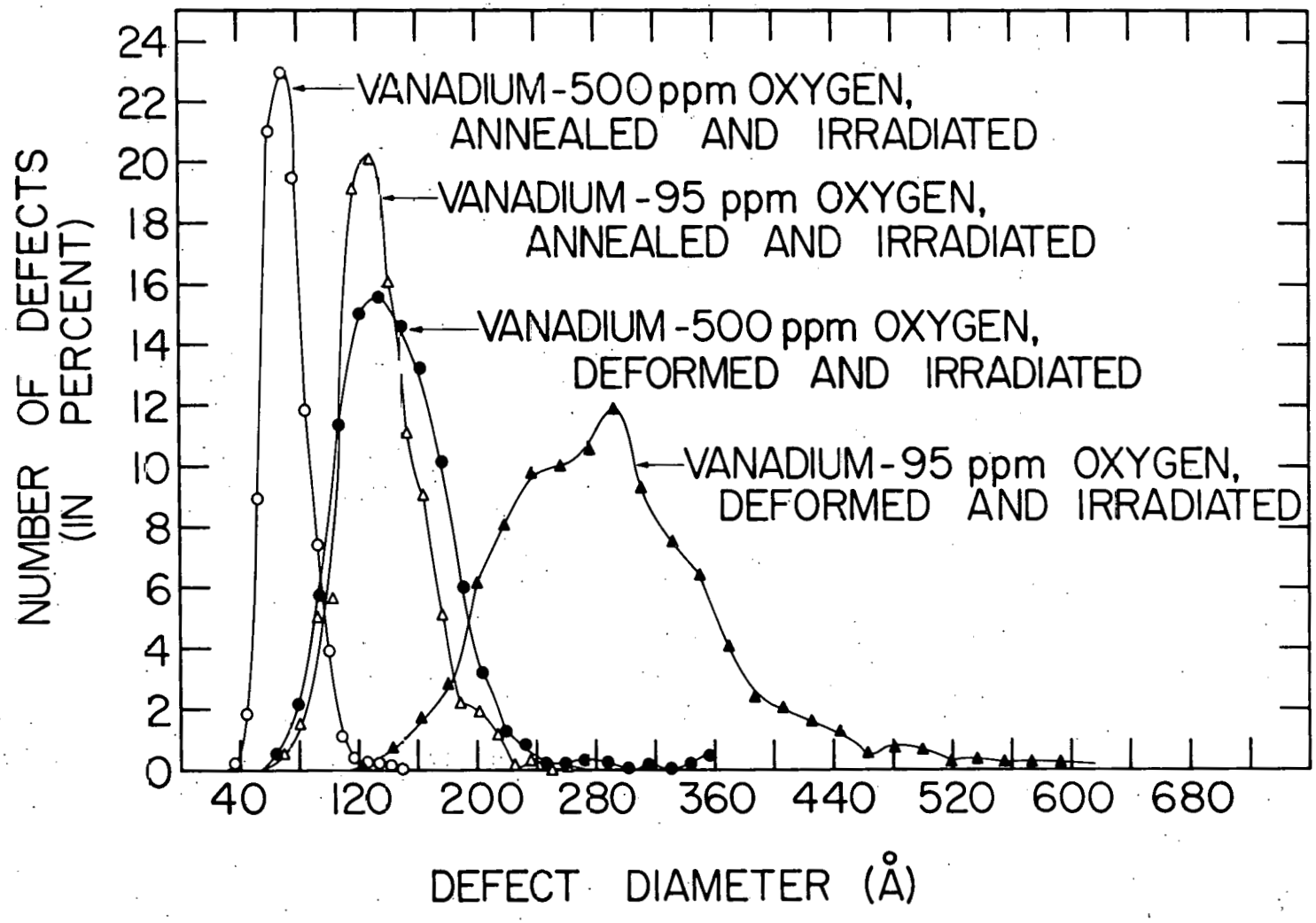
NUMBER OF DEFECTS (IN PERCENT)
0
2
4
6
8
10
12
14
16
18
20
22
24
40
120
200
280
360
440
520
600
680
DEFECT DIAMETER (Å)
VANADIUM-500 ppm OXYGEN, ANNEALED AND IRRADIATED
VANADIUM-95 ppm OXYGEN, ANNEALED AND IRRADIATED
VANADIUM-500 ppm OXYGEN, DEFORMED AND IRRADIATED
VANADIUM-95 ppm OXYGEN, DEFORMED AND IRRADIATED

V. DISCUSSION

A. Defect Clusters

One of the major objectives of this study is to determine the influences of an interstitial impurity, namely oxygen, on the defect clusters observed in as-irradiated and post-irradiation annealed vanadium. Figures 13, 15 and 17 show the TEM micrographs of vanadium containing 95, 300 and 500 ppm oxygen, respectively. Table 4 and Figure 20 summarize the defect cluster densities, n, from which it is clear that the defect cluster density increases with increasing oxygen concentration. Figure 54 is a plot of n versus the concentration of impurities in as-irradiated material where the concentration refers to oxygen alone, O+N+C and O+N+C+H, using values given in Table 3 expressed in terms of atomic parts per million. It can be observed from Figure 54 that n is sensitive to the interstitial impurity content, particularly at the lower concentration levels.

Defect clusters in irradiated vanadium have been observed by other authors also, although not as a systematic function of the interstitial impurities. A summary of the results of some of the other authors in addition to results of the present study is presented in Table 6 where the radiation variables (dose and temperatures), interstitial impurity concentrations reported, observed defect cluster densities and average size of the defect clusters are reported. It is difficult to compare the results of various investigators because of many differences in the radiation and material variables involved.

The irradiation conditions employed by Smidt (49), however, were not

Figure 54. Defect cluster density vs concentration of interstitial impurities for as-irradiated vanadium. Concentrations refer to oxygen alone, O + N + C and O + C + N + H in atomic ppm

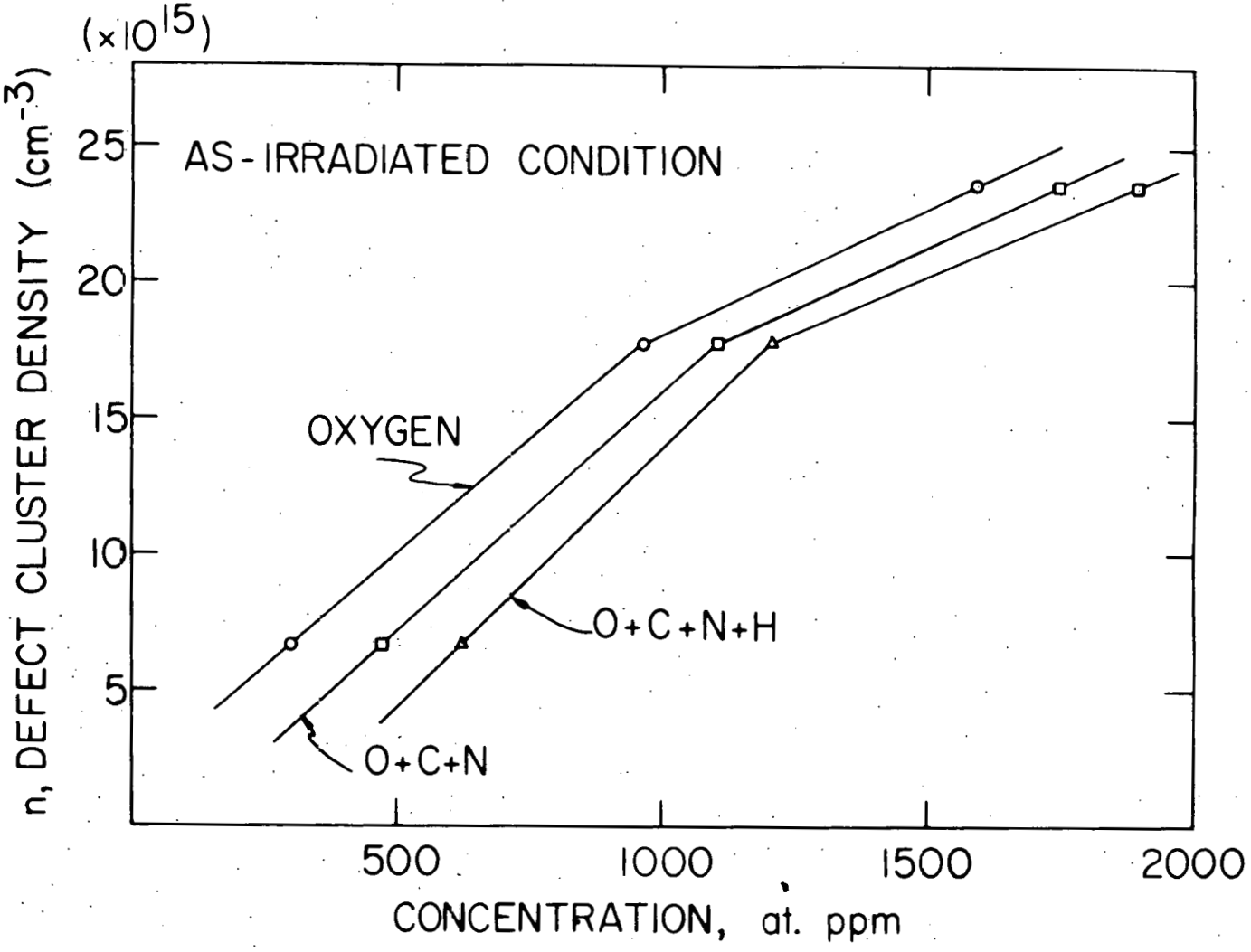
(×10^15)
n, DEFECT CLUSTER DENSITY (cm^-3)
25
20
15
10
5
AS-IRRADIATED CONDITION
OXYGEN
O+C+N+H
O+C+N
500
1000
1500
2000
CONCENTRATION, at. ppm

Table 6. Defect cluster density and average size in as-irradiated vanadium

Item	Dose (n/cm^2, E>1 MeV)	Irradiation temperature (°C)	Interstitial impurity Conc. (wt. ppm)				As-irradiated defect cluster density, $n(cm^{-3})$	Average size d_c(Å)	Reference
			O	C	N	H			
A	1.0×10^{19}	55	112	57	3	3	3.7×10^{16}	29	Smidt (49)
B	8.2×10^{19}	189-220	240	32	41	6	1.4×10^{16}	70	Shiraishi et al. (50)
C	1.0×10^{18}	50	190	38	5	15	4×10^{15}	~ 30	Shiraishi et al. (47)
D	2.4×10^{19}	70	190	38	5	15	5×10^{16}	~ 30	Shiraishi et al. (47)
E	5.0×10^{19}	80	Unspecified				2.3×10^{16}	70	Elen (179)
F	5.4×10^{19}	70	29	53	128	20	$10^{16} - 10^{17}$	25-50	Rau and Ladd (178)
G	$(0.33\text{-}1.0)\times10^{19}$	150-250	110	300	200		2×10^{16}	30	Boček and Elen (73)
H	1.0×10^{19}	250-350	110	330	200		2×10^{15}	30	Boček and Elen (73)
I	1.4×10^{19}	95	95	37	3	3	6.6×10^{15}	125	Present Study
J	1.4×10^{19}	95	305	29	5	2	1.8×10^{16}	80	Present Study
K	1.4×10^{19}	95	500	30	6	3	2.4×10^{16}	73	Present Study

greatly different than those of the present study. Smidt observed a defect cluster density of 3.6×10^{16} cm^{-3} and an average size of 29 Å (Item A, Table 6) in vanadium irradiated to a dose of 1.0×10^{19} n/cm^2 (E>1 MeV) at 55°C. The chemical analysis of vanadium reported by Smidt (the vendor's analysis) was 112, 57, 3, and 3 wt. ppm of O, C, N, and H, respectively, corresponding atomic concentrations for O, O+C+N and O+C+N+H of 357, 609, and 761 at. ppm, respectively. For these concentrations, Figure 54 predicts a defect cluster density of about (8-9) $\times 10^{15}$ cm^{-3} and thus it appears that the defect cluster density observed by Smidt is about 4 times higher than it to be expected from the vendor's analysis according to present study.

It is worthwhile to pursue this matter further and compare the hardness values reported by Smidt (49) and that of the present study. The diamond pyramid hardness of unirradiated vanadium reported by Smidt is 118 DPH as compared to about 57 DPH for unirradiated V-95 material of comparable purity (concentrations of 302, 470 and 622 at. ppm for O, O+C+N, and O+C+N+H, respectively) as shown in Figure 12.

Bradford and Carlson (226) and Loria (227) have reported the dependence of diamond pyramid hardness on oxygen concentration. Bradford and Carlson's curve (Reference 226, Figure 2) of DPH as a function of oxygen concentration (other interstitial impurities at 150, 5 and 1 wt. ppm for C, N and H, respectively) predicts a value of about 60 DPH for material used by Smidt containing 112 wt. ppm oxygen as compared to the observed value of 118 DPH. Loria (227) has reported the following equation

$$DPH = 47 + 600\ C_o + 790\ C_c + 900\ C_n$$

where C_o, C_c, and C_n are the concentrations of O, C and N, respectively, in weight percent. Applying this equation to Smidt's analysis of 112, 57 and 3 wt. ppm for O, C, and N, respectively, we obtain a hardness of 58 DPH, again to be compared with the reported value of 118 DPH. Using Loria's equation for V-95 material (analysis given in Table 3) we obtain a hardness of 56 DPH, which agrees with the value for 95 wt ppm oxygen on Bradford and Carlson's curve and the value of 58 and 60 DPH measured in the present study after post-irradiation annealing at 1000°C (Figure 12). The above brief discussion seems to indicate that the higher hardness and defect cluster density of Smidt's vanadium compared to those of the present study may be due to an actual impurity concentration of his vanadium which is higher than given in the vendor's analysis.

The defect cluster densities observed by Shiraishi et al. (46,50), Rau and Ladd (178) and Elen (179) are difficult to compare with the results of the present study because of differences in radiation conditions and purity of material. Shiraishi et al. (50) observed a defect cluster density of 1.4×10^{16} cm^{-3} for a dose of 8.2×10^{19} n/cm^2 (Item B, Table 6), which appears to be rather low for the dose used, but this may be due to the rather high irradiation temperature of 180-220°C. The defect cluster densities reported by Shiraishi et al. (46), Elen (179), Rau and Ladd (178) and Boček and Elen (73) (Items C-H, Table 6) seem roughly consistent with the present work (Items I-K, Table 6), but no exact comparison can be made for the reasons stated above. However, the results of this study alone indicate quite clearly that the differences in interstitial impurity concentrations are responsible in part for the variations in n values reported

in the literature for irradiated vanadium.

Figure 19 shows that the average defect cluster size, $\overline{d}_c$, tends to decrease with increasing oxygen concentration in as-irradiated vanadium. The increased density and decreased size of defect clusters with increasing oxygen concentration points toward the influence of oxygen as the nucleating agent. Single oxygen atoms or small aggregates of oxygen atoms may act as nucleation sites for the formation of defect clusters. Since the number of nuclei is larger in higher oxygen material, the number of radiation-produced point defects per defect cluster is smaller and consequently the individual defect clusters are smaller in size. It must be remembered, however, that the atomic density of defect clusters is considerably lower than the atomic density of oxygen atoms. In fact, as shown in Table 7, the ratio of oxygen atoms to defect clusters increases from about 3000 for V-95 to 5000 for V-500 material.

It is of interest to calculate whether sufficient number of point defects are expected to be produced upon irradiation to give rise to the observed defect cluster densities. It should be pointed out here that no attempt was made in this study to determine uniquely whether the defect clusters are of interstitial, vacancy or mixed nature. The determination of character of defect clusters requires a careful application of diffraction contrast theory and stereo microscopy. In certain cases ambiguous results have been obtained even in the best of circumstances.

In neutron-irradiated copper, for example, some investigators (137,138, 228,229) reported the clusters to be of vacancy type, while another group of investigators (230,231), using the same analysis technique, concluded

Table 7. Atomic densities of oxygen atoms, n_o, and defect clusters, n. As-irradiated condition

Purity	n (cm^{-3})	n_o (cm^{-3})	$\frac{n_o}{n}$
V-95	6.6×10^{15}	2.18×10^{19}	3260
V-300	1.77×10^{16}	6.95×10^{19}	3910
V-500	2.36×10^{16}	1.15×10^{20}	4770

that they are of interstitial nature. In still another case, both types of defect clusters were reported (232). For neutron-irradiated vanadium Elen (179) analyzed the defect clusters and concluded that the irradiation "results in a high density of arrays of presumably interstitial clusters of about 70 Å" (see Item E, Table 6). Furthermore, after annealing at 400-600°C, large vacancy loops lying on {111} planes with a Burgers vector of 1/2 a_o <111> were observed. Bocek and Elen (73), however, reported that the damage consists of a mixed population of small vacancy and interstitial loops. Smidt (49) determined the nature of the loops in vanadium irradiated to 1×10^{19} n/cm^2 (E>1 MeV) at 50°C and post-irradiation annealed at 600°C, using constrast and tilting experiments. He found the large loops to be of interstitial nature in agreement with Shiraishi et al. (46) for vanadium irradiated to 5×10^{19} n/cm^2 (E>1 MeV) and annealed at 500°C or 550°C. However, in a specimen irradiated to 1×10^{20} n/cm^2

(E>1 MeV) and annealed at 550°C, Shiraishi et al. (46) analyzed the loops to be of vacancy nature. In short, then, we conclude that the determination of the nature of radiation-produced defect clusters are not conclusive in metals in general and in vanadium in particular.

Although the nature (interstitial or vacancy) of defect clusters is controversial, it has been well established by various investigators (46, 49,179) that the defect clusters in neutron-irradiated vanadium are prismatic {111}, 1/2 a_o <111> dislocation loops, presumably of circular shape. Assuming this, we may estimate the number of atomic sites (vacancy or interstitial) making up the defect clusters, by calculating the total areas of defect clusters per unit volume of the sample, A_c, and dividing by the areal density of atoms on the (111) plane.

The total area of defect clusters is given by

$$A_c = \frac{\pi}{4} \sum_{j=1}^{N} n_j d_j^2 = \frac{\pi}{4} \, n \sum_{j=1}^{N} f_j d_j^2 \qquad (33)$$

where, as before, n_j and f_j are density and fractional numbers, respectively, of defect clusters in the size interval j centered at diameter d_j, and j is the density of defect clusters of all sizes. A_c is tabulated in Table 4 and plotted in Figure 55. It can be seen that the values of A_c do not vary in a regular manner with oxygen concentration and, even upon annealing up to 400°C, A_c stays fairly constant at about $(10 \pm 1) \times 10^3$ cm^{-1}. The density of atomic sites on {111} planes is given by

$$\rho_A = \frac{1}{\sqrt{3} a_o^2} \quad . \qquad (34)$$

Figure 55. Total defect cluster area per unit volume, A_C, vs post-irradiation-annealing temperature for single crystal vanadium containing various concentrations of oxygen

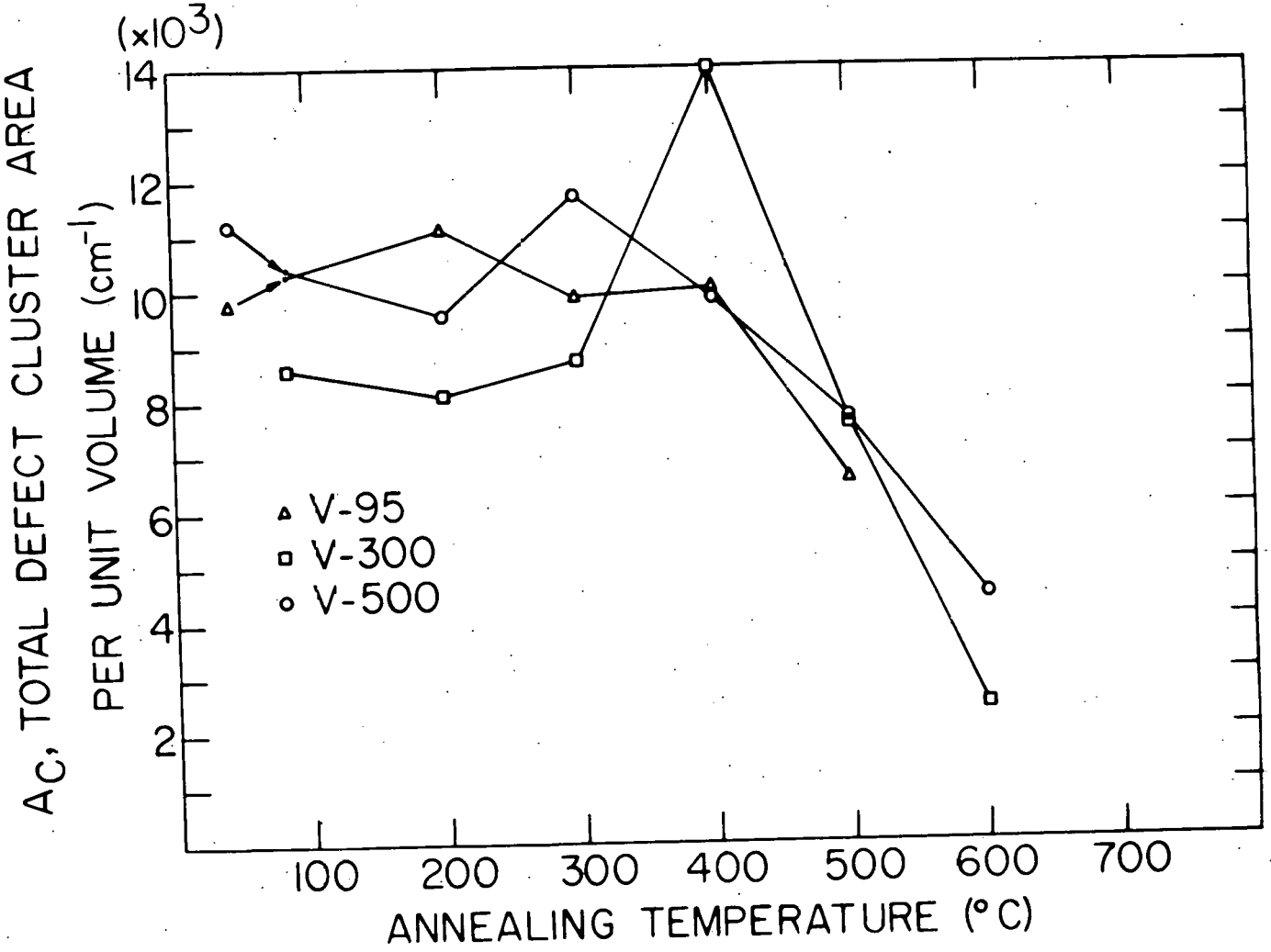
A_C, TOTAL DEFECT CLUSTER AREA
PER UNIT VOLUME (cm^{-1})
($\times 10^3$)
14
12
10
8
6
4
2
V-95
V-300
V-500
100
200
300
400
500
600
700
ANNEALING TEMPERATURE (°C)

Taking a_o = 3.026 Å for the lattice parameter (226), we obtain $\rho_a = 6.3 \times 10^{14}$ cm^{-2}. The effective density, then, of vacancy or interstitials making up all the defect clusters (assuming that all the defect clusters are of one type) is

$$\rho_{i-v} = A_c \rho_A = 6.3 \times 10^{18} \text{ cm}^{-3} \quad . \tag{35}$$

For a rough estimation of the density of displacements produced upon irradiation we may interpolate from Elen's value (179) of 6.9×10^{21} displacements per cm^3 for vanadium irradiated to 7.4×10^{19} n/cm^2 (E>0 MeV) or 5.0×10^{19} n/cm^2 (E>1 MeV) assuming a fission spectrum. For the dose of 1.4×10^{19} n/cm^2 (E>1 MeV) used in present study, a displacement density of 1.9×10^{21} displacements per cm^3 is deduced. Comparing this density with the one in Equation 35, we see that if only one displacement in $(1.9 \times 10^{21})/(6.3 \times 10^{18}) = 300$ contributes a vacancy or interstitial to the defect cluster, a sufficient area of defect clusters is produced to agree with the observed density and size distribution of as-irradiated material.

The fact that A_c in Figure 55 does not show any regular dependence on oxygen concentration can be rationalized by realizing that A_c is a measure of the number of radiation-produced point defects absorbed into defect clusters. Its value should not depend on the oxygen concentration, which has its major effect on the nucleation of the defect clusters. It is interesting to note that A_c does not begin to decrease upon post-irradiation annealing until the annealing temperature of 500°C is reached even for V-95 (Figure 55), although the total defect cluster density, n, has

already decreased at 400°C to 43% of its maximum value (Figure 20) and the average defect cluster size, $\bar{d}_c$, has already increased at 400°C to 45% of its maximum value (Figure 19). This suggests that the reduction in n and the growth of defect cluster size d_c upon annealing up to 400°C occurs by the migration of point defects from the smaller to the larger defect clusters, without any significant annihilation at various sinks.

An examination of Figures 19 and 20 reveals that the as-irradiated values of the total density (Figure 20) and average size (Figure 19) of the defect clusters persist to a higher temperature upon annealing as the oxygen concentration is increased. Thus, it can be seen in Figure 20 that n begins to decrease fairly rapidly at 400°C for V-95 whereas 500°C is required for extensive annealing of V-500 material suggesting that oxygen tends to stabilize the defect clusters and that greater amounts of oxygen are segregated at the defect clusters in the higher oxygen material. The total line length of the defect clusters per unit volume is given by

$$L_c = \pi \, n \, \bar{d}_c \, . \tag{36}$$

Table 4 and Figure 56 give L_c for as-irradiated and post-irradiation annealed materials. L_c is equal to 2.9×10^{10}, 4.3×10^{10} and 5.5×10^{10} cm^{-2} for V-95, V-300 and V-500 materials, respectively, in the as-irradiated condition whereas the corresponding total densities of oxygen atoms (Table 7) are 2.2×10^{19}, 7.0×10^{19} and 11.5×10^{19} oxygen atoms per cm^3. This corresponds to the number of oxygen atoms per Å of dislocation loop length of about 8, 16 and 21 for V-95, V-300 and V-500, respectively. Considering the distance between atoms along the dislocation loop lying on a (111) plane

Figure 56. Total defect cluster loop length, L_C vs post-irradiation annealing temperature for single crystal vanadium containing various concentrations of oxygen

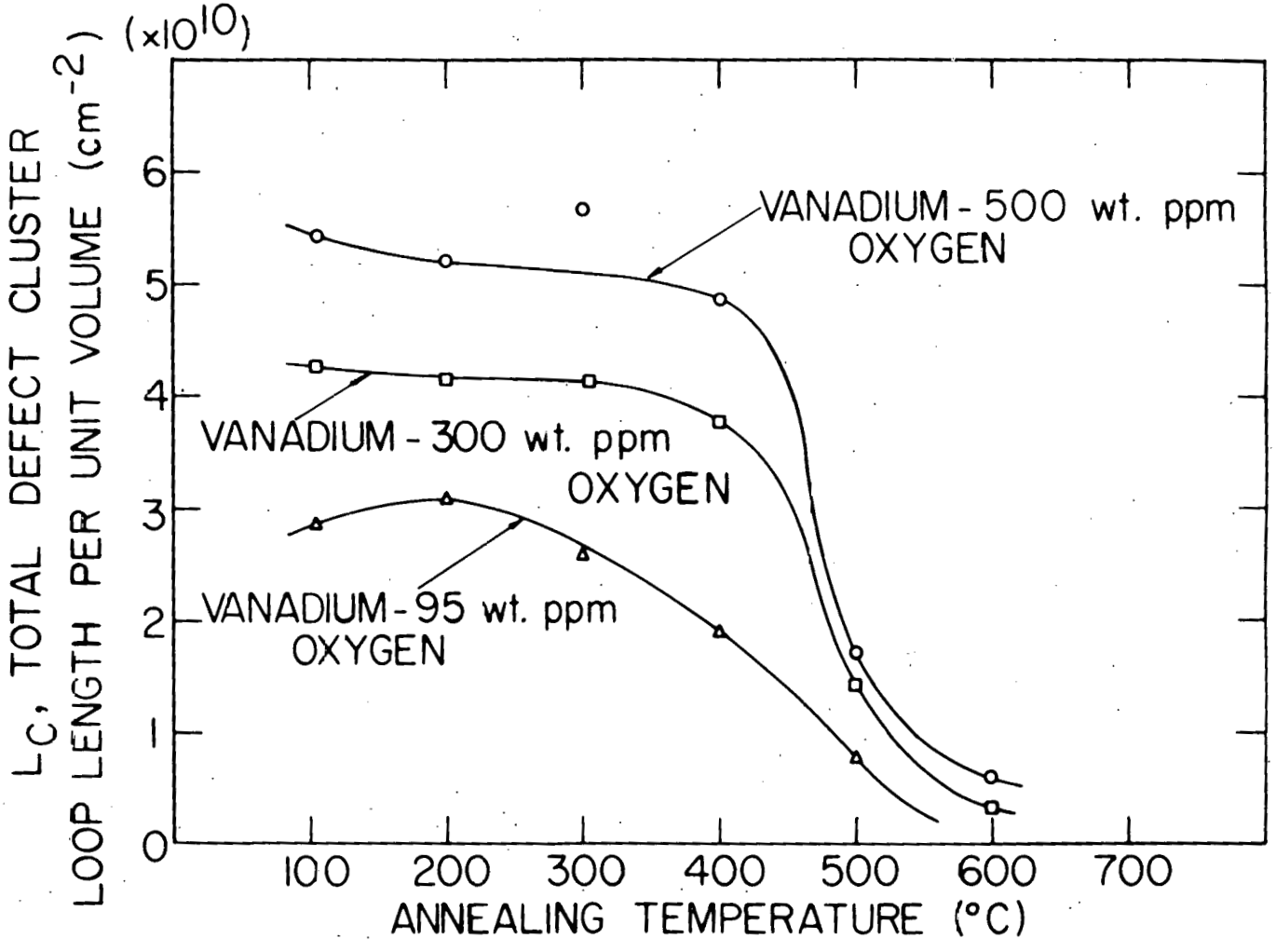
(×10^10)
L_C, TOTAL DEFECT CLUSTER LOOP LENGTH PER UNIT VOLUME (cm^-2)
0
1
2
3
4
5
6
100
200
300
400
500
600
700
ANNEALING TEMPERATURE (°C)
VANADIUM - 500 wt. ppm OXYGEN
VANADIUM - 300 wt. ppm OXYGEN
VANADIUM - 95 wt. ppm OXYGEN

with Burgers vector $\frac{a_o}{2}$ [111] to be equal to the interatomic distance along <110>, i.e., $\sqrt{2}\, a_o$ = 4.28 Å, the number of oxygen atoms available per atom along the dislocation line is 33, 70 and 91, respectively. This indicates that more oxygen is available per unit length or per atom along the dislocation loop in the higher oxygen material, which might well be responsible for the increased stability of defect clusters against annealing with increased oxygen content.

B. Radiation Hardening

The effects of neutron irradiation on the strength of vanadium containing various amounts of oxygen was determined by using lower yield stress measurements on polycrystalline samples and indentation hardness measurements (diamond pyramid hardness) on single crystal samples. The single crystal samples were prepared from the same material as was used for defect cluster density and size distribution studies described above.

Figure 57 summarizes the results of various studies on lower yield stress values as a function of oxygen concentration for unirradiated vanadium polycrystals. The numbers adjacent to the plotted points refer to the items in Table 8, which gives information concerning the chemical composition, grain size, strain rates and yield stresses reported in the literature and from the present study. It is seen that the values do not correlate generally with oxygen concentrations since so many other variables are also involved. Some attempt was made to correct for grain size and strain rate, realizing that such corrections can only be approximate. For the correction of grain size, the Petch relation

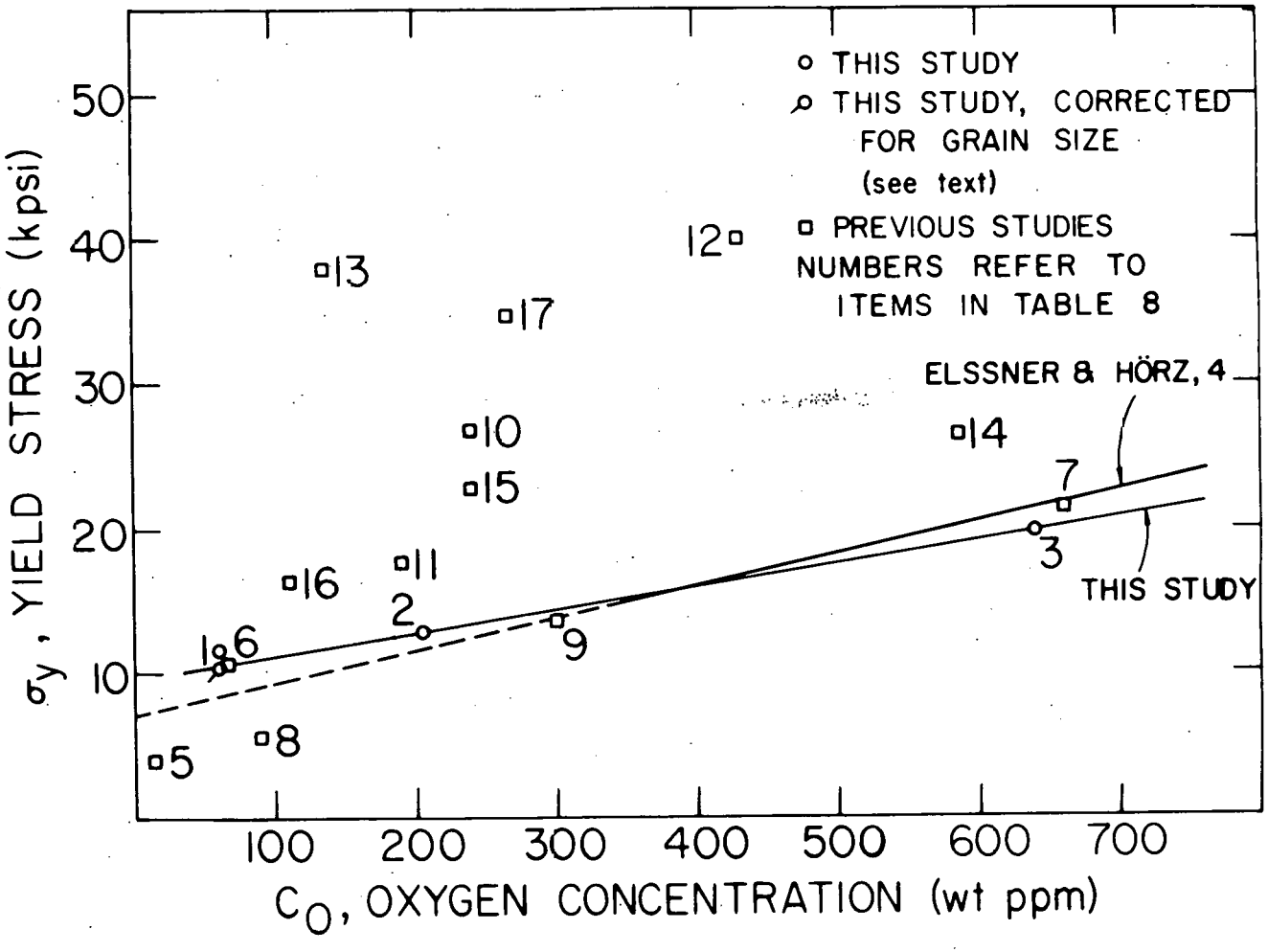

Figure 57. Yield stress vs oxygen concentration for unirradiated vanadium reported by various investigators

Table 8. Yield stresses for room temperature tests on vanadium polycrystals in the unirradiated condition

(1) Item no.	(2) Interstitial Impurity concentration (wt ppm)				(3) Grain size (mm)	(4) Strain rate (10^{-4} sec^{-1})	(5) Yield Stress as measured (kpsi)	(6) Yield Stress corrected[a] (kpsi)	(7) Reference
	O	N	C	H					
1	60	1-6	30-40	2-8	0.024	1.67	11.6	10.3	This study
2	205	2-6	50	10-12	0.142	1.67	12.8	12.8	This study
3	640	2-6	60-80	15-18	0.146	1.67	19.8	19.8	This study
4	b	20	16	<10	b	0.47	b		Elssner and Hörz (232)
5	14	2	9		~ 0.381	1.67	4.0	4.2	Alexander and Carlson (233)
6	66	2	9		0.145	1.67	10.7	10.7	Wechsler et al. (71)
7	660	2	9		9.145	1.67	21.3	21.3	Wechsler et al. (71)
8	90	10-30	<5		not given	1.0-1.2	5.6	5.6[c]	Arsenault and Pink (70)[d]

[a]Corrected for grain size and strain rate; see text.

[b]Various oxygen concentrations employed; see text

[c]Corrected for strain rate only.

[d]Compression tests.

Table 8. (Continued)

(1) Item no.	(2) Interstitial Impurity concentration (wt ppm)				(3) Grain size (mm)	(4) Strain rate (10^{-4} sec^{-1})	(5) Yield Stress as measured (kpsi)	(6) Yield Stress corrected[a] (kpsi)	(7) Reference
	O	N	C	H					
9	300	130	< 5		not given	1.0-1.2	13.6	13.7[c]	Arsenault and Pink (70)[d]
10	240	41	32	6	0.016	2.83	26.8	23.3	Shiraishi et al. (50)
11	190	5	38	15	0.038	2.83	17.6	16.3	Shiraishi et al. (50)
12	430	3.5	50	21	0.038	2.83	40.0	37.2	Shiraishi et al. (50)
13	136	95	166	7	< 0.120	0.83	38.0	> 37.3	Smolik and Chen (48)
14	586	78	77	< 1	0.120	0.83	26.5	25.7	Smolik and Chen (48)
15	240	340	530		0.150	2.55	22.7	21.2	Boček et al. (47)
16	110	200	330		0.050	2.55	16.3	15.3	Boček and Elen (73)
17	266	320	520	9	0.174	3.3	34.7	34.0	Venetch et al. (84)

$$\sigma = \sigma_o + k_y d_G^{-1/2} \tag{37}$$

was used, where σ is the yield stress, σ_o and k_y are constants and d_G is one-half the grain diameter. If d_1 and d_2 are the d_G factors for a given material, then the corresponding yield stresses are related by

$$\sigma_2 - \sigma_1 = k_y (d_2^{-1/2} - d_1^{-1/2}) . \tag{38}$$

For tests at 273°K, k_y as a function of oxygen concentrations is given by

$$k_y = A C_o + B \tag{39}$$

according to Loria, Keith and Rowe (234) who studied the effect of O, N and C on the tensile properties of vanadium of various grain sizes. A in above equation was found to be 4.73 kpsi $cm^{-1/2}$ per wt percent oxygen, B = 0.049 kpsi $cm^{-1/2}$, and C_o is the concentration of oxygen. Thus, equations 38 and 39 were used to correct for grain size differences. The strain rate corrections were made using the following relation

$$\ln \frac{\sigma_2}{\sigma_1} = S \ln \frac{\dot{\varepsilon}_2}{\dot{\varepsilon}_1} \tag{40}$$

where σ_1 and σ_2 are yield stresses corresponding to strain rates $\dot{\varepsilon}_1$ and $\dot{\varepsilon}_2$, respectively, and S is the strain rate sensitivity parameter. Carlson and Alexander (235) reported a value of S = 0.0237 for room temperature tests on vanadium containing 264 wt. ppm oxygen. This value was used, assuming that the strain rate sensitivity is independent of oxygen concentration at the levels shown in Table 8. Using Equations 38 and 40 we corrected the

as-measured yield stresses in Table 8 to values appropriate to a grain size of 0.144 mm (the grain size for our V-205 and V-640 material; see Table 2) and our strain rate of 1.67×10^{-4} sec^{-1}. It is seen in Table 8 that the corrections to the yield stress values due to differences in grain size and strain rates are not very large, and the wide variations in yield stress values shown in Figure 57 still remain.

Elssner and Hörz (232) studied the effect of nitrogen and oxygen on the yield stress of electro-refined vanadium obtained from U.S. Bureau of Mines, Boulder City, Nevada. This is the same source as for vanadium used in the present study (See Chapter III). They obtained the relationship for room temperature tests

$$\sigma(k_g/mm^2) = 5.0 + 52.0\ C_n\ (at.\ \%) + 50.0\ C_o\ (at.\ \%) \qquad (41)$$

where C_n and C_o are the concentrations of nitrogen and oxygen, respectively. After a recrystallization anneal their vanadium contained 20 wt ppm nitrogen. Substituting this value and converting hield stress into kpsi, the following relation is obtained for yield stress as a function of oxygen concentration:

$$\sigma(kpsi) = 7.2 + 0.0222\ C_o\ (wt\ ppm)\ . \qquad (42)$$

The above relationship is plotted in Figure 57.

The yield stress values obtained in the present study are also plotted in Figure 57 (points 1, 2 and 3). Points 2 and 3 refer to samples with a grain size of about 0.144 mm, whereas the sample for point 1 had a grain size of 0.024 mm (Table 2). Correcting the yield stress of V-60 for grain size in the manner described above results in a value of 10.3 kpsi (from

11.6 kpsi), which falls on a straight line with points 2 and 3 as shown in Figure 57. This line agrees well with the one obtained by Elssner and Hörz (232). The small differences may be due to differences in concentrations of impurities other than oxygen, or to differences in grain structure. Elssner and Hörz report that their material had an "almost ideal bamboo structure" with specimen axis along <110> , whereas our samples had an equiaxed grain structure.

The yield stress values as a function of neutron irradiation for polycrystalline material investigated by various authors are summarized in Table 9 for comparison. It is seen that the radiation hardening observed by various investigators varies extensively. Boček et al. (47) studied the dose dependence of the yield stress of vanadium containing fairly high interstitial contents (Item 15, Table 8) and also 3000 wt ppm yttrium, which is expected to act as an internal getter for interstitial impurities. They observed an increase in yield stress upon irradiation which varied as the square-root of the dose for irradiations carried out at 150-250°C (see Figure 58). It should be noted that the irradiation temperatures were in the range where radiation-anneal hardening takes place, as seen in Figures 9, 10 and 12. Boček and Elen (73) studied the dose dependence of radiation hardening, again at 150-250°C in vanadium containing somewhat lower concentrations of interstitial impurities (Item 16, Table 8) but without any yttrium addition. The yttrium-free material exhibited less radiation hardening than material containing 3000 wt ppm yttrium (Figure 58). The present work (Figures 9, 10 and 12) indicates that radiation hardening increases with increasing oxygen concentration.

Table 9. Effect of irradiation on the yield stress of vanadium polycrystals. Room temperature tests. Various investigations[a]

Oxygen Concentration (wt. ppm)	Dose (10^{19} n/cm^2)	Irradiation Temperature (°C)	Yield Stress (kpsi)	Item No., Table 8	Reference
60	0		11.6	1	This study
	1.4	105	23.6		
205	0		12.8	2	This study
	1.4	105	29.7		
640	0		19.8	3	This study
	1.4	105	40.3		
66	0		10.7	6	Wechsler et al. (71)
	1.5	85	25.5		
660	0		21.3	7	Wechsler et al. (71)
	1.5	85	42.5		
90	0		5.6	8	Arsenault and Pink (70)
	2	60-100	20.6		
300	0		13.6	9	Arsenault and Pink (70)
	2	60-100	35.2		
240	0		26.8	10	Shiraishi et al. (50)
	8.2	180-220	46.5		
190	0		17.6	11	Shiraishi et al. (50)
	0.02	70	20.2		

[a]Doses and yield stresses are taken from published plots in most cases and are approximate.

Table 9. (continued)

Oxygen Concentration (wt. ppm)	Dose (10^{19} n/cm^2)	Irradiation Temperature (°C)	Yield Stress (kpsi)	Item No., Table 8	Reference
	0.1	50	25.0		
	2.4	70	52.7		
430	0		40.0	12	Shiraishi et al. (46)
	5	70	71.3		
	10	70	65.3		
136	0		38.0	13	Smolik and Chen (48)
	1.8	107	64.5		
	3.6	107	93.0		
	4.0	107	~ 100		
240	0		22.7	15	Boček et al. (47)
	0.0022	150-250	23.7		
	0.028	150-250	26.7		
	0.056	150-250	29.7		
	0.11	150-250	31.8		
	0.24	150-250	35.3		
	0.48	150-250	41.9		
	1.3	150-250	54.3		
	2.7	150-250	66.2		
110	0		16.3	16	Boček and Elen (73)
	0.0016	150-250	25.7		
	0.016	150-250	26.5		
	0.092	150-250	31.7		
	0.17	150-250	35.3		
	0.33	150-250	39.9		
	1.0	150-250	52.9		

Table 9. (continued)

Oxygen Concentration (wt. ppm)	Dose (10^{19} n/cm^2)	Irradiation Temperature (°C)	Yield Stress (kpsi)	Item No., Table 8	Reference
266	0		34.7	17	Venetch et al. (84)
	∿ 0.07	60	45.5		

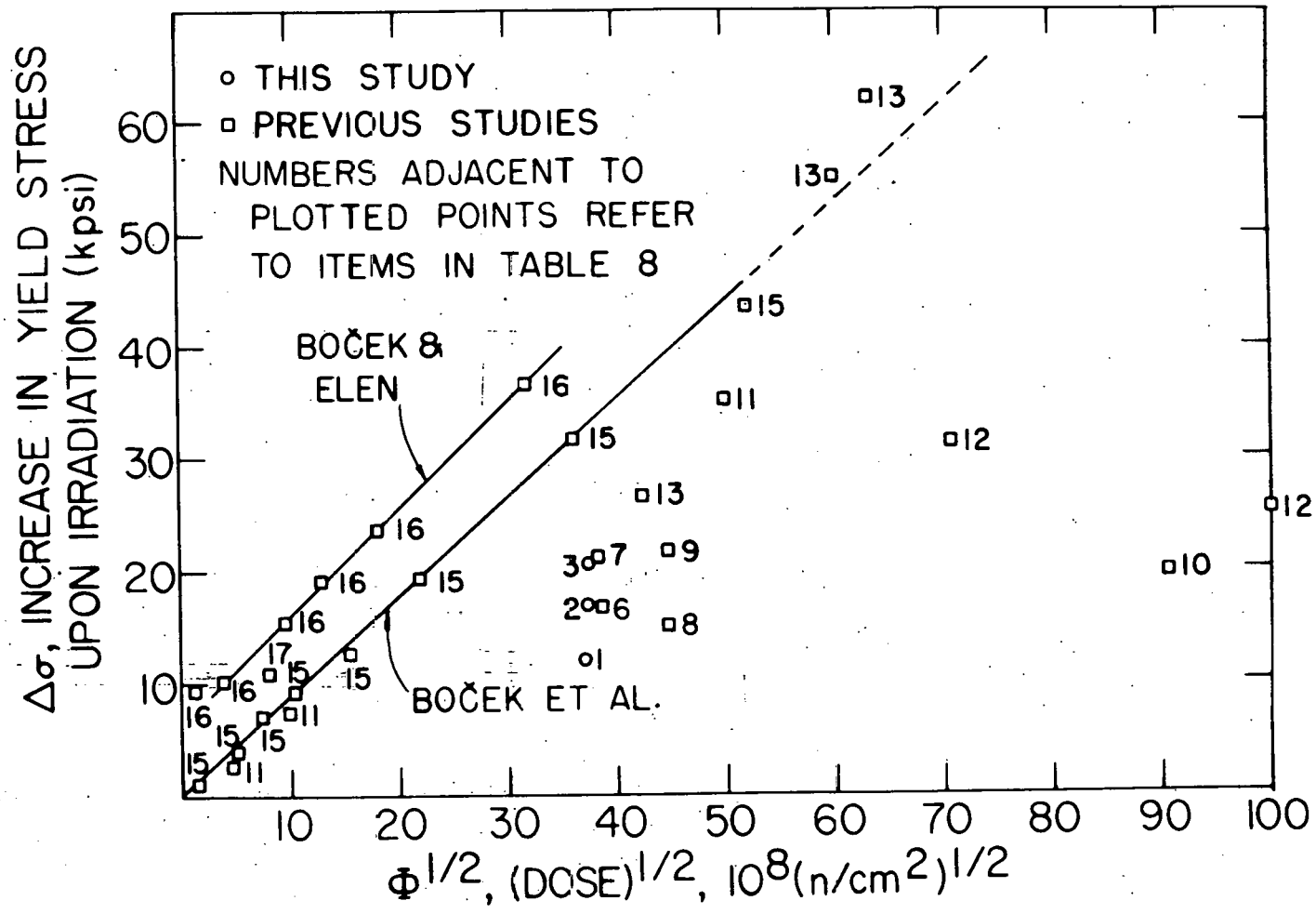

Figure 58. Increase in yield stress upon irradiation, $\Delta\sigma$, vs square root of irradiation dose, $\Phi^{\frac{1}{2}}$, reported by various investigators

It appears that the effective interstitial impurity concentration in vanadium containing 3000 wt ppm yttrium studied by Boček et al. (47) was reduced due to yttrium, as expected. It is seen in Figure 58 that, in general, the radiation hardening observed by various investigators shows wide variations which are attributed to the differences in material (purity, grain size and structure, prior heat treatments) and radiation (dose, flux, irradiation temperature) variables.

Figure 59 shows the increase in yield stress as a function of square root of oxygen concentration (in wt ppm) and the square root of the sum of oxygen, nitrogen and carbon concentration (in wt ppm) for our V-60, V-205 and V-640 polycrystalline material. The increase in radiation hardening with increasing interstitial impurity concentration is evident from this figure.

Similar measurements of radiation hardening were made by measuring indentation hardness upon irradiation in single crystal material containing 95, 300 and 500 wt ppm oxygen. Figure 60 is a plot of results obtained. It is seen, again, that radiation hardening increases with increasing impurity concentration. Figure 60 also shows results obtained by Smidt (49) upon irradiation to 1×10^{19} n/cm^2 (E>1 MeV) at 55°C. It was stated above that the hardness value of 118 DPH observed for unirradiated material seems to indicate a higher interstitial impurity concentration than given in the vendor's analysis. Nevertheless, the increase in hardness upon irradiation was only 18 DPH, which seems consistent with the oxygen concentration of 112 wt ppm (see Table 6) in comparison to our results. In Figure 60 a point is also plotted which shows Smidt's observation corrected for difference in

Figure 59. Plot of increase in yield stress upon irradiation, $\Delta\sigma$, vs square root of interstitial concentrations for polycrystalline vanadium. Concentrations refer to oxygen alone and O + N + C in wt. ppm and atomic ppm, respectively

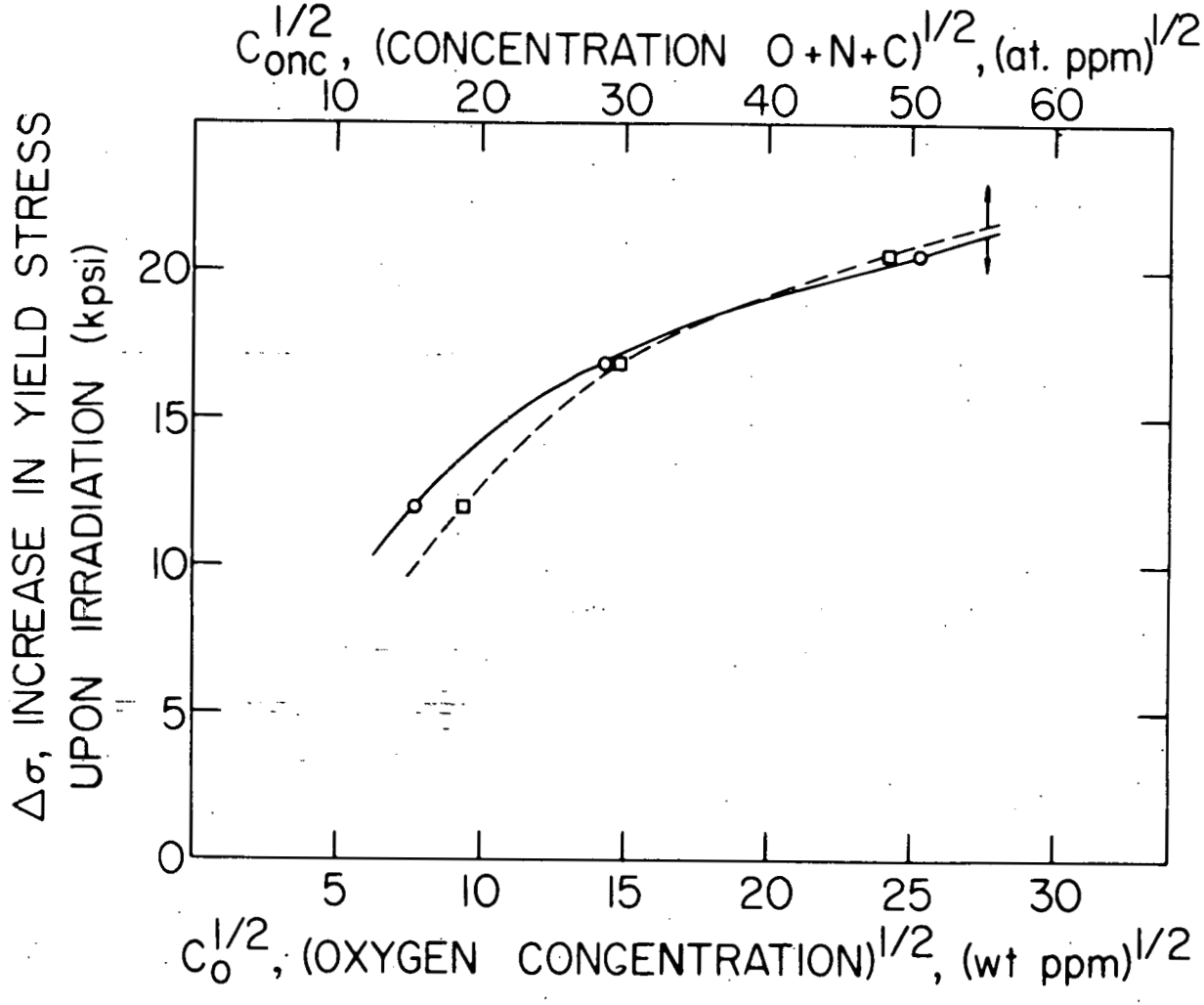
$C_{onc}^{1/2}$, (CONCENTRATION O+N+C)$^{1/2}$, (at. ppm)$^{1/2}$
10
20
30
40
50
60
$\Delta\sigma$, INCREASE IN YIELD STRESS UPON IRRADIATION (kpsi)
0
5
10
15
20
$C_o^{1/2}$, (OXYGEN CONCENTRATION)$^{1/2}$, (wt ppm)$^{1/2}$
5
10
15
20
25
30

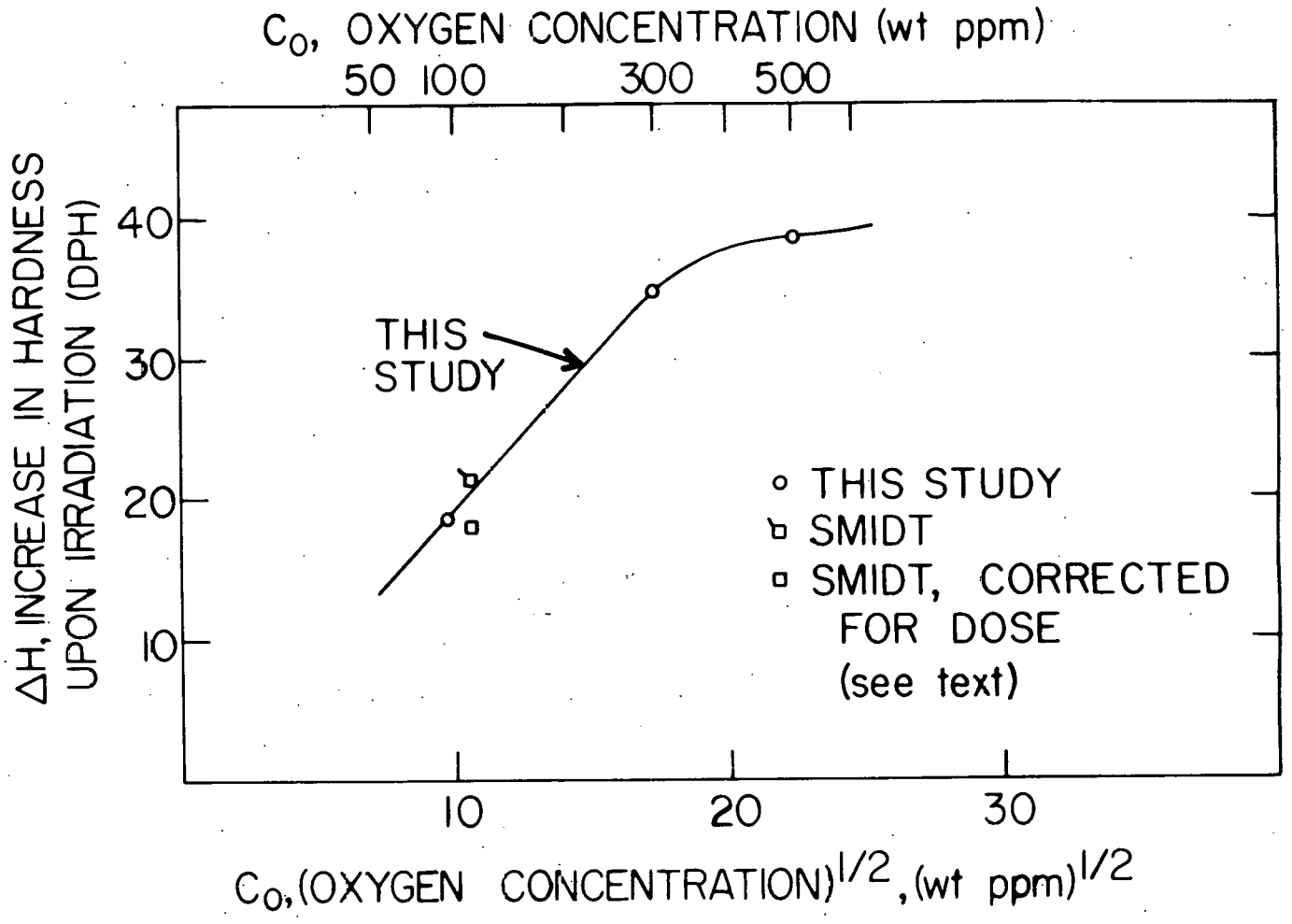

Figure 60. Plot of increase in diamond pyramid hardness upon irradiation, ΔH, vs square root of oxygen concentration in wt ppm for single crystal vanadium

dose in his irradiation (1.0×10^{19} n/cm^2) and ours (1.4×10^{19} n/cm^2) using a $\phi^{1/2}$ power hardening dependence as indicated by Boček et al. (47) and shown in Figure 58. It may be fortuitous that Smidt's ΔH value agrees so well with the value obtained in the present study, since his measurements were carried out on 0.002 in. (0.051 mm) thick foils using a 50 gram load, whereas we used 0.5 mm thick samples and a 1 kilogram load. Furthermore, the vendor's analysis indicated 57 wt ppm carbon for Smidt's material compared to our carbon contents of 37, 29 and 30 wt ppm for V-95, V-300 and V-500 material, respectively (see Table 3).

In order to correlate radiation hardening with defect cluster density and size distribution, Smidt (49) has used the following empirical formula relating increase in hardness, ΔH, and increase in yield stress, $\Delta\sigma$, upon irradiation:

$$\frac{\Delta H}{\Delta\sigma} = 3.0 \frac{\text{DPH}}{\text{kg/mm}^2} = 2.1 \frac{\text{DPH}}{\text{kpsi}} \quad . \tag{43}$$

Interpolating from Figure 59 we find that $\Delta\sigma$ = 14.0, 18.2 and 19.7 kpsi for V-95, V-300 and V-500 material, respectively. The observed ΔH values for the three materials (Figure 60) were 18.5, 34.8 and 38.5 DPH, respectively. Thus, we deduce values of $\Delta H/\Delta\sigma$ of 1.3, 1.9 and 2.0 DPH/kpsi to be compared with Smidt's value of 2.1 DPH/kpsi. We applied the small correction to allow for differences in dose for our yield stress measurements (1.2×10^{19} n/cm^2) and hardness measurements (1.4×10^{19} n/cm^2) using the $\phi^{1/2}$ dependence. This reduces the $\Delta H/\Delta\sigma$ values by a factor of $(1.2/1.4)^{1/2}$ to 1.2, 1.76 and 1.85 DPH/kpsi for V-95, V-300 and V-500

respectively, which indicates that the values for the ratio $\Delta H/\Delta\sigma$ for V-300 and V-500 are less by about 15% than indicated by Smidt's (49) empirical relation in Equation 43.

C. Strain Aging

There are two theories most generally accepted which explain strain aging in b.c.c. metals. The first one is the "dislocation locking theory" proposed by Cottrell and Bilby (207) according to which the solute atoms pin the dislocation, until under the applied stress the dislocations break away from the solute atmosphere, resulting in increased number of mobile dislocations and leading to the observed yield point. The other theory due to Johnston and Gilman (208) was extended to b.c.c. metals by Hahn (209). It is called "dislocation multiplication theory" whereby the dislocations surrounded by the solute atmosphere remain locked and the yield point is the result of rapid multiplication of mobile dislocation and the stress dependence of dislocation velocity. Either of the two theories can explain the observed results, since the main point of interest is the pinning of dislocations by the solute atoms.

In Table 5, the times for reappearance of yield drop have been listed for unirradiated and irradiated samples. It can be observed that the time for reappearance of yield drop decreases with increasing oxygen for both unirradiated and irradiated material. According to the Cottrell-Bilby theory, the number of solute atoms migrating to the dislocations is proportional to $t^{2/3}$, where t is the time for reappearance of yield drop. The Cottrell-Bilby theory predicts

$$N(t) = 3\left(\frac{\pi}{2}\right)^{1/3} N_o \left(\frac{Dc}{kT}\right)^{2/3} t^{2/3} \qquad (44)$$

where N(t) is the number of solute (oxygen) atoms segregated per unit length of dislocation line. N_o is the number of solute atoms per cm^3, D is the diffusion constant, k and T are Boltzmann's constant and temperature of anneal in °K, respectively. c is related to the strength parameters and is given by

$$c = \frac{4}{3} G b \varepsilon r^3 \left(\frac{1+\nu}{1-\nu}\right) \qquad (45)$$

where G is the shear modulus, b is the Burgers vector, ν is Poisson's ratio, r is the radius of the solvent atom and $r(1+\varepsilon)$ that of the solute atom.

c can also be expressed as

$$c = \Delta v G b \left(\frac{1+\nu}{1-\nu}\right) \qquad (46)$$

as suggested by Szkopiak and Eliasz (236), where Δv is the change in lattice volume due to presence of interstitial atoms. At a particular aging temperature, N(t) is proportional to $N_o t^{2/3}$. For the validity of the Cottrell-Bilby theory, $N_o t^{2/3}$ should be constant for the three types of vanadium samples. Table 10 lists $N_o t^{2/3}$ values for unirradiated and irradiated vanadium, where t at 175°C is the time for reappearance of the yield drop.

From Table 10 it can be seen that $N_o t^{2/3}$ for unirradiated vanadium of three oxygen contents is fairly constant as predicted by the Cottrell-Bilby theory. $N_o t^{2/3}$ for irradiated material is also reasonably constant.

Table 10. $N_o t^{2/3}$ values for irradiated and unirradiated vanadium

Sample	$N_o t^{2/3}$ (cm^{-3} $sec^{2/3}$)	
	Unirradiated	Irradiated
V-60[a]	1.24×10^{21}	1.67×10^{22}
V-200	2.03×10^{21}	3.90×10^{22}
V-640	1.4×10^{21}	2.15×10^{22}

[a]The unirradiated low oxygen material was prepared in a separate batch. It contained 37 wt. ppm oxygen and had an average grain diameter 0.113 mm.

The variations may be due to variations in the dislocation structure caused by the presence of dislocation channels.

Before explaining the reasons for delay in the reappearance of yield drop in the irradiated material, let us calculate the number of atoms segregating per dislocation line giving rise to the yield point. An average value of $N_o t^{2/3}$ can be taken as $1.6 \times 10^{21} cm^{-3} sec^{2/3}$ for unirradiated material.

The values for factors D, G, B, ν and Δv were taken as 8.79×10^{-17} cm^2/sec at 175°C, 4.76×10^3 kg/mm^2, 2.62 Å, 0.36 and $4.6 \times 10^{-24} cm^3$, respectively. Δv was calculated using the Bradford and Carlson (226) lattice parameter for vanadium containing oxygen, extrapolating to the ratio of interstitial to vanadium atoms equal to 0.5 or 33.3 at % oxygen. Substituting the above factors in Equation 44, one arrives at the value of 3.85×10^5 atoms segregating per cm of dislocation line or 0.0385 atoms

per Å. If we consider atomic spacing along the line to be equal to b = 2.62 Å, then we have 0.038 x 2.62 = 0.1 atoms per atomic spacing, or one atomic site in ten is occupied by oxygen, which give rise to yield drop. Although this number appears quite low, the observations made by Bradford and Carlson (226) on strain aging at 175°C agree reasonably well with our observations. They observed a reappearance of the yield drop in vanadium containing 265 wt. ppm oxygen in 5.4 minutes, which corresponds to a 0.18 segregated atoms per atomic spacing.

The retardation in reappearance of yield drop caused by neutron irradiation is quite clear from Table 5 and Figures 25-27. It is concluded that the retardation is caused by the migration of oxygen atoms at first to the radiation-produced defect clusters where they are trapped. The oxygen atoms migrate to dislocations only after the defect clusters become saturated and therefore the oxygen atoms participate in the strain-aging later than in unirradiated material. A question arises here as to the distance that an oxygen atom has to be moved to reach a defect cluster or a dislocation. From the single crystal TEM observations extended to polycrystalline specimens, the volume density of defect clusters can be approximated, and therefore the spacing between the defect clusters $S' = (1/n)^{1/3}$ can be calculated. Table 11 lists the approximate cluster density and calculated cluster spacings for the three materials obtained from extrapolation of density values of a single crystal material annealed at 200°C.

To determine the spacing between dislocations, the number density of the dislocation should be known. In b.c.c. metals the dislocation density

Table 11. Inter-cluster spacing in irradiated vanadium

Material	n = Volume density (cm^{-3})	Spacing between clusters $S' = (1/n)^{1/3}$ (Å)
Vanadium-60 ppm oxygen	5.4×10^{15}	570 Å
Vanadium-205 ppm oxygen	1.28×10^{16}	427 Å
Vanadium-640 ppm oxygen	2.50×10^{16}	342 Å

increases with increasing interstitial content as shown by Köthe (212) in tantalum, by Ke (237) in niobium and Thomas and Leak (238) in alpha iron. In the experiments described here, the yield drop in the material with higher oxygen content occurs at lower strain than in material with low interstitial content. This effect thus counteracts the effect of increased density of dislocations due to increased interstitial content. A representative density in b.c.c. metal at the strain under consideration here can be taken as 10^9 to 10^{10} cm^{-2} implying an average spacing between dislocations of about 1000 to 3200 Å, which is larger than the spacing between defect clusters (Table 7). The dislocation densities of 10^9 to 10^{10} are overestimates because large regions of the irradiated and deformed material are expected to experience little strain due to the influence of dislocation channeling. Therefore it can be assumed that oxygen atoms migrate to the defect clusters first (since a smaller number of jumps is required to reach the defect clusters), where they are trapped and do not participate in strain aging until the defect clusters are saturated. It can

be shown that all the oxygen available in the samples does not get trapped, because if this did occur, the yield drop would not return. Cochardt et al. (239) have predicted that the number of atoms that an edge dislocation can accommodate per atomic site for carbon in alpha iron is 8. Assuming the same value for oxygen in vanadium, one can calculate the amount of oxygen required to saturate all the defect clusters in the three kinds of material, knowing the average defect cluster diameter. The average defect cluster or dislocation loop diameter extrapolated from single crystal observations (on samples annealed one hour at 200°C) are 155 Å, 94 Å, and 70 Å for V-60, V-205 and V-640 materials, respectively. The amount of oxygen required to saturate these clusters is calculated to be 112 at. ppm, 161 at. ppm and 234 at. ppm, respectively, and the fractions of oxygen removed are 0.59, 0.25 and 0.12, respectively. From this it can be concluded that there is more than enough oxygen available to pin the dislocations after the defect clusters or dislocation loops have been saturated. The times during which the trapping occurs are 1.6×10^5 sec, 5.6×10^4 sec, and 3.30×10^2 sec for V-60, V-205 and V-640 materials, respectively (these times are the cumulative times of annealing before yield drop reappears). It is clear from the above that the time required to remove 112 at. ppm oxygen from V-60 material is much longer than that required to remove 234 at. ppm oxygen from V-640 material. This is in a qualitative agreement with results of McIlwain et al. (83), which show that the annealing time required at 175°C to precipitate a given amount of oxygen decreases with increasing oxygen concentration.

In the bottom portions of Figures 25-27 the true stress - true strain

curves for irradiated V-60, V-205 and V-640 materials are shown. A careful examination of these curves shows that in the first few steps of deformation (before the time for the reappearance of yield drop) there is softening of the material (flow stress decreases in the next loading after annealing).

The softening continues to more deformation steps in V-60 than in V-205 and V-640 material. The softening can be explained on the basis of dislocation channeling. In the initial stages of deformation, the channels play an important role. The deformation occurs by the process of widening of the channel, until they become saturated with dislocations. These dislocations give rise to a back stress so that no new dislocations can glide in the channels and new channels form. In case of V-640 materials the dislocation density is high; therefore the channels saturate sooner than for the other two materials. Once the yield drop reappears, dislocation pinning and unpinning predominate over channeling. The load-unload-anneal-reload experiments should not be confused with radiation-anneal hardening experiments. In the latter case the role of channeling is nonexistent, since the lower yield stress upon first loading is measured.

Figures 28-30 show the true stress - true strain curves for isochronal anneals. The top portions of Figures 28-30 show the behavior of unirradiated material. There is a general recovery which sets in at about 450-500^{o}C (0.32-0.34 T_m) in all the three materials and the yield drop is lost. This recovery can be explained to be due to oxygen going back into solution and leaving the dislocation sites, and also to annihilation of dislocations themselves as a result of formation of attractive junctions, which causes a

reduction of dislocation line length. Similar observations have been made by Stephens and Form (210) in tungsten at about 0.34 T_m.

The behavior of irradiated material is not so easy to explain. There appear to be three distinct regions: 150 to 300°C, 300 to 500°C, and 500°C and above. The recovery stage about 500°C is similar to that observed for unirradiated material. The first region is characterized by appearances of yield drops, although they are not very well defined in the case of the two low interstitial alloys. In this region the oxygen is being trapped by defect clusters and dislocations giving rise to yield drops. At the temperatures where clear yield drops are observed in V-200 ppm oxygen and V-640 ppm oxygen, the oxygen has enough mobility to reach dislocations and pin them.

The region between 300°C and 500°C, where stress drops and then increases until the third stage sets in, is a result of many processes occurring simultaneously and it is difficult to separate their contributions. It will suffice here to point out the processes that may contribute to this stage. They are: 1) trapping of oxygen by defect clusters, 2) segregation of oxygen at dislocations, 3) redissolution of oxygen in the matrix, 4) reduction in the number density of dislocation clusters, 5) recovery of polygonization, 6) annihilation of dislocations, and 7) dislocation channeling. The effect of prior strain on strain aging in irradiated material is manifested in Figures 31-33. In Figure 31 it is seen that a prior strain of about 3% followed by a 175°C anneal for 2 hr produces a yield drop only in the V-640 sample and not in the other two. It is contended that 2 hr at 175°C is sufficient time for oxygen to saturate the defect clusters (not

annihilated by dislocation channeling) in V-640 and migrate to dislocations and effectively pin them. Besides, the V-640 sample will have higher dislocation densities than the other two materials. Therefore oxygen atoms have to make fewer jumps to reach the dislocations because: (a) the distance between oxygen atoms is shorter (b) the dislocation density is higher.

It can be seen in Figure 32 that at 6% strain V-205 samples also exhibit a yield drop after 175^{o}C anneal for 2 hr, since now the density of defect clusters is reduced (due to annihilation by dislocation channeling) and the density of dislocations is increased. Therefore, oxygen atoms had enough time to saturate the remaining defect clusters. V-60 material does not show a well-defined yield drop for the same treatment.

Figure 31 (bottom) shows that a second anneal of 6 hr at 175^{o}C for the V-60 sample produced an increase in flow stress even after a prior strain of 3%. This is due to the migration of oxygen to defect clusters causing strengthening (RAH). Similar behavior is observed for V-205 and V-640 in Figures 31-33. Figure 31 shows the stress-strain curves upon instant reloading of samples. The experiments were performed to see if the Haason-Kelly (240) effect was present. The same experiments were done on unirradiated material (not shown here). There was no evidence of the Hasson-Kelly effect in vanadium. Some of the results of strain aging in irradiated vanadium have been presented by Wechsler and Bajaj (225).

D. Dislocation Channeling

As has been described in Chapter II, the term "dislocation channeling" refers to the process of removal of radiation-produced defect clusters by subsequent plastic deformation. Figures 36-38 show the dislocation channels

in vanadium containing 95, 300 and 500 ppm oxygen, respectively. In general, no major differences were evident in dislocation channels in vanadium containing 95-500 ppm oxygen.

Dislocation channels and inhomogeneous deformation of irradiated crystals have been reported previously, in particular in refractory b.c.c. metals by Tucker et al. (67,191) in niobium and Huang and Arsenault (192) and Shiraishi et al. (50) in vanadium. In the present study, dislocation channels have been observed in vanadium independent of the oxygen content, which is in agreement with the results of Huang and Arsenault (192). Figure 36 shows a typical channeling phenomenon in V-95 material where the channels are essentially devoid of the defect clusters. At the channel intersections, however, one can observe dislocation tangles. The dislocation tangles are not only present at the intersection of the channels, but within the channels as well, independent of the oxygen concentration as is evident in Figures 37-39 for V-300, V-500 and V-95, respectively. The dislocation density within the channels generally increases with increasing oxygen content and the thickness of the foil under observation. This is also in agreement with results of Huang and Arsenault (192).

Figure 36 shows an interesting feature. In the center of Figure 36 and at the right hand bottom one can see intersecting channels with offsets. The offsets provide some measure of the amount and direction of the shear displacement produced by the dislocation producing the channels. At the intersection in the center of the figure, the offset is about half the width of channel (1500 Å) in the $[1\bar{1}0]$ direction, and at the bottom right it is about the width of the channel running from top to bottom. These offsets

correspond to about 1-2 dislocations moving along the channels per atomic plane, which is in agreement with estimates provided by Sharp (188) and Tucker et al. (67,191) in copper and niobium, respectively.

The concentration of the strain within the channel results in the coarsening of slip lines observed on polished surfaces of irradiated metals, as is seen in Figures 34 and 35 in vanadium. Tucker et al. (67,191) have shown from the observation of channel boundary intersections that, although the strain is inhomogeneously distributed as a whole in irradiated metals, the strain within the channel is distributed uniformly. Although no such intersections were observed in the present study, the rather uniform width of a given channel and also the constancy of the width on both sides of the intersection suggest that the strain is distributed uniformly and that the source of dislocations producing the slip dislocations is the same and no new source operates at the intersection of the channels. The intersections of channels in Figure 37 do not reveal offsets very clearly. This is due to the fact that the channel plane is not perpendicular to the electron beam direction. This also is the reason why the channels do not appear completely cleared of the radiation-produced defect clusters. Another reason for the apparent absence of the offset may be the similar magnitude of the strain associated with the intersecting channels.

Dislocation channeling has also been observed in post-irradiation annealed samples in the present study. Tucker et al. (67,191) concluded that in niobium, post-irradiation annealed for two hours in the temperature range near 400^{o}C where maximum radiation anneal hardening is observed, there is little evidence of dislocation channeling and considerable dislocation

structure in regions rich in defect clusters. The decreased tendency for dislocation channel formation was taken as evidence that post-irradiation annealing in some way makes the removal of defect clusters more difficult by slip dislocations. Tucker et al. (191) suggested that interstitial impurities migrate to radiation-produced defect clusters during annealing, strengthen them and cause the slip dislocations to bow around the defect clusters instead of breaking through them. In the vanadium used in this study, however, dislocation channels were observed in the post-irradiation-annealed condition (annealed at 300°C and 400°C) independent of oxygen content. The essential differences between channels in post-irradiation-annealed and as-irradiated material are that for the post-prradiation-annealed material: (a) channel walls are not well defined, (b) there are many more tangles and dislocations inside the channels, and (c) defect clusters were observed inside the channels. The above three observations can be explained on the basis that the defect clusters in the post-irradiation-annealed material are relatively strong and provide more resistance to slip dislocations during their passage through the matrix. The dislocations get pinned at the defect clusters resulting in tangles or move around them leaving the defect clusters inside the channels. During the observation of dislocation channels caution should be exercised in choosing the area for observations. As an example, one may erroneously conclude from Figure 44 that there are no dislocation channels in the material and only dislocation tangles are present. The area under observation shows many tangles and no well-defined channel denuded of defect clusters. Other areas in the same sample, however, show channels which are relatively well

defined. The presence of dislocation channels in post-irradiation-annealed vanadium is in agreement with the observations of Shiraishi et al. (50) who observed channels in vanadium post-irradiation annealed at 400°C.

Figure 40 shows a dislocation channel in irradiated vanadium deformed at liquid nitrogen temperature. The channel appears to have a wedge shape and the inside of the channel is cleared of the defect clusters. However, the channel wall is not well-defined and some clusters can be observed inside the channel at the top left-hand side. The width of the channel in V-95 deformed at 77°K appears to be larger than in the same material deformed at room temperature. However, Sharp (188) has found the reverse to be true for copper. No explanation can be given for this effect at the present time because of lack of available information.

In the process of formation of dislocation channels the most important step is the elimination of defects by glide dislocations. Various mechanisms have been proposed for this event. The following mechanisms are worth consideration:

a) Sweeping of the defect clusters

b) Annihilation of defects by anti-defects

c) Elimination by dislocation-cluster interaction

d) Annealing of the defect clusters by heat of plastic deformation.

The mechanism of sweeping of the defect clusters by dislocations in a manner of a snowplow can be rejected for the case of channels in irradiated vanadium since the concentrations of defect clusters near the wall of the channels is about the same as in the matrix.

The annihilation of defect clusters by anti-defects involves generation

of defects of opposite nature by moving dislocations (vacancies if the defect clusters are interstitial loops and vice-versa). This mechanism is unlikely in view of the observation by Sharp in which dislocation channeling was observed in copper deformed at $4^{o}K$ where atomic diffusion is minimal. In the present case, channels were observed in irradiated vanadium deformed at liquid nitrogen temperature as shown in Figures 40 and 41.

Various mechanisms have been proposed by which the slip dislocations interact with the defect clusters (dislocation loops), incorporate them into slip dislocations, convert them to glissile configuration or alter the shape to facilitate elimination. If the dislocation loop and the slip dislocation have the same or opposite Burgers vectors, the loop can be partially incorporated into the slip dislocation by a mechanism proposed by Saada and Washburn (203). However, not all the loops will have Burgers vectors in the favorable orientations was pointed out by Sharp (188). Strudel and Washburn (205) have proposed another mechanism of interaction of dislocation loops with moving dislocations in f.c.c. metals. Foreman and Sharp (204) have also proposed a mechanism for f.c.c. metals which is shown in Figure 5 in Chapter II.

A mechanism of elimination of defect clusters by heat of deformation has been proposed by Tucker et al. (191). According to this mechanism the defect clusters can be eliminated by the local heat produced by the inhomogeneous deformation. It has been said above that the shear strains produced during the channel formation are of the order of 1.8. The increase in temperature during plastic deformation can be calculated knowing the shear

stress and shear strain and assuming adiabatic conditions. The calculated temperature rise for V-500 is about 110°C. For example, for V-500 material the shear stress τ can be approximated as 32.6 Kg/mm^2. Assuming that on the average 1.5 dislocations operate per plane, then the shear strain γ produced is 1.5 x $\sqrt{3}$ / $\sqrt{2}$ since b = $\sqrt{3}$(a/2) and {110} spacing is $\sqrt{2}$a/2 where a is the lattice parameter. The energy of plastic deformation per unit volume is then

$$E_{PD} = \tau\gamma = 32.6 \text{ Kg/mm}^2 = 76 \text{ cal/cm}^3 \quad .$$

Vanadium has a specific heat of about 0.116 cal/g.deg (241).

Therefore, under adiabatic conditions the temperature rise would be 110°C if all the energy of plastic deformation converted to heat. This increase of 110°C above room temperature is insufficient to cause the annihilation of defect clusters within the channels. However, the above calculation assumes that the energy of plastic deformation is distributed uniformly among all the atoms in the channels. If one assumes that the energy is dissipated under adiabatic conditions among the atoms in a volume in the proximity of the defect clusters comprising a fraction of the volume of atoms in channel, the local increase in temperature would be enough to anneal the defect clusters. For example, assuming the fraction to be one tenth, the rise in temperature would be about 1100°C which is more than sufficient to annihilate the defect clusters.

Although no definite mechanism of elimination of defect clusters can be forwarded because of the complexity of the process, the mechanism of annealing of defects by heat of deformation seems quite plausible. More careful work

needs to be done to verify the concept.

The formation of dislocation channeling is of major importance in mechanical properties of irradiated materials. The irradiated materials deform inhomogeneously in channels, consequently the work hardening rate and the uniform elongation are reduced. The loss of uniform elongation is of concern with regards to the use of materials in nuclear environments.

E. Radiation-Anneal Hardening

Figure 21 shows a plot of hardness versus post-irradiation annealing temperature for vanadium containing three levels of oxygen. Figures 9 and 10 show plots of yield stress and difference in yield stress between irradiated and unirradiated vanadium containing three oxygen levels versus annealing temperature. From Figures 9, 10 and 12 it can be concluded that the radiation-anneal hardening in vanadium increases with increasing oxygen concentration. This result tends to support the interpretation made earlier by Ohr et al. (78) for Nb that RAH is due to trapping of interstitial impurities at radiation-produced defect clusters, in contrast to interpretations based on the motion of lattice vacancies (77,81).

Figure 61 shows diamond pyramid hardness plotted as a function of post-irradiation annealing temperature from the present study and from the work of Smidt (49). Again we see that Smidt's hardness values are higher than those of present work, despite the fact that the interstitial concentration (609 at. ppm for O+C+N) was roughly comparable to that for our V-95 material (622 at. ppm for O+C+N). However, when the increase in hardness is plotted (Figure 62), Smidt's radiation-anneal hardening curve is reasonably consistent with that obtained in the present study.

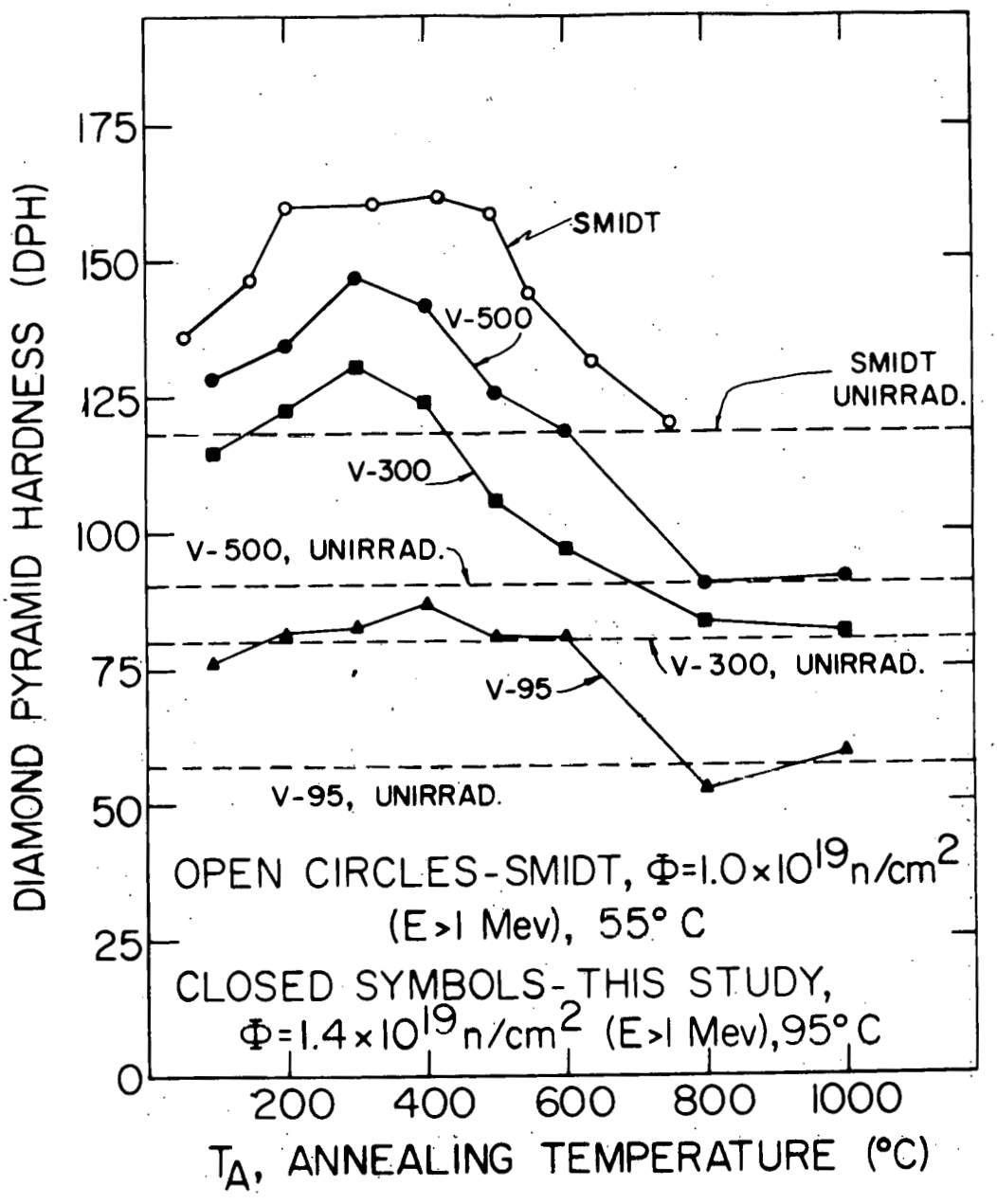

Figure 61. Diamond pyramid hardness vs post-irradiation-annealing temperature for single crystal vanadium used in this study. Figure also shows results of Smidt (49)

Figure 62. Increase in diamond pyramid hardness above unirradiated value, ΔH, vs post-irradiation-annealing temperature for single crystal vanadium used in this study. Figure also shows results of Smidt (49)

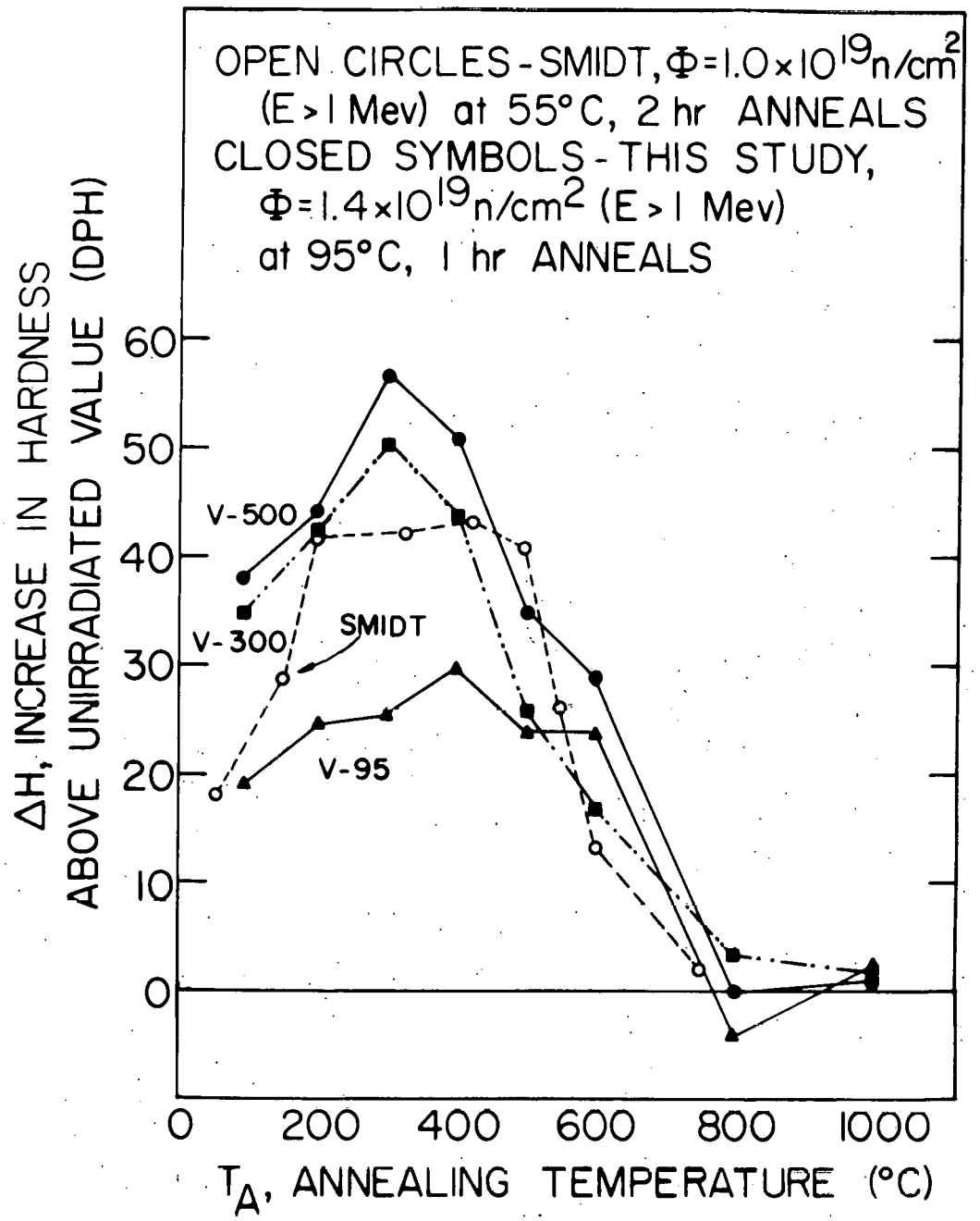
OPEN CIRCLES - SMIDT, Φ = 1.0 × 10^19 n/cm^2 (E > 1 Mev) at 55°C, 2 hr ANNEALS
CLOSED SYMBOLS - THIS STUDY, Φ = 1.4 × 10^19 n/cm^2 (E > 1 Mev) at 95°C, 1 hr ANNEALS
ΔH, INCREASE IN HARDNESS ABOVE UNIRRADIATED VALUE (DPH)
V-500
V-300
SMIDT
V-95
0
10
20
30
40
50
60
0
200
400
600
800
1000
T_A, ANNEALING TEMPERATURE (°C)

Figure 63 shows results of yield stress measurements upon post-irradiation annealing obtained in the present study and those obtained by other authors. The general shapes of the curves are quite similar with two exceptions. First Smolik and Chen (48) did not observe any radiation-anneal hardening for their material designated as Lot A (Item 13, Table 8) irradiated to 4.0×10^{19} n/cm^2 at 107°C. These results are consistent with the observations of Shiraishi et al. (46), who reported reducing amounts of RAH with increasing dose and no RAH for a dose of 1.0×10^{20} n/cm^2 (although they did observe a small amount of RAH for 5×10^{19} n/cm^2). Secondly, Shiraishi et al. (46) observed a small dip in the RAH curve at about 200°C. This is similar to the observation of Ohr et al. (78) for neutron irradiated Nb. The dip in the RAH curve was interpreted by Ohr et al. to delineate two separate RAH peaks, one due to oxygen and the other due to carbon. For the case of vanadium, however, the oxygen and carbon peaks should be unresolved since the activation energies for diffusion of oxygen and carbon in vanadium are almost equal; namely, 1.25 eV for oxygen and 1.18 eV for carbon, respectively (79).

Based on the measurements of yield stress and the density and size distribution of defect clusters, it is possible to evaluate k_1/k_2 as given in Equation 22, viz.

$$\frac{K_1}{K_2} = \frac{(\sigma_I - \sigma_U)}{2Gb} \left(\sum_i n_{I_i} d_{I_i} \right)^{-\frac{1}{2}} . \qquad (48)$$

The factor involving the sum over i is equal to the average interbarrier distance $\bar{\ell}$ as given in Table 4 and plotted in Figure 21 for the V-95, V-300,

Figure 63. Yield stress vs post-irradiation-annealing temperature for neutron-irradiated polycrystalline vanadium reported by various investigators

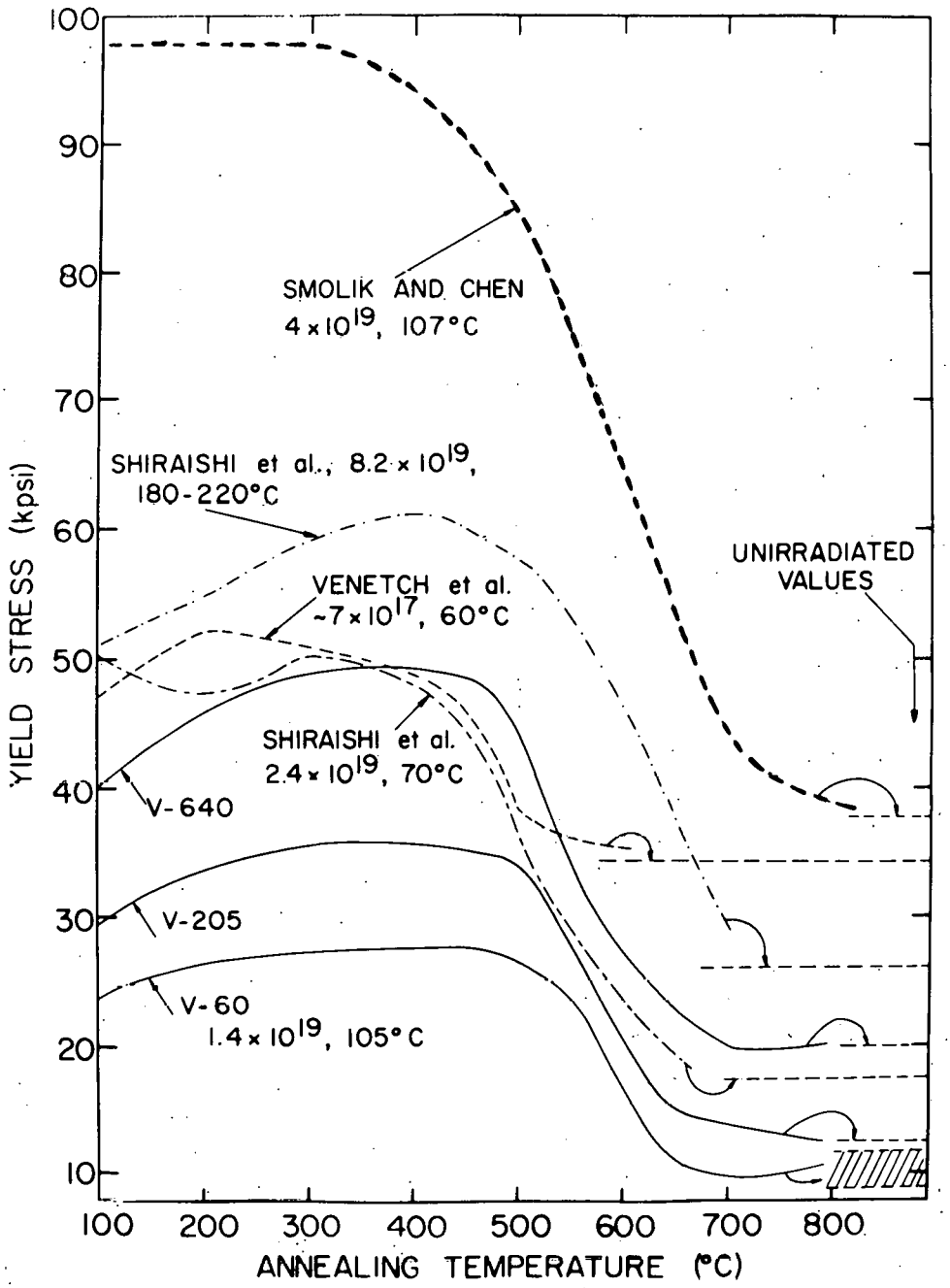
YIELD STRESS (kpsi)
ANNEALING TEMPERATURE (°C)
100
90
80
70
60
50
40
30
20
10
100
200
300
400
500
600
700
800
SMOLIK AND CHEN
4 × 10^19, 107°C
SHIRAISHI et al., 8.2 × 10^19,
180-220°C
VENETCH et al.
~7 × 10^17, 60°C
SHIRAISHI et al.
2.4 × 10^19, 70°C
UNIRRADIATED
VALUES
V-640
V-205
V-60
1.4 × 10^19, 105°C

and V-500 single crystals. However, the polycrystalline samples used for yield stress measurements contained 60, 205 and 640 wt. ppm O. To determine the $\bar{\ell}$ corresponding to these oxygen levels, the following quadratic equation was used to interpolate and extrapolate $\bar{\ell}$ for 60, 205 and 640 wt ppm oxygen:

$$\bar{\ell} = a + b\, C_o + c(C_o)^2 \ . \qquad (49)$$

The values of a, b, and c were determined for C_o = 95, 300 and 500 wt ppm oxygen and then $\bar{\ell}$ was evaluated from Equation 49 for 60, 205 and 640 wt ppm oxygen. Figure 64 shows the plot of oxygen concentration versus $\bar{\ell}$ for various temperatures. Knowing the values of $\bar{\ell}$ at various temperatures from Figure 64 and $\Delta\sigma = \sigma_I - \sigma_U$ from Figure 10, K_1/K_2 could easily be obtained. The values of G and b used for the calculations were 4.76×10^3 kg/mm^2 and 2.62 Å, respectively. Figure 65 shows a plot of K_1/K_2 versus post-irradiation annealing temperature for polycrystalline samples. From Figure 65 it can be seen that K_1/K_2 increases with increasing temperature of annealing for all three kinds of vanadium, and that K_1/K_2 increases with increasing oxygen concentration from 60 wt ppm to 205 wt ppm. However, for vanadium containing 640 wt ppm oxygen K_1/K_2 is very close to or slightly lower than that for 205 wt ppm oxygen.

From Figure 65 it can be seen that K_1/K_2, which is proportional to the barrier strength, increases from a value of ($\sim$ 0.36 - 0.45) and approaches the value of 1.0 for the three materials. The increase in K_1/K_2 with post-irradiation annealing suggests the strengthening of the defect clusters upon annealing. It is believed that the impurities (mainly oxygen) migrate to the defect clusters and strengthen them as barriers to the dislocations.

Figure 64. Interbarrier distance versus oxygen concentration for as-irradiated and post-irradiation-annealed vanadium

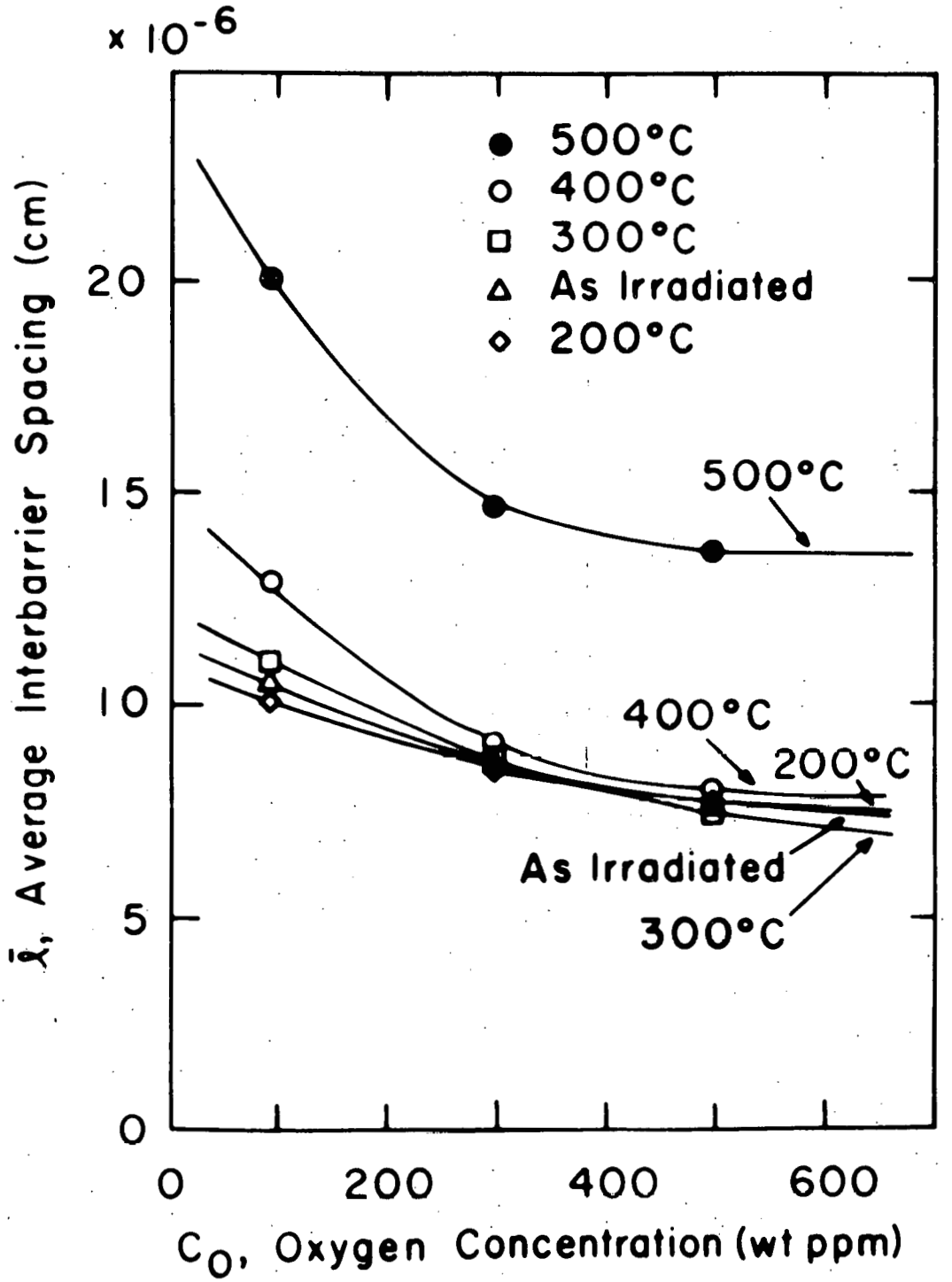
x 10-6
500°C
400°C
300°C
As Irradiated
200°C
500°C
400°C
200°C
As Irradiated
300°C
λ̄, Average Interbarrier Spacing (cm)
20
15
10
5
0
0
200
400
600
C0, Oxygen Concentration (wt ppm)

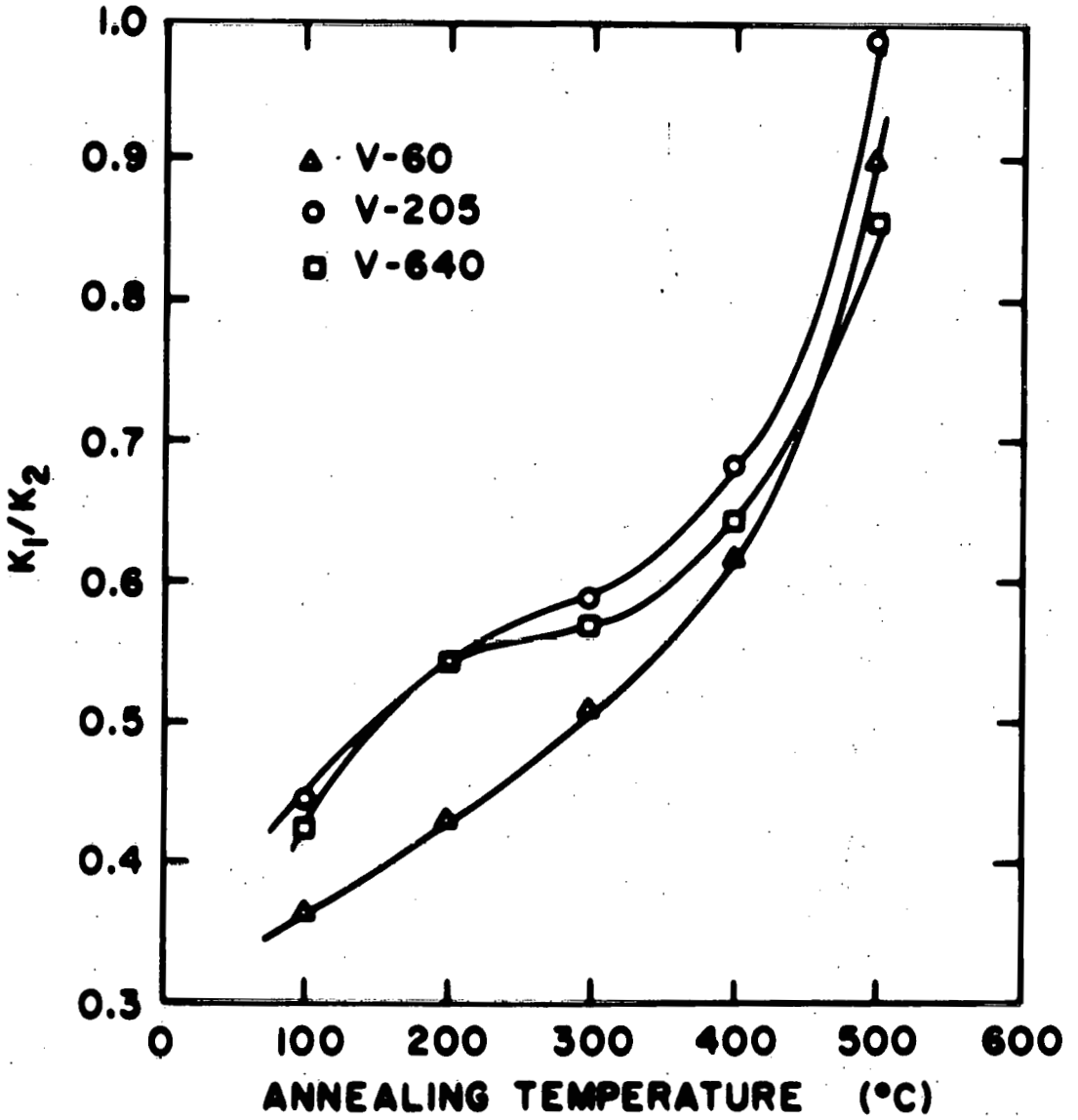

Figure 65. Plot of K_1/K_2 versus post-irradiation annealing temperature

As the temperature of annealing increases, more and more oxygen atoms migrate to the defect clusters.

It can also be seen that at least to a temperature of about 400°C, K_1/K_2 for V-60 lies below that of V-640 and V-205 material, suggesting that the strengthening in V-60 due to migration of oxygen is smaller than in V-640 and V-205 materials. However, K_1/K_2 for V-640 is equal to, or slightly smaller than that for V-205 up to a temperature of 400°C. The reason for this could be two-fold. First, the slight difference may be due to experimental scatter in measurement of yield stress and defect cluster densities. Secondly, the defect clusters become saturated with oxygen and can accommodate no more oxygen atoms available at that temperature. Therefore, the K_1/K_2 parameter does not change significantly although more oxygen is available; or even if more oxygen precipitates on the defect clusters, the strength of the clusters as barriers to dislocation motion remains unchanged.

VI. CONCLUSIONS

Investigation on some aspects of radiation damage in vanadium containing various amounts of interstitial impurity (namely, oxygen) irradiated to a fluence of about $1x10^{19}$ n/cm^2 (E>1 MeV) at a temperature of 95-105°C leads to the following conclusions.

1. The irradiation with fast neutrons causes an increase in yield stress and hardness in vanadium. The increase in hardness is dependent on the oxygen content of vanadium, in that the increase in yield stress and hardness is larger in material containing higher concentrations of oxygen.
2. There is a further increase in yield stress and hardness upon post-irradiation annealing up to temperatures of about 400°C. This increase in yield stress and hardness, termed radiation-anneal hardening, increases with increasing oxygen content. Recovery to the pre-irradiation yield stress and hardness is completed at about 700-800°C.
3. The radiation-anneal hardening in stage III is caused by migration of oxygen to the radiation-produced defect clusters. The precipitation of oxygen on the defect clusters converts them from weak barriers to impenetrable barriers.
4. Transmission electron microscopy of defect clusters in single crystal vanadium irradiated to $1.4x10^{19}$ n/cm^2 (E>1 MeV) at 95°C and post-irradiation annealed at various temperatures shows that:

A. In the as-irradiated condition, the number of defect clusters per cm^3 increases with increasing oxygen content and the average size of defect clusters decreases with increasing oxygen content.

B. Upon post-irradiation annealing, defect clusters increase in size and decrease in density. The temperature of coarsening of defect clusters increases with increasing oxygen concentration.

5. Strain aging studies on unirradiated and irradiated vanadium containing various amounts of oxygen indicate that:

   A. The time of reappearance of yield drop increases with decreasing oxygen content in unirradiated material. The time of reappearance of yield drop is longer in irradiated than in unirradiated material. This leads to the conclusion that irradiation causes retardation in strain-aging tendency (i.e. reappearance of yield drop is delayed).

   B. The retardation of strain aging tendency increases with decreasing oxygen content in vanadium.

   C. The delay in reappearance of yield drop in irradiated vanadium is caused by trapping of oxygen at the defect clusters.

6. Dislocation channels cleared of radiation-produced defect clusters are produced upon deformation of as-irradiated and post-irradiation-annealed vanadium. No major differences

have been observed in channeling with oxygen content of vanadium. No clear mechanism of dislocation channeling can be delineated. A mechanism of annealing of defect clusters by heat of deformation seems plausible.

VII. BIBLIOGRAPHY

1. F. Seitz and J. S. Koehler in "Solid State Physics," F. Seitz and D. Turnbull, Eds., Academic Press, New York, N.Y., 1956, p. 307.

2. H. Brooks in "Annual Review of Nuclear Science," Vol. 6, J. G. Beckerley, M. D. Kamen and L. I. Schiff, Eds., Annual Reviews Inc., Palo Alto, California, 1956, p. 215.

3. G. J. Dienes and G. H. Vineyard, "Radiation Effects in Solids," Interscience Publishers, Inc., New York, N.Y., 1957.

4. D. S. Billington in "Proceedings of the International School of Physics Enrico Course XVIII," Academic Press, New York, N.Y., 1962.

5. A. Seeger in "Proceedings of the Second International Conference on Peaceful Uses of Atomic Energy," Vol. 6, United Nations, New York, N.Y., 1962.

6. J. A. Brinkman, J. Appl. Phys., 25, 961 (1954).

7. L. T. Chadderton, "Radiation Damage in Crystals," Methuen and Co. Ltd., London, 1965.

8. D. S. Billington and J. H. Crawford, Jr., "Radiation Damage in Solids," Princeton University Press, Princeton, N.J., 1961.

9. J. A. Brinkman and H. Wiedersich in "Flow and Fracture of Metals and Alloys in Nuclear Environments," ASTM-STP-380, American Society for Testing and Materials, Philadelphia, PA., 1965, p. 3.

10. A. Seeger in "Radiation Damage in Solids," Vol. 1, International Atomic Energy Agency, Vienna, 1972, p. 101.

11. A. Seeger and U. Essmann in "Radiation Damage in Solids," Academic Press, New York, N.Y., 1962, p. 717.

12. C. O. Smith, "Nuclear Reactor Materials," Addision Wesley Publishing Co., Menlo Park, California, 1967.

13. R. H. Silsbee, J. Appl. Phys., 30, 1388, (1959).

14. M. S. Wechsler in "Neutron Cross Sections and Technology," NBS Special Publication 299, D. T. Goldman Ed., 1968, p. 67.

15. B. Domeij, F. Brown, J. A. Davies, G. R. Piercy and E. V. Kornelsen, Phys. Rev. Lett., 12, 363 (1964).

16. O. S. Oen and M. T. Robinson, Appl. Phys. Lett., 2, 83 (1963).

17. T. S. Noggle and O. S. Oen, Phys. Rev. Lett., 16, 395 (1966).

18. E. Orowan, Discussion in "Symposium on Internal Stresses," The Institute of Metals, London, 1947, p. 451.

19. D. K. Holmes in "The Interaction of Radiation with Solids," R. Strumane, J. Nihoul, R. Gevers and S. Amelinckx, Eds., North-Holland Publishing Co., Amsterdam, 1964, p. 147.

20. R. L. Fleischer, Acta Met., 10, 835 (1962).

21. A. J. E. Foreman and M. J. Makin, Phil. Mag., 14, 911 (1966).

22. J. Friedel in "Electron Microscopy and Strength of Crystals," G. Thomas and J. Washburn, Eds., Interscience Publishers, New York, N.Y., 1963, p. 605.

23. A. J. E. Foreman, Phil. Mag., 15, 1011 (1967).

24. V. F. Kocks, Phil. Mag., 13, 541 (1966).

25. K. H. Westmacott, Phil. Mag., 14, 239 (1966).

26. F. Kroupa and P. B. Hirsch, Discussion Faraday Soc., 38, 49 (1964).

27. K. H. Westmacott, C. W. Fountain and R. J. Stirton, Acta Met., 14, 1628 (1966).

28. A. J. E. Foreman, Phil. Mag., 17, 353 (1968).

29. U. F. Kocks, Acta Met., 14, 1629 (1966).

30. C. Schwink and G. Grieshammer, Phys. Stat. Sol., 6, 665 (1964).

31. J. Friedel, "Dislocations," Pergamon Press Ltd., New York, N.Y., 1964.

32. R. L. Fleischer, J. Appl. Phys., 33, 3504 (1962).

33. R. Peierls, Proc. Phys. Soc., 52, 34 (1940).

34. N. J. Petch, J. Iron Steel Inst., 174, 25 (1963).

35. R. P. Tucker and M. S. Wechsler, Rad. Effects, 3, 73 (1970).

36. T. H. Blewitt, R. R. Coltman, R. E. Jamison and J. K. Redman, J. Nucl. Mater., 2, 277 (1960).

37. J. Diehl in "Radiation Damage in Solids," Vol. 1, International Atomic Energy Agency, Vienna, 1962, p. 129.

38. A. Rukwied and J. Diehl, Z. Metallk., 55, 266 (1964).

39. G. P. Seidel, Phys. Stat. Sol., 25, 175, (1968).

40. J. Diehl, G. P. Seidel and M. Weller in "Proceedings of International Conference on Strength of Metals and Alloys," Suppl. to Trans. Japan Inst. of Metals, 9, 219 (1968).

41. S. B. McRickard, Phil. Mag., 18, 915 (1968).

42. I. L. Mogford and D. Hull, J. Iron Steel Inst., 201, 55 (1963).

43. B. A. Loomis and S. B. Gerber, Acta Met., 21, 165 (1973).

44. A. S. Wronski, G. A. Sargent and A. A. Johnson in "Flow and Fracture of Metals in Nuclear Environments," ASTM-STP-389, American Society for Testing and Materials, Philadelphia, Pa., 1965, p. 361.

45. P. R. V. Evans, A. F. Weinberg and R. J. Van Thyne, Acta Met., 11, 143 (1963).

46. K. Shiraishi, K. Fukaya and Y. Katano, J. Nucl. Mater. 54, 275 (1974).

47. M. Boček, H. Bohm and W. Schneider, J. Nucl. Mater., 40, 249 (1971).

48. G. R. Smolik and C. W. Chen, J. Nucl. Mater., 35, 94 (1970).

49. F. A. Smidt, Jr., Rad. Effects, 10, 205 (1971).

50. K. Shiraishi, K. Fukaya and Y. Katano, J. Nucl. Mater., 44, 228 (1972).

51. T. J. Koppenaal, Phil. Mag., 11, 1257 (1965).

52. T. J. Koppenaal, Phil. Mag. 8, 1313 (1963).

53. T. J. Koppenaal, Acta Met., 12, 487 (1964).

54. M. J. Makin and F. J. Minter, Acta Met., 8, 691 (1960).

55. V. J. Fischer, A. Naturf. 17a, 603 (1962).

56. T. J. Koppenaal and R. J. Arsenault, Phil. Mag., 12, 951 (1965).

57. J. Diehl and G. P. Seidel, Phys. Stat. Sol., 17, 43 (1966).

58. S. M. Ohr, R. P. Tucker and M. S. Wechsler in "Proceedings of the International Conference on the Strength of Metals and Alloys." Suppl. to Trans. Japan Institute of Metals 9, 187 (1968).

59. J. G. Y. Chow, S. B. McRickard and D. H. Gurinsky in "Symposium on Radiation Effects on Metals and Neutron Dosimetry," ASTM-STP-341, American Society for Testing and Materials, Philadelphia, Pa., 1963, p. 46.

60. F. A. Smidt, Jr. and A. L. Bement in "Dislocation Dynamics," A. R. Rosenfield, G. T. Hahn, A. L. Bement and R. I. Jaffee, Eds., McGraw Hill Book Co., New York, N.Y. 1968.

61. M. S. Wechsler, R. G. Berggren, N. E. Hinkle and W. J. Stelzman in "Proceedings of the Symposium on Effects of Radiation on Structural Metals," Special Technical Publication 457, American Society for Testing and Materials, Philadelphia, Pa., 1968, pp. 242-260.

62. D. F. Hasson, Y. Huang, E. Pink and R. J. Arsenault, Trans. Met. Soc., AIME, 5, 371 (1974).

63. R. J. Arsenault and E. Pink in "Second International Conference on the Strength of Metals and Alloys," American Society for Metals, Metals Park, Ohio, 1970, pp. 731-735.

64. M. J. Makin and F. Gillies, J. Inst. Metals, 86, 108 (1957).

65. R. E. Reed, H. D. Guberman, and R. W. Armstrong, Phys. Stat. Sol. 37, 647 (1970).

66. S. M. Ohr, M. S. Wechsler, C. W. Chen, and N. E. Hinkle in "Second International Conference on the Strength of Metals and Alloys," American Society for Metals, Metals Park, Ohio, 1970, pp. 742-746.

67. R. P. Tucker, Ph.D. Thesis, The University of Tennessee, Knoxville, Tenn., 1969.

68. M. S. Wechsler, R. P. Tucker and R. Bode, Acta Met., 17, 541 (1969).

69. R. J. Arsenault, Acta Met., 15, 1853 (1967).

70. R. J. Arsenault and E. Pink, Mater. Sci. Eng., 8, 141 (1971).

71. M. S. Wechsler, D. G. Alexander, R. Bajaj and O. N. Carlson in "Defects and Defect Clusters in BCC Metals and Their Alloys," Nuclear Metallurgy, Vol. 18, R. J. Arsenault, Ed., National Bureau of Standards, Gaithersburg, Maryland, 1973, pp. 127-146.

72. M. S. Wechsler in "Defects in Refractory Metals," R. deBatist, J. Nihoul, and L. Stals, Editors, Studiecentrum voor Kernenergie, Mol, Belgium, 1972, pp. 257-274.

73. M. Boček and J. D. Elen, J. Nucl. Mater., 44, 194 (1972).

74. D. F. Hasson and R. J. Arsenault, Rad. Effects, 21, 203 (1974).

75. J. Moteff, D. J. Michel, and V. K. Sikka in "Defects and Defect Clusters in BCC Metals and Their Alloys," R. J. Arsenault, Ed., National Bureau of Standards, Gaithersburg, Md., 1973, pp. 198-215.

76. R. C. Rau and J. Moteff, Rad. Effects 8, 99 (1971).

77. M. J. Makin and F. J. Minter, Acta Met., 7, 361 (1959).

78. S. M. Ohr, R. P. Tucker and M. S. Wechsler, Phys. Stat. Sol. (a) 2, 559 (1970).

79. R. W. Powers and M. V. Doyle, J. Appl. Phys. 30, 514 (1949).

80. M. E. Downey and B.L. Eyre,Phil. Mag., 11, 53 (1965).

81. A. S. Wronski and A. A. Johnson, Phil. Mag., 8, 1067 (1963).

82. J. Moteff in "Radiation Effects," W. F. Sheely, Ed., Gordon and Breach Science Publishers, Inc., New York, N.Y., 1967, p. 727.

83. J. F. McIlwain, C. W. Chen, R. Bajaj and M. S. Wechsler in "Effects of Radiation on Substructure and Mechanical Properties of Metals and Alloys," ASTM-STP-529, American Society for Testing and Materials, Philadelphia, Pa., 1973, p. 529.

84. J. Venetch, A. A. Johnson and K. Mukherjee, J. Nucl. Mater., 34, 343 (1970).

85. M. Eto, K. Fukaya and K. Shiraishi, J. Nucl. Mater., 48, 365 (1973).

86. D. F. Hasson in "Defects and Defect Clusters in BCC Metals and Their Alloys," R. J. Arsenault, Ed., National Bureau of Standards, Gaithersburg, Md., 1973, pp. 147-162.

87. N. E. Hinkle, S. M. Ohr and M. S. Wechsler in "The Effects of Radiation on Structural Materials," American Society for Testing and Materials, Philadelphia, Pa., 1967, p. 573.

88. M. S. Wechsler in "Defects in Refractory Metals, R. deBatist, J. Nihoul, and L. Stals, Editors, Studie-Centrum voor Kernenergie, Moe, Belgium, 1972, pp. 235-240.

89. D. G. Martin, Acta Met., 5, 371 (1957).

90. G. H. Kinchin and M. W. Thompson, J. Nucl. Energy, 6, 275 (1958).

91. D. E. Peacock and A. A. Johnson, Phil. Mag., 8, 563 (1963).

92. J. Nihoul in "Radiation Damage in Solids," Vol. 1, International Atomic Energy Agency, Vienna, 1962, p. 309.

93. J. Nihoul, Phys. Stat. Sol., 2, 308 (1964).

94. L. Stals and J. Nihoul, Phys. Stat. Sol. 8, 785 (1965).

95. H. Schultz, Acta Met., 12, 649 (1964).

96. J. H. Perepezko, R. F. Murphy and A. A. Johnson, Phil. Mag., 19, 1 (1969).

97. A. A. Johnson, Scripta Met. 7, 1 (1973).

98. A. A. Johnson, Scripta Met. 7, 15 (1973).

99. J. M. Williams, W. E. Brundage and J. T. Stanley, Met. Sci. J., 2, 93 (1968).

100. R. Bullough, J. T. Stanley and J. M. Williams, Met. Sci. J., 2, 93 (1968).

101. F. Schlat and A. Kothe, Acta Met., 14, 425 (1966).

102. A. Kothe and F. Schlat, J. Mater., Sci., 2, 201 (1967).

103. R. J. Dinter, Z. Metallk, 58, 70 (1967).

104. L. J. Cuddy, Phil. Mag., 12, 855 (1965).

105. L. J. Cuddy and J. C. Raley, Acta Met. 14, 440 (1966).

106. F. E. Fujita and A. C. Damask, Acta Met., 12, 331 (1964).

107. A. R. Rosenfield, Acta Met., 12, 119 (1964).

108. J. Nihoul and L. Stals, Phys. Stat. Sol., 17, 295 (1966).

109. L. Stals, J. Nihoul and R. Gevers, Phys. Stat. Sol., 15, 717 (1966).

110. J. T. Stanley, J. M. Williams, W. E. Brundage and M. S. Wechsler, Acta Met., 20, 191 (1972).

111. M. S. Wechsler, J. M. Williams and J. T. Stanley, Scripta Met. 7, 7 (1973).

112. J. Silcox and P. B. Hirsch, Phil. Mag. 4, 1356 (1959).

113. "Lattice Defects in Quenched Metals," R. J. J. Cotterill, M. Doyama, J. J. Jackson and M. Meshii, Eds., Academic Press, New York, N.Y. (1965).

114. "International Conference on Vacancies and Interstitials in Metals," J. Diehl, W. Schilling and D. Schumacher, Eds., KFA - Jülich, 1969.

115. S. Amelinckx in "The Interaction of Radiation with Solids," R. Strumane, J. Nihoul, R. Gevers and S. Amelinck, Eds., North Holland Publishing Co., Amsterdam, 1964, p. 682.

116. S. Amelinckx in "Direct Observation of Dislocations," Solid State Physics, Suppl. 6, Academic Press, New York, N.Y., 1964.

117. "Modern Diffraction and Imaging Techniques in Material Science," S. Amelinckx, R. Gevers, G. Remaut and J. Van Landuyt, Eds., North Holland Publishing Co., Amsterdam, 1970.

118. S. Amelinckx in "Trace Characterization Chemical and Physical," W. W. Meinke, B. R. Scribner, Eds., National Bureau of Standards, U.S. Department of Commerce, NBS Monograph 100, U.S. Government Printing Office, Washington, D.C., 1967.

119. M. Ruhle in "Radiation-Induced Voids in Metals," J. W. Corbett and L. C. Ianniello, Eds., U.S. Atomic Energy Commission Office of Information Service, Washington, D.C., 1972, p. 255.

120. "Radiation Damage in Reactor Materials," Symposium Proceedings, International Agency for Atomic Energy, Vienna, 1969.

121. M. Wilkens in "Vacancies and Interstitials in Metals," A. Seeger, D. Schumacher, W. Schilling and G. Diehl, Eds., North Holland Publishing Co., Amsterdam, 1970, p. 485.

122. E. Reudl and E. Staroste in "Proceedings of 7th International Congress on Electron Microscopy," Vol. 11, International Federation of Sicieties of Electorn Microscopy, 1970, p. 343.

123. P. B. Hirsch, A. Howie, R. B. Nicholson, D. W. Pashley and M. J. Shelan, "Electron Microscopy of Thin Crystals," Butterworths, London, 1965.

124. B. Edmundson and G. K. Williamson, Phil. Mag., 9, 277 (1964).

125. H. Hashimoto, A. Howie and M. J. Whelan, Proc. Roy. Soc. (London), A269, 80, 1962.

126. A. Howie and M. J. Whelan, Proc. Roy. Soc. (London), A263, 217 (1961).

127. D. J. Littler, Ed., "Properties of Reactor Materials and the Effects of Radiation Damage," Butterworths, London, 1962.

128. H. Hashimoto, A. Howie and M. J. Whelan, Phil. Mag., 5, 967 (1960).

129. J. B. Newkirk and J. H. Wernick, Eds., "Direct Observation of Imperfections in Crystals," Interscience Publishers, New York, N.Y., 1962.

130. G. Thomas, "Transmission Electron Microscopy of Metals," John Wiley and Sons Inc., New York, N.Y., 1962.

131. G. Thomas and W. L. Bell in "Lattice Defects and Their Interactions," R. B. Hasiguti, Ed., Gordon and Breach Science Publishers, New York, N.Y., 1967.

132. R. Von Jan in "The Nature of Small Defect Clusters," Vol. 1, M. J. Makin, Ed., Atomic Energy Research Establishment, Harwell, Report AERE-R5269, H. M. Stationery Office, London, 1966.

133. G. Thomas and J. Washburn, Eds., "Electron Microscopy and Strength of Crystals," Interscience Publishers, New York, N.Y., 1963.

134. M. Wilkens, Phys. Stat. Sol., 5, 175 (1964).

135. M. J. Makin, A. D. Whapham and F. J. Minter in "Proceedings of the European Regional Conference on Electron Microscopy, (Delft) Vol. 1, 1960, p. 423.

136. M. J. Makin, A. D. Whapham and F. J. Minter, Phil. Mag., 6, 465 (1961); Phil. Mag. 7, 285 (1962).

137. M. Rühle, Phys. Stat. Sol., 19, 263, 1967.

138. M. Rühle, M. Wilkens and U. Essmann, Phys. Stat. Sol., 11, 819 (1965).

139. J. A. Brinkman, A. Sosin and A. Grenall, J. Nucl. Mater., 4, 332 (1961).

140. A. Bourret and D. Dautreppe, Phys. Stat. Sol., 24, K173 (1967).

141. R. M. J. Cotterill and T. J. Koppenaal, Appl. Phys. Lett., 4, 156 (1964).

142. J. C. Crump, Bull. Amer. Phys. Soc., 13, 462 (1968).

143. A. N. Goland, J. Nucl. Mater., 7, 101 (1962).

144. J. Silcox in "Proceedings of the European Regional Conference on Electron Microscopy," Vol. 1, 1962, p. 362.

145. W. R. Thomas and J. L. Whitton, Acta Met., 9, 1075 (1961).

146. T. K. Bierlein and B. Mastel, J. Appl. Phys., 33, 2873 (1962).

147. K. H. Westmacott, A. C. Roberts and R. S. Barnes, Phil. Mag., 7, 2035 (1962).

148. R. J. Arsenault, Editor, "Defects and Defect Clusters in BCC Metals and their Alloys," Nuclear Metallurgy, Vol. 18, National Bureau of Standards, Gaithersburg, Md., 1973.

149. R. deBatist, J. Nihoul, and L. Stals, "Defects in Refractory Metals," Studiecentrum voor Kernenergie, Mol, Belgium, 1972.

150. "Effects of Radiation on Substructure and Mechanical Properties of Metals and Alloys," Special Technical Publication 529, American Society for Testing and Materials, Philadelphia, 1973.

151. J. W. Corbett and L. C. Ianniello, Editors, "Radiation-Induced Voids in Metals," U.S. Atomic Energy Commission, Washington, D.C., 1972.

152. P. Hull and I. Mogford, Phil. Mag., 7, 535 (1962).

153. B. L. Eyre, Phil. Mag., 7, 2107 (1962).

154. B. L. Eyre and A. F. Bartlett, Phil. Mag., 12, 261 (1965).

155. J. S. Bryner in "Radiation Effects," W. F. Sheeley, Ed., Gordon and Breach Science Publishers, Inc., New York, N.Y., 1967, p. 213.

156. J. S. Bryner, Acta Met. 14, 323 (1966).

157. S. M. Ohr in "Sixth International Confress for Electron Microscopy," Maruzen Co., Tokyo, Japan, 1966, p. 427.

158. B. C. Masters, Phil. Mag. 11, 881 (1965).

159. B. C. Masters, Nature 200, 254 (1963).

160. K. Lacefield, J. Moteff and J. P. Smith, Phil. Mag., 13, 1079 (1966).

161. R. C. Rau, J. Moteff and R. L. Ladd, J. Nucl. Mater., 24, 164 (1967).

162. V. K. Sikka and J. Moteff, J. Nucl. Mater., 46, 217 (1973).

163. V. K. Sikka and J. Moteff, J. Appl. Phys. 43, 4942 (1972).

164. K. F. Kerridge, S. S. Sheinin, A. A. Johnson and H. I. Mathews, Phil. Mag., 7, 1073 (1962).

165. B. Mastel, H. E. Kissinger, J. J. Laidler and T. K. Bierlein, J. Appl. Phys., 34, 3637 (1963).

166. J. D. Meakin and I. G. Greenfield, Phil. Mag., 11, 277 (1965).

167. J. L. Brimhall, B. Mastel and T. K. Bierlein, Acta Met., 16, 781 (1968).

168. J. L. Brimhall, B. Mastel and T. K. Bierlein, J. Appl. Phys., 36, 2585 (1965).

169. J. L. Brimhall and B. Mastel, Acta Met., 14, 539 (1966).

170. P. Rao and G. Thomas, Acta Met., 15, 1153 (1967).

171. D. M. Maher and B. L. Eyre, Phil. Mag., 17, 1 (1968).

172. B. L. Eyre and M. E. Downey, Met. Sci. J. 1, 5 (1967).

173. D. M. Maher and B. L. Eyre, Phil. Mag. 23, 409 (1971).

174. B. L. Eyre, D. M. Maher and A. F. Bartlett, Phil. Mag. 23, 439 (1971).

175. J. L. Brimhall, Trans. Met. Soc., AIME 233, 1737 (1965).

176. R. P. Tucker and S. M. Ohr, Phil. Mag., 16, 643 (1967).

177. R. P. Tucker, S. M. Ohr and M. S. Wechsler, in "Radiation Damage in REactor Materials," Vol. I, International Atomic Energy Agency, Vienna, 1969, pp. 215-231.

178. R. C. Rau and R. I. Ladd, J. Nucl. Mater., 33, 297 (1969).

179. J. D. Elen in "Reactor Centrum Nederland Report RCN-96," Dec. 1967, p. 52.

180. R. Carlander, S. D. Harkness and A. T. Santhanam in "Effects of Radiation on Substructure and Mechanical Properties of Metals and Alloys," ASTM-STP-529, American Society for Testing and Materials, Philadelphia, Pa., 1973, p. 399.

181. A. T. Santhanam, A. Taylor and S. D. Harkness in "Proceedings of the 1973 International Conference on Defects and Defect Clusters in BCC Metals and Their Alloys," R. J. Arsenault Ed., Nuclear Metallurgy, 18, 302 (1973).

182. F. W. Wiffen in "Radiation Induced Voids in Metals," J. W. Corbett and L. C. Ianniello Eds., U.S. Atomic Energy Commission Office of Information Service, Washington, D.C., 1972, p. 386.

183. A. H. Cottrell in "Vacancies and Other Point Defects in Metals and Alloy," The Institute of Metals, London, U.K., 1958, p. 1.

184. I. G. Greenfield and H. G. F. Wilsdorf, Naturw., 47, 395 (1960); J. Appl. Phys. 32, 827 (1961).

185. A. Seeger in "The Relation Between the Structure and Mechanical Properties of Metals," Vol. 1, H. M. Stationery Office, London, 1963, p. 3.

186. U. Essmann and A. Seeger, Phys. Stat. Sol., 4, 177 (1964).

187. M. S. Wechsler in "The Inhomogeneity of Plastic Deformation," American Society for Metals, Metals Park, Ohio, 1972, pp. 19-52.

188. J. V. Sharp, Phil. Mag., 16, 77 (1967).

189. J. L. Brimhall and B. Mastel, Appl. Phys. Lett., 9, 127 (1966).

190. R. B. Adamson, Phil. Mag. 17, 681 (1968).

191. R. P. Tucker, M. S. Wechsler and S. M. Ohr, J. Appl. Phys., 40, 400 (1969).

192. Y. Huang and R. J. Arsenault, Rad. Effects, 17, 3 (1973).

193. C. H. Pitt and J. L. Brimhall, Rad. Effects, 10, 71 (1971).

194. R. Vandervoort and J. Washburn, Phil. Mag., 5, 24 (1960).

195. P. W. Shin and M. Meshii, J. Metals, 15, 80 (1963).

196. M. Meshii in "Lattice Defects in Quenched Metals," R. M. J. Cotterill, M. Doyama, J. J. Jackson and M. Meshii, Eds., Academic Press, New York, N.Y., 1965, p. 387.

197. R. Maddin and A. H. Cottrell, Phil. Mag., 46, 735 (1955).

198. T. Mori and M. Meshii, Acta Met., 17, 167 (1969).

199. I. Crivelli-Visconti and I. G. Greenfield, J. Appl. Phys., 39, 2865 (1968).

200. M. V. Bapna, T. Mori and M. Meshii, Phil. Mag., 17, 177 (1968).

201. S. Yoshida, M. Kiritani, J. Deguchi and N. Kamigaki, Suppl. Trans. Jap. Inst. Met., 9, 83 (1968).

202. F. A. Smidt and B. Mastel, Phil. Mag., 20, 651 (1969).

203. G. Saada and J. Washburn, Suppl. J. Phys. Soc. Japan, 18, 43 (1963).

204. A. J. E. Foreman and J. V. Sharp, Phil. Mag., 19, 931 (1969).

205. J. L. Strudel and J. Washburn, Phil. Mag., 9, 491 (1964).

206. A. H. Cottrell and B. A. Bilby, Proc. Phys. Soc., 62A, 49 (1949).

207. R. Bullough and R. C. Newman, Proc. Royal Soc., A266, 198 (1962).

208. W. G. Johnston and J. J. Gilman, J. Appl. Phys., 30, 129 (1959).

209. G. T. Hahn, Acta Met., 10, 727 (1962).

210. J. R. Stephens and G. W. Form in "High Temperature Refractory Materials," Vol. 34, Part 2, R. W. Fountain, J. Malt and L. S. Richardson, Eds., Gordon and Breach Science Publishers, Inc., New York, N.Y., 1962.

211. W. R. Baird and C. S. Hartley, J. Inst. Met., 92, 181 (1962-63).

212. A. Köthe, Acta Met., 16, 357 (1968).

213. Z. C. Szkopiak, Acta Met., 16, 381 (1968).

214. Z. C. Szkopiak and L. W. Derry, J. Nucl. Mater., 13, 130 (1964).

215. P. Soo, Phys. Stat. Sol., 32, 815 (1969).

216. S. A. Bradford and O. N. Carlson, Trans. Met. Soc., AIME, 22, 224 (1964).

217. G. H. Keith and H. G. Iverson, U.S. Bureau of Mines Report, RI 7222, 1969.

218. R. W. Thompson and O. N. Carlson, J. Less Common Metals, 7, 321 (1964).

219. J. W. Edington, T. C. Lindley and R. E. Smallman, Acta Met., 12, 1025 (1964).

220. H. Wagenblast and A. C. Damask, J. Phys. Chem. Solids, 23, 221 (1962).

221. J. T. Stanley in "Diffusion in Body-Centered Cubic Metals," American Society for Metals, Metals Park, Ohio, 1965.

222. A. L. Bement, Report HW-66425, Hanford Atomic Products Operation, Richland, Washington, 1960.

223. K. Veevers and W. B. Rotsey, J. Nucl. Mater., 27, 108 (1968).

224. K. Veevers, W. B. Rotsey and K. U. Snowden in "Applications-Related Phenomena for Zirconium and its Alloys," ASTM STP-458, American Society for Testing and Materials, Philadelphia, 1969, p. 194.

225. M. S. Wechsler and R. Bajaj, Scripta Met., 8, 885 (1974).

226. S. A. Bradford and O. N. Carlson, Trans. ASM 55, 169 (1962).

227. E. A. Loria, J. Less-Common Met. 10, 296 (1966).

228. U. Essmann and M. Wilkens, Phys. Stat. Sol., 4, K 53 (1964).

229. M. Wilkens and M. Rühle in "The Nature of Small Defect Clusters," Vol. 2, M.J. Makin, Ed., Atomic Energy Research Establishment, Harwell Report AERE - R5269, H.M. Stationery Office, London, 1966, p. 365.

230. K. G. McIntyre, Phil. Mag., 15, 205 (1967).

231. K. G. McIntyre and L. M. Brown in "The Nature of Small Defect Clusters," Vol. 2, M. J. Makin, Ed., Atomic Energy Research Establishment, Harwell Report AERE-R5269, H. M. Stationery Office, London, 1966, p. 361.

232. G. Elssner and G. Hörz, J. Less-Common Met. 23, 237 (1971).

233. D. G. Alexander and O. N. Carlson, private communication.

234. E. A. Loria, G. H. Keith, and E. A. Rowe, "Correlation of Yield Behavior in Electrorefined Vanadium with Interstitial Impurities," Report No. 6716, Bureau of Mines, U.S. Department of the Interior, Washington, 1965.

235. O. N. Carlson and D. G. Alexander, "Effects of Oxygen and Nitrogen on the Mechanical Properties of Vanadium Metal," Reviews on High-Temperature Materials," to be published.

236. Z. C. Szkopiak and W. Eliasz, J. Less-Common Met. 11, 273 (1966).

237. T. S. Kê, Phys. Rev. 71, 533 (1947).

238. W. R. Thomas and G. M. Leak, J. Iron and Steel Inst. 180, 155 (1955).

239. A. W. Cochardt, G. Schoek and H. Wiedersich, Acta Met. 3, 533 (1965).

240. P. Haasen and A. Kelly, Acta Met. 5, 192 (1957).

241. R. C. Weast, Ed., "Handbook of Physics and Chemistry," 51st Edition, Chemical Rubber Company, Cleveland, Ohio, 1970.

VIII. ACKNOWLEDGMENTS

I would like to express my sincerest gratitude to Dr. M. S. Wechsler for his constant direction, patient consultation and sincere interest throughout the course of this investigation. Thanks are due the technical staff of the Ames Laboratory, ALRR facility, without whose help the experimental work could not have been carried out. Special thanks are due Wayne Buttry, Dean Woods, Marvin Hill, S. Diamond, T. Dimuzio, Marilyn Martini and Ardythe Hovland for their help.

I would also like to express my appreciation to Drs. Paul Okamoto and Hartmut Wiedersich of the Materials Science Division, Argonne National Laboratory, for providing the electron microscope facility. I sincerely appreciate the help rendered by Dr. G. Taylor of Oxford University, U.K. during the early stages of this investigation.

Thanks of more personal nature are due the author's parents and members of his family for their patience, understanding and moral support throughout the months of this investigation.

The author is grateful to the Ames Laboratory, ERDA and Iowa State University for the assistantship provided for the study.